Final Report UNLV-6

DEVELOPMENT OF NON-PROPRIETARY ULTRA-HIGH-PERFORMANCE CONCRETE AND RAILWAY TIE APPLICATION

By

Ariful Hasnat
Graduate Research Assistant
Department of Civil and Environmental Engineering and Construction
University of Nevada, Las Vegas

and

Nader Ghafoori, Ph.D., Professor
Civil and Environmental Engineering and Construction
4505 S Maryland Pkwy Box 454026,
Las Vegas, NV 89154-4026
nader.ghafoori@unlv.edu

May 2024

DISCLAIMER

The contents of this report reflect the views of the authors, who are responsible for the facts and the accuracy of the information presented herein. This document is disseminated in the interest of information exchange. The report is funded, partially or entirely, by a grant from the U.S. Department of Transportation's University Transportation Centers Program. However, the U.S. Government assumes no liability for the contents or use thereof.

ABSTRACT

This study reports on properties of non-proprietary ultra-high-performance concretes (UHPCs) for railway ties. The research work is divided into three major phases. The first phase reports on optimization of cementitious materials and aggregates and selection of the most suitable water-to-cementitious materials ratio. In the second phase, the transport and durability properties of the optimized UHPCs are determined. In the third phase of the study, assessment on the structural behavior of the full-scale UHPC railway ties is reported. The major variables of this study are binder types (Type V cement, class F fly ash, silica fume, Ground granulated blast-furnace slag, natural pozzolan), binder combinations (binary, ternary, quaternary), aggregate-to-cementitious materials ratio (0.80, 1.00, and 1.20), steel fiber types (hooked and straight), and steel fiber content (0%, 2%, and 3%). The experimental program assesses the fresh properties (flow), demolded unit weight, mechanical properties (compressive, tensile, and flexural strengths, and modulus of elasticity), transport properties (water absorption, volume of permeable void, water penetration, rapid chloride penetration, and surface resistivity), durability (freezing and thawing resistance, deicing salt resistance, and abrasion resistance), and dimensional stability (drying shrinkage). The structural performance of non-proprietary UHPC ties is examined under static center negative moment test, static rail-seat moment test, and center negative cyclic loading conditions.

The outcome of this study revealed that the selected optimized UHPCs displayed excellent bulk properties and dimensional stability. Amongst the utilized cementitious material combinations, UHPCs made with the combined silica fume and class F fly ash, as a partial replacement of cement, performed the best, while the companion mixtures incorporating only class F fly ash exhibited the contrary. An apparent strain-hardening and -softening was observed in the load-deflection response of steel fiber-reinforced UHPCs. Due to better steel to concrete surface adhesion, straight steel fibers had a more positive influence on the mechanical properties and dimensional stability of the studied UHPCs than those of the hooked fibers. Overall, this experimental study supports that, with proper gradations and proportioning, traditional fine aggregates can be used as an effective substitute for the expensive filler materials used to produce the proprietary UHPCs without compromising their mechanical properties and dimensional stability.

The findings of this study also indicated that the type and combination of cementitious materials had a greater influence on surface resistivity and chloride ion penetration resistance than on the strength of the studied UHPCs. The inclusion of silica fume reduced water absorption and permeable voids, while ternary UHPCs with silica fume and fly ash showed a significant reduction in charge passed compared to the reference UHPC. The study also highlighted the unsuitability of the RCPT test for assessing chloride transport through steel fiber-reinforced UHPCs since fibers can short the circuit to result in invalid indication of conductance. The surface resistivity results showed excellent correlation with RCPT findings.

The investigated UHPCs also exhibited exceptional resistance against freezing and thawing deterioration. The post-F-T exposed UHPCs gained strength due to the availability of unhydrated pozzolanic materials, coupled with a favorable curing environment. Amongst the utilized pozzolanic material combinations, the UHPCs made with silica fume and class F fly ash, as a partial replacement for the cement, performed best against freezing and thawing, whereas the companion mixtures containing only class F fly ash, to replace a portion of the cement, showed the highest mass loss. The addition of straight steel fibers had a more positive influence on the freezing and thawing resistance than hooked fibers. The studied UHPCs also exhibited excellent resistance to de-icing salts, with ternary blend UHPCs and steel fibers further enhancing the material's resistance by arresting crack development.

The studied UHPCs also displayed excellent resistance against wear, well above that of the typical concrete currently used in prestressed concrete sleepers/ties. Amongst the utilized cementitious material combinations, the UHPCs made with silica fume as a partial replacement of cement performed best against

abrasion, whereas mixtures containing fly ash showed the highest depth of wear. The relative gain in abrasion of the studied UHPCs was independent of cementitious materials compositions, and steel fiber content and type.

The UHPC Ties constructed using grade 468 MPa steel reinforcing bars exhibited higher ductility and energy absorption. Although the UHPC ties made with grade 738 MPa reinforcing bars sustained higher ultimate loads, they exhibited lower bending displacement at the peak load. Attributed to the shorter span and larger sectional size, the static support negative moment test showed higher ultimate load capacity compared to the static center moment test. The UHPC ties subjected to cyclic loading performed similarly to their static loading counterparts, with the ties made with grade 468 MPa steel reinforcing bars demonstrating higher ultimate load capacity, better energy absorption, and greater ductility. The studied UHPC ties exhibited flexural type failure with vertical cracks, and the observed crack frequencies were slightly higher under cyclic loading. Good bond behavior between reinforcing rebars and concrete was observed for all the studied UHPC ties. Unlike the UHPC ties constructed using grade 738 MPa reinforcing bars, the load-strain response of the UHPC ties made with grade 468 reinforcing bars indicated clear yielding under both static and cyclic loading conditions.

TABLE OF CONTENTS

LIST OF TABLES

LIST OF FIGURES

CHAPTER 1-INTRODUCTION

1.1 General

Railway ties/sleepers play a very important role in transferring the load from rail to ballast. The ties also resist the axial movement of the rail and secure the railway track system. At present, timber is the most common choice of material used in railway ties for its availability, adaptability, and economy. Currently, more than two and half billion timber ties are in use all over the world (Amtrak, 2012). The United States replaces over 14 million timber ties each year. (Railway Technology, 2020). However, physical and mechanical deterioration of timber can result in early-age replacements. In addition to long-term durability issues, according to Manolo et al. (2010), "the most frequent problem that railway industries are facing is the scarcity of quality timbers." Despite of the above-mentioned concerns, most countries still rely on hardwood timber ties.

The highest railway service speed achieved before introducing Shinkansen in Japan in 1964 was nearly 100 miles/hour. Shinkansen increased the train service speed to levels of 125 miles/hour. The new requirements called for a tie component that allowed secure connectivity for the rail, more extended service life, and higher lateral track stiffness (Esveld, 2001). A new generation of railway tracks also have different loading patterns than the older ones. Due to the physical, mechanical, and durability requirements of these new forms of railway, the rail track system must have additional qualities that timber ties do not. For this reason, pre-stressed concrete ties have become common for use in these tracks (Bezgin, 2017). However, prestressed concrete has frequently fallen short of expectations (Ferdous and Manalo, 2014; Janeliukstis et al., 2019). Amtrak built 120,000 concrete ties in 1997, but they only lasted four years before they needed to be replaced (Zeman et al., 2009). Early deterioration of concrete made it challenging for the railway industry to use pre-stressed concrete as a railway tie (Ferdous and Manalo, 2014).

1.2 History and Development of Railway Tie

Railroad ties were possibly first introduced in England in 1837, when separated stone supports were replaced with wooden ties (Morgan 1971). In 1884, J. Monier first patented the use of reinforced concrete in the production of railway ties (Figure 1.1). Later, the first concrete tie experiment was conducted in Germany in 1906 between the line Nuremberg and Bamberg (Railway-technology.com, 2020). In the early 1940s, during World War II, structural designers started to use partial prestressing in making concrete ties. Abeles (1945) conducted partial prestressing to improve ties performance during World War II (only tensioning 40% of the wires in the beams). However, not until early 1960, when prestressed concrete ties became popular in the railway industry.
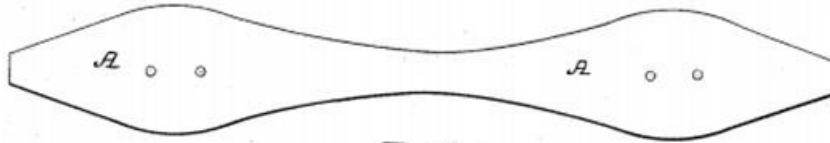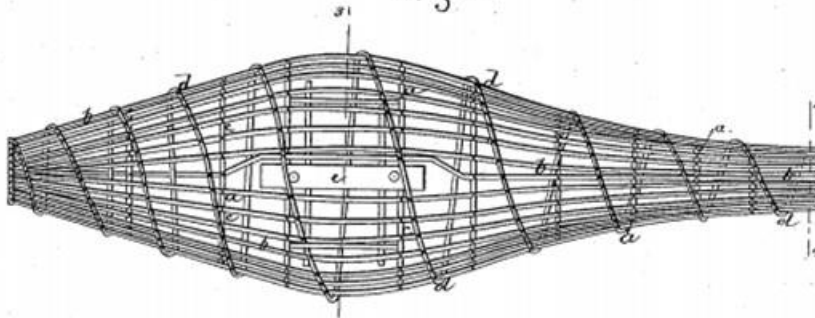
Figure 1.1 Design of first reinforced concrete tie (Monier, 1884)

1.3 Prestressed Concrete (PC) Tie

Concrete was first used for ties in the 1950s due to its numerous advantages. Concrete ties are generally made as precast concrete beams, reinforced with prestressed steel (BSI 2009c; Taylor 1993). Its great load carrying capabilities and extended service life make it more desirable than timber ties, and its heavier weight offers track stability. Nowadays, nearly 500 million railway ties are produced using prestressed concrete, which constitutes more than 50% of the total market (fib bulletin 37, 2006). The typical prestressed concrete tie shape and dimension is depicted in Figure 1.2.
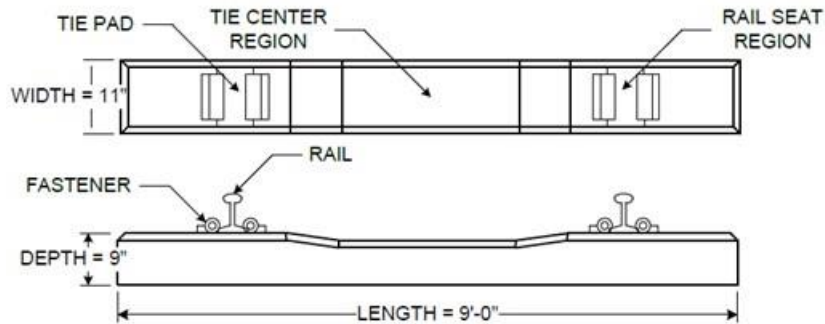
Figure 1.2 Typical prestressed concrete tie shape and dimension (Lutch, 2009) (1 inch=25.4 mm)

Different countries adopted different guidelines for designing PC ties. In the US, the American Railway Engineering and Maintenance-of-Way Association (AREMA) produces the rail standards/guidelines. However, the final authority lies with the tie producers. The European Union (EU) has norms specifically

established for PC ties (EN 13230). The International Union of Railways distributes a design supplement called UIC 713, which offers an example tie design using the EN 13230 (Freudenstein 2007). AREMA and EN 13230 followed different parameters in designing the railway tie. EN 13230 specifies that the train speed factors only change at speeds above and below 124 mph. As can be seen in Figure 1.3, AREMA considers rail seat load as point load, whereas UIC 713R specifies it as a distributed load (Figure 1.4). As a result, different moments were achieved for the same rail seat loading (Figure 1.5) for the given load distribution. Moreover, the EN 13230 completely disregards the influence of tonnage (Freudenstein, 2007). With these backgrounds, in this study, AREMA guidelines were adopted to proceed with further design and analysis of PC ties.
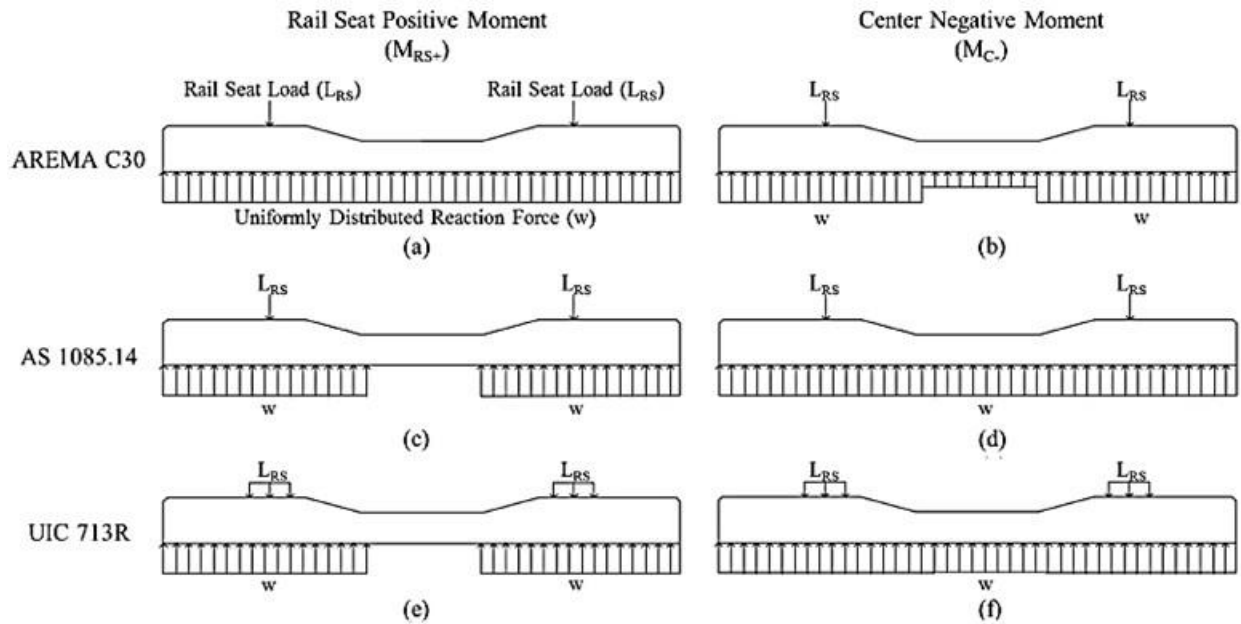
Figure 1.3 Support conditions used in different standards (Gao et al., 2017)
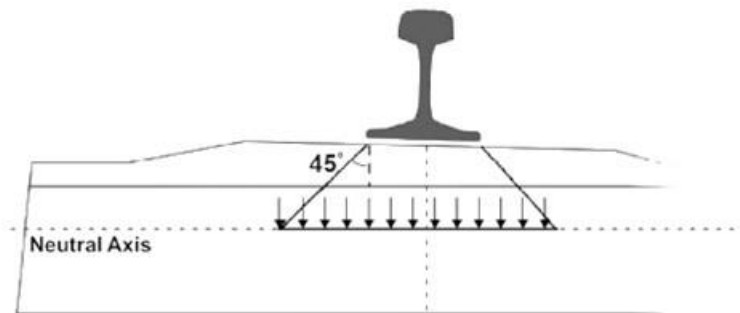
Figure 1.4 Load distribution according to UIC 713R (Gao et al., 2017)
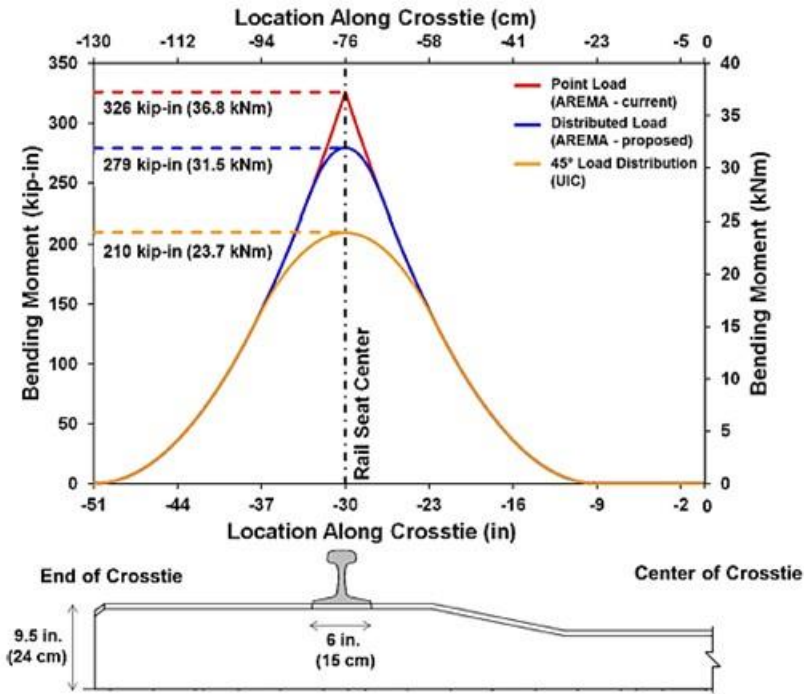
Figure 1.5 Rail seat bending moment comparison for AREMA and UIC (Gao et al., 2017)

1.4 Prestressed Concrete Tie Design per AREMA Guidelines

1.4.1 Design Considerations

In the United States, AREMA provides detailed guidelines for PC tie design. Additional guidelines can be adopted from ACI 318 and ASTM standards. Due to the stiffness of the track, the load from an axle is divided over multiple ties when a train travels along it (Figure 1.6) (Hanna, 1979). A single tie typically carries approximately 50% of an axle load. However, the load distribution depends on rail stiffness, spacing between ties, rail fastening quality, ballast, and subgrade conditions (AREMA 2009).
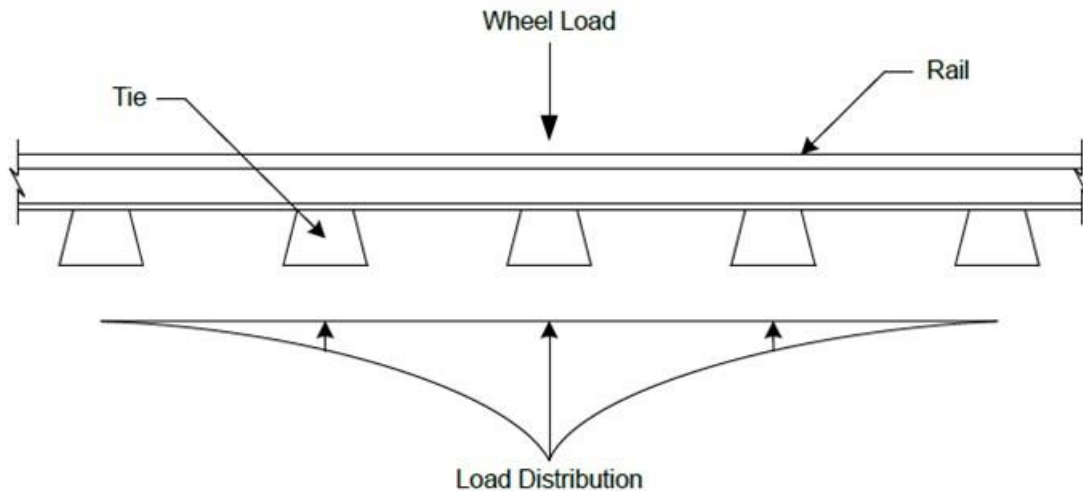
Figure 1.6 Single axle load distribution (Lutch, 2009)

4

1.4.1.1 Load and Moment

Figure 1.7 shows the axle loads carried by a single tie as a function of center-to-center tie spacing distance. For instance, a tie spacing of 610 mm (24 inches) corresponds to each tie carrying 50% of the imposed axle weight. Load distribution according to AREMA is summarized as follows:

(i)   AREMA covers the center-to-center spacings of cross ties of between 508 mm and 762 mm (20 inches and 30 inches).

(ii)   AREMA specifications cover tie designs between 2362 mm (7 ft-9 in) and 2743 mm (9 ft-0 in) in length and between 203 mm (8 in) and 330 mm (13 in) in width at their bottom surface.

(iii)   An impact factor of 200% of static vertical loads has been assumed to evaluate the dynamic effect of wheel and rail irregularities.

(iv)   Maximum allowable ballast pressure should be less than 0.586 MPa (85 psi).
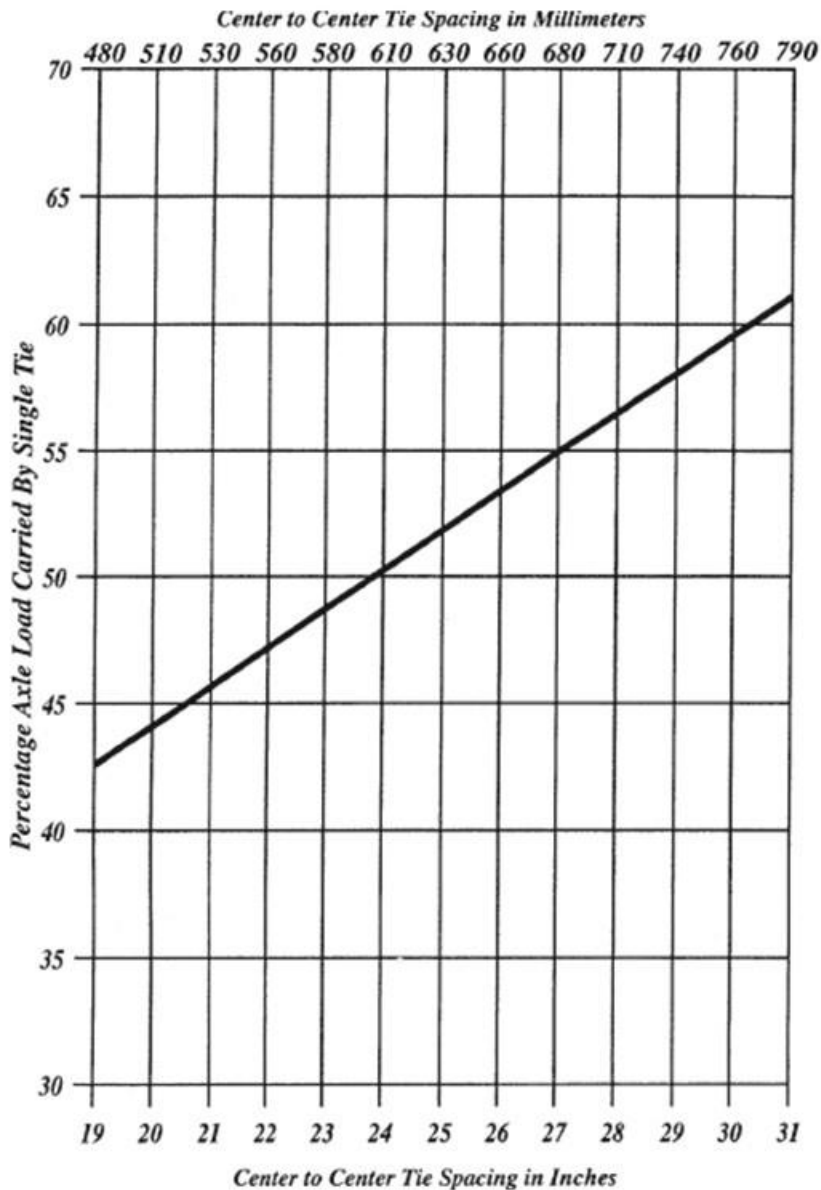
Figure 1.7 Estimated load distribution (AREMA, 2014)

5

By breaking down the load into the axle arrangement known as the Cooper E 80 load, Figure 1.8 illustrates how the growing demand for freight rail transportation increases the maximum capacity from 1272 to 1401 kN (286 to 315 kip) car. As can be seen the 1401 kN (315 kip) load has been equally distributed among four axles spaced at 1524 mm (60 inches) (78 kip/axle or 345 kN/axle). A rail seat load of 286 kN (64.35 kips) is determined in accordance with AREMA requirements, as shown below (AREMA 2014).

$$P_{rail\ seat} = \frac{Axle\ load}{2} * distribution\ factor * \left(1 + \frac{Impact\ factor}{100}\right) \qquad (1.1)$$

$$P_{rail\ seat} = \frac{78}{2} * 0.55 * \left(1 + \frac{200}{100}\right) = 64.35\ kips\ (286\ kN) \qquad (1.2)$$
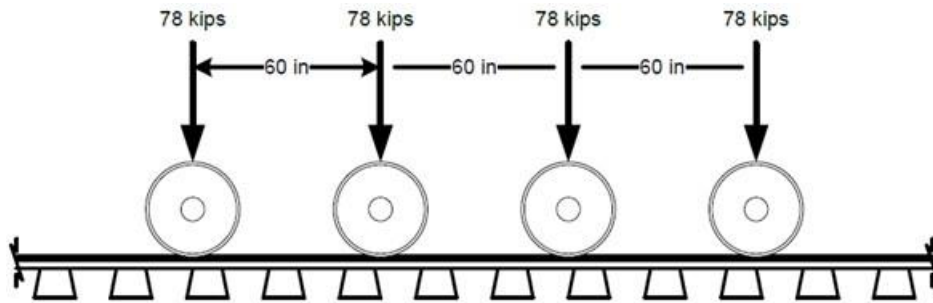
Figure 1.8 Cooper E 80 load configuration (Lutch, 2009) (1 kip=4.448 kN)

Figure 1.9 shows the effects of train speed (V) and tonnage (T) on the rail seat load (AREMA 2014; Freudenstein 2007). For example, using typical values for high speed and tonnage characteristic of railroad such as 120 mph with an annual tonnage of 55 MGT the following rail seat design load was determined:

$$P_{factored} = P_{rail\ seat} * V * T = 64.35 * 1.2 * 0.99 = 76.45\ kips(340\ kN) \qquad (1.3)$$
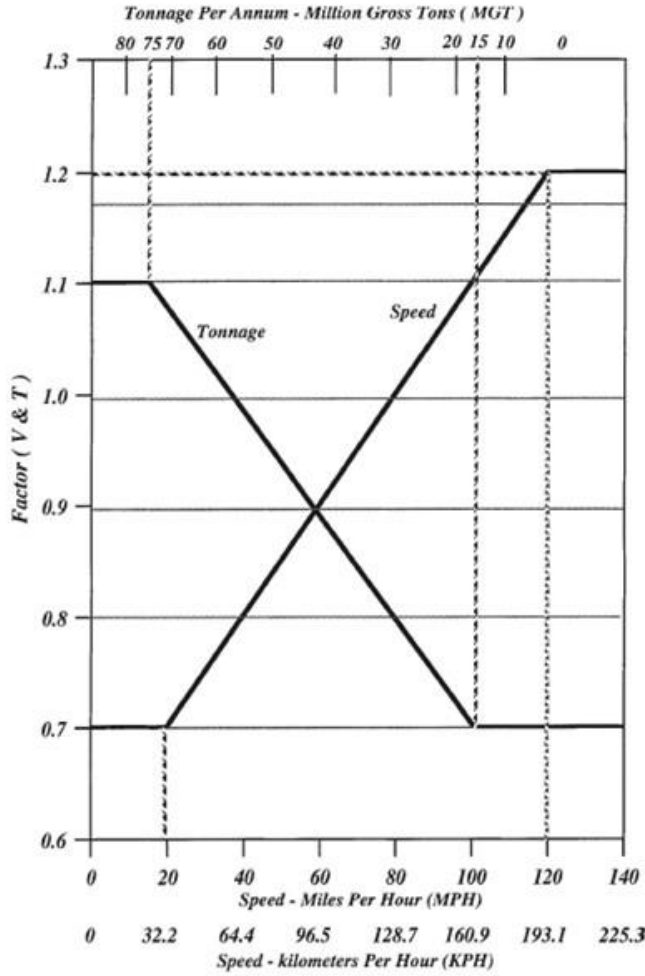
Figure 1.9 AREMA load factor charts (AREMA 2014)

Two load cases are usually considered in designing PC ties. The first load case considers the positive moment produced in the rail seat section due to less support in the center part of the tie (Figure 1.10). The second load case is typical of a heavily used track segment that has not undergone much ballast maintenance. (Figure 1.11).
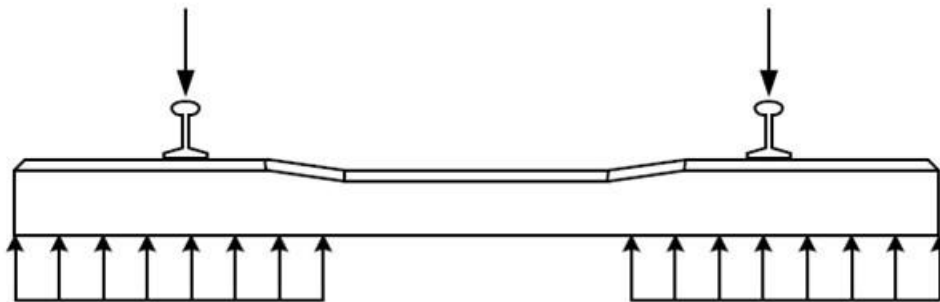
Figure 1.10 Generation of positive moment in rail seat section (Case I) (Freudenstein 2007)
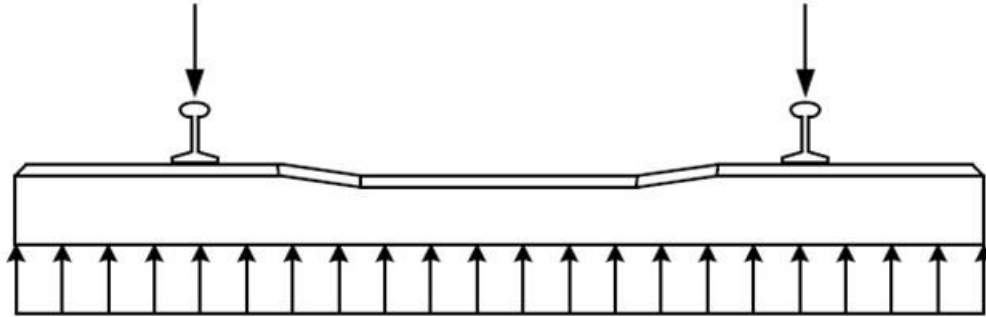
Figure 1.11 Generation of negative moment at center section and continuous positive moment at rail seat (Case II) (Freudenstein 2007)

1.4.1.2 Material Properties and Prestressing

AREMA obtains specifications on the concrete material and prestressing properties from the American Concrete Institute (ACI) Building Code Requirements for Structural Concrete and Commentary (ACI 318). The properties such as allowable tensile and compressive stresses, and allowable prestressing stress are documented in Table 1.1 and Table 1.2, respectively.

Table 1.1 Allowable concrete stress as per ACI 318-08

Allowable Concrete Stresses	Stress Case Description	ACI Code Specification (psi)
Allowable stress at transfer of prestress (before losses)		
σ_{ci}	Extreme fiber stress in compression at prestress transfer, ACI 318-08 18.4.1 (a)	$0.6f'_{ci}$
σ_{ti}	Extreme fiber stress in tension at prestress transfer, ACI 318-08 18.4.1 (b)	$3f'^{0.5}_c$
Allowable stress under service loads (after losses)		
σ_{cs1}	Extreme fiber stress in compression at service (P/S and SDL), ACI 318-08 18.4.2 (a)	$0.45f'_c$
σ_{cs2}	Extreme fiber stress in compression at service (P/S and total load), ACI 318-08 18.4.2 (b)	$0.6f'_c$
σ_{ts}	Extreme fiber stress in tension at service, ACI 318-08 18.3.3 Class U	$7.5f'^{0.5}_c$

Table 1.2 Allowable prestressing stress as per ACI 318-08

Allowable Prestressing Stresses	Stress Case Description	ACI Code Specification (ksi)
f_{pi}	Due to prestressing steel jacking	$0.94f_{py}$
f_{pi}	Due to prestressing steel jacking	$0.80f_{pu}$
f_{pi}	Immediately after prestress transfer	$0.82f_{py}$
f_{pi}	Immediately after prestress transfer	$0.74f_{pu}$

1.4.1.3 Materials Used to Produce PC Ties

The AREMA recommended guidelines for selecting different ingredients of concrete are in Chapter 4 Section 4.2.2. According to AREMA, the minimum concrete compressive strength should be 48 MPa (6960 psi) in order to be accepted in the use of making PC ties. However, many researchers suggested that, higher compressive strength is required to ensure proper prestressing without unwanted cracks in the concrete.

Typically, 7-wire strand or individual strand having ultimate strength of 1862 MPa and 1758 MPa (270 and 255 ksi), respectively, are used to produce PC ties in the north American countries (Figure 1.12).

(a)   **(b)**
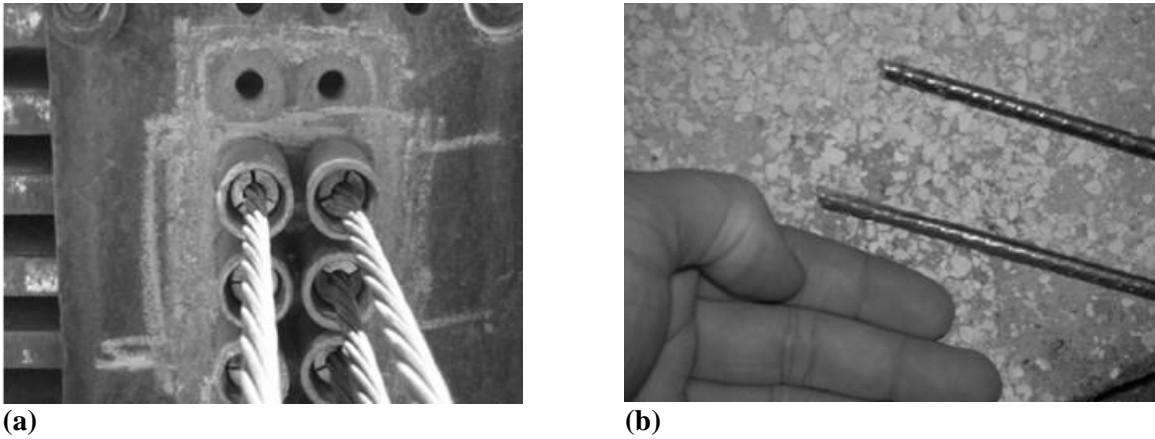
Figure 1.12 Prestressing strands, (a) 7-wire strand, (b) single wire (Lutch, 2009)

1.5 Problem Associated with Prestressed Concrete Ties

The failures of concrete ties have been the subject of investigations by researchers around the globe (Ferdous and Manalo, 2014). The common causes of concrete tie failures are presented in Figure 1.13. As can be seen, the most critical cause of concrete tie failure is rail-seat deterioration. The choice of materials, design, and geometry can change depending on the region. Different problems associated with the prestressed concrete ties are discussed in the following subsections.
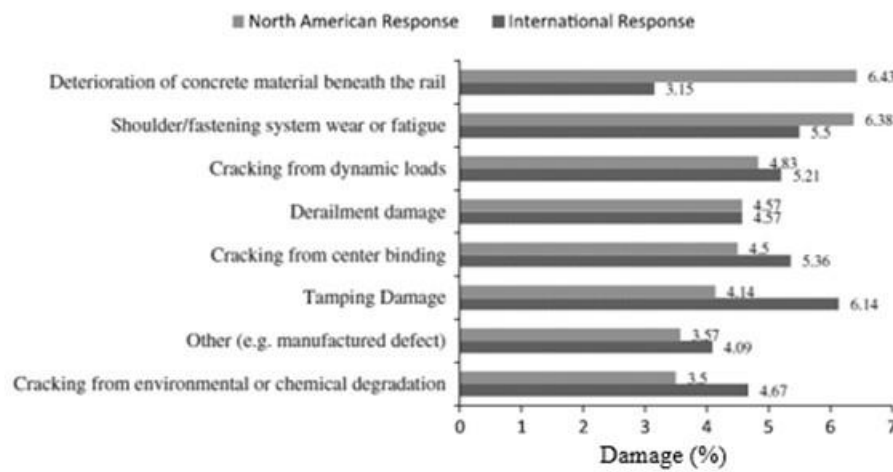
Figure 1.13 Common causes of deterioration in PC ties (Ferdous and Manalo, 2014)

1.5.1 Flexural Crack

A concrete tie's center-span is where flexural fractures are most frequently found, and these cracks are typically caused by anomalies in either the wheel or the rail, such as flat wheels and dipping rails (Murray et al., 1998). Wheel flats can generate 90 kip (400 kN) force in less than 10 ms. In another study Freudenstein (2007) identified two major reason for flexural failure: (i) center negative moment due to

9

ballast consolidation (ii) track vertical deformation due to cyclic loading. Figure 1.14 shows PC tie failure due to negative bending in the center of ties, generated due to heavy vertical load in the rail seat.

Figure 1.14 Flexural failure of PC tie due to negative bending (UK railway forums/broken tie, 2014)

1.5.2 Rail-Seat Abrasion

The rail-seat abrasion failure is caused either by wear in rail-seat, erosion caused by hydro-abrasive force, freezing and thawing of concrete, or hydraulic pressure cracking (Ferdous and Manalo, 2014). Lutch et al. (2009) identified the reasons for the rail-seat abrasion. They are, (i) continuous water presence, (ii) substantial axle loading, (iii) fasteners failure, (iv) poor quality tie pads, (v) sheer track slopes, and (vi) track curves greater than 2°. Figure 1.15 shows an example of a rail-seat abrasion.

Figure 1.15 Rail-seat abrasion failure (Zeman et al., 2009)

1.5.3 Tensile Fracture

Railway track that carries industrial freight commonly faces tensile fracture (González-Nicieza et al., 2008). As can be seen in Figure 1.16a, a X shaped vertical cracks developed in the upper middle part of the PC tie resulted from tensile fracture. In another study, Rezaie et al. (2012) reported extensive longitudinal cracking as a result of pre-tension forces that created tensile stress in the transverse direction around the rawlplug hole.

(a)   **(b)**

Figure 1.16 Tensile fracture failure of railway tie (a) Tensile fracture, (b) Longitudinal cracking
(Gonzalez-Nicieza et al., 2008)

1.5.4 Derailment/Impact Damage

Sometimes railway tracks become inoperable due to manpower faults. Figure 1.17a illustrates damages occurred in the B70 railway ties due to derailment. Figure 1.17b shows failure of PC ties due to impact between trackway machinery and the ties.

(a)   **(b)**

Figure 1.17 Failure of PC ties due to manpower fault (a) Derailment failure of concrete ties, (b) Impact
damage due to trackway machinery (Kaewunruen and Remennikov, 2011)

1.5.5 Fatigue

Typically, from a single train more than hundred wheel axles act successively on each tie during the passageway. This can create a dynamic effect called fatigue. Permanent strains in the concrete rise as a result of the repetitive cyclic loading, and as a result of that, macro-cracks eventually reach the point of rupture. Small cracks do not seem to affect the load carrying capacity, and the load carrying capacity rapidly decreases when the cracking is quite severe (Parvez and Foster, 2017). According to Mallet (1991), cyclic loading may also result in stress concentration at the prestressing wire surface and induce abrupt failure. To avoid fatigue induced failure, AREMA recommended for fatigue testing in their PC design guidelines.

1.5.6 Freezing and Thawing

AREMA requires concrete should have a minimum of 90% of its original performance after completion of freezing and thawing test. As shown in Figure 1.18, conical type failure near the fastener were observed due to freezing and thawing stress.

(a)   **(b)**

Figure 1.18 (a) Railway track covered in snow, (b) Conical crack at the end of a fastener due to freezing and thawing action (Zi et al., 2012)

1.5.7 Sulfate Attack

Sulfates of Na, K, Mg, and Ca may be present in the aggregates used to make PC ties, and these sulfates react with the cement paste's C_3A or CH components when they are in a solution. The product of these reactions causes cracking of the concrete (Ferdous and Manalo, 2014). Additionally, the concrete may deteriorate as a result of delayed ettringite formation (DEF), which is brought on by an internal sulphate attack. Tepponen and Eriksson (1987) reported the development of microcracks as a result of the heat treatment used during the pre-casting process (Figure 1.19).

Figure 1.19 Cracking of prestressed concrete tie due to delayed ettringite formation (Hime, 1996)

1.5.8 Alkali Aggregate Reaction (AAR)

Alkali aggregate reaction (AAR) or alkali silica reaction (ASR) is a significant issue that causes premature deterioration of concrete structures by expanding and creating tensile forces in the concrete, leading to cracking and spalling. It occurs when hydroxyl ions from the pore solution of concrete attack the amorphous silica in the aggregate (Islam and Ghafoori, 2015). Portland cement is the primary source of alkalis in concrete, but other sources such as unclean sand containing sodium chloride, admixtures (super-plasticizers), and mixing water can also be internal sources (Neville, 1995). Alkaline cement solutions' hydroxyl ions may react with silica-containing aggregates like chert, quartzite, opal, and strained quartz crystals, resulting in destructive expansion (Figure 1.20).

Figure 1.20 Cracking in concrete tie due to alkali aggregate reaction (Fournier et al., 2004)

1.5.9 Corrosion

PC ties corrode in regions where saline materials are abundant in the supporting soil or ballast. Despite both being constructed of steel, the risk of corrosion for a PC tie is significantly higher than it is for a rail since a tie establishes close contact with the ballast and subgrade materials. A variety of salts from the soil,

groundwater, or aggregates may come into contact with PC ties and may react with the steel, causing corrosion and tie failure (Figure 1.21).

Figure 1.21 Failure of concrete tie as result of bar corrosion (Mohammadzadeh and Vahabi, 2011).

1.6 Challenges of PC Tie Design and Construction

Based on the literature survey, the following limitations were identified in the existing design and construction of PC ties:

(i) Presently, neither unbalanced loads nor uneven wheel load circumstances are covered by the AREMA specification (AREMA, 2014). This simplifying assumption may be insignificant at slow speeds. However, at faster speeds, there will be more load on the outside rail of a curved segment. When determining the design load for high-speed rail with a significant speed increase, uneven load effects should be taken into account. Furthermore, due to the stiff effects of the track structure discussed in earlier sections, once the axle load is distributed between the individual wheels it must be divided further between the individual ties.

(ii) The approximations provided in ACI 318 are valid for conventional structural concrete but may not be appropriate for high strength concrete (69 MPa (10000 psi) and above), such as those used to make prestressed concrete ties (AREMA, 2014). ACI 363R-92 is used as a guide when designing concrete that has compressive strengths more than 69 MPa (10000 psi) (ACI 363R, 1992). However, ACI 363R-92 does not include all allowable stress limits.

(iii) Current design guidelines for prestressed concrete ties only consider static and quasi-static loading scenarios and do not account for high-magnitude impact loads (Ferdous and Manalo, 2014).

(iv) The likelihood of fatigue failure is minimal as long as the prestressed concrete tie is not cracked. However, fatigue resistance may become crucial if cracking occurs (2006 Fib Bulletin No. 37).

1.7 History and Development of Ultra-High Performance-Concrete (UHPC)

The first documented UHPC was developed in 1972 by Yudenfreund et al. having a compressive strength of 230 MPa (33350 psi) in 180 days by using water-to-cementitious materials ratio of 0.20. Later in 1981, Birchall et al. made some improvement in the mechanical properties by using superplasticizer and pozzolanic admixtures. However, the term Ultra-High Performance Concrete (UHPC) was first used by De Larrard in 1994. In 1998, Lafarge came up with a commercial proprietary UHPC mixture containing 6% steel fiber. During that time, few other proprietary UHPCs were also developed by different companies. Up

until, early 2010s, most of the researchers followed the proprietary mixtures to assess the physical, mechanical, and durability properties of UHPCs. In 2012, Wille et al. used locally available sand as a replacement of expensive quartz sand without compromising the mechanical properties of UHPC. In last 8 years, many attempts have been made to reduce the cost of UHPC by utilizing locally available sand, secondary cementitious materials, various curing condition, and use of different mixing techniques. After 46 years since UHPC was first developed, ASTM C1856/C1856M-17 was the first standard that was published where guidelines for evaluation of fresh and hardened properties of UHPC were presented and first formal definition of UHPC was given in a technical document. ASTM C1856 defined UHPC as a, "cementitious mixture with a specified compressive strength of at least 120 MPa (17500 psi) accompanied with specified durability, ductility, and toughness requirements." In the following year, ACI 239-18 published their first technical report on UHPC. Table 1.3 summaries the historical development of UHPC with breakthrough.

Table 1.3 Development of UHPCs from 1972 to 2020 (1972 to 1992 data from Namman and Wille, 2012)

Year	Reference	Compressive strength (MPa)	Summary
1972	Yudenfreund, Skany, et al.	230	• Paste • Vacuum mixing
1972	Roy et al.	510	• Paste • High pressure and high heat
1981	Birchall et al.	200	• Paste • Polymer addition • Flexural strength up to 150 MPa
1983	Hjorth	120-250	• Normal curing • Use of silica fume
1980's all*	Lankard; Namman	Up to 210	• Mortar • Use of high volume steel fibers (8-15%)
1992	Li and Wu		• Mortar • Synthetic fiber • Strain hardening behavior in tension
1994	De Larrard	Up to 150	• Optimized material with dense particle packing • Use of ultra fine particles
1995	Richard & Cheyrezy	Up to 800	• Heat and pressure curing • Particle packing
1998	Lafarge (DUCTAL)	Up to 200	• 90°C heat curing for three days • Steel fibers up to 6%
2000	CEMTEC	Up to 200	• Hybrid combinations • Up to 9% fibers
2005	CARDIFRC	Up to 140	• Optimized particle packing • Optimized mixing method
2011	Accorsi & Meyar	>150	• First US Workshop on UHPC
2012-2018	Karim et al.	>120	• Use of locally available fine aggregate • Mix design optimization. • Transport properties assessment
2017	ASTM C1856	>120	• First ASTM document on testing of UHPC
2018	ACI 239		• First document published by ACI on UHPC
2020	Bae & Pyo	>140	• First performance evaluation of UHPC in railway tie application

1.8 Application of UHPC in Different Projects

To this date, over hundred UHPC projects have been built successfully in different parts of the world. The US Department of Transportation made a report on UHPC and summarized the application of this concrete in different structural applications in the North America, Europe, Australia and Asia. Some pictorial representation of various structures that used UHPC is given in Figure 1.22. As can be seen, nearly all the UHPCs applications were in bridge constructions.

| (a) | (b) | (c) |
| (d) | (e) | (f) |
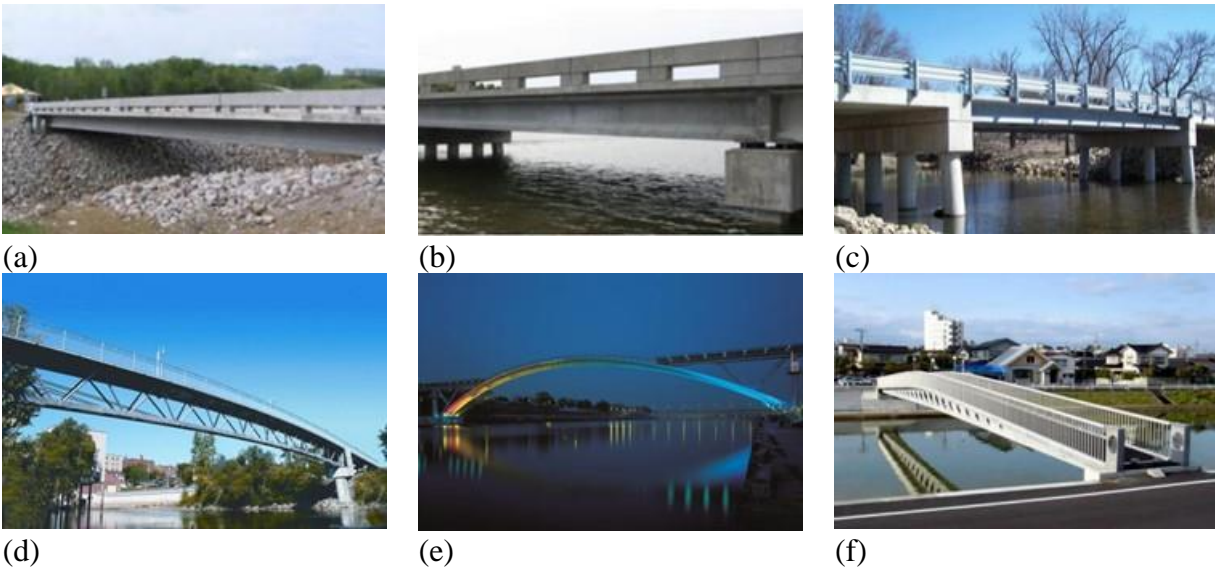
Figure 1.22 UHPC applications (a) Mars Hill Bridge, Wapello County, IA, (b) Route 64 over Cat Point Creek, Richmond County, VA, (c) Jakway Park Bridge, Buchanan County, IA, (d) Pedestrian bridge, Sherbrooke, Quebec, Canada, (e) Footbridge of Peace, Seoul, South Korea, (f) Sakata-Mirai bridge, Sakata, Japan. (FHWA-HRT-13-060)

1.9 Properties of UHPC

1.9.1 Mixing of UHPC

To produce UHPC with the necessary qualities, mixing time, speed, temperature, and order all need to be properly considered (Dils et al. 2012). Because the materials for UHPC are significantly smaller than those for conventional concrete, a specialized mixing technique is used to ensure that the agglomerated small particles are broken up and distributed evenly (Sohail et al., 2018). UHPC requires more energy to mix than conventional concrete, hence the mixing period must be extended. UHPC may overheat as a result of increased input energy, high cementitious material percentages, decreased or omitted coarse aggregate, and low water content. Consequently, appropriate mixing techniques that prevent overheating are needed (Graybeal and Russell 2013). Most studies obtain a homogeneous dry mix of all UHPC constituents before adding water and HRWRs (Wille et al., 2011). Dry mixing results in a higher packing density and, as a result, fewer pores that need to be filled with water.

1.9.2 Fresh Properties of UHPC

Due to a very low w/cm and incorporation of fibers, without chemical admixture, it is not possible to produce a homogenous UHPC mixture that can possess the desired plastic and hardened properties. For this reason, nearly all the documented UHPCs were self-consolidating. To this end, all UHPCs contain a very

high amount of high-range water reducing admixtures (HRWRA). Valipour and Khayat (2020) evaluated the demand of HRWRAs for different pozzolanic materials combinations. They concluded that UHPCs containing fly ash demanded lowest HRWRA, whereas slag and silica fume required the highest HRWRA in the UHPC mixtures. A study conducted by Aldahdooh et al. (2013) showed that silica fume decreased the workability of UHPC. A study utilizing nano-silica revealed that the workability of UHPCs reduced significantly (Yu et al., 2014). It was explained that nano-silica reduced the amount of available water within the interparticle voids and increased the yield stress and plastic viscosity of the UHPC. It was observed that, with the increase of steel fiber content in the UHPCs, workability tends to decrease due to the high cohesive force between the UHPC and fiber matrix (Yu et al., 2014). Abbas et al. (2016) summarized that, higher dosage of chemical admixtures increased the air content of UHPCs.

1.9.3 Bulk Properties of UHPC

1.9.3.1 Compressive Strength

One of the most fundamental properties of any cement-based materials is the compressive strength. Depending on the user requirements, up until now, up to 800 MPa (116000 psi) compressive strength has been documented in the literatures. However, in most of the literatures, 28-day compressive strength of UHPCs found to be between 120 and 150 MPa (17500 and 21750 psi). Most of the researchers used either small cylinder (50-75 mm diameter and 100-150 mm height) or mortar cube (40-100 mm) to determine the compressive strength of UHPCs. Alsalman et al. (2017) compared the shape effect of cylinder and cube samples on compressive strength and observed that, cubes showed higher compressive strength than cylindrical samples. Wang observed that, 12 days steam cured UHPC displayed higher compressive strength as compared to that of the 28 days moisture curing in room temperature. As nearly all UHPCs contain some percentages of steel fibers to avoid the explosive brittle failure and to have higher ductility. Meng and Khayat (2017) documented that positive effect of steel fibers was observed up to 3% steel fiber addition to UHPCs. Once that percentage was exceeded, due to fiber agglomeration and entrapped air, compressive strength reduced. Le Hoang and Fehling (2017) also documented similar findings for the mixes with 3% of fiber. In contrast, few investigations showed substantial increases in the compressive strength (even >50%) with the inclusion of 3% steel fibers (Ibrahim et al., 2017; Wu et al., 2016).

1.9.3.2 Tensile Strength

The UHPC exhibits considerable tensile strength as compared to that of normal strength concrete. As per ACI 239, UHPC should have the minimum splitting-tensile strength of 6 MPa (870 psi). However, different researchers adopted different method to assess the tensile strength behavior of UHPCs (Shaikh et al., 2020). Commonly used tests were, splitting tensile strength test, direct tensile strength test, pull out test, un-notched dog bone test. It is very difficult to compare the performance amongst these test methods as the values varied largely due to the test setup and procedures. Meng and Khayat (2017) assessed the effect of different cementitious materials combinations on splitting tensile strength of UHPCs and concluded that UHPCs containing silica fume and slag showed 12% higher splitting tensile strength when compared to the mixture with 100% Portland cement.

1.9.3.3 Flexural Strength

UHPC displays high flexural strength due to steel fiber addition and dense microstructure (Greybeal and Hartmann, 2003). Generally, with the increase of steel fiber content, flexural strength also increases (Kang et al., 2010). In addition, fiber aspect ratio plays an important role in flexural performance of UHPC. Higher aspect ratio resulted in higher flexural capacity (Ye et al, 2012). Magureanu et al. (2012) reported more

than 140% flexural capacity increase with UHPC sample containing 2.5% steel fibers as compared to that of the plain UHPC. Lappa et al. (2004) evaluated the effect of pouring method of freshly mixed UHPCs had significant effect on the flexural performance. They stated that compared to the same concrete put into the mold at various locations, the concrete poured from one end of the mold demonstrated a 56% improvement in flexural strength. The strong fiber orientation parallel to the flow direction was attributed for this. Bornemann and Faber (2004) showed that as specimen size increased, UHPC's flexural strength decreased. This was attributed to the increased wall effect of fibers in the smaller specimens. According to Nguyen et al. (2013), as specimen size was decreased, the overall number of cracks and the crack spacing also decreased.

1.9.3.4 Elastic Modulus

Only a few research works reported the elastic modulus of UHPCs. In general, the elastic modulus of UHPCs varied from 40 to 60 GPa at 28-day testing (ACI 239, 2018). ACI committee 363 proposed an equation to predict the elastic modulus from compressive strength value for high strength concrete. However, as UHPC composition is very different form normal strength and high strength concrete, this equation should not be valid for UHPC. Few researchers have attempted to develop a correlation between compressive strength and elastic modulus of UHPCs (Hasnat and Ghafoori, 2021). Alsalman et al. (2017) developed a correlation between compressive strength and elastic modulus of UHPC made from natural sand as aggregate. They mentioned that, use of fly ash and natural sand reduced the elastic modulus as compared to control UHPC mix. Graybeal (2007), determined the elastic modulus at various curing regimes.

1.9.4 Transport Properties of UHPC

1.9.4.1 Permeability

In last 10 years, a number of researchers have assessed the effect of water-to-cementitious materials ratio (w/cm), fiber content, fiber type, curing type, testing age, supplementary cementitious materials on durability properties of UHPCs. Peng et al. (2011) concluded that, UHPC showed 93% lower water absorption as compared to that of convention concrete due to lower water-to-cementitious materials ratio, use of secondary cementitious materials, and lower pore diameter. Tam et al. (2012) assessed the effect of w/cm on permeability of UHPCs (Figure 1.23) and concluded that, with the increase of w/cm, permeability of UHPC also increased. The use of SCMs and nanoparticles in UHPC, particularly silica fume and nano-SiO_2, can increase the production of C-S-H via pozzolanic reactions and nucleation effects, resulting in reduced fine pores and improved dysconnectivity.
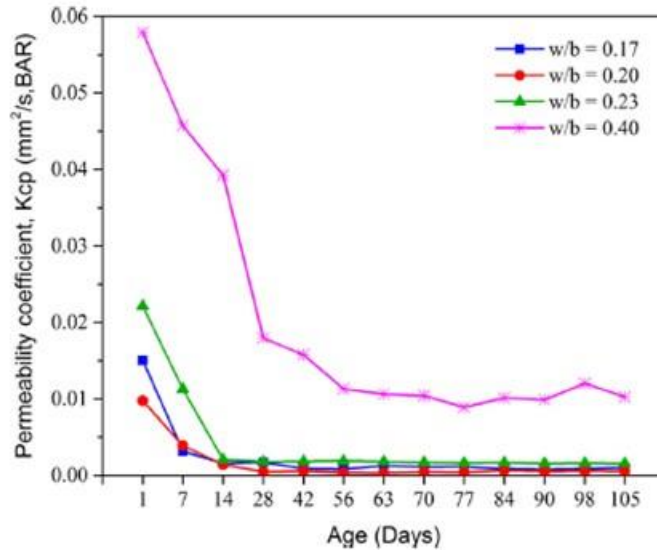
Figure 1.23 Effect of w/cm on water permeability of UHPC (Tam et al., 2012)

1.9.4.2 Chloride-Ion Diffusion

Excellent protection against corrosion was observed in UHPCs due to the presence of a high alkaline cementitious pore solution. Roux et al. (1996) conducted chloride ion diffusion test for UHPC at 365 days testing age at 3% NaCl solution and found the diffusion value of 0.2×10^{-13}. On the other hand, Scheydt and Müller (2012) conducted 63 days test with 3% NaCl solution and found chloride diffusion value 1.3×10^{-13} m^2/s. Variation in chloride diffusion observed due to variation in curing regime, w/cm, solution concentration, fiber type and percentage, and testing age. An et al. (2007) showed that Cl diffusion coefficients of UHPC and HPC were 2.2×10^{-13} and 15.4×10^{-13} m^2/s, respectively. It should be noted that UHPC's Cl diffusion coefficient is at least a factor of ten or more lower than either high-performance or conventional concrete's (Chuang and Huang, 2013).

1.9.4.3 Rapid Chloride Penetration Test (RCPT)

In order to assess whether concrete is vulnerable to chloride ingress or not, the RCPT method measures concrete conductivity across a specimen using an applied electric potential (Li et al., 2020). According to Bonneau et al. (1997), less than 10 Coulombs of charge passed through UHPC specimens over the course of six hours as they were being water-cured at various ages and temperatures. El-Dieb (2009) found that increasing the amount of steel fiber enhanced the chloride permeability of UHPC specimens. Arora et al. (2019) compared the chloride penetration of conventional concrete, HPC with UHPCs. They concluded that the total charge passed through plain UHPCs were extremely low and as per ASTM C1202, it falls under the category "very low" (Figure 1.24). Although ASTM C1856 deems the Rapid Chloride Permeability Test (RCPT) unsuitable for concrete containing metal fibers due to the potential for fiber-induced short circuits and inaccurate conductance readings (ASTM C1856-18). However, there have been reports of utilizing ASTM C1202 to obtain RCPT results for steel fiber-reinforced UHPC, despite the limitations mentioned in ASTM C1856 regarding the presence of metal fibers and the potential for short circuits and unreliable conductance readings (El-Dieb, 2009; Abbas et al., 2015).
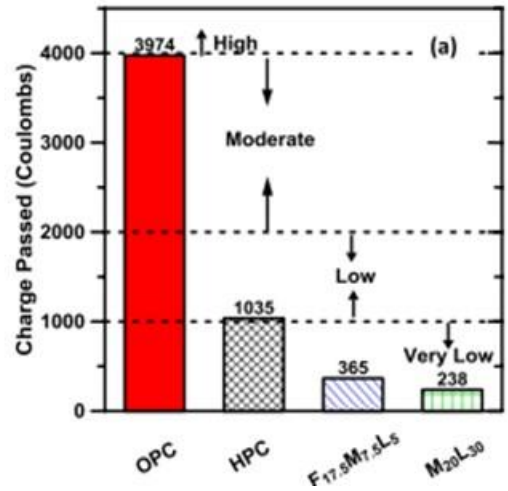
Figure 1.24 Charge passed after 6 hours of RCPT (Arora et al., 2019)

1.9.4.4 Surface Resistivity

Measuring the surface electrical resistivity is another quicker and non-destructive method of determining a concrete material's resistance to chloride ion penetration. The 28-day surface resistivity of different types of concrete is shown in Figure 1.25. Sohail et al. (2021) observed that the electrical resistivity of the UHPC was 18 times higher than that of the conventional concrete. In the case of UHPC, the increased resistance to electrical current indicates a reduced number of smaller, unconnected pores.
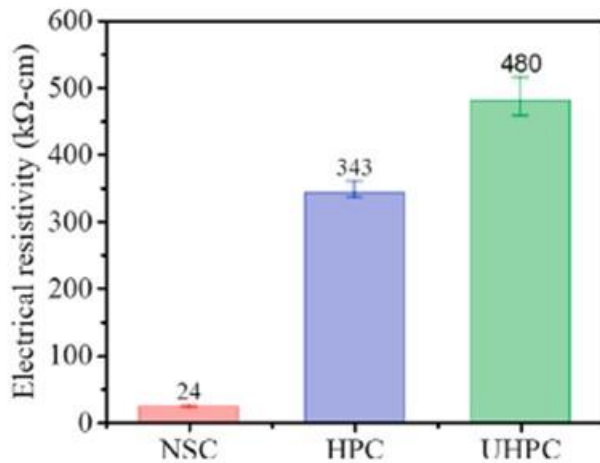
Figure 1.25 Surface resistivity of different types of concrete (Sohail et al., 2021)

1.9.4.5 Alkali-Silica Reaction

Graybeal (2006), evaluated the potential alkali-silica reaction (ASR) ability of UHPC and found that after 28 days, the expansion values were 0.012% which was lower than the threshold value suggested by ASTM. They concluded that, due to very low permeability of UHPC, ASR is not a concern for UHPC (Graybeal and Tanesi, 2007). Soliman and Tagnit-Hamou (2017) found that the highest expansion at 16 days was substantially lower than the specified limit of 0.1%.

20

1.10 Research Objectives and Scope of Work

The main goal of this research is to fully replace expensive Quartz sand and to partially replace the Portland cement with pozzolanic materials to produce sustainable non-proprietary ultra-high-performance concrete (UHPC). It's hypothesized that this goal can be achieved through proper gradation of locally sourced fine aggregates and different cementitious materials compositions with lower water-to-cementitious materials ratio.

The following objectives were set within the scope of this study:

(i) To investigate the role of different cementitious materials compositions and aggregate-to-cementitious materials ratios, and various steel fiber content and shapes on the properties of a non-proprietary UHPCs.

Phase I → Optimized UHPCs → **Phase II** → UHPC Tie → **Phase III**

Objectives and key elements:
-Optimize cement and SCM contents
-Optimize cement and SCM compositions
-Optimize w/cm
-Optimize steel fiber type and dosage
-Optimize fine aggregate compositions and gradations
-Assess fresh, bulk, and drying shrinkage performances

Objectives and key elements:
-Assess transport properties of UHPCs
-Assess freeze-thaw and de-icing salt resistance of UHPCs
-Assess abrasion resistance of UHPCs
-Optimize fine aggregate content

Objectives and key elements:
-Assess static negative center moment capacity of UHPC tie
- Assess cyclic negative center moment capacity of UHPC ties
- Assess static negative support moment capacity of UHPC tie
-Determine the effect of steel grade on the static and cyclic moment capacity of UHPC ties

Materials:
Fine aggregate (concrete sand and masonry sand), cement, silica fume, fly ash, slag, water, fiber, and admixtures
Designed Experiments:
Slump flow, Compressive strength, Modulus of rupture, Elastic modulus, and Drying shrinkage

Materials:
Fine aggregate, cement, silica fume, fly ash, slag, water, fiber, and admixtures
Designed Experiments:
Slump flow, Compressive strength, Tensile strength, RCPT, Absorption, Abrasion, freezing/thawing, Deicing salt, water penetration, SEM

Materials:
Steel reinforcement, Fine aggregate, cement, silica fume, fly ash, and admixture
Designed Experiments:
Slump flow, Compressive strength, load capacity, load-deflection response, load-strain response, crack width, failure map

Figure 1.26 Experimental laboratory program

(ii) To investigate the transport properties and de-icing salt resistance of non-proprietary UHPCs.

(iii)   To examine the freezing and thawing performance of selected plain and fiber-reinforced non-proprietary UHPCs made with different cementitious materials types and combinations, and with varying steel fiber content and shapes.

(iv)   To determine abrasion resistance of selected UHPCs made with different cementitious materials combinations, and varying steel fiber content and shape.

(v)   To determine the static and cyclic performance of non-propriety (UHPC) ties using the optimized UHPC.

The total research work is divided in three phases. The summary of the experimental program is presented in Figure 1.26.

1.11 Outline of Research

This research follows an article-based format which encompasses five standalone articles besides one introductory chapter. Among those five articles, three of them already have been published in peer-reviewed journals; one of them is under a journal peer-review, and one is under process of submission. Thus, the report is organized into a total of six chapters as follows.

Chapter 1-Introduction: Provides an overview of the research topic and problem statement along with the specific objectives of the research and scope of work. The literature review consisted of history and development of prestressed concrete tie, design and problems associated with PC ties and history, application, performance of UHPCs.

Chapter 2-Properties of Ultra-High Performance Concrete Using Optimization of Traditional Aggregates and Pozzolans (*Hasnat, A., & Ghafoori, N. (2021). Properties of ultra-high performance concrete using optimization of traditional aggregates and pozzolans. Construction and Building Materials, 299, 123907.*): Provides development and optimization of the locally sourced fine aggregates and cementitious materials compositions and effect of steel fiber types and replacement percentage on the fresh, bulk, and shrinkage properties of non-proprietary UHPCs.

Chapter 3-Transport Properties and De-icing Salt Resistance of Blended Ultra High-Performance Concrete (*Hasnat, A., & Ghafoori, N. (2024). Transport Properties and De-icing Salt Resistance of Blended Ultra High-Performance Concrete. Journal of Cold Regions Engineering, 38(2), 04024003*): Provides transport properties and de-icing salt resistance of a number of binary and ternary non-proprietary plain and fiber-reinforced UHPCs containing Type V cement, and various dosages and combinations of micro silica and class F fly ash. The studied transport properties included water absorption, volume of permeable voids, water penetration, rapid chloride penetration, and surface resistivity.

Chapter 4- Freeze–Thaw Resistance of Nonproprietary Ultrahigh-Performance Concrete (*Hasnat, A., & Ghafoori, N. (2021). Freeze–Thaw Resistance of Nonproprietary Ultrahigh-Performance Concrete. Journal of Cold Regions Engineering, 35(3), 04021008:* Provides the mass loss/gain and loss/gain in compressive and splitting tensile strengths of the UHPCs after 70 severe repeated F–T cycles under water. The effects of the binary and ternary composition of pozzolanic materials, and steel fiber contents and shapes on the F–T performance of the studied UHPCs were examined.

Chapter 5-Abrasion Resistance of Ultra-High-Performance Concrete for Railway Sleepers (*Hasnat, A., & Ghafoori, N. (2021). Abrasion resistance of ultra-high-performance concrete for railway sleepers. Urban Rail Transit, 7(2), 101-116.*): Provides the abrasion resistance performance of UHPCs made with different cementitious material combinations, and varying steel fiber contents and shapes. Additionally, findings are compared with those of the high-strength concrete typically used in the production of railway ties.

Chapter 6-Behavior of Railway Ties Made Using Ultra-High-Performance Concrete: Presents the experimental investigation conducted on non-proprietary UHPC ties under static center negative moment test, static support negative moment test, and center negative cyclic tests. A total of five full-scale UHPC ties were prepared inhouse using 60 and 100 grade steel rebars.

Additionally, a total of five appendices are provided. Appendix A contains the sample calculation of the predicted load capacity of railway ties. Appendices B to E consist of the experimental data presented in Chapters 2 to 6, respectively.

References

1. Abbas, S. M. L. N., Nehdi, M. L., & Saleem, M. A. (2016). Ultra-high performance concrete: Mechanical performance, durability, sustainability and implementation challenges. International Journal of Concrete Structures and Materials, 10(3), 271-295.
2. ACI 239R-18 Committee. (2018). Ultra High Performance Concrete: An Emerging Technology Report, USA.
3. ACI Committee 363 State-of-the art report on high strength concrete (ACI 363R-92). (1992) American Concrete Institute, Farmington Hills (MI).
4. ACI Committee, & International Organization for Standardization. (2008). Building code requirements for structural concrete (ACI 318-08) and commentary. American Concrete Institute.
5. Aldahdooh, M. A. A., Bunnori, N. M., & Johari, M. M. (2013). Evaluation of ultra-high-performance-fiber reinforced concrete binder content using the response surface method. Materials & Design (1980-2015), 52, 957-965.
6. Alsalman, A., Dang, C. N., & Hale, W. M. (2017). Development of ultra-high performance concrete with locally available materials. Construction and Building Materials, 133, 135-145.
7. Amtrak. (2012). Evolution of Amtrak's Concrete Crosstie and Fastening System Program. PowerPoint presentation. Presented at the International Concrete Crosstie and Fastening System Symposium. University of Illinois at Urbana-Champaign, Urbana, IL, USA.
8. An, M., Yang, X., Wang, J., & Cui, N. (2007). Research on durability of RPC [J]. Architecture Technology, 38(5), 367-368.
9. AREMA Manual for Railway Engineering (2009) American Railway Engineering and Maintenance-of-Way Association (AREMA), Landover, Maryland, V 1, Ch. 30.
10. AREMA. Manual for railway engineering (Chapter 30): Concrete ties. American Railway Engineering and Maintenance-of-Way Association 2006.
11. ASTM C1856 / C1856M-17, Standard Practice for Fabricating and Testing Specimens of Ultra-High Performance Concrete, ASTM International, West Conshohocken, PA, 2017, www.astm.org
12. Birchall, J. D., Howard, A. J., & Kendall, K. (1981). Flexural strength and porosity of cements. Nature, 289(5796), 388-390.
13. Bornemann, R., & Faber, S. (2004, September). UHPC with steel-and noncorroding high strength polymer fibres under static and cyclic loading. In Proceedings of the International Symposium on Ultra-High Performance Concrete, Kassel, Germany (pp. 673-681).
14. BSI (British Standards Institution). 2009c. Railway applications. Track. Concrete sleepers and bearers. Part 2: Prestressed mono-block sleepers. BS EN 13230-2. London: British Standards Institution
15. C. Esveld, Modern Railway Track, MRT Productions, Zaltbommel, the Netherlands, 2001.
16. Chuang, M. L., & Huang, W. H. (2013). Durability analysis testing on reactive powder concrete. In Advanced materials research (Vol. 811, pp. 244-248). Trans Tech Publications Ltd.
17. de Larrard, F., & Sedran, T. (1994). Optimization of ultra-high-performance concrete by the use of a packing model. Cement and concrete research, 24(6), 997-1009.
18. Euro-International Committee for Concrete, & Comité euro-international du béton. (1992). Durable concrete structures: design guide (Vol. 183). Thomas Telford.

19. Fédération international du béton (fib). Precast concrete railway track systems. State-of-art report, fib Bulletin No. 37, Lausanne, Switzerland; 2006.

20. Ferdous, W., & Manalo, A. (2014). Failures of mainline railway sleepers and suggested remedies–review of current practice. Engineering Failure Analysis, 44, 17-35.

21. Fournier B, Bérubé MA, Thomas MDA, Smaoui N, Folliard KJ. (2004). Evaluation and management of concrete structures affected by alkali–silica reaction – a review. In: Seventh CANMET/ACI international conference on recent advances in concrete technology. Farmington Hills, Michigan.

22. Freudenstein, S. (2007, September). Concrete ties designed for high dynamic loads. In AREMA Conference Proc. 2007, American Railway Engineering and Maintenance-of-way Association(AREMA), Landover, Maryland.

23. Gao, Z., Qian, Y., Dersch, M. S., & Edwards, J. R. (2017). Compressive stress distribution in prestressed concrete and its effect on railroad crosstie design. Construction and Building Materials, 151, 147-157.

24. González-Nicieza, C., Álvarez-Fernández, M. I., Menéndez-Díaz, A., Álvarez-Vigil, A. E., & Ariznavarreta-Fernández, F. (2008). Failure analysis of concrete sleepers in heavy haul railway tracks. Engineering Failure Analysis, 15(1-2), 90-117.

25. Graybeal, B. A. (2007). Compressive behavior of ultra-high-performance fiber-reinforced concrete. ACI materials journal, 104(2), 146-152.

26. Graybeal, B. A., & Hartmann, J. L. (2003, October). Strength and durability of ultra-high performance concrete. In Concrete Bridge Conference (p. 20).

27. Hanna, A. N. (1979). Prestressed Concrete Ties for North American Railroads. PCI journal, 24(5), 29.

28. Hime, W. G. (1996). Delayed ettringite formation-A concern for precast concrete? PCI journal, 41(4), 26-30.

29. Hwang CL, Chen CT, Lee LS, Bui LAT, Hou BS, Hsieh HY. The material and mechanical property of heavy-duty prestressed concrete sleeper. Appl Mech Mater 2011;2011(97–98):408–13.

30. Ibrahim, M. A., Farhat, M., Issa, M. A., & Hasse, J. A. (2017). Effect of material constituents on mechanical and fracture mechanics properties of ultra-high-performance concrete. ACI Materials Journal, 114(3), 453-465.

31. International Federation for Structural Concrete. fib bulletin 37: Precast concrete railway track systems, state-of-art report; 2006.

32. J. Monier (US302664A). Construction of railway sleepers. U.S. Patent No. 302,664. Patented Jul 29, 1884

33. Janeliukstis, R., Clark, A., Papaelias, M., & Kaewunruen, S. (2019). Flexural cracking induced acoustic emission peak frequency shift in railway prestressed concrete sleepers. Engineering Structures, 178, 493-505.

34. Kaewunruen, S., & Remennikov, A. M. (2011). Experiments into impact behaviour of railway prestressed concrete sleepers. Engineering Failure Analysis, 18(8), 2305-2315.

35. Kang, S. T., Lee, Y., Park, Y. D., & Kim, J. K. (2010). Tensile fracture properties of an Ultra High Performance Fiber Reinforced Concrete (UHPFRC) with steel fiber. Composite Structures, 92(1), 61-71.

36. Lappa, E. S., Braam, C. R., & Walraven, J. C. (2004, September). Static and fatigue bending tests of UHPC. In Proceedings of the International Symposium on Ultra-High Performance Concrete, Kassel, Germany (pp. 449-458).

37. Le Hoang, A., & Fehling, E. (2017). Influence of steel fiber content and aspect ratio on the uniaxial tensile and compressive behavior of ultra high performance concrete. Construction and Building Materials, 153, 790-806.

38. Li, J., Wu, Z., Shi, C., Yuan, Q., & Zhang, Z. (2020). Durability of ultra-high performance concrete–A review. Construction and Building Materials, 255, 119296.

39. Lutch, R. H. (2009). Capacity optimization of a prestressed concrete railroad tie.MSc Thesis. Michigan Technological University.

40. Lutch, R. H., Harris, D. K., & Ahlborn, T. M. (2009). Causes and preventative methods for rail seat abrasion in North America's railroads. In Cold Regions Engineering 2009: Cold Regions Impacts on Research, Design, and Construction (pp. 455-466).
41. Magureanu, C., Sosa, I., Negrutiu, C., & Heghes, B. (2012). Mechanical Properties and Durability of Ultra-High-Performance Concrete. ACI Materials Journal, 109(2).
42. Magureanu, C., Sosa, I., Negrutiu, C., & Heghes, B. (2012). Mechanical Properties and Durability of Ultra-High-Performance Concrete. ACI Materials Journal, 109(2), 177-184.
43. Mallett, G. P. (1991). Fatigue of reinforced concrete. STATE-OF-THE-ART REVIEW. Her Majesty's Stationery Office (HMSO) (2).
44. Manalo, A., Aravinthan, T., Karunasena, W., & Ticoalu, A. (2010). A review of alternative materials for replacing existing timber sleepers. Composite Structures, 92(3), 603-611.
45. Meng, W., & Khayat, K. H. (2017). Improving flexural performance of ultra-high-performance concrete by rheology control of suspending mortar. Composites Part B: Engineering, 117, 26-34.
46. Mohammadzadeh, S., & Vahabi, E. (2011). Time-dependent reliability analysis of B70 pre-stressed concrete sleeper subject to deterioration. Engineering Failure Analysis, 18(1), 421-432.
47. Morgan, B. 1971. Industrial archaeology civil engineering: Railways. London: Longman Group
48. Murray, M., & Cai, Z. (1998). Prestressed concrete sleeper: Literature review. Report ARA Project Ref, 15250.
49. Naaman, A. E., & Wille, K. (2012). The path to ultra-high performance fiber reinforced concrete (UHP-FRC): five decades of progress. Proceedings of Hipermat, 3-15.
50. Neville, A. M. (1995). Properties of concrete (Vol. 4). London: Longman.
51. Nguyen, D. L., Kim, D. J., Ryu, G. S., & Koh, K. T. (2013). Size effect on flexural behavior of ultra-high-performance hybrid fiber-reinforced concrete. Composites Part B: Engineering, 45(1), 1104-1116.
52. Parvez, A., & Foster, S. J. (2017). Fatigue of steel-fibre-reinforced concrete prestressed railway sleepers. Engineering Structures, 141, 241-250.
53. Peng, Y. Z., Chen, K., & Hu, S. G. (2011). Study on interfacial properties of ultra-high performance concrete containing steel slag powder and fly ash. In Advanced Materials Research (Vol. 194, pp. 956-960). Trans Tech Publications Ltd.
54. Peters N, Mattson SR. CN 60E concrete tie development. In: AREMA conference proc. Landover, Maryland; 2004.
55. Peters N, Mattson SR. CN 60E concrete tie development. In: AREMA conference proc. Landover, Maryland; 2004.
56. Peters SR. J.A. Cesare & Associates Inc: 8. Abrasion testing of epoxy-coated concrete ties (using symons product No. 301 epoxy); 2007.
57. Peters, N., & Mattson, S. (2004). CN 60E concrete tie development. In AREMA Conference Proc.
58. Peters, S. R. (2007). Abrasion Testing of Epoxy-Coated Concrete Ties (Using Symons Product No. 301 Epoxy), JA Cesare & Associates.
59. Railway Technology (2020) At a Glance: Railway Sleeper Materials. https://www.railway-technology.com/features/feature92105/. Accessed 25th April 2020
60. Rezaie, F., Shiri, M. R., & Farnam, S. M. (2012). Experimental and numerical studies of longitudinal crack control for pre-stressed concrete sleepers. Engineering Failure Analysis, 26, 21-30.
61. Roux, N., Andrade, C., & Sanjuan, M. A. (1996). Experimental study of durability of reactive powder concretes. Journal of materials in civil engineering, 8(1), 1-6.
62. Russell, H. G., Graybeal, B. A., & Russell, H. G. (2013). Ultra-high performance concrete: A state-of-the-art report for the bridge community (No. FHWA-HRT-13-060). United States. Federal Highway Administration. Office of Infrastructure Research and Development.
63. Sadeghi, J., Tolou Kian, A. R., & Shater Khabbazi, A. (2016). Improvement of mechanical properties of railway track concrete sleepers using steel fibers. Journal of Materials in Civil Engineering, 28(11), 04016131.

64. Scheydt, J. C., & Muller, S. (2012). Microstructure of ultra high performance concrete (UHPC) and its impact on durability. In Proceedings of the 3rd International Symposium on UHPC and Nanotechnology for High Performance Construction Materials, Kassel, Germany (pp. 349-356).

65. Shaikh, F. U. A., Luhar, S., Arel, H. Ş., & Luhar, I. (2020). Performance evaluation of Ultrahigh performance fibre reinforced concrete–A review. Construction and Building Materials, 232, 117152.

66. Shin, H. O., Yang, J. M., Yoon, Y. S., & Mitchell, D. (2016). Mix design of concrete for prestressed concrete sleepers using blast furnace slag and steel fibers. Cement and Concrete Composites, 74, 39-53.

67. Shurpali AA, Kernes RG, Edwards, Dersch MS, Lange DA, Barkan CPL. Investigation of the mechanics of rail seat deterioration (RSD) and methods to improve the abrasion resistance of concrete sleeper rail seats. In: 10th International heavy haul association conference, New Delhi, India. 4–6 February 2013.

68. Shurpali, A. A., Kernes, R. G., Edwards, J. R., Dersch, M. S., Lange, D. A., & Barkan, C. P. (2013, February). Investigation of the mechanics of rail seat deterioration (RSD) and methods to improve the abrasion resistance of concrete sleeper rail seats. In 10th International heavy haul association conference, New Delhi, India (pp. 4-6).

69. Tam, C. M., Tam, V. W., & Ng, K. M. (2012). Assessing drying shrinkage and water permeability of reactive powder concrete produced in Hong Kong. Construction and Building Materials, 26(1), 79-89.

70. Taylor, H. P. J. 1993. "The railway sleeper: 50 years of pretensioned, prestressed concrete." Struct. Eng. 71 (16): 281–295.

71. Tepponen, P., & Eriksson, B. E. (1987). Damages in concrete railway sleepers in Finland. Nordic Concrete Research, (6), 199-209.

72. UK railway forums/Infrastructure & station/Broken sleeper http://i225.photobucket.com/albums/dd281/ainsworth74/Rail/Photo-0001.jpg; 15 January 2014.

73. Valipour, M., & Khayat, K. H. (2020). Robustness of Ultra-High-Performance Concrete to Changes in Material Temperature. ACI Materials Journal, 117(4), 47-56.

74. Van Dyk, B. J., Dersch, M. S., & Edwards, J. R. (2012). International concrete crosstie and fastening system survey–final results. University of Illinois at Urbana-Champaign.

75. Wille, K., Naaman, A. E., El-Tawil, S., & Parra-Montesinos, G. J. (2012). Ultra-high performance concrete and fiber reinforced concrete: achieving strength and ductility without heat curing. Materials and structures, 45(3), 309-324.

76. Wu K, Yan A, Yao W, Zhang D. Effect of metallic aggregate on strength and fracture properties of HPC. Cem Concr Res 2001;31:113–8.

77. Wu, Z., Shi, C., He, W., & Wu, L. (2016). Effects of steel fiber content and shape on mechanical properties of ultra high performance concrete. Construction and building materials, 103, 8-14.

78. Yu, R., Spiesz, P., & Brouwers, H. J. H. (2014). Effect of nano-silica on the hydration and microstructure development of Ultra-High Performance Concrete (UHPC) with a low binder amount. Construction and Building Materials, 65, 140-150.

79. Yudenfreund, M., Odler, I., & Brunauer, S. (1972). Hardened portland cement pastes of low porosity I. Materials and experimental methods. Cement and Concrete Research, 2(3), 313-330.

80. Zeman, J. C., Edwards, J. R., Barkan, C. P., & Lange, D. A. (2009, June). Failure mode and effect analysis of concrete ties in North America. In Proc. of the 9th International Heavy Haul Conference (pp. 270-278).

81. Zeman, J. C., Edwards, J. R., Barkan, C. P., & Lange, D. A. (2009, June). Failure mode and effect analysis of concrete ties in North America. In Proc. of the 9th International Heavy Haul Conference (pp. 270-278).

82. Zhou, J., Qian, S., Ye, G., Copuroglu, O., van Breugel, K., & Li, V. C. (2012). Improved fiber distribution and mechanical properties of engineered cementitious composites by adjusting the mixing sequence. Cement and Concrete Composites, 34(3), 342-348.

83. Zi, G., Lee, S. J., Jang, S. Y., Yang, S. C., & Kim, S. S. (2012). Investigation of a concrete railway sleeper failed by ice expansion. Engineering Failure Analysis, 26, 151-163.

CHAPTER 2-PROPERTIES OF ULTRA-HIGH PERFORMANCE CONCRETE USING OPTIMIZATION OF TRADITIONAL AGGREGATES AND POZZOLANS

Abstract

The properties of ultra-high performance concretes (UHPCs) made with traditional fine aggregates, different cementitious materials types and combinations, and varying steel fiber contents and shapes were studied. In the first phase, a total of 78 UHPCs were used to assess their compressive and splitting-tensile strengths, and drying shrinkage, which led to identifying 40 optimized mixtures for the second phase of the investigation for which their compressive, splitting-tensile, and flexural strength, modulus of elasticity, load-deflection response, and drying shrinkage properties were obtained. The outcome of this study revealed that the optimized UHPCs displayed excellent bulk properties and dimensional stability. Amongst the utilized cementitious materials combinations, UHPCs made with the combined silica fume and class F fly ash, as a partial replacement of cement, performed the best, whereas the companion mixtures incorporating only class F fly ash exhibited the contrary. A clear strain hardening and softening was observed in the load-deflection response of steel fiber-reinforced UHPCs. Due to better steel to concrete surface adhesion, straight steel fibers had a more positive influence on the mechanical properties and dimensional stability of the studied UHPCs when compared to those of the hooked fibers. Overall, this experimental study supports that, with proper gradations and proportioning, traditional fine aggregates can be used as an effective substitute for the expensive filler materials used for production of the proprietary UHPCs without compromising their mechanical properties and dimensional stability.

Keywords: Conventional fine aggregate; Ultra-high performance concrete; Bulk properties; Cementitious materials; Steel fiber; Drying shrinkage

2.1 Introduction

In recent years, the utilization of advanced chemical admixtures and fibers; specialized aggregates with excellent packing density; very high binder content; low water-to-cementitious materials ratio; and customized mixing and curing has led to the development of ultra-high performance concrete (UHPC) (Ahlborn et al. 2015, 2. Wille et al. 2011,Wang et al. 2012, Magureanu et al. 2012, Lee et al. 2013, Alkaysi et al. 2016, Yalçınkaya & Yazıcı 2017, Ragalwar et al. 2020). According to ACI 239R (2018), "Ultra-high performance concrete (UHPC) is a class of advanced cementitious materials with greater strength, tensile ductility, and durability properties when compared to conventional or even high-performance concrete. UHPC is limited to concrete that has a minimum specified compressive strength of 22,000 psi (150 MPa) with specified durability tensile ductility and toughness requirements; fibers are generally included to achieve specified requirements." In ASTM C1856 (2017), it is mentioned that, UHPC should have "specified compressive strength of at least 120 MPa, with nominal maximum size aggregate of less than 5 mm and a flow between 200 and 250 mm." UHPC provides the following advantages over conventional concrete:

(i)   The very high compressive, tensile, and flexural strengths, and modulus of elasticity of UHPC results in significant reduction in the sectional size of the concrete members, which saves floor space and reduces structural dead load. Blais and Couture (1999) mentioned that UHPC members may weigh only one-third to one-half of corresponding conventional concrete members.

(ii) Superior ductility and energy absorption provide greater reliability even under extreme conditions, such as earthquakes or blasts. Moreover, fibers inside UHPC enable the concrete to sustain structural integrity towards tensile load after first cracking, by bridging cracks and transferring the load across the cracks (Larsen & Thorstensen 2020).

(iii)   The superior durability of UHPC leads to a long service life with reduced maintenance. UHPC is nearly impermeable, allowing almost no carbonation nor chloride or sulfate penetration (Karim et al. 2019). Bonneau et al. (2000) documented that only 26% of cement hydration is required for UHPC to achieve discontinuous capillary pores.

(iv)   A significant amount of unhydrated cement in the hardened UHPC provides a self-healing potential under cracking conditions (Jacobsen & Sellevold1996).

(v)   The absence of coarse aggregate in UHPC allows for high quality surface finishes (Blais & Couture 1999).

(vi)   The circulation of stray current through conventional steel reinforcement is known to cause accelerated corrosive damage to steel. Unlike conventional steel reinforcement in concrete, fiber-reinforced UHPC does not usually have a continuous conductive path for an electric current (Tang 2017).

Some suggestions of drawbacks associated with the use of UHPCs reported in the literature are:

(i)   Only a few proprietary blends have been used by different researchers in the assessment of UHPC properties. The utilization of a very high amount of silica sand, steel fibers, chemical admixtures, and silica fume in proprietary UHPCs make the production costs of such mixtures about 10 to 20 times higher than conventional concrete (Ragalwar et al. 2020, Yang et al. 2019, Zhong et al. 2018).

(ii)   Under normal curing condition, UHPCs are susceptible to higher autogenous and drying shrinkage due to their higher amounts of cementitious materials and high range water reducing admixture (Tam et al. 2012).

(iii)   High shear mixers are needed to properly batch UHPC's ingredients. This kind of mixers may not be available at construction sites (Sohail et al. 2018). Additionally, specific procedures maybe needed including the use of ice cubes instead of water to provide the shearing action and to reduce heat of hydration and mixing time.

(iv)   There is lack of design codes for using UHPCs (Ahlborn et al. 2011).

The first structural application of UHPC was in 1997, when UHPC was used to construct a pre-stressed hybrid pedestrian bridge in Sherbrooke, Canada (2004). After that, applications of UHPC were successfully demonstrated in several countries [23, 24]. However, the widespread use of UHPC is still limited due to high initial production cost. A number of researchers have tried to compensate for the very high production costs of UHPCs by using different materials and methods (Table 2.1). Karim et al. (2019) used masonry sand as a replacement for expensive quartz sand, while Arora et al. (2019) used coarse and fine aggregates collectively to reach a compressive strength of 150 MPa. Yang et al. (2019) reduced the total cost of UHPC by utilizing supplementary cementitious materials, such as fly ash and ground granulated blast-furnace slag (GGBS), as a partial replacement for Portland cement. Alsalman et al. (2017) reported that more than 10% silica fume content, as a partial replacement of Portland cement, had a minimal effect on compressive strength, whereas other researchers emphasized using a high volume of silica fume to achieve the desired properties (Chan et al. 2004, Graybeal 2006, Ganesh & Murthy 2019).

Table 2.1 Studies on UHPCs with conventional aggregates

Reference	Materials used as aggregates	Properties evaluated[a]
Sobuz et al. (2014)	Fine aggregate: washed river sand, mined sand, manufactured sand, and granulated lead smelter slag; Coarse aggregate: crushed bluestone	Compressive strength (121-153 MPa); elastic modulus (10.2-40.9 GPa); strain at peak stress (0.00426-0.0091)

Meng et al. (2017)	Missouri river sand, masonry sand	Compressive strength (120-135 MPa); splitting-tensile strength (10-14 MPa); flexural strength (20-24 MPa); elastic modulus (46-53 GPa); Drying shrinkage (56-600 µm/m)
Alsalman et al. (2017)	Arkansas river sand, class C fly ash	Compressive strength (124.1-162.4); elastic modulus (36.9-45.9 GPa)
Karim et al. (2019)	Conventional fine aggregate, masonry sand	Splitting-tensile strength (10.1-11.8 MPa); drying shrinkage (0.110-0.148%)

ᵃ Properties relevant to present study

An essential constituent in UHPC is discontinuous fiber reinforcement. The inclusion of fiber is necessary to improve the ductility required for structural safety. Meng et al. (2017)] employed hybrid fibers, and evaluated the fresh and mechanical properties of non-proprietary UHPCs. When compared to conventional concrete, due to the presence of fiber reinforcement, UHPC has exhibited considerable tensile strength, even after first cracking (Larsen & Thorstensen 2020). Another study reported a profound improvement in flexural tensile strength corresponding to an increase in fiber content (Abbas et al. 2015, Máca et al. 2013) used steel fiber and reported that the highest flexural strength is obtained when a 3% fiber volume is used. In another study, Yoo et al. (2014) concluded that an increase in steel fiber content resulted in an improved elastic modulus up to 3% of fibers. Wille et al. (2011) pointed out that twisted steel fibers led to lower tensile strength than straight steel fibers at elevated load rates. Yoo et al. (2014) also found that straight fibers outperformed twisted/hooked fibers in flexural tensile strength performance. In contrast, other studies have reported better performance by twisted or hooked fibers in flexural/tensile strength performance, as compared to that of straight fibers (Wu et al. 2016, Park et al. 2012).

In recent years, a number of researchers have conducted studies in optimization of UHPC's compositions with limited information available to date (Karim et al. 2019, Alsalman et al. 2017, Meng et al. 2017). In particular, literature suffers from limited data on utilization of various supplementary cementitious materials in production of sustainable and cost-effective UHPCs. This paper aimed to investigate the role of different cementitious materials compositions and aggregate-to-cementitious materials ratios, as well as various steel fiber contents and shapes, on properties of the studied UHPCs. The investigated properties included compressive strength, splitting-tensile resistance, flexural strength, load-deflection response, flexural strain, elastic modulus, and drying shrinkage. The outcome of this investigation will add to the body of knowledge in utilization of locally available aggregates and different supplementary cementitious materials in production of UHPCs.

2.2 Experimental Program

This study was divided into two Phases. In the Phase I, various cementitious materials types and combinations, aggregate gradations, water-to-cementitious materials ratios, and aggregate-to-cementitious materials ratios were evaluated to identify the optimized plain UHPCs. During Phase II of this study, the effects of steel fiber contents and shapes on the bulk properties and dimensional stability of the optimized UHPCs were investigated. As this study has two Phases (Phase I and II), all materials and method section explained at the Experimental Program Section, with the exception of mixture design of Phase II (as these mixtures were selected once Phase I was completed).

2.2.1 Materials

A quest for UHPC optimization using traditional aggregates was undertaken based on standard tests. In the production of the UHPCs, ASTM Type V Portland cement (C), class F fly ash (F), natural pozzolan (N), ground granulated blast-furnace slag (S), and silica fume (SF) were used as cementitious materials. Type V cement (with 4% C_3A) was selected to ensure the resistance against severe sulfate action. The chemical characteristics of the cementitious materials are presented in Table 2.2, and scanning electron microscopic (SEM) images are shown in Figure 2.1 Figure 2.2 represents the particle size distribution of the cementitious materials. Silica fume, slag, industrial (Class F fly ash), and natural pozzolans were used at different replacement levels of cement content. The natural pozzolan was sourced from a vitrified rhyolite as a silica-rich volcanic ash. Several investigators assessed the effect of steel fiber content (up to 3%) on properties of UHPCs [38-40]. In the Phase II of this study, two types of steel fibers (straight and hooked), with 13 mm length and 0.30 mm width (aspect ratio of 43) were used at the levels of 2 and 3% of the total concrete volume. The specific gravity of the steel fibers was 7.86 and met the minimum tensile strength requirement of ASTM A820 (2016).

Table 2.2 Chemical compositions of the Type V cement and pozzolanic materials

Composition	Type V cement (%)	Class F fly ash (%)	Natural pozzolan (%)	GGBS (%)	Silica fume (%)
SiO_2	21	59.93	71.0	31.0	94.72
CaO	62.4	4.67	2.3	43.64	-
Al_2O_3	4	22.22	7.9	11.5	-
Fe_2O_3	3.7	5.16	0.70	0.80	-
MgO	2.6	-	-	4.7	-
SO_3	2.2	0.38	0.1	4.85	0.23
$Na_2O + K_2O$	0.54	1.29	7.5	-	0.47
Loss on Ignition (LOI)	2.0	0.32	3.4	0.30	2.82

30
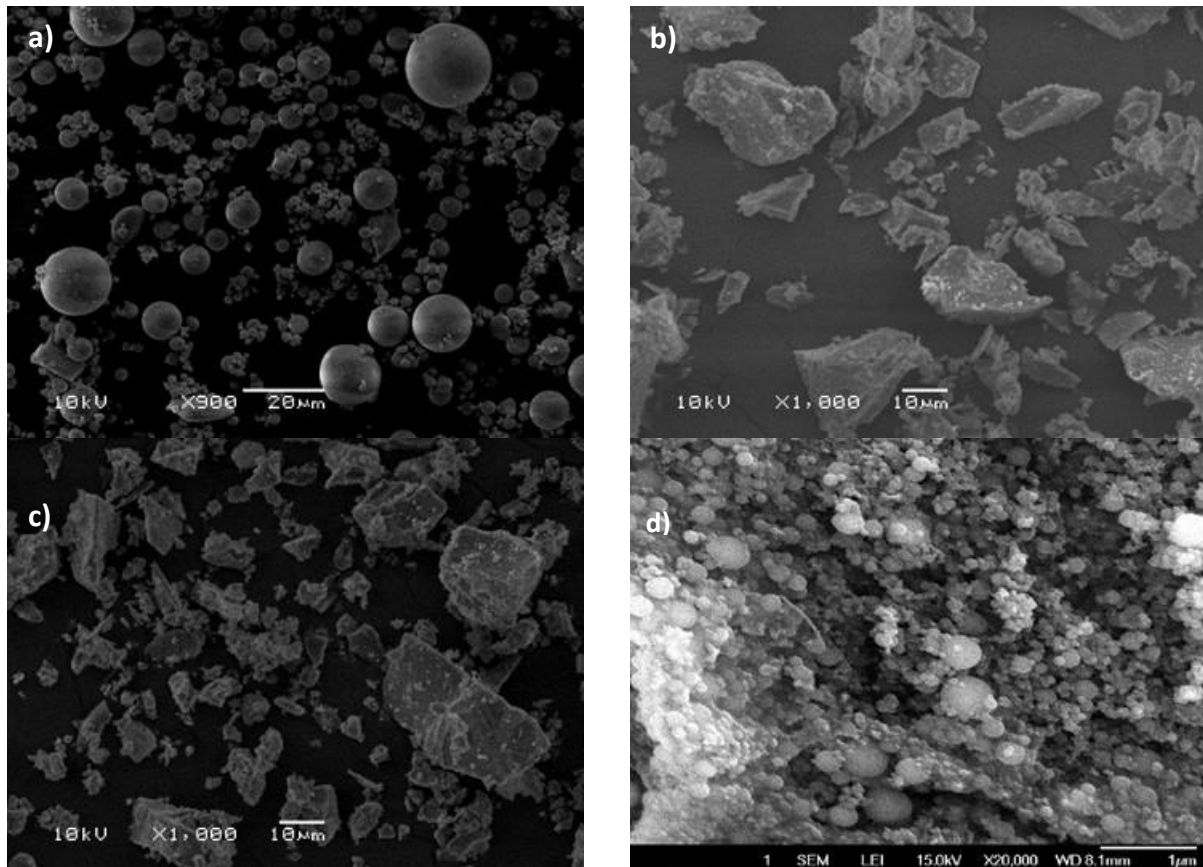
Figure 2.1 Scanning electron microscopic (SEM) image of cementitious materials (a) class F fly ash, (b) natural pozzolan, (c) ground granulated blast-furnace slag, and (d) silica fume
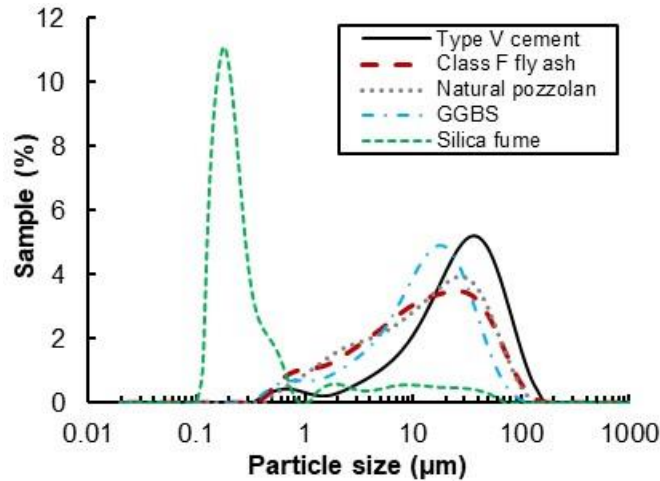
Figure 2.2 Particle size distribution of cementitious materials

2.2.2 Selection of Cementitious Materials Combinations, w/cm, and HRWRA content

At first, 100% cement was batched at various water-to-cementitious materials ratios (*w/cm* = 0.16-0.24) and tested for flow to obtain the minimum water content required to achieve the minimum relative flow, as shown in Figure 2.3a. A total of 30 combinations of cementitious materials (15 binary, 10 ternary, and four quaternary cementitious material compositions) were batched at various water-to-cementitious material ratios (w/cm = 0.16-0.24), and tested for flow to obtain the minimum water content (Figure 2.3b) and HRWRA (polycarboxylate based) requirement of different binder combinations, in comparison with 100% cement. Based on the findings of flow test conducted in accordance with ASTM C230 (2021), a total of 26 combinations of binders were selected with the water-to-cementitious materials ratio of 0.21. The correlation between the relative flow and required HRWRA to achieve the flow of 250±25 mm is given in Figure 2.3c.
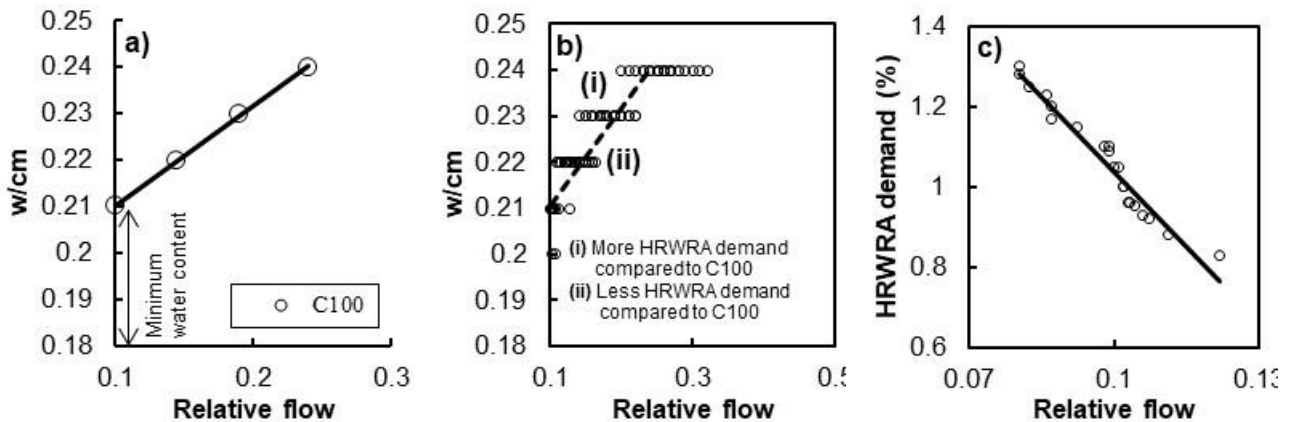
Figure 2.3 Criteria for the selection of cementitious material combination: (a) minimum water content required for Type V cement (C100), (b) relative water demand at different w/cm, (c) demand of HRWRA based on relative flow

31

2.2.3 Aggregate Gradation

Two types of locally produced fine aggregates were used; their size gradation varied from 0.075 mm to 4.75 mm. To obtain the maximum packing density and minimum porosity, a uniquely-sized graded manufactured fine aggregate was determined and stored separately for each size gradation. Unit weight was measured for the graded aggregates at different distribution moduli (0.19-0.23), using the modified Andreasen and Andersen model, as shown in Figure 2.4 [43]. The unit weight of the aggregates was determined as per ASTM C29 (rodding method) (2017). The modified Andreasen and Andersen particle packing model is based on the following equation:

$$P(D) = \frac{D^Q - D^Q_{min}}{D^Q_{max} - D^Q_{min}} \qquad (2.1)$$

where, $P(D)$ represents the weight percentage of aggregate passing the sieve with size D; D_{max} is the maximum particle size (µm); D_{min} is the minimum particle size (µm); and Q is the distribution modulus, which is related to the aggregate particle size. The maximum unit weight with minimum void percentage was obtained using the distribution modulus of 0.21. Sieve analysis of aggregate I, aggregate II, and the combined Andreasen and Andersen sizes (optimized curve) for the distribution modulus of Q=21 is presented in Figure 2.5. The combined fine aggregates had a specific gravity of 2.80, a fineness modulus of 2.92 and an absorption of 0.45%.
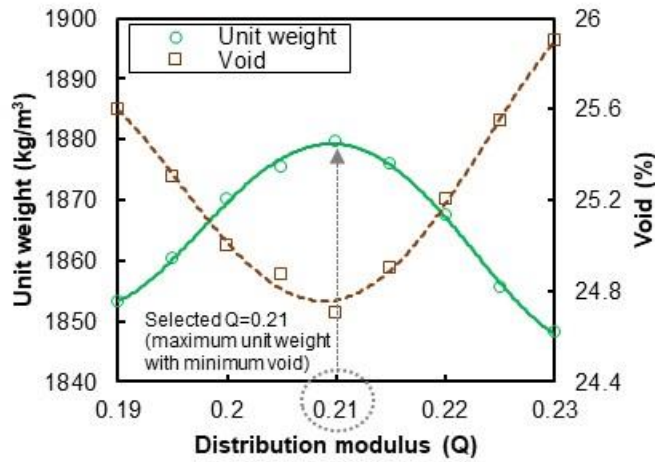
Figure 2.4 Selection of distribution modulus based on unit weight of fine aggregate
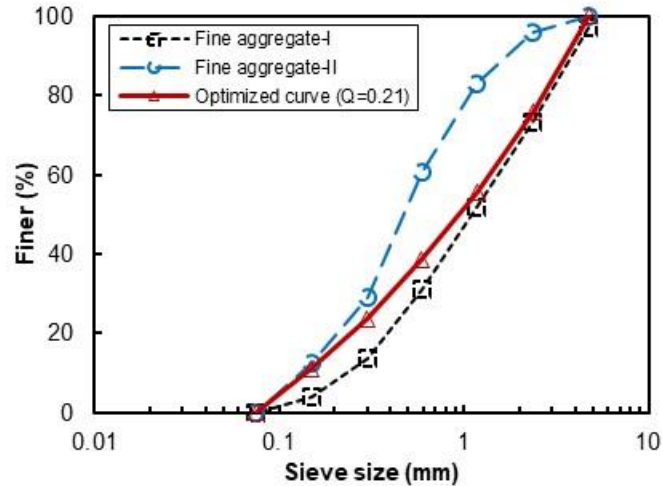
Figure 2.5 Aggregate gradation of UHPCs, as per modified Andreasen and Andersen model

2.2.4 Mixture Proportions of Plain UHPCs

A total of 78 plain UHPC mixture compositions were selected to determine their compressive and splitting-tensile strengths and drying shrinkage. The aggregate-to-cementitious materials ratio (V_A/V_{cm}) plays an important part in the strength development of UHPC (Karim et al. 2019). Most researchers selected a V_A/V_{cm} between 0.60 to 1.4 (Willi et al. 2011, Meng et al. 2017). In this study, to observe the effect of the aggregate/cementitious materials ratio, the V_A/V_{cm} varied at 0.80, 1.0, and 1.2. For each V_A/V_{cm}, 26 cementitious compositions were investigated, which consisted of the control (C100), along with 13 binary, nine ternary, and three quaternary cementitious compositions. The unit contents of the selected UHPC constituents for various aggregate-to-cementitious materials ratios (V_A/V_{cm}) are given in Table 2.3. The water-to-cementitious materials ratio (w/cm) of 0.21 was kept constant for all mixtures. The actual water content of the UHPCs varied due to variation in the required HRWRA dosage to maintain uniform flowability.

Table 2.3 Mixture proportions of plain UHPCs

Classification	Mixture ID[a]	V_A/V_{cm}	w/cm	C[b]	F[b]	N[b]	S[b]	SF[b]	Agg[b]	HRWRA[b]	W[b]
								kg/m³			
Control	C100	0.8	0.21	1280					910	12.0	262
Binary	C90F10	0.8	0.21	1152	95				910	11.1	256
	C80F20	0.8	0.21	1024	189				910	10.9	249
	C70F30	0.8	0.21	896	284				910	10.3	243
	C60F40	0.8	0.21	768	379				910	10.2	236
	C90N10	0.8	0.21	1152		84			910	11.2	254
	C80N20	0.8	0.21	1024		149			910	11.2	241
	C70N30	0.8	0.21	896		195			910	10.4	224
	C90S10	0.8	0.21	1152			105		910	11.8	258
	C80S20	0.8	0.21	1024			187		910	12.0	248
	C70S30	0.8	0.21	896			245		910	12.3	233
	C95SF5	0.8	0.21	1216				43	910	12.3	258
	C90SF10	0.8	0.21	1152				82	910	12.4	252
	C85SF15	0.8	0.21	1088				116	910	12.5	246
Ternary	C80F15SF5	0.8	0.21	1024	142			36	910	11.3	247
	C80N15SF5	0.8	0.21	1024		112		36	910	11.5	240
	C80S15SF5	0.8	0.21	1024			140	36	910	12.1	246
	C70F20SF10	0.8	0.21	896	189			63	910	12.1	235
	C70N20SF10	0.8	0.21	896		130		63	910	12.1	222
	C70S20SF10	0.8	0.21	896			163	63	910	12.3	229

Classification	Mixture ID[a]	V_A/V_{cm}	w/cm	C[b]	F[b]	N[b]	S[b]	SF[b]	Agg[b]	HRWRA[b]	W[b]
				kg/m³							
	C50F30SF20	0.8	0.21	768	284			109	910	12.6	237
	C50N30SF20	0.8	0.21	768		167		109	910	12.7	213
	C50S30SF20	0.8	0.21	768			210	109	910	13.0	221
Quaternary	C60F15S15SF10	0.8	0.21	768	142		105	54	910	12.4	218
	C60F10S20SF10	0.8	0.21	768	95		140	54	910	12.5	215
	C50F20N20SF10	0.8	0.21	640	189	93		45	910	12.3	197
Control	C100	1	0.21	1184					1052	12.0	243
Binary	C90F10	1	0.21	1065	88				1052	11.1	237
	C80F20	1	0.21	947	175				1052	10.9	230
	C70F30	1	0.21	828	263				1052	10.2	224
	C60F40	1	0.21	710	350				1052	10.2	218
	C90N10	1	0.21	1065		77			1052	11.1	235
	C80N20	1	0.21	947		138			1052	11.1	222
	C70N30	1	0.21	828		181			1052	10.3	207
	C90S10	1	0.21	1065			97		1052	11.8	238
	C80S20	1	0.21	947			173		1052	12.0	229
	C70S30	1	0.21	828			226		1052	12.3	215
	C95SF5	1	0.21	1124				40	1052	12.2	238
	C90SF10	1	0.21	1065				75	1052	12.4	233
	C85SF15	1	0.21	1006				107	1052	12.5	227
Ternary	C80F15SF5	1	0.21	947	131			34	1052	11.3	228
	C80N15SF5	1	0.21	947		103		34	1052	11.4	222
	C80S15SF5	1	0.21	947			129	34	1052	12.1	227
	C70F20SF10	1	0.21	828	175			59	1052	12.0	217
	C70N20SF10	1	0.21	828		120		59	1052	12.1	206
	C70S20SF10	1	0.21	828			151	59	1052	12.3	212
	C50F30SF20	1	0.21	710	263			101	1052	12.5	219
	C50N30SF20	1	0.21	710		155		101	1052	12.7	196
	C50S30SF20	1	0.21	710			194	101	1052	12.9	204
Quaternary	C60F15S15SF10	1	0.21	710	131		97	50	1052	12.4	201
	C60F10S20SF10	1	0.21	710	88		129	50	1052	12.5	199
	C50F20N20SF10	1	0.21	592	175	86		42	1052	12.2	182
Control	C100	1.2	0.21	1101					1174	11.9	226
Binary	C90F10	1.2	0.21	991	81				1174	11.0	220
	C80F20	1.2	0.21	881	163				1174	10.8	214
	C70F30	1.2	0.21	771	244				1174	10.2	209
	C60F40	1.2	0.21	660	326				1174	10.1	203
	C90N10	1.2	0.21	991		72			1174	11.1	218
	C80N20	1.2	0.21	881		128			1174	11.0	207
	C70N30	1.2	0.21	771		168			1174	10.2	193
	C90S10	1.2	0.21	991			90		1174	11.8	221
	C80S20	1.2	0.21	881			160		1174	11.9	213
	C70S30	1.2	0.21	771			211		1174	12.3	200
	C95SF5	1.2	0.21	1046				37	1174	12.2	222
	C90SF10	1.2	0.21	991				70	1174	12.4	217
	C85SF15	1.2	0.21	936				99	1174	12.5	211
Ternary	C80F15SF5	1.2	0.21	881	122			31	1174	11.3	212
	C80N15SF5	1.2	0.21	881		96		31	1174	11.4	206
	C80S15SF5	1.2	0.21	881			120	31	1174	12.0	211
	C70F20SF10	1.2	0.21	771	163			55	1174	12.0	202
	C70N20SF10	1.2	0.21	771		112		55	1174	12.0	191
	C70S20SF10	1.2	0.21	771			140	55	1174	12.2	197
	C50F30SF20	1.2	0.21	660	244			94	1174	12.5	204
	C50N30SF20	1.2	0.21	660		144		94	1174	12.7	182
	C50S30SF20	1.2	0.21	660			181	94	1174	12.9	190
Quaternary	C60F15S15SF10	1.2	0.21	660	122		90	47	1174	12.4	187
	C60F10S20SF10	1.2	0.21	660	81		120	47	1174	12.5	185
	C50F20N20SF10	1.2	0.21	550	163	80		39	1174	12.1	169

1 kg/m³ = 1.685 lb/yd³
[a] Mixture ID: number after C, F, N, S, and SF indicates percentage of respective cementitious materials. For example, C90F10 means 90% cement and 10% class F fly ash.
[b]C: Cement; [b]F: Class F fly ash; [b]N: Natural pozzolan; [b]S: Ground granulated blast-furnace slag; [b]SF: Silica fume; [b]Agg: Aggregate; [b]HRWRA: High-range water reducing admixture; [b]W: Water

2.2.5 Mixing, Sampling, Curing, and Testing

Due to the high quantity of small-sized particles, coupled with the low water-to-cementitious materials ratio, and the addition of steel fibers (used in Phase II), a longer mixing time and higher energy were required for UHPC production as compared to traditional concrete. The mixing time, mixing speed, mixing sequence, temperature, and relative humidity were closely monitored and uniformly maintained. The mixing sequence is shown in Figure 2.6. The flow properties were evaluated according to the modified ASTM C230 (as all the UHPCs were self-consolidating, 25 drops of blow were skipped) before they were poured into cylinders and beam-shaped molds (Karim et al. 2019). The specimens were kept for 24 hours in a controlled-moisture curing room at $22 \pm 3°C$ and 95% relative humidity. After 24 hours, the specimens were demolded and returned to the moisture room for additional days, depending on the curing duration and test scheme. The detailed test scheme of the studied UHPCs (both plain and fiber-reinforced) are presented in Table 2.4. The displacement at the mid-span of the beam was evaluated using an LVDT placed at the bottom center of the beam specimen. The flexural strength of the studied UHPCs was determined according to ASTM C1609 (2019).
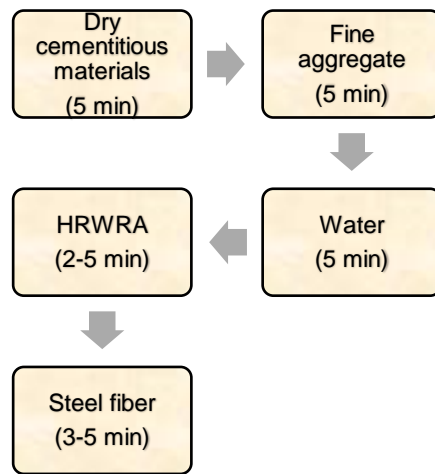
Figure 2.6 UHPCs' mixing sequence

Table 2.4 Test details of the studied UHPCs

Phase I: Plain UHPCs			
Tests	Specimen details	Test age (days)[b]	Standards
Flow	Freshly mixed UHPCs	-	ASTM C230 (2021)
Unit weight	Disk (100 mm diameter and 50 mm height)	1	ASTM C642 (2013)
Compressive strength	Cylinder (50 mm diameter and 100 mm height)	1, 7, 28, and 90	ASTM C39 (2020)
Splitting-tensile strength	Cylinder (50 mm diameter and 100 mm height)	28	ASTM C496 (2017)
Drying shrinkage	Beam (25×25×250 mm)	120	ASTM C596 (2018)
Phase II: Fiber-reinforced UHPCs[a]			
Flow	Freshly mixed UHPCs	-	ASTM C230 (2021)
Unit weight	Disk (100 mm diameter and 50 mm height)	1	ASTM C642 (2013)
Compressive strength	Cylinder (50 mm diameter and 100 mm height)	28	ASTM C39 (2020)

Splitting-tensile strength	Cylinder (50 mm diameter and 100 mm height)	28	ASTM C496 (2017)
Load-deflection response	Beam (50×50×200 mm)	28	ASTM C1609 (2019)
Flexural strength	Beam (50×50×200 mm)	28	ASTM C1609 (2019)
Flexural strain	Beam (50×50×200 mm)	28	ASTM C1609 (2019)
Elastic modulus	Cylinder (75 mm diameter and 150 mm height)	28	ASTM C469 (2014)
Drying shrinkage	Beam (25×25×250 mm)	120	ASTM C596 (2018)

[a] For comparison 11 plain UHPCs were also selected for these tests, [b] four specimen prepared per test age.

2.3 Experimental Results on Plain UHPCs (Phase I)

The results of compressive and splitting-tensile strengths, along with drying shrinkage for different V_A/V_{cm} as functions of curing durations are presented in Table 5. For the 28-day cured UHPCs, the compressive strength varied from 119 to 149 MPa, 118 to 151 MPa, and 108 to 139 MPa for V_A/V_{cm} of 0.80, 1.0, and 1.20, respectively. Similarly, the splitting-tensile strength ranged between 8.7 to 10.8 MPa, 8.6 to 10.5 MPa, and 8.1 to 10.3 MPa for the same V_A/V_{cm}. The average 120-day drying shrinkages were 0.1062, 0.0979, and 0.0896% for V_A/V_{cm} of 0.80, 1.0, and 1.20, respectively. The relative performance of binary, ternary, and quaternary UHPCs, as compared to that of the control (C100) UHPC, are illustrated in Figure 2.7. The effects of cementitious materials compositions and V_A/V_{cm} on the bulk and dimensional stability properties of the studied plain UHPCs are discussed in the following sub-sections.

Table 2.5 Compressive and splitting-tensile strength, along with drying shrinkage of UHPCs at different V_A/V_{cm}

Classifications	Mixture ID	$\frac{V_A}{V_{cm}}=0.8$						$\frac{V_A}{V_{cm}}=1.0$						$\frac{V_A}{V_{cm}}=1.2$					
		f'_{c-1D}	f'_{c-7D}	f'_{c-28D}	f'_{c-90D}	f_{t-28D}	D_{120D} (%)	f'_{c-1D}	f'_{c-7D}	f'_{c-28D}	f'_{c-90D}	f_{t-28D}	D_{120D} (%)	f'_{c-1D}	f'_{c-7D}	f'_{c-28D}	f'_{c-90D}	f_{t-28D}	D_{120D} (%)
		(MPa)						(MPa)						(MPa)					
Control	C100	63	105	134	153	9.4	0.103	62	102	128	152	9.3	0.092	61	100	125	150	9.1	0.087
Binary	F10	57	103	133	-	9.4	0.086	54	91	129	-	9.2	0.078	54	91	123	-	9.1	0.071
	F20	53	94	128	158	9.6	0.084	51	89	128	154	9.2	0.076	52	84	122	151	9.0	0.068
	F30	53	103	133	160	9.3	0.076	50	85	126	150	9.0	0.070	50	81	120	150	8.8	0.064
	F40	49	95	124	157	9.2	0.072	46	74	119	147	8.6	0.066	46	74	113	150	8.1	0.061
	N10	56	98	129	166	9.4	0.095	53	97	126	144	9.2	0.088	54	88	121	143	9.0	0.075
	N20	54	97	127	151	9.3	0.086	54	89	123	145	8.9	0.078	52	84	119	146	8.9	0.071
	N30	48	99	130	143	8.8	0.081	50	87	118	133	8.7	0.072	50	81	116	138	8.6	0.065
	S10	59	93	125	167	8.8	0.110	65	103	127	149	8.9	0.098	61	96	123	148	8.9	0.087
	S20	63	111	134	149	9.4	0.100	64	100	129	148	9.2	0.091	56	89	119	143	9.2	0.086
	S30	64	111	134	152	8.9	0.096	68	104	127	148	8.9	0.084	57	91	119	139	8.8	0.080
	SF5	73	118	140	165	9.8	0.116	71	114	140	171	9.5	0.106	65	109	131	168	9.4	0.096
	SF10	74	120	149	168	10.5	0.120	74	124	147	175	10.0	0.110	71	117	138	164	9.8	0.101
	SF15	75	120	149	-	10.8	0.130	75	126	151	177	10.5	0.116	72	119	139	-	10.3	0.103
Ternary	F15SF5	71	116	141	147	9.8	0.109	64	113	137	165	9.6	0.100	61	101	129	153	9.5	0.093
	N15SF5	70	115	139	150	9.6	0.110	60	107	134	158	9.5	0.102	59	96	127	151	9.3	0.094
	S15SF5	69	102	128	139	9.5	0.116	67	115	132	159	9.5	0.106	64	104	124	149	9.5	0.096
	F20SF10	64	120	148	131	9.8	0.121	60	103	140	144	9.9	0.114	59	97	131	132	9.2	0.098
	N20SF10	59	112	144	136	9.7	0.122	57	105	136	151	9.8	0.112	59	99	130	145	9.1	0.100
	S20SF10	65	109	139	148	10.3	0.125	62	106	135	145	9.8	0.114	63	101	130	146	9.3	0.098
	F30SF20	53	97	126	138	9.4	0.127	52	84	126	145	9.2	0.111	45	75	116	128	8.7	0.101
	N30SF20	56	91	119	133	10.1	0.137	53	86	120	129	9.3	0.119	45	76	113	121	8.5	0.106
	S30SF20	57	99	127	149	9.3	0.140	54	91	122	134	8.7	0.122	50	83	117	125	8.3	0.108
Quaternary	F15S15SF10	59	109	132	144	8.7	0.112	52	92	125	140	8.6	0.100	48	82	116	127	8.6	0.093
	F10S20SF10	60	102	131	151	9.2	0.097	47	88	127	145	9.2	0.113	46	80	112	131	9.2	0.118
	F20N20SF10	54	72	123	154	9.2	0.090	45	70	118	148	9.2	0.107	40	72	108	137	9.1	0.109

Note: 1 MPa= 145 Psi; f'_{c-1D}, f'_{c-7D}, f'_{c-28D}, and f'_{c-90D} denotes compressive strength at 1-day, 7-day, 28-day, and 90-day, respectively; f_{t-28D} denote splitting tensile strength at 28-day; D_{120D} denote drying shrinkage at 120-day
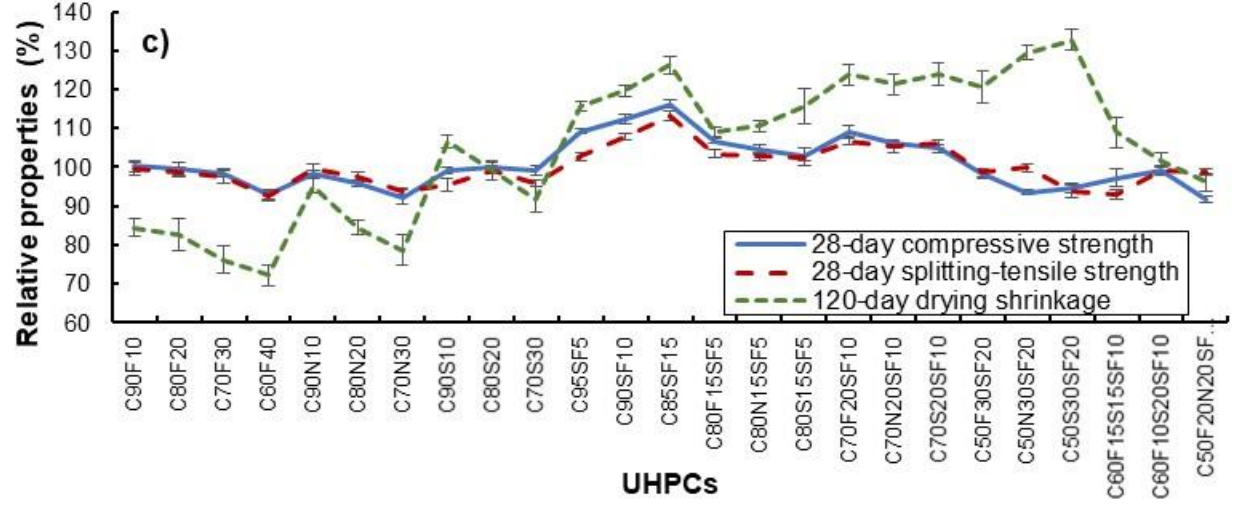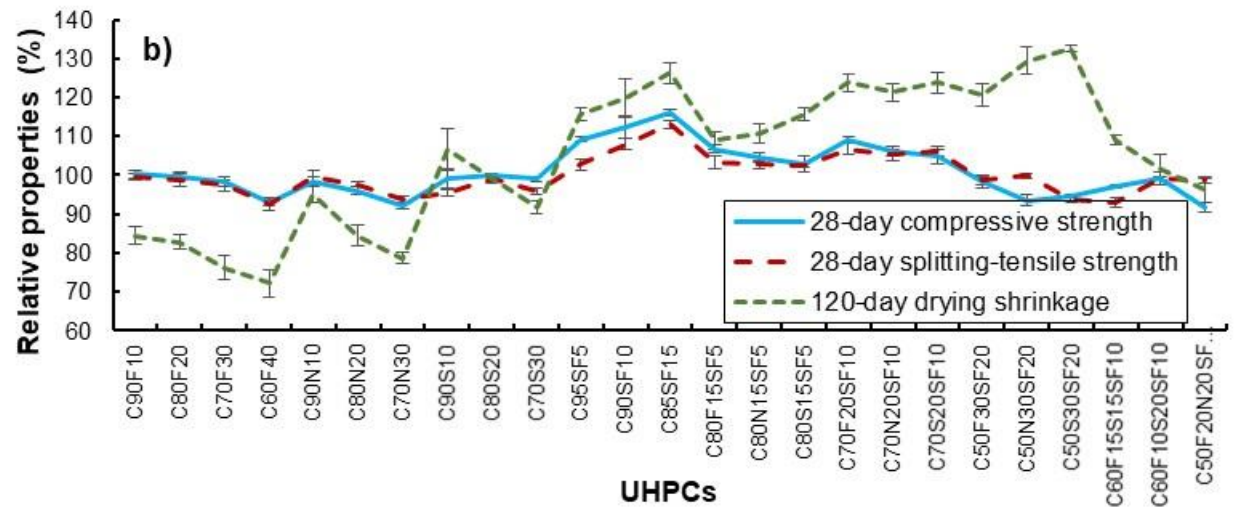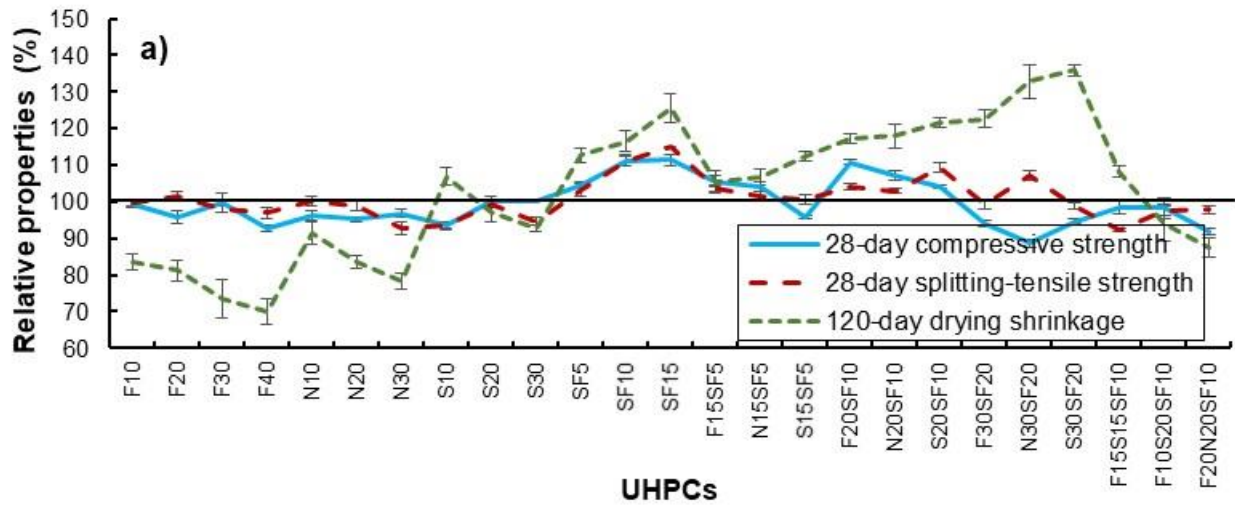
Figure 2.7 Relative properties of the UHPCs, as compared to the control UHPC (C100) (a) for an aggregate-to-cementitious materials ratio of 0.8, (b) for an aggregate-to-cementitious materials ratio of 1.0, (c) for an aggregate-to-cementitious materials ratio of 1.2

2.3.1 Effect of Cementitious Materials Types and Compositions

2.3.1.1 Compressive Strength

The compressive strengths of the plain UHPCs, as a function of cementitious materials compositions and V_A/V_{cm}, are shown in Table 2.5 and Figure 2.7. All UHPCs gained strength with the increase in testing duration due to their continued hydration. The UHPCs with binary fly ash combinations showed slower compressive strength development at early ages, as compared to the control UHPC (C100). However, due to increased pozzolanic reactivities, the 90-day cured binary UHPCs incorporating fly ash displayed similar or higher compressive strength when compared to the control UHPC. The binary UHPCs with natural pozzolans followed a similar trend as did fly ash in the binary UHPCs. The binary UHPCs containing GGBS followed the same trend as the control UHPC in compressive strength development over time. On the other hand, the UHPC with silica fume, as a partial replacement of Portland cement, surpassed the strength gains of the control UHPC at all curing ages. The presence of reactive fine silica helped the UHPCs to develop higher early strengths, as compared to the control UHPC. Irrespective of cementitious materials types and combinations, similar trends were observed for every V_A/V_{cm}.

Overall, the UHPCs containing fly ash or natural pozzolan displayed higher long-term compressive strengths, whereas UHPCs made with silica fume showed higher compressive strengths at early ages. In comparison to the control UHPC, GGBS containing UHPCs produced slightly lower compressive strengths at all cement replacement levels. Once calcium hydroxide (CH) was produced from the primary hydration reaction, the secondary pozzolanic reaction produced stronger calcium silicate hydrate (C-S-H), which was responsible for better later-age strength performance of the studied UHPCs having fly ash and natural pozzolans (Langan et al. 2002). On the other hand, as shown in Figure 2.2, silica fume had higher particle fineness than that of other cementitious materials which enabled it to produce superior early-age cementitious reactivities (Jalal et al. 2015).

When 10% Portland cement was replaced by secondary cementitious materials, the UHPCs with 10% silica fume displayed the highest compressive strength, whereas the natural pozzolan showed the lowest results. At a 20% cement replacement level, UHPCs having GGBS showed higher compressive strength than UHPCs with fly ash and natural pozzolan. However, after 90 days of curing, the test samples incorporating fly ash showed the highest compressive strength amongst all binary mixtures with 20% cement replacement. When 30% of the Portland cement was replaced by secondary cementitious materials, the one and seven-day cured UHPCs' incorporating GGBS had higher compressive strengths. However, as the curing age increased, UHPCs with 30% fly ash and natural pozzolan showed higher compressive strengths, as compared to the UHPCs containing GGBS.

As mentioned earlier, an increase in fly ash/natural pozzolan content resulted in lower early strength development due to the pozzolanic materials' inactivity. With CH production, the secondary cementitious reaction of pozzolanic materials with CH resulted in better strength results for 90-day cured samples. However, the threshold for using these secondary cementitious materials depends on CH production in the matrix, as without it, these pozzolanic materials only act as filler materials in the UHPC matrix. Overall, in the binary blend UHPCs, mixtures with fly ash or silica fume performed better than slag and natural pozzolan. The spherical shape of the fly ash and silica fume enabled them to fill the micro voids within the matrix better than the irregular shaped GGBS or natural pozzolan (Figure 2.1). As a result, slightly better strength performance can be seen with the binary UHPCs made with fly ash or silica fume, as compared to the UHPCs with same amount of natural pozzolan or GGBS.

Most of the mixtures having ternary blend displayed better compressive strength as compared to the control UHPC. Among all the ternary compositions, C80F15SF5, C80N15SF5, C70F20SF10, and C70N20SF10

displayed excellent compressive strength, with a minimum 28-day strength of 120 MPa and 90-day compressive strength of 150-MPa. Early age pozzolanic reactivity of the silica fume facilitated the early strength development, while the secondary pozzolanic activity of fly ash/natural pozzolan helped in the long-term compressive strength gain of the studied UHPCs. UHPCs with more than 30% of Portland cement replaced by fly ash/GGBS/natural pozzolan did not achieve the target 28- and 90-day compressive strengths of 120 MPa or 150 MPa, respectively. The probable reason is that with conventional curing, UHPCs with a high amount of fly ash/GGBS/natural pozzolan did not react entirely. For this reason, several investigators have tried heat curing to maximize the pozzolanic material hydration [53, 54].

Quaternary UHPCs incorporating a high amount of fly ash, GGBS, and natural pozzolan displayed lower compressive strengths at one and seven days curing durations. However, six out of nine mixtures achieved compressive strengths of 120 MPa and 150 MPa at 28- and 90-day curing. Perhaps, the amount of secondary cementitious materials in the quaternary mixtures exceeded the availability of CH to effectively activate these secondary cementitious materials (Langan et al. 2002).

When 20% of Portland cement replaced with 20% fly ash (Binary UHPC), compared with 15% fly ash and 5% silica fume having UHPC (Ternary UHPC), improvement was observed in the ternary UHPC. Similar improvements were also observed for ternary natural pozzolan and silica fume, as well as ternary GGBS and silica fume having UHPC, when compared to the binary UHPC with 20% natural pozzolan/GGBS as a partial replacement of Portland cement. At the 30% Portland cement replacement level, all ternary UHPCs displayed superior performance over binary UHPCs. Smaller particle size of silica fume contributed to the larger surface area which enabled silica fume to react at the early stages with free lime to produce C-S-H. In addition, the unreacted spherical silica fume had the ability to fill the smaller voids that other pozzolanic materials could not reach. For this reason, most of the ternary UHPCs displayed higher compressive strength as compared to that of the quaternary and binary UHPC blends. However, for quaternary blends, the presence of very high amounts of primarily unreactive pozzolans and a lack of CH produced from the binders to trigger the secondary reaction, as well as the size of the pozzolanic materials and availability of free water for secondary hydration, played important roles in the lower compressive strength gains, when compared to those of the binary/ternary UHPC blends. To support this statement, Yazici et al. (2013) reported that, large number of cementitious particles remains unhydrated even after 28 days of curing due to lack of available water for hydration. Mehta and Monterio [56] mentioned that, pozzolanic material larger than 45µm does not have the ability to participate in the secondary pozzolanic reaction to produce hydration product. As can be seen in Figure 2.2, some of the fly ash/natural pozzolan/slag had particle size larger than 45µm which explains the lower strength development at higher pozzolan replacement for quaternary blends.

2.3.1.2 Splitting-Tensile Strength

The splitting-tensile strengths of the plain UHPCs, as a function of cementitious materials compositions and V_A/V_{cm} are documented in Table 2.5 and Figure 2.7. Nearly all splitting-tensile strengths of the binary, ternary, and quaternary UHPCs displayed similar trends to those of the compressive strength. However, for the studied plain UHPCs, a higher cementitious material content had less influence in improving tensile strength than it had on compressive strength. The average compressive-to-splitting-tensile strength ratios were 14, 13.95, and 13.6, for aggregate-to-cementitious material ratios of 0.80, 1.0, and 1.2, respectively, whereas for conventional concrete the ratio mostly varies between 8-12 (Gerges et al. 2015). A study on UHPCs conducted by Meng et al. [31] also found a very high compressive-to-splitting-tensile strength ratio of 16.8. It is possible that the absence of coarse aggregate changes the interfacial transition zone of the plain UHPCs in sustaining tensile force. This limitation is not well documented in the literature, as nearly all studied UHPCs contained some sort of fiber to compensate for the brittle failure of plain UHPCs. Therefore, it can be said that using plain UHPCs will not be sufficient for the requirement of all mechanical properties.

The average 28-day cured splitting-tensile strength of the fly ash incorporating binary UHPCs varied from 9.2 to 9.4 MPa, 8.6 to 9.2 MPa, and 8.1 to 9.1 MPa, for aggregate-to-cementitious materials ratios of 0.80, 1.0, and 1.2, respectively. The binary UHPCs with natural pozzolan/GGBS showed similar splitting-tensile strengths at the 28-day testing age. With an increase of the fly ash/natural pozzolan content from 10 to 30%, the split tensile strength decreased. In contrast to fly ash/natural pozzolan, increases in silica fume content in the binary UHPCs improved the splitting tensile strength results. The binary UHPCs with silica fume displayed average 3, 9, and 14% increases in splitting-tensile strength, as compared to the control UHPCs at 5, 10, and 15% replacement levels. When fly ash was substituted for portions of Portland cement at 10 and 20% by weight, nearly no decrease in splitting tensile strength was observed. However, with 30 and 40% fly ash, on average 3 and 7% lower splitting tensile strengths were observed as compared to that of the control UHPC. Amongst all the studied UHPCs, C85SF15 displayed the highest splitting-tensile strength for all aggregate-to-cementitious material ratios, whereas, C60F15S15SF10 and C60F40 displayed the lowest average splitting-tensile strength values as compared to that of the control UHPC.

Overall, in the binary blend UHPCs, the increase of natural pozzolan/fly ash/ slag resulted in decreased splitting-tensile strength when compared to that of the control UHPC, whereas, increased silica fume content improved the splitting-tensile strength of the binary silica blended UHPCs. This phenomenon can be explained by the highly reactive silica triggering early hydration and fly ash/slag/natural pozzolan's inability to be reactive during early hydration ages. This is also in-line with the compressive strength performance, as at 28 days, the compressive strength of UHPCs incorporating fly ash/natural pozzolan were lower than the control UHPC. However, 90-day binary UHPCs with cured fly ash surpassed the control UHPC. The splitting-tensile strength of ternary and quaternary blend UHPCs followed a similar pattern as compressive strength discussed in the previous section.

2.3.1.3 Drying Shrinkage

Table 2.5 and Figure 2.7 document the 120-day drying shrinkage results of the 78 studied UHPCs. Secondary cementitious materials had significant effects on the concretes' drying shrinkage, with fly ash performing the best and silica fume performing the worst against drying shrinkage. UHPCs made with GGBS displayed similar shrinkage performance as the control mixture. The presence of unhydrated cementitious particles having fly ash/natural pozzolan minimized drying shrinkage by filling the voids, which provided additional dimensional stability to the UHPCs. On the other hand, extra fine silica fume consumed more water for hydration and resulted in higher drying shrinkage. Karim et al. (2019) also concluded that higher silica fume amounts resulted in higher drying shrinkage.

All ternary blend UHPCs displayed higher drying shrinkage as compared to the control UHPC, and mixtures with silica fume triggered UHPC drying shrinkage increases. However, UHPCs with 5% silica fume and 15% fly ash/natural pozzolan displayed only 6.5% higher drying shrinkage in comparison to that of the control UHPC. UHPC blends having 20% silica fume displayed highest drying shrinkage amongst all mixtures. However, ternary and quaternary blend UHPCs made using both silica fume and natural pozzolan and/or fly ash displayed better performance against drying shrinkage compared to those of the binary UHPCs with silica fumes. Quaternary blend UHPCs with 20% fly ash and 20% natural pozzolan and 10% silica fume showed lower drying shrinkage as compared the control UHPC. The presence of fly ash and natural pozzolan compensated for the higher drying shrinkage exhibited by the silica fume, as seen in the binary blend UHPCs made with silica fume (Van Quan et al. 2020).

2.3.2 Effect of V_A/V_{cm} on Compressive and Splitting-Tensile Strengths, and Drying Shrinkage

Table 2.5 and Figure 2.8a present the effect of V_A/V_{cm} on the average compressive strength of the plain UHPCs at various curing durations. With the increase in curing age, the compressive strength also increased. On average, the UHPCs with $V_A/V_{cm} = 0.80$ attained 46 and 78% of their 28-day compressive

strength at one and seven days, respectively. Similar compressive strength developments were found for V_A/V_{cm} =1.0 and 1.20. On average, the 90-day compressive strengths were 13, 17, and 18% higher than the 28-day compressive strength for the UHPCs having V_A/V_{cm} =0.80, 1.0, and 1.2, respectively. For V_A/V_{cm} = 0.80 and 1.0, fifteen out of the twenty-six UHPCs achieved the minimum compressive strengths of 120 and 150 MPa, respectively, at 28 and 90 days curing durations. When the V_A/V_{cm} =1.2 was used, 12 out of 26 UHPCs produced the minimum compressive strength of 120 and 150 MPa for the same curing ages.

Generally, with the increase of V_A/V_{cm} from 0.80 to 1.2, the compressive strength decreased. However, the effects were minimal at later curing durations. For example, at the 7-day testing an average of 6 and 12% reduction in compressive strength was observed for UHPCs having V_A/V_{cm} =1.0 and 1.2, respectively, whereas for 90-day testing, the reduction in compressive strengths were 3 and 7% when compared to those of the UHPC with V_A/V_{cm} = 0.80. Overall, while cementitious materials content can make a sizeable impact on strength, the proportions of aggregate-to-cementitious materials also plays a role on strength, due to contributions of quality and amount of aggregate on the resulting w/cm, porosity, and interfacial zone.

The effect of V_A/V_{cm} on the average 28-day splitting-tensile strength of the plan UHPCs is shown in Figure 2.8b and Table 2.5. Similar to the results of strength in compression, with the increase of V_A/V_{cm}, a decrease in the splitting-tensile strength was observed. On average, 9.5, 9.3, and 9.0 MPa splitting-tensile strengths were obtained for the studied UHPCs using V_A/V_{cm} =0.80, 1.0, and 1.20, respectively. Also, on average, 2.4 and 4.8% reductions in splitting-tensile strengths were observed for V_A/V_{cm} =1.0 and 1.2, respectively, as compared to V_A/V_{cm} =0.80. Higher cementitious material amounts resulted in slightly higher tensile strength values; however, the differences were not significant. As previously discussed, significantly high 28-day compressive strength-to-splitting-tensile strength ratio was observed for the studied UHPCs; however, as the V_A/V_{cm} increased, this strength ratio decreased, indicating the higher fine aggregate amounts improved splitting-tensile strength more than the compressive strength. Therefore, the use of very high cementitious material amounts does not improve compressive strength more than splitting-tensile strength. For this reason, in nearly all studies conducted on UHPCs, researchers included some sort of fibers to improve tensile strength performance.

The effect of V_A/V_{cm} on the average 120-day drying shrinkage of the plain UHPCs is shown in Figure 2.8c and Table 2.5. In general, with the increase of V_A/V_{cm}, a decrease in drying shrinkage was observed. On average, 0.106, 0.097, and 0.087% drying shrinkage was obtained using V_A/V_{cm} of 0.80, 1.0, and 1.20, respectively. Moreover, on average, a 9.1 and 17.7% reduction in drying shrinkage were observed for V_A/V_{cm} of 1.0 and 1.2, respectively, as compared to that of the V_A/V_{cm} of 0.80. This can be attributed to the lower cementitious materials content and higher restraining effect of the filler materials as the V_A/V_{cm} of the UHPCs increased.
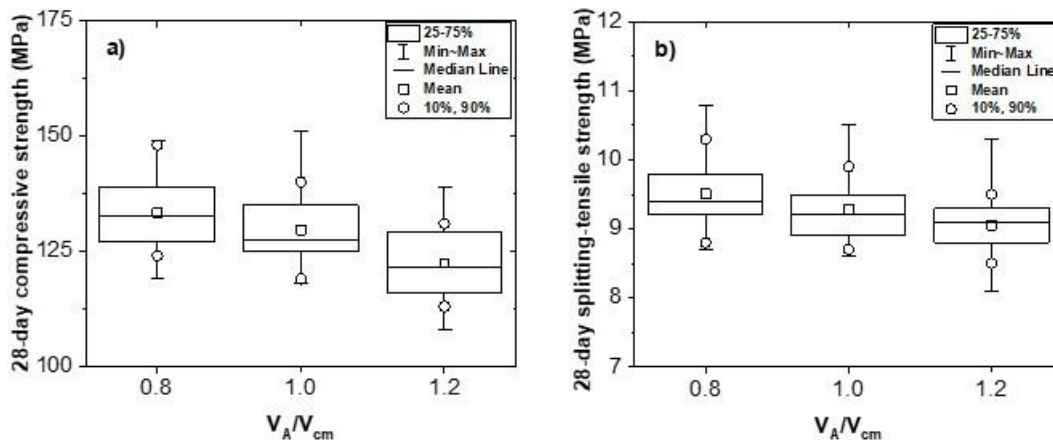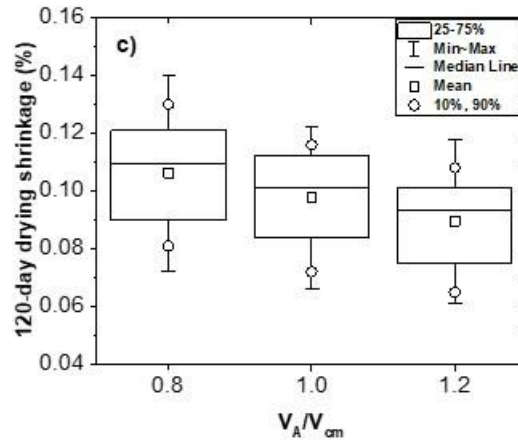
Figure 2.8 Effects of aggregate-to-cementitious materials ratios on UHPCs' (a) 28-day compressive strength, (b) 28-day splitting-tensile strength, and (c) 120-day drying shrinkage

2.3.3 Optimized plain UHPCs

In the first phase of the study, three aggregate-to-cementitious materials ratios (0.80, 1.0, and 1.20) were used to assess the bulk properties and dimensional stability of the studied UHCs. The average 28-day compressive strength test shows that UHPCs with the V_A/V_{cm} equals to 1.20 displayed 7% lower compressive strength and 5% lower splitting-tensile strength than that of the V_A/V_{cm} of 0.80. Interestingly, as the curing duration increased from 28-day to 90-day, the average compressive strength of UHPCs made using V_A/V_{cm} of 1.20 was only 3% lower than the V_A/V_{cm} of 0.80. In contrast, the average 120-day drying shrinkage of UHPCs having V_A/V_{cm} of 0.80 was significantly (22%) higher than that of the UHPCs made using V_A/V_{cm} of 1.20. Considering these outcomes, V_A/V_{cm} of 1.20 was selected for the Phase II of this study.

Amongst the 26 cementitious material compositions used in the first phase of this study, four binary (out of 13), four ternary (out of nine), and two quaternary (out of three) cementitious compositions were selected based on their mechanical and dimensional stability performance within their own respective groups. Additionally, concrete cost was considered when similar properties were obtained in the same cement blend group. The price distribution of Portland cement and slag is similar, and it seemed that addition of GGBS did not add much benefit to the bulk and dimensional stability of the UHPCs incorporating GGBS. On the other hand, class F fly ash and natural pozzolan significantly improved the long-term strength properties, as well as the 120-day drying shrinkage behavior. For this reason, in the Phase II, GGBS was only incorporated in one fiber-reinforced UHPC. Silica fume addition improved bulk properties significantly, however, it negatively impacted dimensional stability. Silica fume with fly ash/natural pozzolan provided both higher bulk properties and lower dimensional stability. For these reasons, the ternary UHPCs selected for Phase II study contained silica fume combined with fly ash or natural pozzolan.

2.4 Fiber-Reinforced UHPCs (Phase II)

Based on the results of the strength properties and drying shrinkage of the UHPCs studied in Phase I, a total of 40 UHPCs (11 plain UHPCs and 29 steel fiber-reinforced UHPCs) with 11 binder combinations were selected to study the performance of fiber-reinforced UHPCs. The Phase II mixture proportions for fiber-reinforced UHPCs are presented in Table 6. Their batching procedure was the same as the one presented in Section 2.5. The investigated properties included compressive strength, splitting-tensile resistance, flexural strength, load-deflection response, flexural strain, elastic modulus, and drying shrinkage. The details of all the tests performed in this phase are given in Table 2.4.

2.5 Experimental Results on Fiber-Reinforced UHPC (Phase II)

Table 2.7 summarizes the bulk, shrinkage, and flexural strain properties of fiber-reinforced UHPCs and UHPCs without steel fibers. A detailed discussion is provided in the following sub-sections.

2.5.1 Flow and Unit Weight

The UHPCs' flow diameters and demolded unit weights are presented in Table 2.7. A satisfactory flow spread diameter of 250±25 mm was attained for all UHPCs. UHPCs containing steel fibers required additional HRWRA to maintain the required flow spread diameter. Fly ash's spherical shape (Figure 2.1) gave the mixtures additional flowability and a lower demand for HRWRA. On the other hand, UHPCs containing silica fume, with a very high surface area, (Figure 2.2) required a higher amount of HRWRA. On average, 2402, 2490, and 2546 kg/m^3 unit weight was obtained using 0, 2, and 3% steel fibers, respectively. A typical unit weight of UHPCs varies from 2300 to 2700 kg/m^3 (Sohail et al. 2018). Due to the high relative density of the steel fibers, the UHPCs containing 2 and 3% steel fibers showed higher unit weights as compared to those of the companion plain UHPCs.

Table 2.6 Mixture proportions of fiber-reinforced UHPCs

Mixture ID[a]	V_A/V_{cm}	w/cm	C[b]	F[b]	N[b]	S[b]	SF[b]	Agg[b]	HRWRA[b]	W[b]	Fiber[b]
							kg/m^3				
C100-2%H	1.2	0.21	1101					1174	13.1	224	156
C95SF5-2%H	1.2	0.21	1046				37	1174	13.4	220	156
C90SF10-2%H	1.2	0.21	991				70	1174	13.6	216	156
C80F20-2%H	1.2	0.21	881	163				1174	11.9	213	156
C70F30-2%H	1.2	0.21	771	244				1174	11.2	208	156
C80F15SF5-2%H	1.2	0.21	881	122			31	1174	12.4	211	156
C80N15SF5-2%H	1.2	0.21	881		96		31	1174	12.5	205	156
C70F20SF10-2%H	1.2	0.21	771	163			55	1174	13.2	201	156
C70N20SF10-2%H	1.2	0.21	771		112		55	1174	13.2	190	156
C60F10S20SF10-2%H	1.2	0.21	660	81		120	47	1174	13.7	184	156
C50F20N20SF10-2%H	1.2	0.21	550	163	80		39	1174	13.3	168	156
C100-2%S	1.2	0.21	1101					1174	13.1	224	156
C95SF5-2%S	1.2	0.21	1046				37	1174	13.4	220	156
C80F20-2%S	1.2	0.21	881	163				1174	11.9	213	156
C70F30-2%S	1.2	0.21	771	244				1174	11.2	208	156
C80F15SF5-2%S	1.2	0.21	881	122			31	1174	12.4	211	156
C80N15SF5-2%S	1.2	0.21	881		96		31	1174	12.5	205	156
C100-3%H	1.2	0.21	1101					1174	14.9	222	234
C95SF5-3%H	1.2	0.21	1046				37	1174	13.2	220	234
C80F20-3%H	1.2	0.21	881	163				1174	12.4	214	234
C70F30-3%H	1.2	0.21	771	244				1174	13.7	208	234
C80F15SF5-3%H	1.2	0.21	881	122			31	1174	13.9	210	234
C80N15SF5-3%H	1.2	0.21	881		96		31	1174	16.5	202	234
C100-3%S	1.2	0.21	1101					1174	14.7	223	234
C95SF5-3%S	1.2	0.21	1046				37	1174	13.8	218	234
C80F20-3%S	1.2	0.21	881	163				1174	15.2	209	234
C70F30-3%S	1.2	0.21	771	244				1174	15.4	205	234
C80F15SF5-3%S	1.2	0.21	881	122			31	1174	18.3	205	234
C80N15SF5-3%S	1.2	0.21	881		96		31	1174	16.3	204	234

1 kg/m^3 = 1.685 lb/yd^3

[a] Mixture ID: number after C, F, N, S, and SF indicates percentage of respective cementitious materials. 2%S, 2%H, 3%S, and 3%H after hyphen (-) denotes percentage of steel fiber used. For example, C95SF5-2%H means 95% cement and 5% silica fume and 2% hooked steel fiber.

Table 2.7 Summary of test results of Phase II study

Mixture ID	Flow (mm)	γ_{con} (kg/m^3)	f'_{c-28D} (MPa)	f_{t-28D} (MPa)	f_{r-28D} (MPa)	E_{c-28D} (GPa)	D_{120D} (%)	ε_f (%)
C100	248	2470	125	9.1	11.8	38.9	0.087	0.00005
C95SF5	273	2451	131	9.4	13.2	41.8	0.096	0.00005
C90SF10	268	2432	138	9.8	14.3	44.0	0.101	0.00006
C80F20	270	2405	122	9.0	12.5	37.9	0.068	0.00004
C70F30	250	2374	120	8.8	12.2	37.2	0.064	0.00004
C80F15SF5	253	2388	129	9.5	13.3	42.2	0.093	0.00005
C80N15SF5	236	2386	127	9.3	12.7	41.2	0.094	0.00005
C70F20SF10	274	2372	131	9.2	12.7	41.5	0.098	0.00005
C70N20SF10	267	2369	130	9.1	11.9	39.9	0.100	0.00004
C60F10S20SF10	244	2385	123	9.2	12.7	37.4	0.086	0.00004
C50F20N20SF10	272	2393	120	9.1	10.7	35.3	0.083	0.00004
C100-2%H	241	2536	127	10.5	16.2	39.4	0.079	0.00102
C95SF5-2%H	247	2512	135	11.1	18.0	42.3	0.083	0.00107
C90SF10-2%H	244	2506	143	11.4	18.3	44.7	0.093	0.00119
C80F20-2%H	271	2475	125	10.6	15.4	39.2	0.059	0.00093
C70F30-2%H	269	2440	127	10.4	15.1	39.8	0.056	0.00078
C80F15SF5-2%H	248	2483	136	11.2	16.6	42.5	0.081	0.00165
C80N15SF5-2%H	250	2478	131	10.9	16.9	41.7	0.082	0.00144
C70F20SF10-2%H	248	2504	136	10.7	17.0	42.3	0.086	0.00190
C70N20SF10-2%H	251	2473	135	10.6	16.8	42.1	0.092	0.00187
C60F10S20SF10-2%H	245	2488	131	10.3	15.1	38.1	0.082	0.00111
C50F20N20SF10-2%H	242	2483	123	10.1	14.9	36.7	0.081	0.00099
C100-2%S	256	2531	127	10.6	16.8	39.9	0.078	0.00128
C95SF5-2%S	240	2506	134	11.0	18.5	42.4	0.083	0.00205
C80F20-2%S	247	2491	125	10.7	17.7	39.0	0.059	0.00085
C70F30-2%S	270	2446	128	10.6	17.3	40.1	0.056	0.00107
C80F15SF5-2%S	264	2490	135	11.1	18.7	43.7	0.078	0.00189
C80N15SF5-2%S	245	2481	133	11.0	17.3	42.6	0.080	0.00157
C100-3%H	251	2585	130	12.3	18.7	41.4	0.069	0.00385
C95SF5-3%H	255	2551	139	12.8	22.0	43.1	0.073	0.00449
C80F20-3%H	240	2540	127	12.2	17.5	39.8	0.054	0.00383
C70F30-3%H	246	2498	131	12.1	17.2	43.3	0.052	0.00352
C80F15SF5-3%H	265	2535	140	13.1	22.2	43.9	0.072	0.00532
C80N15SF5-3%H	261	2533	137	12.9	19.9	43.1	0.074	0.00443
C100-3%S	271	2592	131	12.5	20.7	41.9	0.067	0.00403
C95SF5-3%S	250	2583	141	13.0	23.1	44.7	0.074	0.00540
C80F20-3%S	255	2543	128	12.4	20.7	40.4	0.054	0.00448
C70F30-3%S	238	2506	133	12.3	19.7	42.8	0.053	0.00424
C80F15SF5-3%S	243	2535	143	13.1	24.7	45.0	0.068	0.00557
C80N15SF5-3%S	264	2545	137	13.0	23.0	43.9	0.070	0.00509

Note: 1 MPa= 145 Psi; γ_{con} denote unit weight; f'_{c-28D} denotes compressive strength at 28-day; f_{t-28D} denote splitting-tensile strength at 28-day; f_{r-28D} denote flexural strength at 28-day; E_{c-28D} denote elastic modulus at 28-day; D_{120D} denote drying shrinkage at 120-day; ε_f denote flexural strain at peak load

2.5.2 Effect of Steel Fiber Content and Shape

2.5.2.1 Compressive Strength

The 28-day compressive strength of the UHPCs containing 2 and 3% hooked and straight steel fibers is documented in Table 2.7 and Figure 2.9a. In general, the introduction of fibers improved the UHPCs' compressive strength to some extent, and UHPCs made with 3% steel fibers produced slightly higher compressive strengths than those UHPCs incorporating 2% steel fibers. When 2% hooked steel fiber was added, the average compressive strength improved by 3% as compared to the control UHPC without steel fibers. With the introduction of 3% hooked fiber, the corresponding gain in average compressive strength was 6%. The increases in the compressive strength, with increases in fiber content, can be attributed to the anticipated increase in the matrix stiffness of the fiber-containing UHPCs; however, these improvements were minimal. Several other studies also reported similar finding (Le Hoang,& Fehling 2017, Park et al. 2017). The addition of 2 and 3% straight steel fibers to the UHPCs resulted in an average increase of 2% in compressive strength as compared to those of the UHPCs made with the hooked fibers, possibly due to better interfacial bonding between the matrix and straight fibers.

2.5.2.2 Splitting-Tensile Strength

The 28-day splitting-tensile resistance of the UHPCs with 2 and 3% hooked and straight steel fibers is presented in Table 2.7 and Figure 2.9b. The introduction of fibers significantly improved splitting-tensile strength. The UHPCs made with 3% steel fibers produced a significantly higher splitting-tensile strength as compared to the UHPCs made with 2% steel fibers. When 2% hooked steel fiber was added, the average splitting-tensile strength improved by 17% as compared to that of the plain UHPC. With the introduction of 3% hooked fiber, the corresponding gain in the average splitting-tensile strength was nearly 37%. Additionally, the test specimens having 2 and 3% straight fibers increased their average splitting-tensile resistance by 18 and 38%, respectively. This finding can be attributed to the anticipated increase in the matrix stiffness of the fiber-reinforced UHPCs. Additionally, steel fibers distributed localized stress to the surrounding concrete and acted as a crack arrester. The addition of 2 and 3% straight steel fibers resulted in a similar increase in splitting-tensile strength, as compared to those of the UHPCs made with the hooked fibers.
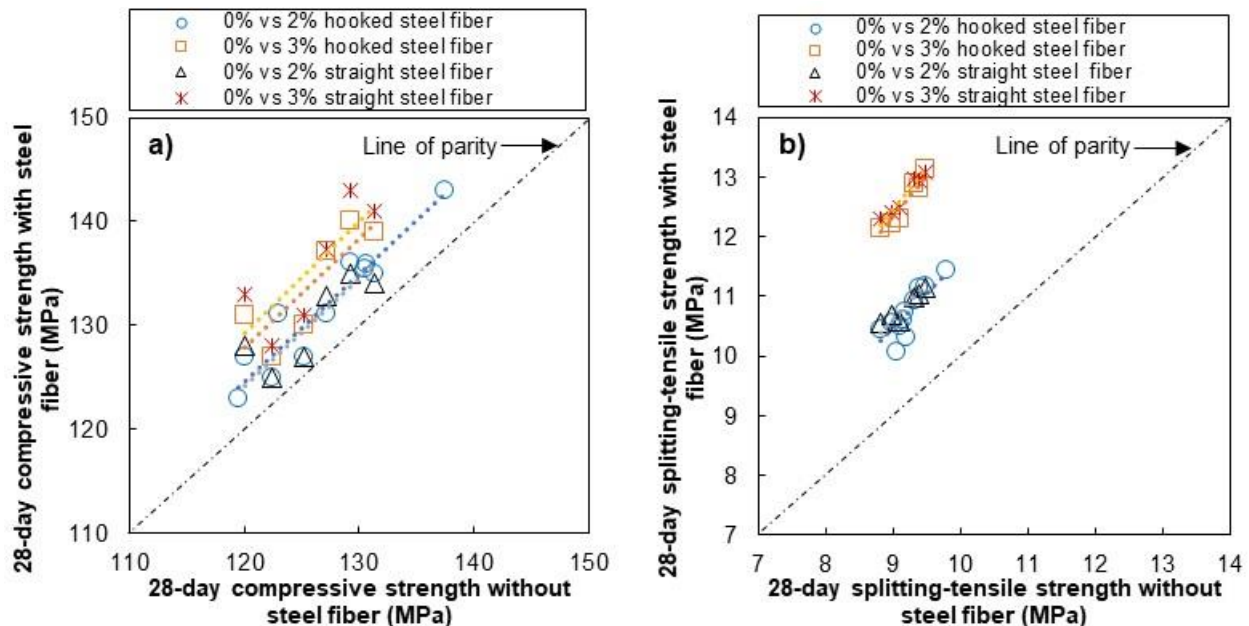
Figure 2.9 Effect of steel fiber content and shape on UHPCs' (a) 28-day compressive strength, (b) 28-day splitting-tensile strength

2.5.2.3 Load-Deflection Response, Flexural Strength, and Flexural Strain

The mid-span load-deflection (P-δ) response of the 28-day cured UHPC beams for both plain and fiber-reinforced UHPCs was determined and the representatives are depicted in Figure 2.10. Figure 2.10a shows the load-deflection response of the control UHPCs incorporating 0, 2 and 3% hooked steel fibers. The P-δ responses of all three UHPCs were linear until the deflection values reached near to 0.1 mm, at which plain UHPC reached its peak load and failed in a brittle manner. An increased load capacity was obtained when the fiber volume increased from 2% to 3%. The fiber-reinforced UHPCs showed a strain hardening response between 0.1 to 0.45 mm deflection for 2% fiber-reinforced UHPCs, and 0.1 to 0.80 mm deflection for 3% fiber-reinforced UHPC specimens. As the fiber content increased from 2 to 3%, the post-peak load retention capacity also increased. A similar trend was found for the UHPCs containing straight steel fibers as depicted in Figure 10b. The failure sequence of fiber-reinforced UHPCs having 3% steel fibers is illustrated in Figure 2.11. The steel fibers acted as a bridge to restrain crack development, and a clear demonstration of the strain-hardening and softening effect is depicted. Arora et al. (2015) also documented a similar strain-hardening trend in the P-δ responses of fiber-reinforced UHPCs.
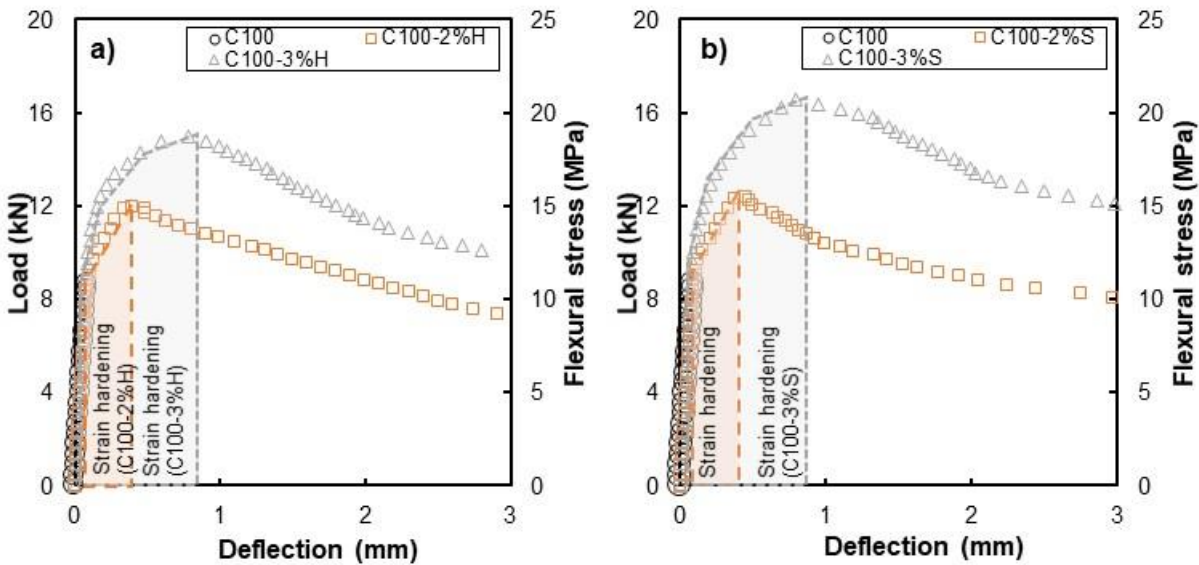
Figure 2.10 Load-deflection response of plain and fiber-reinforced UHPCs: (a) with hooked steel fibers, (b) with straight steel fibers
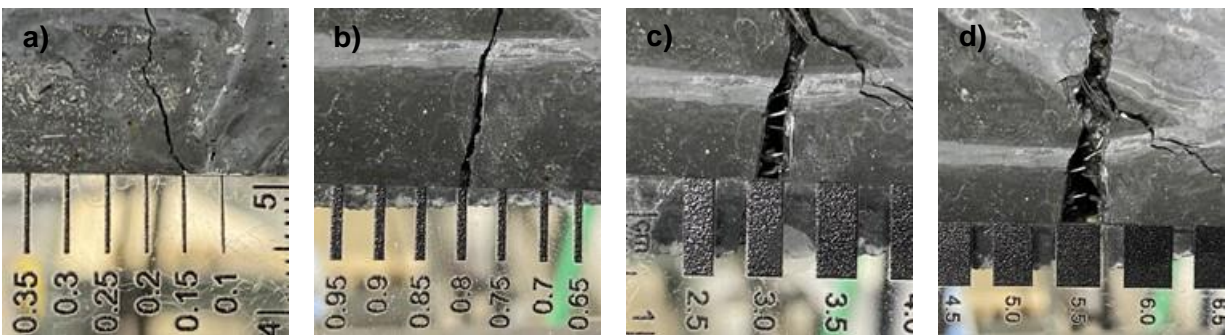
Figure 2.11 Failure sequence of typical fiber-reinforced UHPC (C100-S3%), (a) first crack, (b) strain hardening, (c) softening, (d) failure of sample

The 28-day flexural strength of the studied UHPCs are given in Table 2.7. Overall, significant improvement in flexural strength was observed when steel fibers were incorporated, with the addition of 2 and 3% hooked steel fibers resulting in average increases of 23 and 36%, respectively, when compared to those of the plain UHPCs. In comparison, improvements in the flexural strength of the UHPCs made with 2 and 3% straight steel fibers were 29 and 43%, respectively. The effects of fiber content and shape on the UHPCs' flexural strength is presented in Figure 2.12. From the box-whisker plot, the shape of fiber had only a minor influence on flexural strength of the UHPCs. Mixtures incorporating 2% and 3% straight fibers showed 7 and 11% higher flexural strength, respectively, when compared with those made with hooked fibers. The addition of steel fibers had more influence on the UHPCs' flexural strength resistance than it did on their compressive strength.
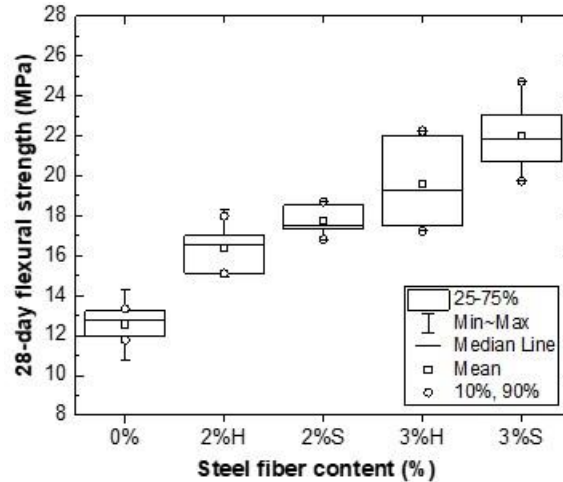
Figure 2.12 Effects of steel fiber content and shape on UHPCs' 28-day flexural strength

The 28-day flexural strain evaluated from the load-deflection responses of the UHPCs are tabulated in Table 2.7. Due to the brittle nature of plain UHPCs, these mixtures had a very low flexural strain at peak load. As shown in Figure 2.13, presence of steel fibers improved the flexural strain by arresting crack growth and generating strain-hardening before the peak strength was reached. The improvement in flexural strain capacity, due to the contribution of steel fibers, corroborates the increased ductility of the studied fiber-reinforced UHPCs.
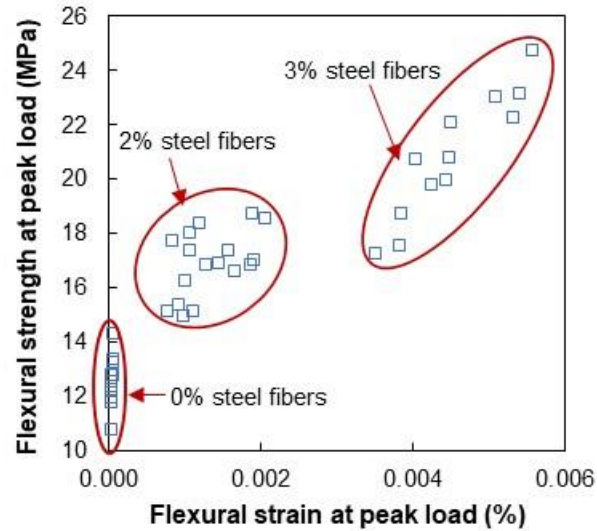
Figure 2.13 Correlation between flexural strength and flexural strain at peak load

2.5.2.4 Elastic Modulus

Table 2.7 documents the 28-day elastic moduli of the studied UHPCs. Similar to the results of compressive strength, the addition of steel fibers did not have significant effects on the elastic moduli of the studied UHPCs. Yoo et al. (2014) also reported minor improvement of elastic moduli in fiber-reinforced UHPCs. Inclusion of 2 and 3% hooked steel fibers resulted in average increases of 3 and 6%, respectively. In comparison, improvements in the elastic moduli of the UHPCs made with 2 and 3% straight steel fibers were 4 and 8%, respectively. Figure 2.14 documents the effects of fiber contents and shapes on the elastic moduli of the studied UHPCs. The UHPCs made with straight steel fibers performed slightly better than the hooked steel fibers. Mixtures containing 2% and 3% straight fibers showed 7 and 11% higher elastic modulus, respectively, when compared to the companion UHPCs containing hooked fibers.
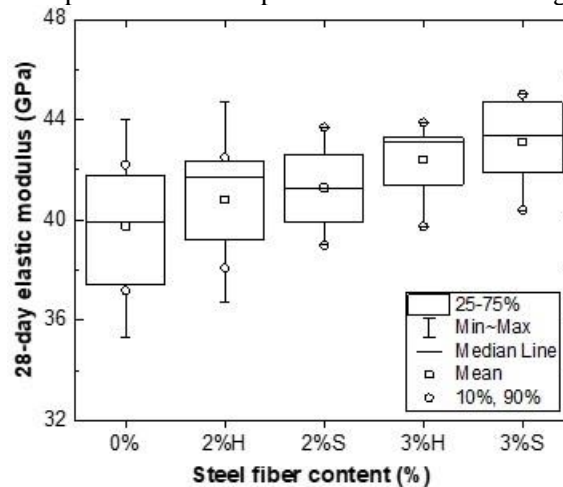
Figure 2.14 Effect of steel fiber content and shape on 28-day elastic modulus of UHPCs

2.5.2.5 Drying Shrinkage

The drying shrinkage of the plain and fiber-reinforced UHPCs is documented in Table 2.7. The effects of the cementitious materials and fine aggregate-to-cementitious materials ratio on the UHPCs' drying

shrinkage were discussed in section 2.3.1.3 and 2.3.2. The effect of steel fiber content and shape on the drying shrinkage as a function of time is shown in Figure 2.15. Inclusion of steel fibers greatly restrained the drying shrinkage. Overall, the drying shrinkage of both plain and fiber-reinforced UHPCs peaked at about 60 days with minor increases thereafter. Straight steel fibers performed slightly better in restraining drying shrinkage due to better fiber to paste surface bonding. This finding is in line with the other mechanical properties, such as flexural strength and elastic modulus. On average, inclusion of 2 and 3% steel fiber resulted in 14 and 26% reductions of drying shrinkage as compared to that of the plain UHPCs. As can be seen, 3% steel fibers were more effective in reducing drying shrinkage than 2% steel fibers. Yoo et al. (2014) also found 3% steel fiber to be optimum in reducing drying shrinkage.
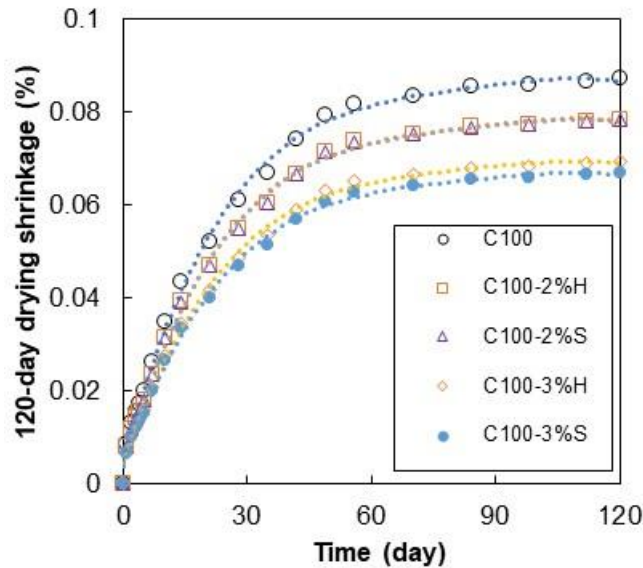
Figure 2.15 Effects of steel fiber content and shape on UHPCs' drying shrinkage

2.6 Relationships Between UHPCs' Bulk Properties

Various correlations were developed amongst compressive strength (120-150 MPa), splitting-tensile resistance, flexural strength, and elastic modulus of the studied plain and fiber-reinforced UHPCs. A suitable relationship, at a 95% confidence level, between 28-day cured compressive strength and splitting-tensile resistance is shown in Figure 2.16. Increases in the UHPCs' compressive strength led to increased splitting-tensile strength for the studied UHPCs. The steel fiber content had more influence on splitting-tensile strength than it had on compressive strength. Increases in steel fiber content also resulted in the reduced compressive-splitting-tensile strength ratios of the studied UHPCs. The relationship between the flexural and splitting-tensile strength of fiber-reinforced UHPCs, with a coefficient of determination (R^2) value of 0.92, is presented in Figure 2.17. The proposed equation can be used to predict the splitting-tensile strength of UHPCs using flexural strength data. Compressive strength and modulus of elasticity relationships are well established in various codes and standards for conventional and high-strength concrete. An attempt was made to develop a correlation between compressive strength and modulus of elasticity of the studied UHPCs. Figure 2.18 documents the most suitable relationship between compressive strengths and elastic moduli, having a coefficient of determination (R^2) value 0.84. The use of high amounts of cementitious materials and omission of coarse aggregate in UHPCs resulted in the relationship between compressive strength and elastic modulus that differed from that of the conventional UHPC concretes. A similar observation was also reported by Alsalman et al. (2017).
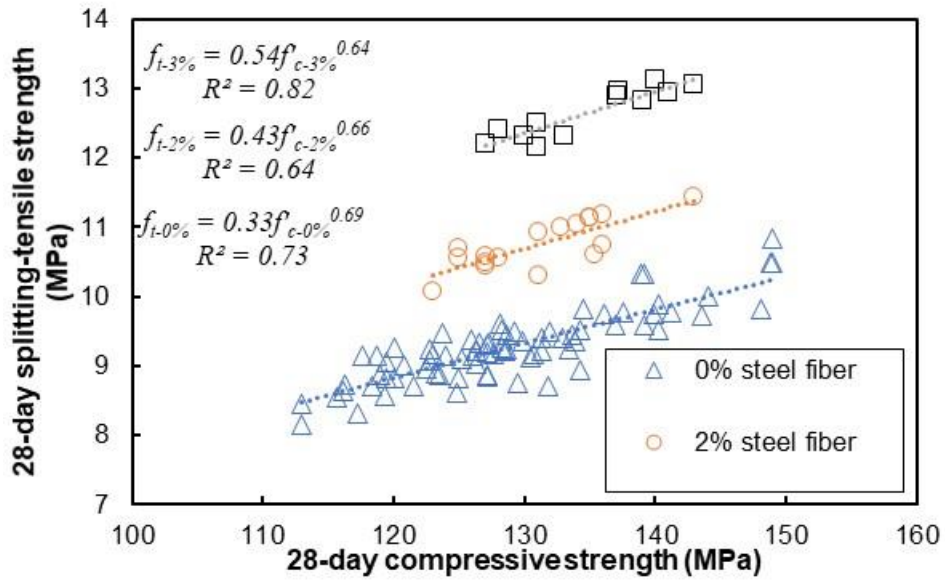
Figure 2.16 Correlation between 28-day compressive and splitting-tensile strengths
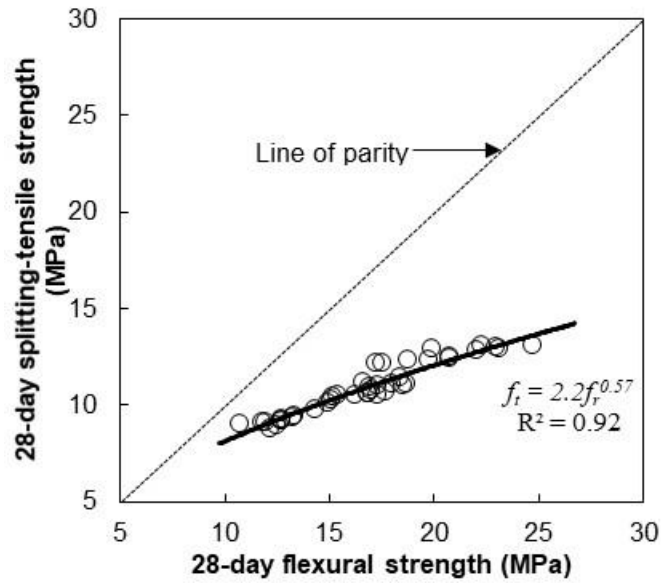
Figure 2.17 Correlation between 28-day splitting-tensile and flexural strengths
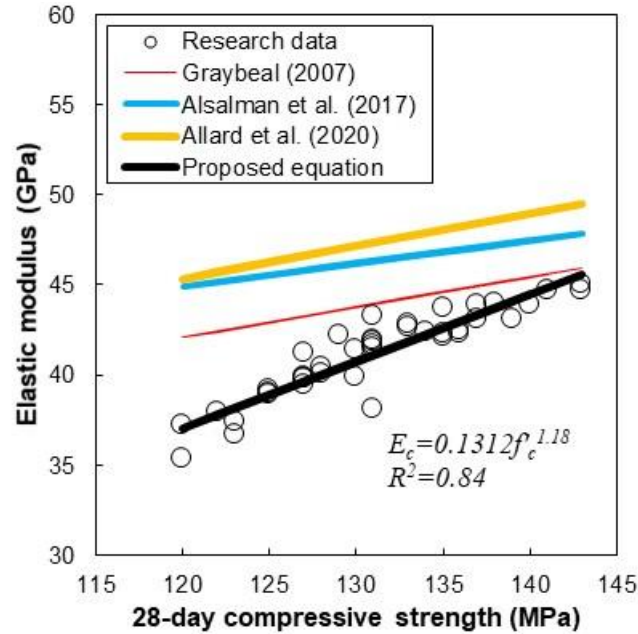
Figure 2.18 Correlation between 28-day compressive strength and elastic modulus

2.7 Conclusions

Based on the results of this study, the following conclusions can be drawn:

(1)   The binary blend UHPCs containing fly ash or silica fume displayed higher strength properties than slag and natural pozzolan. Overall, amongst the studied binary, ternary, and quaternary cement blend UHPCs; ternary blend UHPCs containing fly ash and silica fume exhibited highest bulk properties.

(2)   The increase of aggregate-to-cementitious materials ratio (V_A/V_{cm}) from 0.80 to 1.20 resulted in reduced 28-day compressive strength of the studied UHPCs. However, reduction in compressive strength became less pronounced once curing age was extended to 90-day.

(3)   Cementitious materials types and compositions had more influence than aggregate-to-cementitious materials ratio on the strength properties of the studied UHPCs.

(4)   Inclusion of steel fibers significantly improved splitting-tensile resistance and flexural strength, whereas its effect on compressive strength and elastic modulus was minimal.

(5)   Straight steel fibers produced a slightly better bulk properties and dimensional stability than hooked fibers.

(6)   Drying shrinkage of the plain UHPCs decreased with increases in aggregate-to-cementitious materials ratios (V_A/V_{cm}). Secondary cementitious materials had significant effects on drying shrinkage of the studied UHPCs', with fly ash performing the best and silica fume performing the worst. Addition of fly ash or natural pozzolan and steel fibers compensated for the higher drying shrinkage exhibited by the silica fume in the binary blend UHPCs.

(7)   The studied plain UHPC beams failed in a brittle manner. A clear strain-hardening before peak strength was observed in steel fiber-reinforced UHPCs. An increase in steel fiber content significantly improved post-peak retention capacity of the studied fiber-reinforced UHPCs.

References

1. Ahlborn, T. T. M., Harris, D. K., Misson, D. L., & Peuse, E. J. (2011). Characterization of strength and durability of ultra-high-performance concrete under variable curing conditions. Transportation research record, 2251(1), 68-75.
2. Wille, K., Naaman, A. E., & Parra-Montesinos, G. J. (2011). Ultra-High Performance Concrete with Compressive Strength Exceeding 150 MPa (22 ksi): A Simpler Way. ACI Materials Journal, 108(1), 46-54.
3. Wang, C., Yang, C., Liu, F., Wan, C., & Pu, X. (2012). Preparation of ultra-high performance concrete with common technology and materials. Cement and Concrete Composites, 34(4), 538-544.
4. Magureanu, C., Sosa, I., Negrutiu, C., & Heghes, B. (2012). Mechanical properties and durability of ultra-high-performance concrete. ACI Materials Journal, 109(2), 177-183.
5. Lee, M. J., Lee, M. G., Huang, Y., & Lee, K. L. (2013). UHPC precast concrete under severe freeze-thaw conditions. International Journal of Engineering and Technology, 5(4), 452.
6. Alkaysi, M., El-Tawil, S., Liu, Z., & Hansen, W. (2016). Effects of silica powder and cement type on durability of ultra high performance concrete (UHPC). Cement and Concrete Composites, 66, 47-56.
7. Yalçınkaya, Ç., & Yazıcı, H. (2017). Effects of ambient temperature and relative humidity on early-age shrinkage of UHPC with high-volume mineral admixtures. Construction and Building Materials, 144, 252-259.
8. Ragalwar, K., Heard, W. F., Williams, B. A., & Ranade, R. (2020). Significance of the particle size distribution modulus for strain-hardening-ultra-high performance concrete (SH-UHPC) matrix design. Construction and Building Materials, 234, 117423.
9. ACI Committee 239. (2018). Ultra-High-Performance Concrete: An Emerging Technology Report (ACI 239R-18). Farmington Hills, MI: American Concrete Institute.
10. ASTM C1856 / C1856M-17, Standard Practice for Fabricating and Testing Specimens of Ultra-High Performance Concrete, ASTM International, West Conshohocken, PA, 2017, www.astm.org.
11. Blais, P. Y., & Couture, M. (1999). Precast, prestressed pedestrian bridge – world's first reactive powder concrete structure. PCI journal, 44(5), 60-71.
12. Larsen, I. L., & Thorstensen, R. T. (2020). The influence of steel fibres on compressive and tensile strength of ultra high performance concrete: A review. Construction and Building Materials, 256, 119459.
13. Karim, R., Najimi, M., & Shafei, B. (2019). Assessment of transport properties, volume stability, and frost resistance of non-proprietary ultra-high performance concrete. Construction and Building Materials, 227, 117031.
14. Bonneau, O., Vernet, C., Moranville, M., & Aïtcin, P. C. (2000). Characterization of the granular packing and percolation threshold of reactive powder concrete. Cement and Concrete Research, 30(12), 1861-1867.
15. Jacobsen, S., & Sellevold, E. J. (1996). Self healing of high strength concrete after deterioration by freeze/thaw. Cement and Concrete Research, 26(1), 55-62.
16. Tang, K. (2017). Stray current induced corrosion of steel fibre reinforced concrete. Cement and Concrete Research, 100, 445-456.
17. Yang, S. L., Millard, S. G., Soutsos, M. N., Barnett, S. J., & Le, T. T. (2009). Influence of aggregate and curing regime on the mechanical properties of ultra-high performance fibre reinforced concrete (UHPFRC). Construction and Building Materials, 23(6), 2291-2298.
18. Zhong, R., Wille, K., & Viegas, R. (2018). Material efficiency in the design of UHPC paste from a life cycle point of view. Construction and Building Materials, 160, 505-513.
19. Tam, C. M., Tam, V. W., & Ng, K. M. (2012). Assessing drying shrinkage and water permeability of reactive powder concrete produced in Hong Kong. Construction and Building Materials, 26(1), 79-89.

20. Sohail, M. G., Wang, B., Jain, A., Kahraman, R., Ozerkan, N. G., Gencturk, B., Dawood, M., & Belarbi, A. (2018). Advancements in concrete mix designs: High-performance and ultrahigh-performance concretes from 1970 to 2016. Journal of Materials in Civil Engineering, 30(3), 04017310.
21. Ahlborn, T. T. M., Harris, D. K., Misson, D. L., & Peuse, E. J. (2011). Characterization of strength and durability of ultra-high-performance concrete under variable curing conditions. Transportation research record, 2251(1), 68-75.
22. Acker, P., & Behloul, M. (2004, September). Ductal® technology: A large spectrum of properties, a wide range of applications. In Proc. of the Int. Symp. on UHPC Kassel, Germany (pp. 11-23).
23. M. Schimidt, E. Fehling, Ultra-high-performance concrete: research, development and application in Europe, in: 7th International Symposium on the Utilization of High-Strength- and High-Performance-Concrete, ACI Washington, 2005, SP.228-4, pp. 51–78.
24. Graybeal, B. UHPC in the U.S. highway transportation system, in: Proceedings of the Second International Symposium on Ultra High Performance Concrete, Kassel University Press GmbH, Kassel, Germany, 2008, p. 11.
25. Arora, A., Almujaddidi, A., Kianmofrad, F., Mobasher, B., & Neithalath, N. (2019). Material design of economical ultra-high performance concrete (UHPC) and evaluation of their properties. Cement and Concrete Composites, 104, 103346.
26. Yang, R., Yu, R., Shui, Z., Gao, X., Xiao, X., Zhang, X., Wang, Y. & He, Y. (2019). Low carbon design of an Ultra-High Performance Concrete (UHPC) incorporating phosphorous slag. Journal of Cleaner Production, 240, 118157.
27. Alsalman, A., Dang, C. N., & Hale, W. M. (2017). Development of ultra-high performance concrete with locally available materials. Construction and Building Materials, 133, 135-145.
28. Chan, Y. W., & Chu, S. H. (2004). Effect of silica fume on steel fiber bond characteristics in reactive powder concrete. Cement and concrete research, 34(7), 1167-1172.
29. Graybeal, B. (2006). Material property characterization of ultra-high performance concrete. FHWA, US Department of Transportation. Report No. FHWA-HRT-06-103, McLean, VA.
30. Ganesh, P., & Murthy, A. R. (2019). Tensile behaviour and durability aspects of sustainable ultra-high performance concrete incorporated with GGBS as cementitious material. Construction and Building Materials, 197, 667-680.
31. Meng, W., Valipour, M., & Khayat, K. H. (2017). Optimization and performance of cost-effective ultra-high performance concrete. Materials and Structures, 50(29), DOI: 10.1617/s11527-016-0896-3.
32. Abbas, S., Soliman, A. M., & Nehdi, M. L. (2015). Exploring mechanical and durability properties of ultra-high performance concrete incorporating various steel fiber lengths and dosages. Construction and Building Materials, 75, 429-441.
33. Máca, P., Sovják, R., & Vavřiník, T. (2013). Experimental investigation of mechanical properties of UHPFRC. Procedia Engineering, 65, 14-19.
34. Yoo, D. Y., Shin, H. O., Yang, J. M., & Yoon, Y. S. (2014). Material and bond properties of ultra high performance fiber reinforced concrete with micro steel fibers. Composites Part B: Engineering, 58, 122-133.
35. Wille, K., Kim, D. J., & Naaman, A. E. (2011). Strain-hardening UHP-FRC with low fiber contents. Materials and Structures, 44(3), 583-598.
36. Wu, Z., Shi, C., He, W., & Wu, L. (2016). Effects of steel fiber content and shape on mechanical properties of ultra high performance concrete. Construction and building materials, 103, 8-14.
37. Park, S. H., Kim, D. J., Ryu, G. S., & Koh, K. T. (2012). Tensile behavior of ultra high performance hybrid fiber reinforced concrete. Cement and Concrete Composites, 34(2), 172-184.
38. Kim, D. J., Park, S. H., Ryu, G. S., & Koh, K. T. (2011). Comparative flexural behavior of hybrid ultra high performance fiber reinforced concrete with different macro fibers. Construction and Building Materials, 25(11), 4144-4155.
39. Hassan, A. M. T., Jones, S. W., & Mahmud, G. H. (2012). Experimental test methods to determine the uniaxial tensile and compressive behaviour of ultra high performance fibre reinforced concrete (UHPFRC). Construction and building materials, 37, 874-882.

40. Bae, B. I., Choi, H. K., & Choi, C. S. (2016). Flexural strength evaluation of reinforced concrete members with ultra high performance concrete. Advances in Materials Science and Engineering, 2815247, https://doi.org/10.1155/2016/2815247.
41. ASTM A820 / A820M-16, Standard Specification for Steel Fibers for Fiber-Reinforced Concrete, ASTM International, West Conshohocken, PA, 2016, www.astm.org
42. ASTM C230 / C230M-14, Standard Specification for Flow Table for Use in Tests of Hydraulic Cement, ASTM International, West Conshohocken, PA, 2021, www.astm.org
43. Funk JE, Dinger DR. (1994). Predictive process control of crowded particulate suspensions, applied to ceramic manufacturing. Boston, USA: Kluwer Academic Publishers.
44. ASTM C29 / C29M-17a, Standard Test Method for Bulk Density ("Unit Weight") and Voids in Aggregate, ASTM International, West Conshohocken, PA, 2017, www.astm.org
45. ASTM C642-13, Standard Test Method for Density, Absorption, and Voids in Hardened Concrete, ASTM International, West Conshohocken, PA, 2013, www.astm.org
46. ASTM C39 / C39M-20, Standard Test Method for Compressive Strength of Cylindrical Concrete Specimens, ASTM International, West Conshohocken, PA, 2020, www.astm.org
47. ASTM C496 / C496M-17, Standard Test Method for Splitting Tensile Strength of Cylindrical Concrete Specimens, ASTM International, West Conshohocken, PA, 2017, www.astm.org
48. ASTM C596-18, Standard Test Method for Drying Shrinkage of Mortar Containing Hydraulic Cement, ASTM International, West Conshohocken, PA, 2018, www.astm.org
49. ASTM C1609 / C1609M-19a, Standard Test Method for Flexural Performance of Fiber-Reinforced Concrete (Using Beam with Third-Point Loading), ASTM International, West Conshohocken, PA, 2019, www.astm.org
50. ASTM C469 / C469M-14, Standard Test Method for Static Modulus of Elasticity and Poisson's Ratio of Concrete in Compression, ASTM International, West Conshohocken, PA, 2014, www.astm.org
51. Langan, B. W., Weng, K., & Ward, M. A. (2002). Effect of silica fume and fly ash on heat of hydration of Portland cement. Cement and Concrete research, 32(7), 1045-1051.
52. Jalal, M., Pouladkhan, A., Harandi, O. F., & Jafari, D. (2015). Comparative study on effects of Class F fly ash, nano silica and silica fume on properties of high performance self compacting concrete. Construction and Building Materials, 94, 90-104.
53. Chen, T., Gao, X., & Ren, M. (2018). Effects of autoclave curing and fly ash on mechanical properties of ultra-high performance concrete. Construction and Building Materials, 158, 864-872.
54. Shaikh, F. U., Nishiwaki, T., & Kwon, S. (2018). Effect of fly ash on tensile properties of ultra-high performance fiber reinforced cementitious composites (UHP-FRCC). Journal of Sustainable Cement-Based Materials, 7(6), 357-371.
55. Yazıcı, H., Deniz, E., & Baradan, B. (2013). The effect of autoclave pressure, temperature and duration time on mechanical properties of reactive powder concrete. Construction and Building Materials, 42, 53-63.
56. Mehta, P. K., & Monteiro, P. J. (2005). Concrete Microstructure, Properties and Materials. (3rd ed.), McGraw Hill.
57. Gerges, N. N., Issa, C. A., & Fawaz, S. (2015). Effect of construction joints on the splitting tensile strength of concrete. Case Studies in Construction Materials, 3, 83-91.
58. Van Quan H., Van Tuoi N., Nguyen C.V. (2020) Effect of fly ash on the mechanical properties and drying shrinkage of the cement treated aggregate crushed stone. In: Ha-Minh C., Dao D., Benboudjema F., Derrible S., Huynh D., Tang A. (eds) CIGOS 2019, Innovation for Sustainable Infrastructure. Lecture Notes in Civil Engineering, vol 54. Springer, Singapore. https://doi.org/10.1007/978-981-15-0802-8_65
59. Le Hoang, A., & Fehling, E. (2017). Influence of steel fiber content and aspect ratio on the uniaxial tensile and compressive behavior of ultra high performance concrete. Construction and Building Materials, 153, 790-806.

60. Park, J. J., Yoo, D. Y., Park, G. J., & Kim, S. W. (2017). Feasibility of reducing the fiber content in ultra-high-performance fiber-reinforced concrete under flexure. Materials, 10(2), 118, https://doi.org/10.3390/ma10020118.

61. Sobuz, H. R., Visintin, P., Ali, M. M., Singh, M., Griffith, M. C., & Sheikh, A. H. (2016). Manufacturing ultra-high performance concrete utilising conventional materials and production methods. Construction and Building materials, 111, 251-261.

CHAPTER 3-TRANSPORT PROPERTIES AND DE-ICING SALT RESISTANCE OF BLENDED ULTRA HIGH-PERFORMANCE CONCRETE

Abstract

Premature degradation of concrete, caused by frost damage, has been associated with inadequate transport properties and poor resistance to de-icing salt. In this study, transport properties and de-icing salt resistance of various ultra high-performance concrete (UHPC) containing Type V Portland cement, fly ash and micro silica were investigated. A total of seven combinations of cementitious materials (one reference, three binary, and three ternary) were used to batch UHPCs using a water-to-cementitious materials ratio (*w/cm*) of 0.21. The aggregate-to-cementitious materials ratio (V_a/V_{cm}) of 1.20 was kept constant for all mixtures. The investigated transport properties included water absorption, volume of permeable voids, water penetration, rapid chloride penetration (ASTM C1202), and surface resistivity. The transport properties of the plain UHPCs were also compared to those of the corresponding steel fiber-reinforced UHPCs. The test results showed that the transport properties and de-icing salt resistance of the studied binary and ternary UHPCs improved with inclusion of and increases in micro silica replacing a portion of cement. The addition of steel fiber had a minor effect on strength and transport properties and a moderate increase in de-icing salt resistance of the studied UHPCs. While rapid chloride penetration and surface resistivity tests were found appropriate to assess chloride transport through the studied plain UHPCs, both tests were deemed unsuitable for the companion steel fiber-reinforced UHPCs.

Keywords: Ultra High-Performance Concrete, Bulk Properties, Transport Properties, De-icing Salt Resistance, Micro silica, Class F Fly Ash.

3.1 Introduction

UHPC is a type of concrete that is known for its exceptional strength, durability, and resilience. It is highly durable, can withstand harsh environmental conditions, and requires less maintenance compared to traditional concrete (Akhnoukh and Buckhalter, 2021; Bajaber and Hakeem, 2021). UHPC offers design flexibility, is environmentally friendly, and has a longer lifespan (Dong, 2018; García et al., 2022; Ma et al., 2023). Overall, it is a high-performance building material that offers many benefits over traditional concrete (Sritharan et al., 2018; Hasnat and Ghafoori, 2021a; Hasnat and Ghafoori, 2021b; Hasnat and Ghafoori, 2021c). The first documented UHPC was developed in 1972 by Yudenfreund et al. having a 180-day compressive strength of 230 MPa using a water-to-cementitious materials ratio of 0.20 (Yudenfreund et al., 1972). Later in 1981, Birchall et al. made some improvements in the mechanical properties by using superplasticizer and pozzolanic admixtures (Birchall et al., 1981). In 1997, UHPC was used to construct a bridge in Sherbrooke, Canada (Acker and Behloul, 2004). In 1998, Lafarge came up with a commercial proprietary UHPC mixture containing 6% steel fiber (Schmidt and Fehling, 2005). During that time, a few other proprietary UHPCs were also developed by different companies (Schmidt and Fehling, 2005). ASTM C1856/C1856M-17 was the first standard that was published in 2017 where guidelines for evaluation of fresh and hardened properties of UHPC were presented, and first formal definition of UHPC was given in a technical document (C1856/C1856M-17, 2017). ASTM C1856 defined UHPC as a "cementitious mixture with a specified compressive strength of at least 120 MPa accompanied with specified durability, ductility, and toughness requirements."

While many studies addressed the bulk properties of UHPCs, only a few studies regarding transport properties of UHPCs have been published (Ahlborn et al., 2011; Alkaysi et al., 2016; Karim et al., 2019; Li et al., 2022). Table 3.1 summarizes some of the works reported on UHPCs' absorption capacity and volume of permeable voids. Xie et al. (2018) reported a decrease in voids with the increase in cementitious materials-to-aggregate ratio. In another study, Pyo et al. (2018) concluded that the shape of aggregate

played an important role in the voids of UHPCs. Vigeneswari et al. (2018) used thermally treated rice husk ash to partially replace micro silica in producing UHPC and reported up to 50% reduction in the voids. Salahuddin et al. (2020) investigated the effect of recycled aggregate to partially replace fine aggregate and reported that an increase of recycled aggregate content elevated the voids of UHPCs. Mohammed et al. (2020) reported UHPC containing micro silica and nano-silica displayed excellent resistance against water permeability due to the dense microstructure of UHPCs, Abbas et al. (2015) suggested a positive influence of steel fibers in reducing the voids and fiber length did not influence voids. Pyo and Kim (2017) also reported that the incorporation of steel fibers effectively decreased voids of UHPC. Liu et al. (2020) used Cathode ray tube (CRT) glass as a partial replacement of fine aggregate and that CRT glass increased voids and decreased strength of UHPC.

Table 3.2 summarizes past rapid chloride penetration studies conducted on UHPCs. Vigeneswari et al. (2018) used thermally treated rice husk ash to partially replace micro silica in producing UHPC and reported up to 43% reduction in the chloride penetration. Arora et al. (2019) compared the chloride penetration of high-performance concrete and plain UHPCs using ASTM C1202. The authors concluded that the total charge passed through plain UHPCs was "very low." Mohammed et al. (2020) reported that both nano-silica and micro silica reduced the charge passed through Plain UHPC when compared to that of the plain UHPC made using 100% Portland cement. Mosavinejad et al. (2020) documented 40-62 coulombs of charge with the UHPC strengths ranging from 107 to 121 MPa. While ASTM C1856 finds RCPT unsuitable for concrete containing any metal fibers, since fibers can short the circuit to result in invalid indication of conductance (ASTM C1856-18), there have been reports of RCPT results for steel fiber-reinforced UHPCs using ASTM C1202. Some studies reported "negligible" to "very low" Cl^- penetrability of fiber-reinforced UHPCs (Ahlborn et al., 2008; Haber et al. 2018). While, El-Dieb (2009) concluded that an increase in steel fiber volume resulted in higher Cl^- penetration of UHPCs, Abbas et al. (2015) has also been reported that higher steel fiber dosage improved chloride ion resistance, and change in steel fiber length did not influence chloride permeability. Additionally, different Cl^- concentrations (3%, 3.5%, and 10%) had almost no effect on the total charge passed in the UHPCs, and higher steel fiber dosage reduced total charge passed as compared to that of plain UHPC (Abbas et al., 2015).

Surface resistivity of UHPCs has also been reported. Karim et al. (2019) reported that the increase in micro silica content increased surface resistivity of non-proprietary UHPCs. Muzenski et al. (2019) evaluated the effect of aluminum oxide nano-fibers on surface resistivity performance of UHPCs and concluded that the inclusion of nano-fibers improved surface resistivity. In another study, Homayoonmehr et al. (2022) developed prediction models for assessing chloride diffusivity and surface resistivity, which can be utilized for predicting the service life of concrete and for quality control during the construction phase.

Table 3.1 Research work on absorption and volume of permeable voids of UHPCs

Reference	Fibers (%)	*w/cm*	$f'_{c-28day}$ *(MPa)*	Absorption (%)	Permeable void (%)
Vigneswari et al.	0	0.19	136.9-174.9	-	2.1-4.07
Xie et al.		0.15	125-141	-	1.9-1.99
Pyo and Kim	1	0.22	145-154	-	3-4.8
	2			-	2-2.5
Abbas et al.	0	0.23	151	-	3.6
	1		156	-	3.45
	3		164	-	3.02
	6		171	-	1.11
Pyo et al.	0	0.25	118-165	-	2.60-3.54
Liu et al.	3	0.18	150-180	1.74-2.40	4.75-6.88
Salahuddin et al.	2	0.21	95-113	2.20-4.1	-

In cold climate zones the main durability problem is insufficient resistance to frost damage. To address this issue, de-icing salts are commonly applied to concrete structures to melt ice and snow and ensure safety for pedestrians and vehicles during winter. However, this practice can cause significant harm to concrete structures as the salts penetrate the surface and react with the hydrated cement paste, resulting in expansive chemical compounds that can cause cracks, spalling, and reduced durability. De-icing salts can also accelerate the corrosion of reinforcing steel, which further reduces the strength and integrity of the structure. The long-term effects of de-icing salt exposure on concrete can be significant and costly to repair, making it important to carefully consider the use of these salts and implement appropriate maintenance and repair measures. The Chesapeake Bay Bridge in Maryland is an example of a structure that has suffered severe corrosion due to de-icing salts. Vaitkevicius et al. (2016) have investigated the effect of micro steel fiber content on the salt-scaling effect on UHPCs and found that an increase in micro steel fibers content does not improve the salt scaling of UHPCs. Bonneau et al. (2017) prepared two industrial scale specimen using UHPC and investigated the effect of steel fibers on de-icing salt resistance of UHPCs and observed that UHPC to be frost resistant with a low mass loss. Piérard et al. (2013) found that UHPC performed well against freezing and thawing, while Liu et al. (2018) concluded that the dense matrix of UHPC restricts the ingress of external moisture and the amount of freezable pore water, preventing the occurrence of internal bulk cracking.

Table 3.2 Research work on rapid chloride penetration of UHPCs

Reference	Fibers (%)	*w/cm*	$f'_{c-28day}$ (MPa)	Charge passed (Coulombs)
Arora et al.	0	0.165	139-148	238-365
Mosavinejad et al.	0	0.17	107-121	40-62
Abbas et al.	0	0.23	151	71
	1		156	60
	3		164	45
Mohammed et al.	0	0.20	-	40-70
Vigneswari et al.	0	0.19	136.9-174.9	163-290
Graybeal	2	0.18	-	18-360
Ahlborn et al.	2	0.20	165-207	15-75
Haber et al.	2	-	120-147	302-789

As reported in Tables 3.1 and 3.2, the majority of past studies dealt with the transport properties of proprietary UHPCs or the UHPCs containing unconventional secondary cementitious materials, such as rice husk ash or recycled glass powder. To date, limited studies have been reported on transport properties and de-icing salt resistance of binary and ternary blended non-proprietary UHPCs containing conventional secondary cementitious materials (Arora et al., 2019; Mohammed et al., 2020; Bunnori et al., 2020). To address this knowledge gap, the study presented herein investigated the transport properties and de-icing salt resistance of a number of binary and ternary non-proprietary plain and fiber-reinforced UHPCs containing Type V cement, and various dosages and combinations of micro silica, and class F fly ash. The studied transport properties included water absorption, volume of permeable voids, water penetration, rapid chloride penetration, and surface resistivity.

3.2 Experimental Program

3.2.1 Materials

An ASTM Type V Portland cement, a class F fly ash, and a micro silica were used as cementitious materials. The chemical properties of the Type V cement and secondary cementitious materials are presented in Table 3.3. Their scanning electron microscopic images are depicted in Figure 3.1. Figure 3.2 shows the particle size distribution of the cementitious materials. Two types of locally produced fine aggregates were used (Figure 3.3). The size gradation of fine aggregate varied from 0.075 mm to 4.75 mm. The aggregates had

59

different percentages of retention on various sieve sizes. Specifically, 23.5% of the aggregate was retained on the No. 8 sieve, 20.1% was retained on the No. 16 sieve, 17% was retained on the No. 30 sieve, 15.1% was retained on the No. 50 sieve, 13% was retained on the No. 100 sieve, and 11.3% was retained on the No. 200 sieve. Modified Andreasen and Andersen model was utilized to achieve the maximum packing density with minimum porosity. The aggregate distribution modulus (Q) was used to characterize the gradation of the aggregates. It represents the relative proportion of a specific size fraction in the aggregate. The maximum packing density was obtained from the distribution modulus of 0.21 (Hasnat and Ghafoori, 2021a). The combined fine aggregates had specific gravity of 2.80 and absorption of 0.45%. A low carbon straight steel fiber with 13 mm of length and 0.30 mm of width (aspect ratio of 43) was used. The specific gravity of the steel fibers was 7.86 and met the minimum tensile strength requirement of ASTM A820. A commercially available polycarboxylate-based high-range water-reducing admixture (HRWRA) was used to achieve the desired flowability of the studied UHPCs.

Table 3.3 Chemical compositions of the Type V cement and pozzolanic materials

Composition	Type V cement (%)	Class F fly ash (%)	Micro silica (%)
Silicon dioxide (SiO_2)	21	61.8	94.72
Calcium oxide (CaO)	62.4	5.7	-
Aluminum oxide (Al_2O_3)	4	18.7	-
Iron oxide (Fe_2O_3)	3.7	4.5	-
Magnesium oxide (MgO)	2.6	-	-
Sulfur trioxide (SO_3)	2.2	0.8	0.23
Sodium oxide + Potassium oxide ($Na_2O + K_2O$)	0.54	4.5	0.47
Loss on Ignition (LOI)	2.0	0.3	2.82
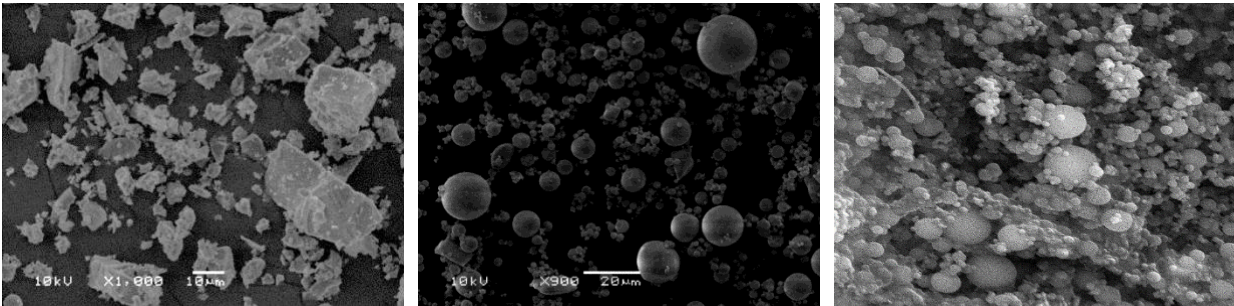
Figure 3.1 SEM image of cementitious materials: (a) Type V cement, (b) class F fly ash, (c) micro silica
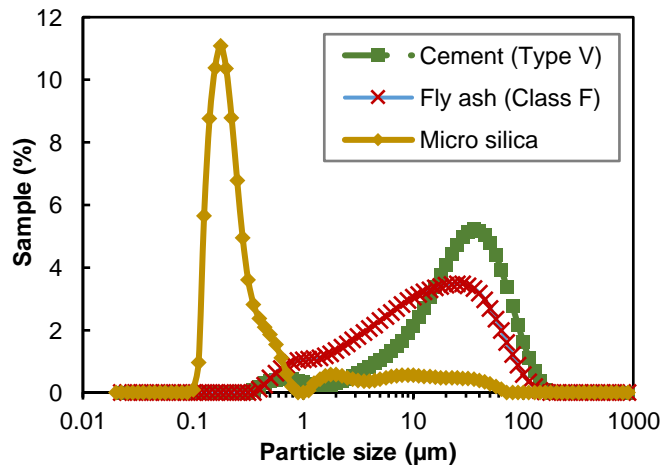
Figure 3.2 Particle size distribution of cement and pozzolanic materials

Figure 3.3 Fine aggregate (concrete sand and masonry sand) used for this study

3.2.2 Mixture Proportions

A total of 14 UHPCs were batched to determine their 28-day compressive strength, transport properties, and de-icing salt resistance. The mixture constituents of the UHPCs are given in Table 3.4. A constant water-to-cementitious material ratio of 0.21 was maintained for all studied UHPCs. The actual water content of the UHPCs varied due to the variation in the required HRWRA dosage to maintain the desired flow. The dosage of HRWRA ranged from 10.1 to 14.3 kg/m^3, depending on the pozzolanic materials type and combination, and steel fiber used. In the binary UHPCs; Type V cement was partially replaced with 10 and 20% fly ash, and 5% micro silica. For the ternary UHPCs, combination of 15% fly ash and 5% micro silica; combination of 10% fly ash and 10% fly ash; and combination of 15% fly ash and 15% micro silica were used. The UHPC containing 100% Type V cement was used as the reference (C100).

Table 3.4 Mixture proportion of UHPCs

Blend type	Mixture designation[a]	w/cm	C[b]	F[b]	MS[b]	Agg[b]	HRWRA[b]	W[b]	Steel fibers
							Kg/m^3		
Reference	C100	0.21	1101	-	-	1174	12.1	226	-
	C100-3%	0.21	1101	-	-	1174	14.3	225	234
Binary	MS5	0.21	1046	-	37	1174	12	215	-
	MS5-3%	0.21	1046	-	37	1174	14.1	214	234
	F10	0.21	991	81	-	1174	11	215	-
	F10-3%	0.21	991	81	-	1174	13	214	234
	F20	0.21	881	163	-	1174	11	215	-
	F20-3%	0.21	881	163	-	1174	13	214	234
Ternary	F15MS5	0.21	881	122	37	1174	11.5	214	-
	F15MS5-3%	0.21	881	122	37	1174	13.6	213	234
	F10MS10	0.21	881	81	55	1174	11.5	214	-
	F10MS10-3%	0.21	881	81	55	1174	13.7	213	234
	F15MS15	0.21	771	122	72	1174	12.3	214	-
	F15MS15-3%	0.21	771	122	72	1174	14.1	213	234

Note: 1 kg/m^3 = 1.685 lb/yd^3; Density of HRWRA=1.08 g/cm^3

[a] C100: 100% Cement; MS5: 95% cement and 5% micro silica; F10: 90% cement and 10% class F fly ash; F20: 80% cement and 20% class F fly ash; F15MS5: 80% cement and 15% class F fly ash and 5% micro silica; F10MS10: 80% cement and 10% class F fly ash and 10% micro silica; F15MS15: 80% cement and 15% class F fly ash and 15% micro silica; 3% represents 3% straight steel fibers by volume.
[b] C: Cement; F: Class F fly ash; MS: Micro silica; HRWRA: High-range water reducing admixture; Agg.: Aggregate; W: Actual water (after adjusting for water absorption and HRWRA liquid content).

3.2.3 Mixing, Sampling, Curing, and Testing

A customized mixing procedure was adopted to prepare the studied UHPCs. The mixing sequence is shown in Figure 3.4. A high-speed Hobart-type mixer with a maximum revolution speed of 60 rpm was employed. As shown in Table 3.4, UHPCs containing micro silica needed a slightly higher amount of High-Range Water Reducing Admixture (HRWRA) than usual due to its adhesive nature which required a longer mixing to achieve the required flowability. For UHPCs containing steel fiber, after incorporating fibers into the mixture, it took approximately 3 to 5 minutes for the UHPC to achieve the desired flowability. The mixing time, mixing speed, mixing sequence, temperature, and relative humidity were closely monitored and maintained. Each batch of UHPC had 0.005 m^3 in volume. The flow properties of the studied UHPCs were evaluated according to the ASTM C230 before they were poured into the molds. The released heat of hydration of the freshly-mixed plain UHPCs was evaluated using digital thermocouples over a duration of 24 hours. The test specimens were kept for 24 hours in a controlled moist curing room at $22 \pm 3°C$ and 95% relative humidity. After 24 hours, the specimens were demolded and returned to the moisture room for an additional 27 days. Cylindrical specimens (50 mm diameter and 100 mm height) were used to evaluate compressive strengths per ASTM C39. Water absorption test using ASTM C642 was conducted to measure the density, absorption, and volume of permeable voids of the hardened UHPCs. The rapid chloride permeability test was performed per ASTM C1202, the water penetration test was performed as per BS EN 12390-8, and the concrete surface resistivity was measured using AASHTO T358. Finally, after 28 days of moist curing, the de-icing salt resistance of the UHPCs was evaluated in accordance with a freezing and thawing duration of 48 hours per cycle for a total of 70 cycles. The 50 mm diameter and 100 mm height cylindrical samples were soaked in a 3% salt water (NaCl) for 24 hours prior to placing them in a freezer for 24 hours. To maintain uniformity in the salt solution, the entire solution was changed every five F-T cycles. The temperature profile of the F–T cycle was maintained at $20 \pm 2°C$ to $-18 \pm 2°C$.
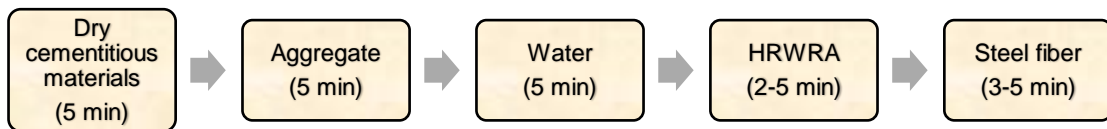
Figure 3.4 UHPCs' mixing sequence

3.3 Results and Discussion

3.3.1 Fresh and Bulk Properties

Table 3.5 summarizes the fresh and bulk properties of the investigated UHPCs. The slump flow was measured immediately upon completion of mixing. Figure 3.5 displays the flow diameter of plain and fiber-reinforced UHPCs. A satisfactory flow spread diameter of 250 ± 25 mm was attained for all studied UHPCs. Overall, the UHPCs containing steel fibers displayed 6% lower slump flow diameter as compared to that of the plain UHPCs. Table 3.5 documents the demolded unit weight of the UHPCs varied from 2374 to 2592 kg/m^3. On average, plain UHPCs resulted in a 6% lower unit weight when compared to that of the fiber-reinforced UHPCs.

The heat of hydration and corresponding peak elapsed time for plain UHPCs are presented in Figure 3.6 and Table 3.5. The lowest and the highest heat of hydration were attained for UHPC prepared with 20% fly ash as a partial substitute for Portland cement and UHPC made with 15% micro silica and 15% fly ash, respectively. In contrast to the reference and binary UHPCs containing fly ash as a partial substitute of Portland cement, binary and ternary UHPCs with micro silica demonstrated higher heat of hydration. A similar pattern can be observed in the highest elapsed time. UHPCs produced using fly ash required longer to reach the peak temperature, but binary and ternary UHPCs made with micro silica required less time. UHPCs containing a higher amount of micro silica experienced a faster early hydration process, resulting in a shorter peak time and higher temperature. Hasnat and Ghafoori (2021a) conducted a study that confirmed this by comparing the early strength development of UHPCs with micro silica to those with fly ash. Xi et al. (2022) also observed that UHPCs with 20% micro silica as a replacement for portion of Portland cement reached peak heat flow quicker than the UHPCs without micro silica.

The compressive strengths of the studied UHPCs are also presented in Table 3.5. The binary UHPCs containing 10 and 20% fly ash showed marginally lower 28-day compressive strength (1 and 2%, respectively), compared to that of the reference UHPC (C100). In contrast, the 28-day cured binary UHPC containing 5% micro silica provided a 6, 8, and 8% higher compressive strength than that of the 28-day cured binary UHPCs containing 0 (reference), 10, and 20% fly ash, respectively. This finding can be attributed to the higher reactivity of micro silica during curing period as compared to the companion UHPCs containing fly ash.

The UHPCs having ternary blends displayed higher strengths compared to the companion reference and binary blend UHPCs. A 13% improvement in strength was observed for the ternary blend UHPC containing 15% fly ash and 5% micro silica as compared to the UHPC containing 20% fly ash (binary UHPC). In comparison to the same binary UHPC, the companion UHPC containing 10% fly ash and 10% micro silica showed 16% improvement in strength. Amongst the ternary UHPCs, the combination of 15% micro silica and 15% fly ash replacing 30% Type V cement displayed the highest compressive strength exceeding that of the reference UHPC by 17%.

The age of testing significantly impacted the compressive strength of the studied UHPCs. UHPCs tested at 365 days displayed more than 30% average increase in strength as compared to the 28-day cured plain UHPCs. This is attributed to the delayed pozzolanic reactivity of the fly ash and continued hydration of cement particles.

With the introduction of steel fibers, only a marginal improvement in compressive strength was observed (4% improvement), mainly due to the improved micro-crack arrest facilitated by steel fibers. Other studies also reported a similar finding (Hoang and Fehling, 2017; Park et al., 2017). For fiber-reinforced UHPCs, age of testing did not affect the compressive strength of the studied UHPCs as compared to the companion plain UHPCs.

Table 3.5 Fresh and bulk properties of UHPCs

ID	Flow (mm)	γ_{con} (kg/m^3)	STDEV	Maximum temperature (°C)	Peak time (Hr)	f'_{c-28D} (MPa)	STDEV	f'_{c-365D} (MPa)	STDEV	Strength increase (%)
C100	271	2470	12.4	89.9	10.4	125.7	2.26	159.9	2.08	27.2
F10	268	2432	10	84.2	10.5	124	3.53	162.9	3.00	31.4
F20	270	2405	7.5	83.0	10.8	122.9	2.52	164.4	1.19	33.8
MS5	258	2451	13.8	92.1	8.1	133.3	3.52	178	2.08	33.5
F15MS5	261	2388	8.4	85.9	9.8	139.1	5.27	181	3.46	30.1

F10MS10	249	2393	13.2	93.3	8.4	142.4	5.5	183.9	4.45	29.1
F15MS15	243	2381	11.3	96.7	8.2	146.3	3.86	193.6	3.20	32.3
C100-3%	248	2592	9.4	-	-	130.8	5.21	161	3.37	23.1
F10-3%	250	2561	8.9	-	-	128.7	3.95	162.9	3.88	26.6
F20-3%	253	2543	16.4	-	-	127.6	1.81	165	2.16	29.3
MS5-3%	255	2583	16.5	-	-	139.3	2.35	180.2	4.69	29.4
F15MS5-3%	243	2535	13.1	-	-	144.2	4.01	180.9	3.11	25.5
F10MS10-3%	238	2521	21.1	-	-	146.3	4.05	186.1	2.34	27.2
F15MS15-3%	233	2518	14.9	-	-	153.5	3.87	194.2	1.26	26.5

Note: γ_{con} = demolded unit weight; STDEV = standard deviation; f'_{c-28D} = 28-day compressive strength; f'_{c-365D} = 365-day compressive strength.
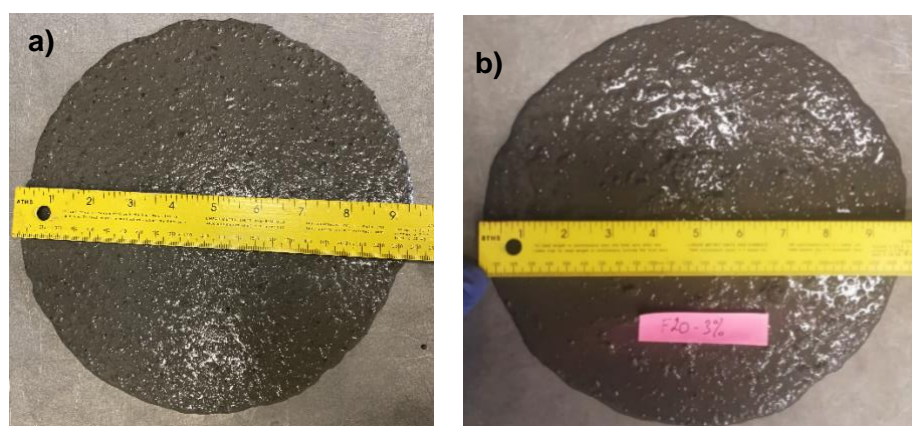
Figure 3.5 Flow diameter of UHPCs: (a) plain UHPC; and (b) fiber-reinforced UHPC
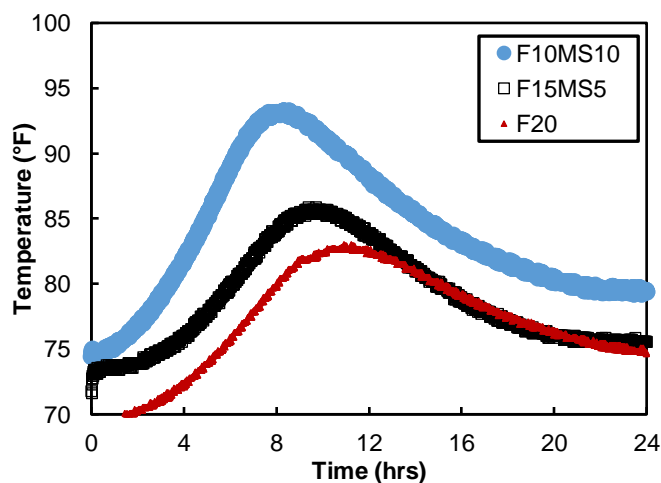
Figure 3.6 Heat of hydration of the selected UHPCs

3.3.2 Water Absorption

The water absorption (after immersion and after immersion and boiling) of the 28-day cured plain and fiber-reinforced UHPCs comprising reference, binary, and ternary cementitious materials is shown in Table 3.6. When compared to the reference UHPC, the UHPC containing 5% micro silica produced the highest

reduction in water absorption (29%) of the three binary UHPCs. The binary UHPC containing 10 and 20% fly ash as a partial replacement of cement displayed 7 and 16% lower absorption, respectively, as compared to that of the reference UHPC.

All ternary blend UHPCs demonstrated significantly lower absorptions judged against that of the reference UHPC. On average, ternary blend plain UHPCs displayed a nearly 42% reduction in water absorption when compared to that of the reference UHPC. The ternary blend UHPC containing 15% fly ash and 5% micro silica showed 24% reduction in water absorption when compared to that of the companion binary UHPC containing 20% fly ash. In comparison with the same binary UHPC, the ternary blend concrete made with 10% fly ash and 10% micro silica produced 27% lower absorption. Overall, ternary UHPC containing 15% fly ash and 15% micro silica resulted in the lowest absorption amongst the studied UHPCs. The micro silica's smaller particle size attributed to its larger surface area, enabling it to have increased reactivities with cement's calcium hydroxide. Additionally, micro silica is completely amorphous and reactive, whereas fly ash can be partially crystalline and non-reactive. In particular, class F fly ash tends to react at a much slower pace than micro silica (Langan et al., 2002; Walker et al., 2011; Naber et al., 2019). The smallest size of aggregate used in this study was 75µm (#200 sieve retained). From the particle size distribution curve presented in Figure 3.2, a portion of the fly ash had a large particle sizes (45-75µm), which might acted only as a filler material to reduce the gap between capillary voids. As a point of reference, Mehta and Monterio (2005) reported that pozzolans larger than 45µm do not participate in the secondary pozzolanic reactions in contributing to the hydration process. This congruous performance of fly ash and micro silica in the ternary blend resulted in lower water absorption as compared to that of the reference and binary UHPCs.

The addition of steel fibers showed a similar or slightly lower absorption for the studied UHPCs. The minor improvement in absorption was possibly due to the support given by steel fibers to narrow the gap amongst the macro voids. A similar observation was also reported by Pyo and Kim (2017).

Table 3.6 Water absorption and volume of permeable voids of UHPCs

ID	$W_{a\text{-immersion}}$ (%)	STDEV	Reduction from reference	$W_{a\text{-boil}}$ (%)	STDEV	Reduction from reference	V_{void} (%)	STDEV	Reduction from reference
C100	1.51	0.29	-	1.81	0.30	-	4.16	0.71	-
F10	1.41	0.14	6.5	1.67	0.21	7.5	3.92	0.35	5.7
F20	1.27	0.04	15.8	1.53	0.03	15.3	3.65	0.08	12.2
MS5	1.08	0.08	28.5	1.24	0.07	31.2	2.99	0.17	28.1
F15MS5	0.97	0.12	35.8	1.09	0.11	39.9	2.52	0.26	39.4
F10MS10	0.93	0.03	38.2	1.09	0.03	39.8	2.49	0.07	40.0
F15MS15	0.83	0.09	45.0	0.98	0.16	45.7	2.11	0.14	49.2
C100-3%	1.39	0.16	-	1.59	0.16	-	3.84	0.36	-
F10-3%	1.35	0.17	2.7	1.63	0.22	-2.3	4	0.22	-4.2
F20-3%	1.34	0.10	3.7	1.61	0.11	-1.4	3.96	0.26	-3.1
MS5-3%	0.74	0.20	46.7	0.88	0.17	44.6	2.15	0.42	43.9
F15MS5-3%	1.01	0.02	27.1	1.11	0.02	30.2	2.81	0.05	26.7
F10MS10-3%	0.92	0.08	33.7	1.08	0.11	32.2	2.47	0.18	35.7
F15MS15-3%	0.53	0.06	61.9	0.63	0.04	60.2	1.60	0.10	58.4

Note: $W_{a\text{-immersion}}$ =Water absorption after immersion; STDEV = Standard deviation; $W_{a\text{-boil}}$ =Water absorption after immersion and boiling; V_{void} =Volume of permeable voids

3.3.3 Volume of Permeable Voids

Table 3.6 document the average volume of permeable voids, as a function of pozzolans replacing a portion of the Type V cement, for the 28-day cured UHPCs. The volume of permeable voids varied from 1.6 to 4%.

The comparison of the 28-day cured plain UHPCs containing fly ash with that of the reference UHPC revealed a nearly 6% reduction in the volume of permeable voids for every 10% cement substitution. The decrease in the volume of permeable voids in UHPC can be attributed to the interaction between fly ash and calcium hydroxide, which generates calcium silicate and calcium aluminate silicate hydrates, ultimately leading to a reduction in pore connectivity in the microstructure (Onaizi et al., 2021; Deja et al., 2016). Additionally, the spherical shape of fly ash allows it to fill and bridge some of the permeable voids. The 28-day cured binary UHPCs containing micro silica replacing 5% of cement exhibited average reductions of 28, 24, and 18% in volume of permeable voids as compared to that of the reference and the UHPC containing 10 and 20% fly ash, respectively.

On average, ternary blend plain UHPCs displayed a nearly 43% reduction in void volume when compared to that of the reference UHPC. The binary UHPC containing 20% fly ash exhibited 31 and 32% higher volume of permeable voids than that of the ternary blend UHPC made with 15% fly ash and 5% micro silica and the UHPC containing equal amount of fly ash and micro silica for 20% cement substitution, respectively. In comparison to the reference, the UHPC containing 15% fly ash and 15% micro silica produced 49% lower volumes of permeable voids. The harmonious chemical and physical characteristics of amorphous micro silica and spherical fly ash (also described in the water absorption section) resulted in the reduction of volume of permeable voids for the studied ternary UHPCs. Similar to the results of water absorption, and as depicted in Table 3.6, steel fibers had insignificant influence on the volume of permeable voids.

As shown in Figure 3.7, a strong linear relationship at 95% confidence level was found between the absorption (after immersion, and immersion and boiling) and volume of permeable voids of the studied UHPCs.
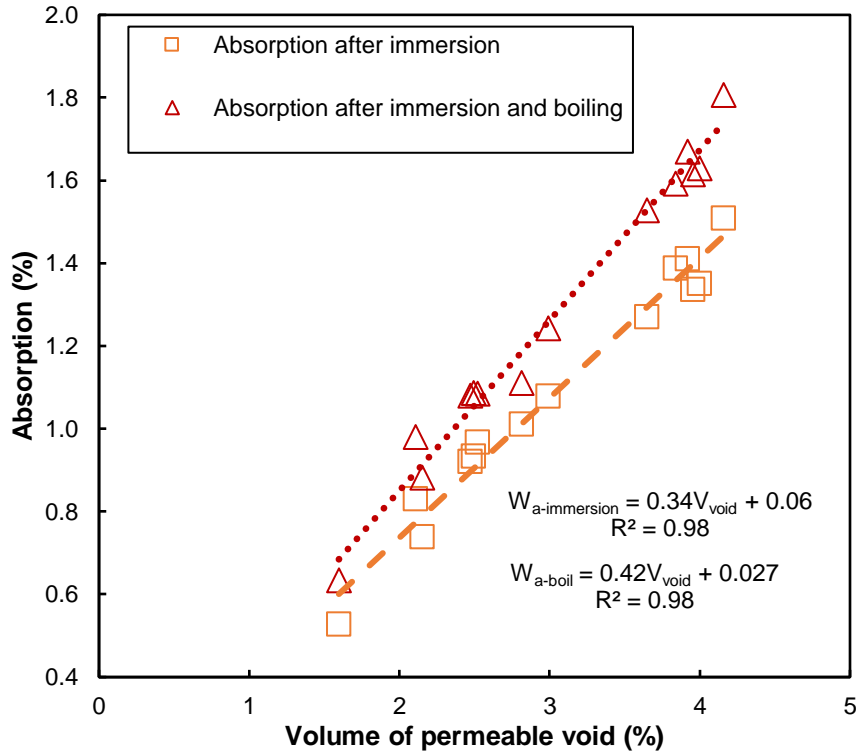
Figure 3.7 Correlation between absorption and volume of permeable voids of UHPCs

3.3.4 Water Penetration

No water penetration was observed in the split-open surface of the UHPC test samples after 72-hour and 90-days of water pressure at the rate of 0.5 MPa. The excellent resistance of UHPCs against water penetration can be attributed to (i) a very low water-to-cementitious materials ratio; (ii) excellent particle-packing density resulted from the customized aggregate gradation; (iii) absence of large size aggregate producing a less interconnected porous matrix, which also allowed for excellent surface finishes; (iv) the highly flowable fresh UHPCs, which produced well-compacted mixtures; and (v) physical and chemical contributions of the pozzolanic materials used in the studied binary and ternary UHPCs.

3.3.5 Rapid Chloride Penetration

The average charges transmitted through the investigated UHPCs are depicted in Figure 3.8. Based on the total charge transmitted, ASTM C1202 divides chloride ion penetrability into five categories. As shown in Figure 3.8, all studied UHPCs fell under the "very low" class of chloride ion penetrability. Overall, the ternary blend UHPC containing 15% fly ash and 15% micro silica as a partial substitute for Type V cement performed the best against chloride penetration, whereas the binary blend UHPC with 20% fly ash displayed the worst.

When compared to the reference UHPC, the 28-day cured binary blend UHPCs containing 10 and 20% fly ash showed 21 and 29% increases, respectively, in chloride penetration. The charge passed through the binary UHPC containing 5% micro silica was 32, 44, and 47% lower than that of the reference, and the 10 and 20% fly ash blended UHPCs, respectively.

The ternary blend UHPC containing 15% fly ash and 5% micro silica, as a partial replacement of cement, displayed 42% higher resistance against chloride penetration than that of the reference UHPC. The ternary UHPC containing 15% fly ash and 5% micro silica showed 54% reduction in chloride penetration when compared to the binary blend UHPC containing 20% fly ash. In comparison to the binary UHPC containing 20% fly ash, the ternary UHPC made with 10% micro silica and 10% fly ash displayed 69% better chloride penetration resistance. The increased resistance to rapid chloride penetration of the ternary blend UHPCs is due in part to pore structure modification caused by increased pozzolanic reactivities of micro silica, resulting in finer porosity and more precipitated C-S-H gels, as well as the filler effect of both micro silica and fly ash, which resulted in decreased mobility of the chloride ions through UHPC as evidenced by absorption and volume of permeable void results. Furthermore, high binding capacity of micro silica reduced the alkali concentration of the matrix, and to maintain solution neutrality, the amount of hydroxile ions (OH^-) also decreases, thus resulting in a decrease in electro-conductivity of the pore solution (El-Enein et al., 1995; Shi, 2004; Sobhani and Najimi, 2013).

Figure 3.9 documents the surface of plain and fiber-reinforced UHPCs taken at the completion of RCPT. Steel fiber-reinforced UHPC sample experienced significant corrosion of steel fibers. It appears that the presence and alignment of steel fibers caused an undesirable temperature rise, which resulted in increased chloride penetration rates to promote corrosion of steel fibers and the subsequent development of concrete surface cracks. Moreover, the fiber presence increased the current passing through the sample, resulting in a secondary conductive path which ultimately increased the coulombs which were measured during the experiment. Additionally, the fiber presence increased the current passing through the sample, resulting in a secondary conductive path that ultimately increased the coulombs which were measured during the experiment. These conditions lent itself to unreliable RCPT results for the steel fiber-reinforced UHPCs. A similar observation was also reported by Karim et al. (2019).
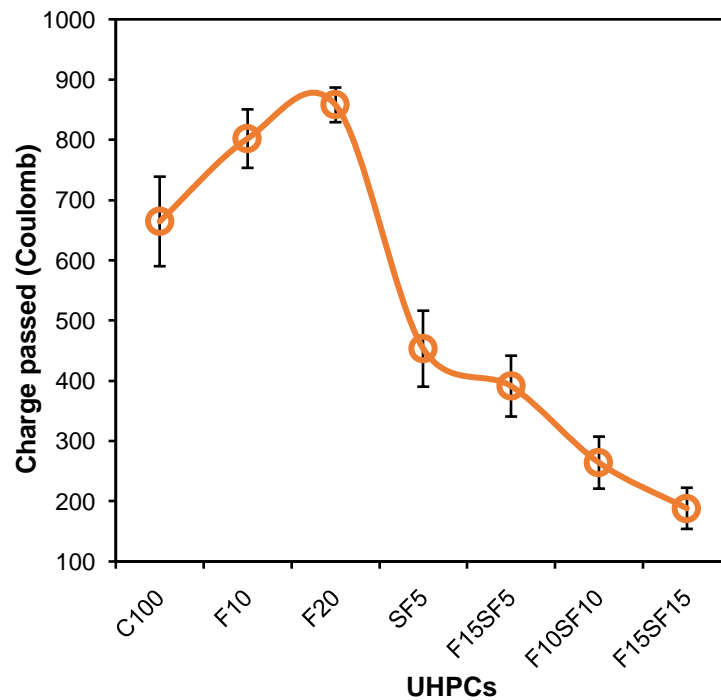
Figure 3.8 RCPT results of plain UHPCs
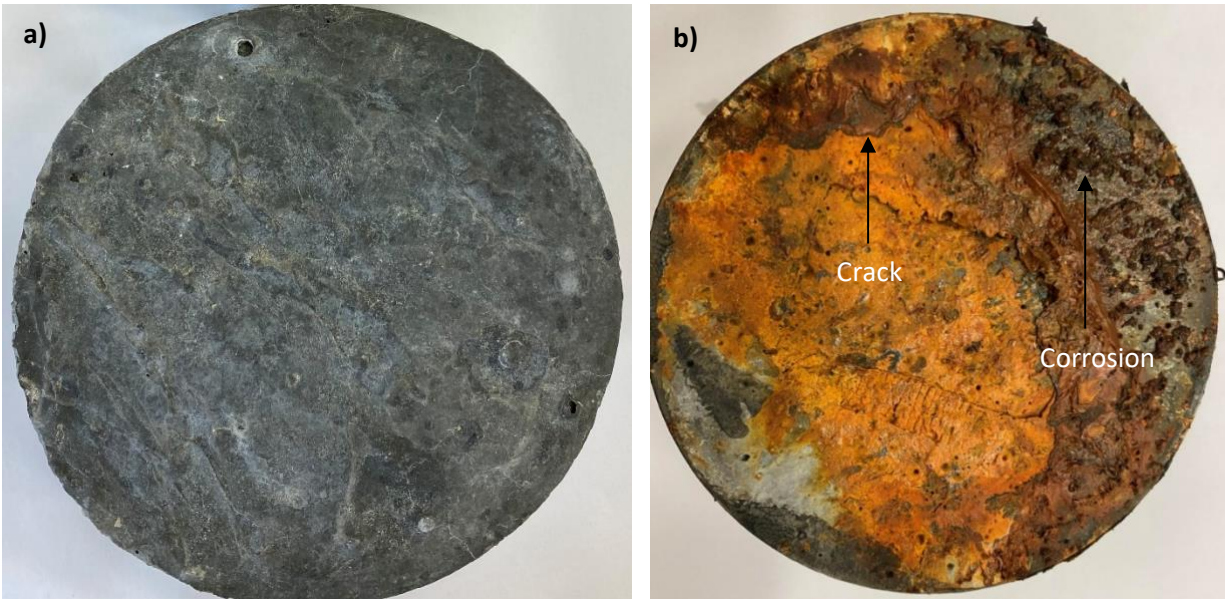
Figure 3.9 Surface of UHPC after RCP test, (a) plain UHPC, (b) steel fiber-reinforced UHPC

3.3.6 Surface Resistivity

The results of surface resistivity (SR) tests conducted after 28 days of curing for the studied UHPCs are presented in Figure 3.10. The surface resistivity varied from 44 to 261 kΩ-cm.

The SR of the UHPCs containing 10% and 20% fly ash by weight of the total cementations materials decreased by 10 and 8%, respectively, in comparison to the reference UHPC. The SR of the reference UHPC increased by 58% with the 5% substitution of cement with micro silica. The UHPC containing 5% micro silica also produced 75 and 71% higher SR than that of the UHPC having 10 and 20% fly ash, respectively.

A significant improvement in SR was observed for the studied ternary blend UHPCs when compared to both reference and binary UHPCs. On average, the SR of ternary blend UHPCs were 2 to 5 times higher than the studied reference and binary UHPCs. Similar to the RCPT results, the mixture containing 15% fly ash and 15% micro silica depicted the highest surface resistivity amongst the studied UHPCs.

As depicted in Figure 3.11, a strong relationship was found between the RCPT results and SR of the studied UHPCs with a R^2 of 0.96. This finding underscores not only the suitability, but the advantages of using SR test, over RCPT, to assess chloride transport through UHPCs. In contrast to RCPT, the SR test does not require expensive equipment and highly trained operators. The testing duration of SR is significantly shorter than that of RCPT. Additionally, as shown with the results of this study, the standard deviations of the SR test results are much lower than the variability seen in the RCPT results.
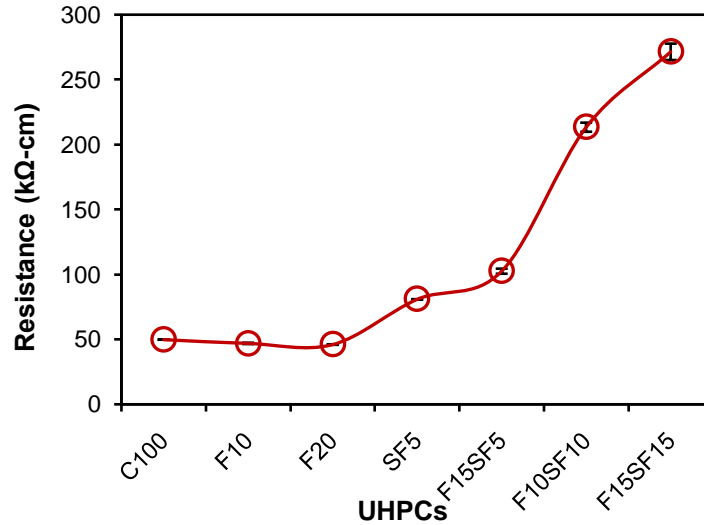
Figure 3.10 Surface resistivity of plain UHPCs
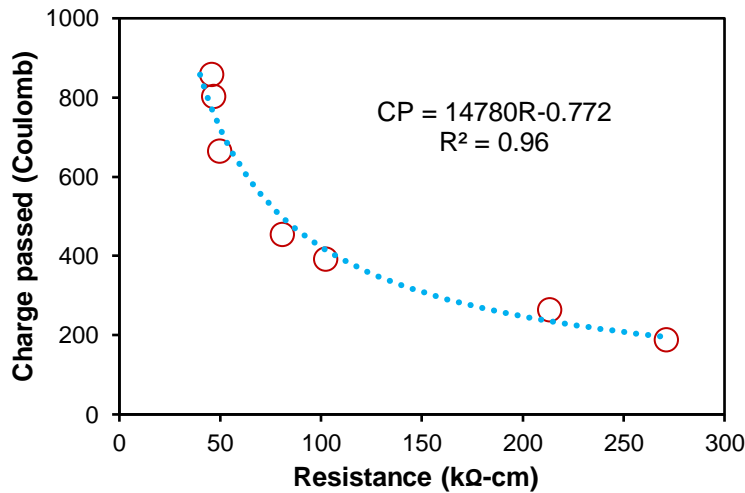
Figure 3.11 Correlation between RCPT results and surface resistivity of plain UHPCs

3.3.7 De-Icing Salt Resistance

The results of de-icing salt resistance of the studied plain and fiber-reinforced UHPCs as functions of cementitious materials type and combination at different F-T cycles are shown in Table 3.7. After 70 freezing and thawing cycles, while immersed in a 3% salt solution, the mass losses of the studied UHPCs varied from +0.052 to -0.49%, well below the RILEM acceptable limit of 5% suggested for the very high-quality concrete. Comparable findings were also reported by other researchers (Graybeal 2006; Wang et al. 2017).

The binary blend plain UHPCs containing 10 and 20% fly ash showed the highest mass loss amongst the studied UHPCs. On average, 87 and 113% increases in mass loss were observed for the UHPCs containing 10 and 20% fly ash, respectively, as compared to that of the reference UHPC. Inclusion of 5% micro silica in the binary UHPC results in 247 and 295% improvements in the de-icing salt resistance of the binary UHPC containing 10 and 20% fly ash, respectively. During the freezing phase, lower rate of pozzolanic

70

reaction slowed down the strength development of the UHPCs containing fly ash and made them comparatively weaker in resisting the internal hydrostatic stress generated from the F–T regimes. Naik et al. (2005) also reported that concrete containing fly ash is weak when resisting hydrostatic pressure generated due to freeze-thaw cycles.

The ternary blend UHPC containing 15% fly ash and 5% micro silica, as a partial replacement of Type V cement, displayed 50% lower mass loss than that of the reference UHPC. The ternary UHPC containing 15% fly ash and 5% micro silica produced nearly 4.5 times lower mass loss than that of the binary blend UHPC containing 20% fly ash. The ternary UHPC made with 10% micro silica and 10% fly ash displayed 10 times better de-icing salt resistance than that of the binary UHPC containing 20% fly ash. The ternary blend UHPC containing 15% fly ash and 15% micro silica barely showed any mass loss after 70 F-T cycles.

As presented in Table 3.7, many studied UHPCs gained mass, some up to 30 freezing and thawing cycles, due to the large quantity of unhydrated cement particles. The combination of high cementitious material content, low water-to-cementitious materials ratio, and continuous curing of unhydrated cement particles resulted in a dense and hard to penetrate microstructure and contributed to the strong de-icing salt resistance of the studied UHPCs.

Table 3.7 Mass losses/gains at different F–T cycles

Mixture Designation	Mass loss/gain at different freezing and thawing cycles (%)							
	0	10	20	30	40	50	60	70
C100	0.000	0.020	0.015	0.007	-0.010	-0.100	-0.150	-0.230
F10	0.000	0.001	-0.036	-0.096	-0.120	-0.200	-0.340	-0.430
F20	0.000	0.001	-0.030	-0.080	-0.150	-0.300	-0.440	-0.490
SF5	0.000	0.027	0.032	0.022	0.010	-0.003	-0.060	-0.124
F15SF5	0.000	0.025	0.028	0.011	-0.020	-0.056	-0.080	-0.113
F10SF10	0.000	0.050	0.073	0.074	0.047	0.019	0.001	-0.049
F15SF15	0.000	0.054	0.076	0.068	0.060	0.028	0.008	-0.020
C100-3%	0.000	0.022	0.016	0.008	0.000	-0.091	-0.136	-0.209
F10-3%	0.000	0.019	-0.004	-0.006	-0.058	-0.108	-0.211	-0.353
F20-3%	0.000	0.001	-0.010	-0.046	-0.090	-0.116	-0.290	-0.407
SF5-3%	0.000	0.030	0.032	0.027	0.019	0.008	-0.058	-0.110
F15SF5-3%	0.000	0.049	0.047	0.029	0.022	0.016	0.002	-0.040
F10SF10-3%	0	0.055	0.078	0.068	0.056	0.04	0.038	0.033
F15SF15-3%	0	0.066	0.085	0.082	0.073	0.064	0.059	0.052

Note: mass gain (+); and mass loss (−).

The effect of steel fibers on the de-icing salt resistance of the studied UHPCs is also presented in Table 3.7. Averagely, after 70 F-T cycles, the inclusion of steel fibers improved the F–T resistance of the studied UHPCs by 40%. When tensile stresses were applied, cracks could develop and propagate through the material. However, when steel fibers were added to concrete, they acted as a reinforcement element and provided an alternative load path for the tensile stresses. The steel fibers helped to distribute the tensile stress across the concrete matrix, thereby reducing the concentration of stress at any particular point. As shown in Figure 3.12, steel fibers acted as a bridge to mitigate the development of tensile cracks. Similar observations were also reported in other studies (Hasnat and Ghafoori, 2021b; Zhang et al., 2019). Figure 3.13 documents the correlation between mass loss, water absorption, and the volume of permeable voids.

It shows how an increase in water absorption and volume of permeable voids can lead to an increase in the mass loss. Therefore, it is crucial to minimize mass loss and water absorption to maintain the structural integrity in order to prevent damages associated with de-icing salt attack.
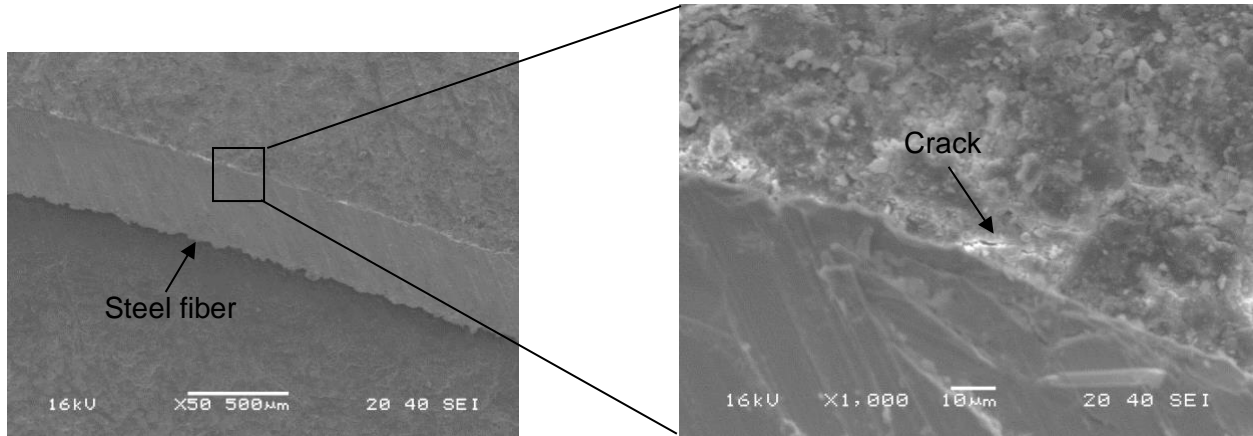
Figure 3.12 Crack arrest mechanism of steel fiber reinforced UHPC

$$W_a = -1.63M_L + 0.99$$
$$R^2 = 0.68$$

$$V_{void} = -4 M_L + 2.34$$
$$R^2 = 0.71$$
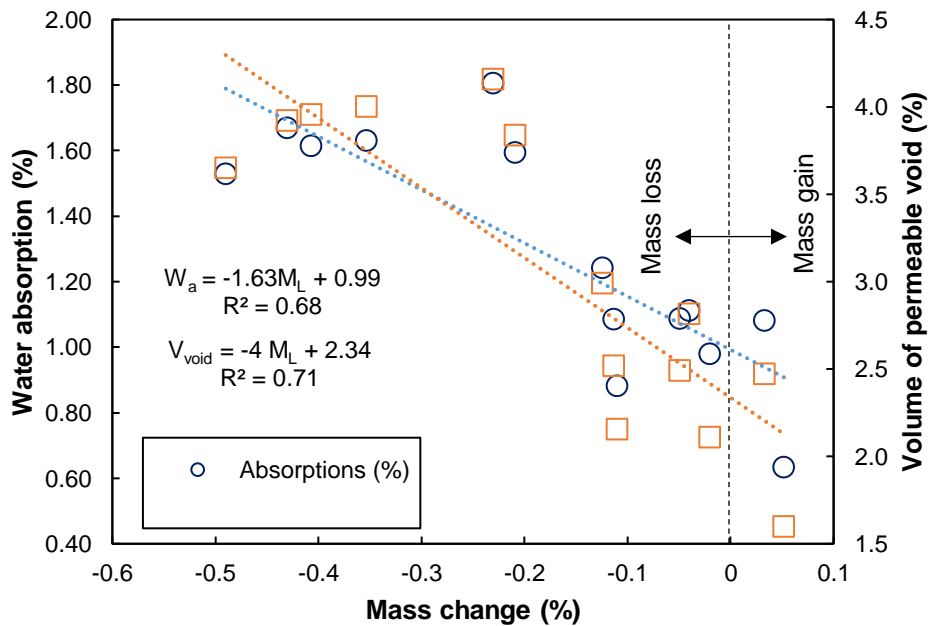
Figure 3.13 Effect of absorption and void on mass loss/gain of UHPCs

3.4 Conclusions

In this study, the transport properties and de-icing salt resistance of non-proprietary plain and fiber-reinforced UHPCs with various combinations of Type V cement, micro silica, and class F fly ash in both binary and ternary forms were investigated. Based on the results of this study, the following conclusions can be drawn:

[1] Cementitious materials type and combination had more influence on surface resistivity and chloride ion penetration resistance than it had on the strength of the studied UHPCs.

72

[2] The water absorption and volume of permeable voids reduced with the inclusion of micro silica in both binary and ternary UHPCs. No visible water penetration was observed in any of the samples tested under five bar pressure for 90 days.

[3] The ternary UHPCs, containing micro silica and fly ash, that were cured for 28 days showed an average reduction of 136% in charge passed compared to the reference UHPC. The RCPT test method, as specified in ASTM C1202, was deemed unsuitable for assessing chloride transport through steel fiber-reinforced UHPCs due to interference in the results caused by the electrical conductivity of the steel fibers.

[4] When a portion of the cement was replaced with micro silica, the surface resistivity of the studied UHPCs increased, whereas substituting cement with fly ash had the opposite effect. The surface resistivity test results correlated well with the findings of the RCPT, and it can be used to predict chloride penetration.

[5] The studied UHPCs showed a maximum mass loss of only 0.50% after undergoing 70 cycles of freeze-thaw testing, indicating excellent resistance against de-icing salts. Ternary blend UHPCs showed the highest resistance to de-icing salt, and the inclusion of steel fibers increased the resistance by 40% by arresting crack development in the material.

References

1. AASHTO T 358 (2019). Standard Method of Test for Surface Resistivity Indication of Concrete's Ability to Resist Chloride Ion Penetration.
2. Abbas, S., Soliman, A. M., & Nehdi, M. L. (2015). Exploring mechanical and durability properties of ultra-high performance concrete incorporating various steel fiber lengths and dosages. Construction and Building Materials, 75, 429-441.
3. Abellán García, J., Fernandez Gomez, J., & Torres Castellanos, N. (2022). Properties prediction of environmentally friendly ultra-high-performance concrete using artificial neural networks. European Journal of Environmental and Civil Engineering, 26(6), 2319-2343.
4. Acker, P., & Behloul, M. (2004, September). Ductal® technology: A large spectrum of properties, a wide range of applications. In Proc. of the Int. Symp. on UHPC Kassel, Germany (pp. 11-23).
5. Ahlborn, T. M., Peuse, E. J., & Misson, D. L. (2008). Ultra-high performance concrete for Michigan bridges, material performance: phase I (No. RC-1525). Michigan. Dept. of Transportation.
6. Ahlborn, T. T. M., Harris, D. K., Misson, D. L., & Peuse, E. J. (2011). Characterization of strength and durability of ultra-high-performance concrete under variable curing conditions. Transportation research record, 2251(1), 68-75.
7. Akhnoukh, A. K., & Buckhalter, C. (2021). Ultra-high-performance concrete: Constituents, mechanical properties, applications and current challenges. Case Studies in Construction Materials, 15, e00559.
8. Alkaysi, M., El-Tawil, S., Liu, Z., & Hansen, W. (2016). Effects of silica powder and cement type on durability of ultra high performance concrete (UHPC). Cement and Concrete Composites, 66, 47-56.
9. Arora, A., Almujaddidi, A., Kianmofrad, F., Mobasher, B., & Neithalath, N. (2019). Material design of economical ultra-high performance concrete (UHPC) and evaluation of their properties. Cement and Concrete Composites, 104, 103346.
10. ASTM A820 / A820M-16, Standard Specification for Steel Fibers for Fiber-Reinforced Concrete, ASTM International, West Conshohocken, PA, 2016, www.astm.org
11. ASTM C1202-12, Standard Test Method for Electrical Indication of Concrete's Ability to Resist Chloride Ion Penetration, ASTM International, West Conshohocken, PA, 2019, www.astm.org
12. ASTM C1856 / C1856M-17, Standard Practice for Fabricating and Testing Specimens of Ultra-High Performance Concrete, ASTM International, West Conshohocken, PA, 2017, www.astm.org.
13. ASTM C230 / C230M-14, Standard Specification for Flow Table for Use in Tests of Hydraulic Cement, ASTM International, West Conshohocken, PA, 2021, www.astm.org
14. ASTM C39 / C39M-12, Standard Test Method for Compressive Strength of Cylindrical Concrete Specimens, ASTM International, West Conshohocken, PA, 2021, www.astm.org

15. ASTM C642-13, Standard Test Method for Density, Absorption, and Voids in Hardened Concrete, ASTM International, West Conshohocken, PA, 2013, www.astm.org

16. Bajaber, M. A., & Hakeem, I. Y. (2021). UHPC evolution, development, and utilization in construction: A review. Journal of Materials Research and Technology, 10, 1058-1074.

17. Birchall, J. D., Howard, A. J., & Kendall, K. (1981). Flexural strength and porosity of cements. Nature, 289(5796), 388-390.

18. BS EN-12390-8. Depth of penetration of water under pressure. British Standards Institution; 2000.

19. Bunnori, N. M., Alani, A. H., Noaman, A. T., Johari, M. M., & Majid, T. A. (2020). Relationships between Compressive strength and transport properties of ultrahigh-strength green concrete utilizing ternary-blended binder. Journal of Materials in Civil Engineering, 32(3), 04020011.

20. Dong, Y. (2018). Performance assessment and design of ultra-high performance concrete (UHPC) structures incorporating life-cycle cost and environmental impacts. Construction and Building Materials, 167, 414-425.

21. El-Dieb, A. S. (2009). Mechanical, durability and microstructural characteristics of ultra-high-strength self-compacting concrete incorporating steel fibers. Materials & Design, 30(10), 4286-4292.

22. El-Enein, S. A., Kotkata, M. F., Hanna, G. B., Saad, M., & Abd El Razek, M. M. (1995). Electrical conductivity of concrete containing silica fume. Cement and concrete research, 25(8), 1615-1620.

23. Graybeal, B. A. (2006). Material property characterization of ultra-high performance concrete (No. FHWA-HRT-06-103). United States. Federal Highway Administration. Office of Infrastructure Research and Development.

24. Haber, Z. B., Munoz, J. F., De la Varga, I., & Graybeal, B. A. (2018). Bond characterization of UHPC overlays for concrete bridge decks: Laboratory and field testing. Construction and Building Materials, 190, 1056-1068.

25. Hasnat, A., & Ghafoori, N. (2021a). Properties of ultra-high performance concrete using optimization of traditional aggregates and pozzolans. Construction and Building Materials, 299, 123907.

26. Hasnat, A., & Ghafoori, N. (2021b). Freeze–Thaw Resistance of Nonproprietary Ultrahigh-Performance Concrete. Journal of Cold Regions Engineering, 35(3), 04021008.

27. Homayoonmehr, R., Rahai, A., & Ramezanianpour, A. A. (2022). Predicting the chloride diffusion coefficient and surface electrical resistivity of concrete using statistical regression-based models and its application in chloride-induced corrosion service life prediction of RC structures. Construction and Building Materials, 357, 129351.

28. Homayoonmehr, R., Ramezanianpour, A. A., & Mirdarsoltany, M. (2021). Influence of metakaolin on fresh properties, mechanical properties and corrosion resistance of concrete and its sustainability issues: A review. Journal of Building Engineering, 44, 103011.

29. Karim, R., Najimi, M., & Shafei, B. (2019). Assessment of transport properties, volume stability, and frost resistance of non-proprietary ultra-high performance concrete. Construction and Building Materials, 227, 117031.

30. Langan, B. W., Weng, K., & Ward, M. A. (2002). Effect of silica fume and fly ash on heat of hydration of Portland cement. Cement and Concrete research, 32(7), 1045-1051.

31. Le Hoang, A., & Fehling, E. (2017). Influence of steel fiber content and aspect ratio on the uniaxial tensile and compressive behavior of ultra high performance concrete. Construction and Building Materials, 153, 790-806.

32. Li, Z., Zhang, H., & Wang, R. (2022). Influence of steel fiber distribution on splitting damage and transport properties of ultra-high performance concrete. Cement and Concrete Composites, 126, 104373.

33. Liu, T., Wei, H., Zou, D., Zhou, A., & Jian, H. (2020). Utilization of waste cathode ray tube funnel glass for ultra-high performance concrete. Journal of Cleaner Production, 249, 119333.

34. Liu, Z., El-Tawil, S., Hansen, W., & Wang, F. (2018). Effect of slag cement on the properties of ultra-high performance concrete. Construction and Building Materials, 190, 830-837.

35. Ma, R., Zhang, L., Song, Y., Lin, G., Qian, X., Qian, K., & Ruan, S. (2023). Feasibility study on preparing economical and environmentally-friendly high-flowability ultra-high performance

cementitious composites with original graded stone powder free recycled manufactured sands. Journal of Cleaner Production, 390, 136190.

36. Mehta, P. K., & Monteiro, P. J. (2005). Concrete Microstructure, Properties and Materials. (3rd ed.), McGraw Hill.

37. Mohammed, A. M., Al-Hadithi, A. I., & Asaad, D. S. (2020). Investigating Transport Properties of Low-Binder Ultrahigh-Performance Concretes: Binary and Ternary Blends of Nanosilica, Microsilica and Cement. Arabian Journal for Science and Engineering, 45(10), 8369-8378.

38. Mosavinejad, S. G., Langaroudi, M. A. M., Barandoust, J., & Ghanizadeh, A. (2020). Electrical and microstructural analysis of UHPC containing short PVA fibers. Construction and Building Materials, 235, 117448.

39. Muzenski, S., Flores-Vivian, I., & Sobolev, K. (2019). Ultra-high strength cement-based composites designed with aluminum oxide nano-fibers. Construction and Building Materials, 220, 177-186.

40. Naber, C., Stegmeyer, S., Jansen, D., Goetz-Neunhoeffer, F., & Neubauer, J. (2019). The PONKCS method applied for time resolved XRD quantification of supplementary cementitious material reactivity in hydrating mixtures with ordinary Portland cement. Construction and Building Materials, 214, 449-457.

41. Naik, T. R., Kraus, R. N., Ramme, B. W., & Chun, Y. M. (2005). Decing salt-scaling resistance: Laboratory and field evaluation of concrete containing up to 70% class C and class F fly ash. Journal of ASTM International, 2(7), 1-12.

42. Onaizi, A. M., Huseien, G. F., Lim, N. H. A. S., Amran, M., & Samadi, M. (2021). Effect of nanomaterials inclusion on sustainability of cement-based concretes: A comprehensive review. Construction and Building Materials, 306, 124850.

43. Park, J. J., Yoo, D. Y., Park, G. J., & Kim, S. W. (2017). Feasibility of reducing the fiber content in ultra-high-performance fiber-reinforced concrete under flexure. Materials, 10(2), 118.

44. Piérard, J., Dooms, B., & Cauberg, N. (2013, October). Durability evaluation of different types of UHPC. In Proceedings of the RILEM-fib-AFGC International Symposium on Ultra-High Performance Fiber-Reinforced Concrete, Marseille, France (pp. 1-3).

45. Pyo, S., & Kim, H. K. (2017). Fresh and hardened properties of ultra-high performance concrete incorporating coal bottom ash and slag powder. Construction and Building Materials, 131, 459-466.

46. Pyo, S., Tafesse, M., Kim, B. J., & Kim, H. K. (2018). Effects of quartz-based mine tailings on characteristics and leaching behavior of ultra-high performance concrete. Construction and Building Materials, 166, 110-117.

47. Salahuddin, H., Qureshi, L. A., Nawaz, A., & Raza, S. S. (2020). Effect of recycled fine aggregates on performance of Reactive Powder Concrete. Construction and Building Materials, 243, 118223.

48. Schmidt, M., & Fehling, E. (2005). Ultra-high-performance concrete: research, development and application in Europe. ACI Spec. Publ, 228(1), 51-78.

49. Shi, C. (2004). Effect of mixing proportions of concrete on its electrical conductivity and the rapid chloride permeability test (ASTM C1202 or ASSHTO T277) results. Cement and concrete research, 34(3), 537-545.

50. Sobhani, J., & Najimi, M. (2013). Electrochemical impedance behavior and transport properties of silica fume contained concrete. Construction and Building Materials, 47, 910-918.

51. Sritharan, S., Doiron, G., Bierwagen, D., Keierleber, B., & Abu-Hawash, A. (2018). First application of UHPC bridge deck overlay in North America. Transportation Research Record, 2672(26), 40-47.

52. Vaitkevičius, V., Šerelis, E., Vaičiukynienė, D., Raudonis, V., & Rudžionis, Ž. (2016). Advanced mechanical properties and frost damage resistance of ultra-high performance fibre reinforced concrete. Construction and Building Materials, 126, 26-31.

53. Vigneshwari, M., Arunachalam, K., & Angayarkanni, A. (2018). Replacement of micro silica with thermally treated rice husk ash in Reactive Powder Concrete. Journal of Cleaner Production, 188, 264-277.

54. Walker, R., & Pavía, S. (2011). Physical properties and reactivity of pozzolans, and their influence on the properties of lime–pozzolan pastes. Materials and structures, 44, 1139-1150.

55. Wang, Y., An, M. Z., Yu, Z. R., Han, S., & Ji, W. Y. (2017). Durability of reactive powder concrete under chloride-salt freeze–thaw cycling. Materials and Structures, 50(1), 1-9.

56. Xi, J., Liu, J., Yang, K., Zhang, S., Han, F., Sha, J., & Zheng, X. (2022). Role of silica fume on hydration and strength development of ultra-high performance concrete. Construction and Building Materials, 338, 127600.

57. Xie, T., Fang, C., Ali, M. M., & Visintin, P. (2018). Characterizations of autogenous and drying shrinkage of ultra-high performance concrete (UHPC): An experimental study. Cement and Concrete Composites, 91, 156-173.

58. Yudenfreund, M., Odler, I., & Brunauer, S. (1972). Hardened portland cement pastes of low porosity I. Materials and experimental methods. Cement and Concrete Research, 2(3), 313-330.

59. Zhang, P., Li, Q., Chen, Y., Shi, Y., & Ling, Y. F. (2019). Durability of steel fiber-reinforced concrete containing SiO2 nano-particles. Materials, 12(13), 2184.

CHAPTER 4-FREEZE-THAW RESISTANCE OF NON-PROPRIETARY ULTRA-HIGH PERFORMANCE CONCRETE

Abstract

In cold regions, early deterioration of concretes due to freezing and thawing is a major concern. This study determined the freezing and thawing resistance of ultra-high performance concretes (UHPCs) made with different pozzolanic-material types (class F fly ash, natural pozzolan, and silica fume) and combinations, as well as varying steel fiber contents (0, 2, and 3%) and shapes (straight and hooked), using conventional fine aggregate. A total of thirty 28-day cured UHPCs were used to assess their mass loss after 70 freezing and thawing cycles (48 hours per cycle). The pre- and post- freeze-thaw compressive and splitting-tensile strengths of the studied UHPCs were also obtained and examined. The outcome of this study revealed that the studied UHPCs displayed excellent resistance against freezing and thawing deterioration. The post F-T exposed UHPCs gained strength due to the availability of un-hydrated pozzolanic materials, coupled with favorable curing environment. Among the utilized pozzolanic-material combinations, UHPCs made with silica fume and class F fly ash, as a partial replacement for the cement, performed the best against freezing and thawing, whereas the companion mixtures containing only class F fly ash to replace a portion of the cement, showed the highest mass loss. The addition of straight steel fibers had a more positive influence on the freezing and thawing resistance than hooked fibers.

Keywords: Freezing and thawing; Ultra high performance concrete; Mass loss; Pozzolanic materials; Steel fiber.

4.1 Introduction

In the northern United States, Canada, and many northern European countries, snow and ice pose severe hazards to concrete pavements and bridges. According to the US Federal Highway Administration (FHWA), in the US, more than 70% of roadways are affected during the winter. Due to the freezing of concrete, the conversion of water from the liquid state to solid-state results in an about 9% volume increase (Karakurt and Bayzant, 2015). This, in return, generates significant hydrostatic pressure inside the concrete. The prolonged exposure to freezing and thawing (F-T) of critically-saturated concrete eventually results in a significant deterioration, in the form of cracking, spalling, or surface scaling. Freezing and thawing damage depends on many circumstances, including the rate of freezing, duration of freezing and thawing, quality of concrete, air-entrainment, water-to-cementitious materials ratio, aggregate properties, and curing (Detwiler et al. 1989).

In recent years, ultra-high performance concrete (UHPC), both proprietary and non-proprietary, has attracted the attention of researchers. UHPC is different than conventional concrete due to its material composition, very low water-to-cement ratio, very high cement content, and absence of coarse aggregate (Matte and Moranville, 1999; Wang et al., 2012; Wille et al., 2011; Yalçınkaya and Yazıcı, 2017; Yang et al., 2009; Ragalwar et al., 2020). While many studies have addressed the deterioration of conventional concrete pavements and bridges, resulting from the freezing and thawing, to date, only a few studies regarding UHPC's resistance to freezing and thawing have been reported. Table 4.1 summarizes some of the recent studies conducted on the freezing and thawing of UHPCs. Karim et al. (2019) conducted a study on non-proprietary UHPCs under 300 F-T cycles and compared their performance with that of two proprietary UHPCs. A negligible mass loss was reported in all the non-proprietary UHPCs. Lee et al. (2013) employed steel fiber in UHPC precast elements under 600 F-T cycles. They found a steady decrease in compressive and flexural strengths, with increases in freezing and thawing cycles. In contrast, a study by Magureanu et al. (2012) showed increased values for the compressive strength and static and dynamic moduli of the studied UHPCs exposed to 1098 repeated freezing and thawing cycles. Ahlborn et al. (2012) also performed F-T tests as per ASTM C 666, procedure B, showing that after 32 freeze-thaw cycles,

UHPCs showed no degradation. Pierard et al. (2013) stated that specimens achieving strength between 140 MPa and 160 MPa displayed no degradation after 112 F-T cycles. To observe the effect of secondary pozzolanic materials, Alkaysi et al. (2016) partially replaced a portion of ordinary Portland cement with up to 25% silica fume and found that after 60 F-T cycles, the silica fume had a minimal effect on F-T performance when compared to UHPCs without silica powder. However, Khan and Abbas (2017) concluded that silica fume played a critical role against F-T deterioration by reducing the permeability of UHPCs more than fly ash did.

Table 4.1 Research work on the freezing and thawing of UHPCs

Ref.	Steel fiber (%)	Cement comp.	w/cm	Standard test	F-T cycles	F-T dur. (Hours)	Temp. per F-T cycle (°C)	ML(%)	RD (%)	f'_c (MPa)
Gu et al. (2018)	0	0.5C,0.4FA, 0.1SF[a]	0.16	GB/T50082	800	4	-20 to +20	1.55	91.1	110[d]
	1							1.27	94.5	125[d]
	2							0.52	95.1	155[d]
	3							0.49	97.5	182[d]
Karim et al. (2019)	2	1C, 0.07-0.25SF[a]	0.20-0.25	ASTM C666/B	300	8	-18 to 4	0.72	93.6	97.2[e]
								0.80	97.5	97.9[e]
Lee et al. (2013)	3	720C, 216SF[b]	0.17	ASTM C666/B[c]	300	3.08	-18 to 4.4	-	96	187.5[f]
					600			-	92	180.3[f]
					1000			-	90	170.2[f]
Magureanu et al. (2012)	0	1C, 0.26SF[a]	0.125	ASTM C666	1098	8	-18 to +22	-	100.4	157[d]
	2.5		0.129		1098			-	100.6	180[d]
Wang et al. (2012)	2	706C, 160SF[b]	0.20	GB/T50082	400	4	-18 to 5	0.17	99.1	124[f]
					800			0.36	99.4	125[f]
					1200			0.58	99.96	114[f]
					1500			0.61	99.98	89[f]

Note: [a]volume fraction; [b]weight/m³ of concrete; [c]thawing in air; [d]28-day compressive strength; [e]7 day compressive strength; [f]post F-T compressive strength; ML=Mass loss; RD= Relative dynamic modulus

To further restrain against F-T deterioration, a number of research studies have added steel fibers in UHPC. Gu et al. (2018) reported that steel fibers in UHPC inhibited the propagation of cracks in the matrix and improved the freezing-thawing performance of UHPC. They also found that after 800 cycles, a 1.5% mass loss was found for plain UHPC, whereas 3% fiber-reinforced UHPC had only a 0.5% mass loss. Moreover, a stronger interfacial transition zone (ITZ) developed between the hydration product and steel fibers of UHPCs, as compared to that of conventional fiber-reinforced concrete, resulted in better F-T resistance of fiber-reinforced UHPC (Sorelli et al., 2008). In contrast, a study conducted by Smarzewski and Barnat-Hunek (2017) reported that, high-steel fiber reinforced UHPC test samples resulted in lower dynamic modulus, as well as significant loss in mass.

Despite the recent interest in binary and ternary pozzolanic materials in making normal-strength and high-strength concretes, little data is available on the effects of binary or ternary-blended concrete, containing ordinary Portland cement/silica fume/class F fly ash/natural pozzolan, on the F-T resistance of UHPCs. Additionally, literatures are silent on the role of fiber shape and prolong freezing and thawing cycles on resistance of plain and fiber-reinforced UHPCs. Thus, the purpose of this study was to examine the freezing and thawing performance of selected plain and fiber-reinforced non-proprietary UHPCs made with various pozzolanic materials types and combinations, along with varying steel fiber contents and shapes. To this end, the mass loss and loss/gain in compressive and splitting-tensile strengths of the studied UHPCs were evaluated after 70 severe repeated freezing and thawing cycles. The effect of the binary and ternary composition of pozzolanic materials, as well as the steel fiber content and shape on the F-T performance of the studied UHPCs were examined. Additionally, correlations amongst the compressive and splitting-tensile strengths, and mass loss of the studied UHPCs were also developed.

4.2 Experimental Program

4.2.1 Materials

In the production of the UHPC mixtures, ASTM Type V Portland cement, class F fly ash, natural pozzolan, and silica fume were used as pozzolanic materials. The chemical characteristics of the Type V cement and pozzolanic materials are presented in Table 4.2. The natural pozzolan was sourced from a vitrified rhyolite as a silica-rich volcanic ash. Two types of locally produced fine aggregates were used; their size gradation varied from 0.075 mm to 4.75 mm. To achieve the maximum packing density with minimum porosity, a uniquely size-graded manufactured fine aggregate was determined. To this end, the relative density was measured for the graded aggregates at different distribution moduli (0.20-0.25), using the modified Andreasen and Andersen model. The maximum packing density was obtained from the distribution modulus of 0.21. The combined fine aggregates had specific gravity of 2.80 and absorption of 0.45%. The gradation curve of the Type V cement, pozzolanic materials, and fine aggregates is shown in Figure 4.1. To observe the effects of fiber shape, two types of low carbon steel fiber (straight and hooked), with 13 mm of length and 0.30 mm of width (aspect ratio of 43) were used. The specific gravity of the steel fibers was 7.86 and met the minimum tensile strength requirement of ASTM A820. A commercially-available, polycarboxylate-based, high-range water-reducing admixture (HRWRA) was used to achieve the desired flowability of the studied UHPCs.

Table 4.2 Chemical compositions of the Type V cement and pozzolanic materials

Composition	Type V cement (%)	Class F fly ash (%)	Natural pozzolan (%)	Silica fume (%)
SiO_2	21	59.93	71.0	94.72
CaO	62.4	4.67	2.3	-
Al_2O_3	4	22.22	7.9	-
Fe_2O_3	3.7	5.16	0.70	-
MgO	2.6	-	-	-
SO_3	2.2	0.38	0.1	0.23
$Na_2O+ K_2O$	0.54	1.29	7.5	0.47
Loss on Ignition (LOI)	2.0	0.32	3.4	2.82
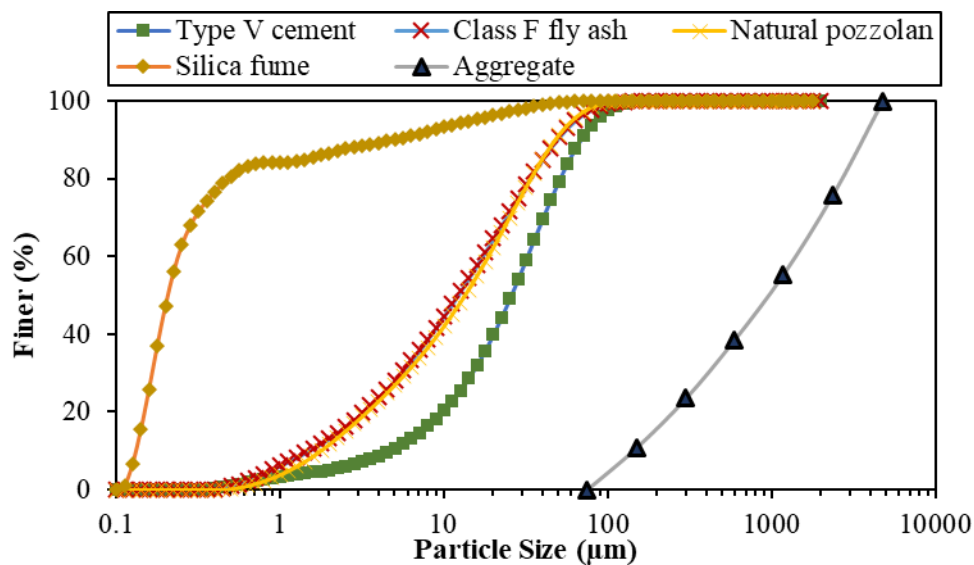
Figure 4.1 Type V cement, pozzolanic materials and aggregate gradation

4.2.2 Selection of Water-to-Cementitious Materials Ratio and HRWRA Content

At first, 100% cement was batched at various water-to-cementitious materials ratios, ranging from 0.16 to 0.24, and tested for flow to obtain the minimum water content required to achieve the minimum relative flow. A total of 30 combinations of pozzolanic materials (15 binary, 10 ternary, and four quaternary pozzolanic material compositions) were batched at various water-to-cementitious material ratios (w/cm = 0.16-0.24), and tested for flow to obtain the minimum water content and HRWRA requirement of different binder combinations, in comparison with 100% cement. Trial batches were also prepared before actual batching to ensure the desired flowability of fiber-reinforced UHPCs. Based on the flow characteristics and bulk properties, a total of six combinations of binding materials were selected for F-T resistance with the water-to-cementitious materials ratio of 0.21.

4.2.3 Mixture Proportions of UHPCs

A total of 30 UHPCs were used to determine their mass losses exposed to freezing and thawing cycles. The unit contents of the mixture constituents of the selected UHPCs is given in Table 4.3. The water-to-cementitious materials ratio of 0.21 was kept constant for all mixtures. The actual water content of the UHPCs varied due to the variation in the required HRWRA dosage to maintain the uniform flow. The dosage of HRWRA ranged from 10.1 to 14.3 kg/m^3, depending on the pozzolanic materials combination and percentage of steel fiber used. In the binary UHPCs, Portland cement was replaced with 20 and 30% class F fly ash; and 5% silica fume. For the ternary UHPCs, combined 15% fly ash and 5% silica fume; and combined 15% natural pozzolan and 5% silica fume. The UHPC containing 100% Portland cement is referred to as the control (C100). The flow diameter of the studied UHPCs is presented in Table 4.3. As can be seen, a satisfactory flow spread diameter of 250±25 mm was attained for all studied UHPCs. The demolded unit weight of the studied UHPCs is given in Table 4.3. The UHPCs with 2 and 3% steel fiber showed higher unit weights as compared to those of the plain UHPCs, due to the high relative density of the steel fibers.

Table 4.3 Mixture proportion of UHPCs (kg/m^3)

Mixture designation[a]	C[b]	F[b]	N[b]	SF[b]	Agg[b]	HRWRA[b]	w/cm	W[b]	Steel Fibers	Flow (mm)	Unit weight[c]
C100	1101	-	-	-	1174	12.1	0.21	226	-	248	2417
C100-H2%	1101	-	-	-	1174	13.2	0.21	226	156	241	2481
C100-S2%	1101	-	-	-	1174	13.2	0.21	226	156	256	2477
C100-H3%	1101	-	-	-	1174	14.3	0.21	225	234	251	2529
C100-S3%	1101	-	-	-	1174	14.3	0.21	225	234	271	2536
SF5	1046	-	-	39	1174	12	0.21	215	-	273	2398
SF5-H2%	1046	-	-	39	1174	13.1	0.21	214	156	247	2458
SF5-S2%	1046	-	-	39	1174	13.1	0.21	214	156	240	2452
SF5-H3%	1046	-	-	39	1174	14.1	0.21	214	234	255	2496
SF5-S3%	1046	-	-	39	1174	14.1	0.21	214	234	250	2527
F20	881	163	-	-	1174	11	0.21	215	-	270	2353
F20-H2%	881	163	-	-	1174	12	0.21	215	156	271	2422
F20-S2%	881	163	-	-	1174	12	0.21	215	156	247	2437
F20-H3%	881	163	-	-	1174	13	0.21	214	234	240	2485
F20-S3%	881	163	-	-	1174	13	0.21	214	234	255	2488
F30	771	244	-	-	1174	10.1	0.21	210	-	250	2323
F30-H2%	771	244	-	-	1174	11.2	0.21	209	156	269	2387
F30-S2%	771	244	-	-	1174	11.2	0.21	209	156	270	2393
F30-H3%	771	244	-	-	1174	12.2	0.21	208	234	246	2444
F30-S3%	771	244	-	-	1174	12.2	0.21	208	234	238	2452
F15SF5	881	122	-	39	1174	11.5	0.21	214	-	253	2337
F15SF5-H2%	881	122	-	39	1174	12.5	0.21	214	156	248	2430
F15SF5-S2%	881	122	-	39	1174	12.5	0.21	214	156	264	2436

Mixture designation[a]	C[b]	F[b]	N[b]	SF[b]	Agg[b]	HRWRA[b]	w/cm	W[b]	Steel Fibers	Flow (mm)	Unit weight[c]
F15SF5-H3%	881	122	-	39	1174	13.5	0.21	213	234	265	2480
F15SF5-S3%	881	122	-	39	1174	13.5	0.21	213	234	243	2480
N15SF5	881	-	120	39	1174	11.6	0.21	214	-	236	2335
N15SF5-H2%	881	-	120	39	1174	12.7	0.21	213	156	250	2425
N15SF5-S2%	881	-	120	39	1174	12.7	0.21	213	156	245	2428
N15SF5-H3%	881	-	120	39	1174	13.7	0.21	212	234	261	2478
N15SF5-S3%	881	-	120	39	1174	13.7	0.21	212	234	264	2490

1 kg/m³ = 1.685 lb/yd³

[a] C100: 100% Cement; SF5: 95% cement and 5% silica fume; F20: 80% cement and 20% class F fly ash; F30: 70% cement and 30% class F fly ash; F15SF5: 80% cement and 15% class F fly ash and 5% silica fume; N15SF5: 80% cement and 15% natural pozzolan and 5% silica fume; S2% and S3% represents 2% and 3% straight steel fibers; H2% and H3% represents 2% and 3% hooked steel fibers.

[b] High-range water reducing admixture; Agg: Aggregate; C: Cement; F: Class F fly ash; SF: Silica fume; N: Natural pozzolan; W: Water;

[c] Demolded unit weight

4.2.4 Mixing, Sampling, Curing, and Testing

Due to the high quantity of small size particles, coupled with the low water-to-cementitious materials ratio and addition of steel fibers, a longer mixing time and higher energy were required for the production of the UHPCs, as compared to traditional concrete. The mixing time, mixing speed, mixing sequence, temperature, and relative humidity were closely monitored and uniformly maintained. The mixing sequence of the studied UHPCs is shown in Figure 4.2. The flow properties of the studied UHPCs were evaluated according to the ASTM C230 before they were poured into cylinders (2 in diameter and 4 in height). Figure 4.3 represents the flow diameter of UHPCs with 2, and 3% steel fibers. As can be seen, freshly-mixed fiber-reinforced UHPCs displayed excellent flow characteristics (250±25 mm). A total of twelve cylindrical specimen (50 mm diameter and 100 mm height) were prepared from each mixture. The specimens were kept for 24 hours in a controlled moist curing room at $22 \pm 3°C$ and 95% relative humidity. After 24 hours, the specimens were demolded and returned to the moisture room for an additional 27 days.
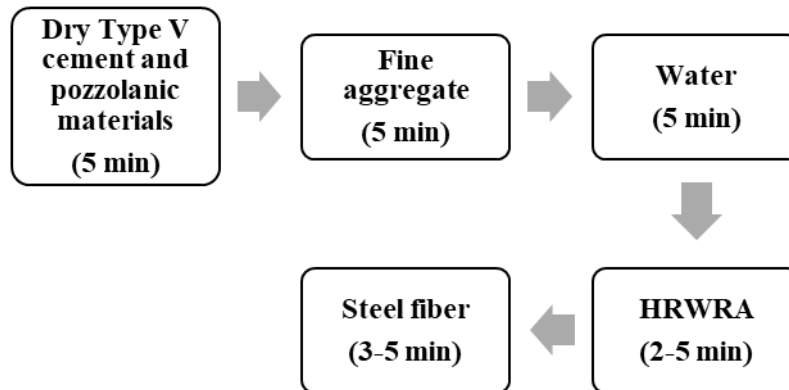
Figure 4.2 UHPCs' mixing sequence

(a)   (b)
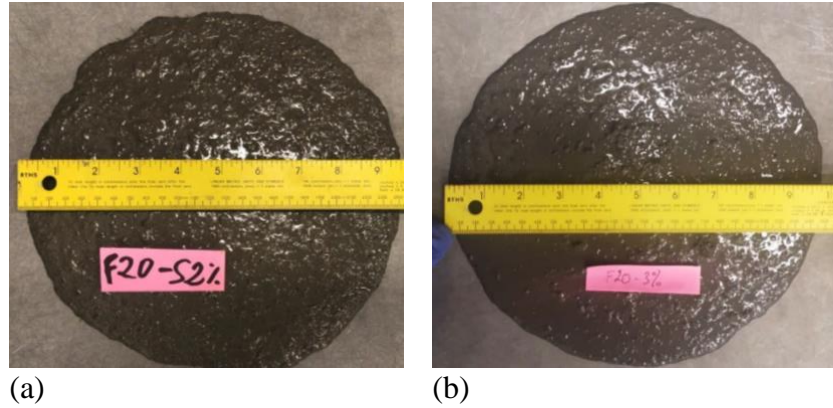
Figure 4.3 Flow diameter of fiber-reinforced UHPCs (a) F20-S2%; (b) F20-S3%

The 28-day cured UHPCs were tested for compressive and splitting-tensile strengths, as per ASTM C39 and C496, respectively. The freeze-thaw resistance of the UHPC specimens was evaluated in accordance with a freeze-thaw duration of 48 h per cycle. The temperature profile of the F-T cycle is shown in Figure 4.4. This process continued for 70 F-T cycles. After completion of the 70 repeated F-T cycles, the test samples were also evaluated for their compressive and splitting- tensile strengths, as per ASTM C39 and C496, respectively.
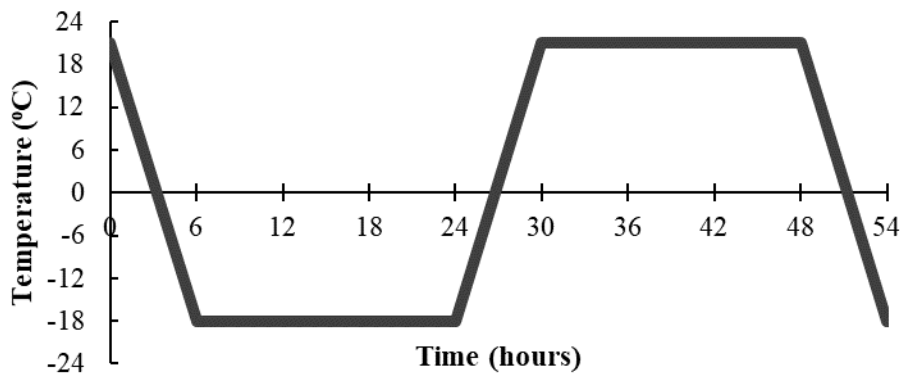
Figure 4.4 Temperature profile of the freeze-thaw test

4.3 Results and Discussion

4.3.1 Effect of Freezing and Thawing on Compressive and Splitting-Tensile Strength of UHPCs

The effect of the 70 F-T cycles on the compressive and splitting-tensile strengths (28 day and after 70 F-T cycles) of the studied UHPCs are shown in Table 4.4 and Figures 4.5-4.6. All samples tested in compression after 70 F-T cycles showed significant improvement in compressive strength. On average, the post F-T exposed UHPCs gained 25% more compressive strength, as compared to that of the 28-day cured UHPCs tested prior to F-T exposure. A similar observation was also reported by other researchers (Munoz et al., 2014; Graybeal, 2006; Lee et al., 2005). The availability of un-hydrated pozzolanic materials, coupled with a favorable curing environment during the F-T cycles, aided the UHPCs to hydrate further. While the hydration of pozzolanic materials was slow due to low temperatures during the freezing period (-18°C); however, higher temperatures during the thawing period (18°C) allowed for the pozzolanic materials to

hydrate at a faster rate. An et al. (2019) studied the rehydration effect on F-T of UHPCs and concluded that hydration continued during the freezing phase at a slower rate and healed the small cracks created due to F-T stress. Jocabson & Sellevold (1996) found that, with the presence of unhydrated cement particles submerged concrete samples can self-heal the microcracks generated during freezing and thawing cycles. The ternary-blend pozzolanic materials showed the highest gain in strength among the studied UHPCs, as compared to those of the other pozzolanic-material compositions. The UHPCs containing 15% fly ash and 5% silica fume, as a partial replacement of Portland cement, showed the highest increases in compressive strength. Early hydration of the silica fume facilitated the early strength development, while the secondary pozzolanic activity of fly ash helped in the long-term compressive strength gain of the studied UHPCs (Langman et al., 2002; Jalal et al., 2015). The steel fiber content and shape had negligible effects on the compressive strength improvement of the UHPC samples tested pre and post F-T cycle. Multipole studies also reported a similar finding (Alsalman et al., 2017; Hoang and Fehling, 2017, Park et al., 2017). Indeed, some studies reported that high amount of steel fibers (greater than 3% of volume of concrete) had adverse effect on compressive strength due to entrapped air resulted from fiber agglomeration (Meng and Khayat, 2018; Hoang and Fehling, 2017).

The UHPCs tested in splitting-tension after 70 F-T cycles also showed improvement in splitting-tensile strength. After 70 F-T cycles, on average, the UHPCs gained 18% more splitting-tensile strength as compared to those of the 28-day cured UHPCs tested prior to F-T exposure. Favorable curing conditions, very high pozzolanic materials, low permeability, and a low water-to-cementitious materials ratio played positive roles in achieving higher splitting-tensile strength, even after 70 severe freezing and thawing cycles (Graybeal, 2006; Granger et al., 2007; Munoz et al., 2014). When compared to the pre F-T compressive and splitting-tensile strengths of the UHPCs, prior to the F-T cycles, the addition of steel fibers, in both content and shape, had little influence on the post F-T strengths of the studied UHPCs. Unlike steel fibers, pozzolanic materials performance greatly influenced by the duration of testing (Hoang and Fehling, 2017).

Table 4.4 Compressive and splitting-tensile strengths of the studied UHPCs

Mixture designation	28-day strength properties (MPa)				70 F-T cycles strength properties (MPa)			
	f'_{c-28D}	STDEV	f_{t-28D}	STDEV	$f'_{c-70F-T}$	STDEV	$f_{t-70F-T}$	STDEV
C100	124.8	2.26	9.1	0.06	159.9	2.35	10.8	0.18
SF5	131.4	3.52	9.4	0.12	167.5	2.86	11.3	0.20
F15SF5	129.4	5.27	9.5	0.09	170.7	5.33	11.4	0.12
N15SF5	127.1	1.98	9.3	0.16	164.1	3.52	11.2	0.23
F20	122.3	2.52	9.0	0.12	153.2	3.02	10.8	0.25
F30	120.4	1.40	8.8	0.12	151.2	1.60	10.7	0.13
C100-H2%	127.2	1.91	10.5	0.17	154.7	2.15	12.4	0.15
SF5-H2%	134.6	2.41	11.1	0.09	170.0	2.41	12.9	0.12
F15SF5-H2%	136.2	2.22	11.2	0.06	173.7	2.76	13.0	0.10
N15SF5-H2%	131.4	0.61	10.9	0.09	167.8	0.82	12.9	0.13
F20-H2%	124.7	1.72	10.6	0.17	155.2	1.81	12.5	0.21
F30-H2%	127.3	2.92	10.4	0.12	154.1	2.88	12.4	0.10
C100-S2%	127.4	3.29	10.6	0.04	156.9	4.00	12.5	0.10
SF5-S2%	133.9	2.68	11.0	0.10	169.8	3.03	13.0	0.19
F15SF5-S2%	135.4	2.51	11.1	0.12	174.7	2.30	13.1	0.09
N15SF5-S2%	133.3	0.82	11.0	0.12	168.5	1.30	12.9	0.06
F20-S2%	125.4	1.37	10.7	0.09	156.6	1.33	12.6	0.21
F30-S2%	128.4	2.62	10.6	0.07	154.3	3.35	12.4	0.20
C100-H3%	130.3	0.68	12.3	0.12	160.1	1.34	14.5	0.10
SF5-H3%	138.6	1.59	12.8	0.15	173.2	2.41	14.9	0.10

Mixture designation	28-day strength properties (MPa)				70 F-T cycles strength properties (MPa)			
	$f'_{c\text{-}28D}$	STDEV	$f_{t\text{-}28D}$	STDEV	$f'_{c\text{-}70F\text{-}T}$	STDEV	$f_{t\text{-}70F\text{-}T}$	STDEV
F15SF5-H3%	140.3	1.92	13.1	0.13	177.6	4.68	15.3	0.17
N15SF5-H3%	136.8	1.19	12.9	0.10	171.2	1.66	15.1	0.12
F20-H3%	127.0	1.34	12.2	0.07	160.2	3.40	14.4	0.08
F30-H3%	130.8	1.86	12.1	0.14	156.4	4.01	14.4	0.21
C100-S3%	131.0	5.21	12.5	0.10	161.3	4.82	14.7	0.10
SF5-S3%	140.5	2.35	13.0	0.10	176.3	4.03	15.1	0.20
F15SF5-S3%	142.7	4.01	13.1	0.05	178.6	1.61	15.4	0.09
N15SF5-S3%	137.4	5.64	13.0	0.13	171.0	4.99	15.3	0.29
F20-S3%	128.2	1.81	12.4	0.10	160.1	2.72	14.7	0.32
F30-S3%	132.6	1.97	12.3	0.14	156.9	2.28	14.5	0.29

Note: STDEV-Standard deviation; $f'_{c\text{-}28D}$-28 day compressive strength; $f_{t\text{-}28D}$- 28day splitting-tensile strength; $f'_{c\text{-}70F\text{-}T}$-70 F-T compressive strength; $f_{t\text{-}70F\text{-}T}$- 70 F-T splitting-tensile strength
1 MPa= 145 Psi
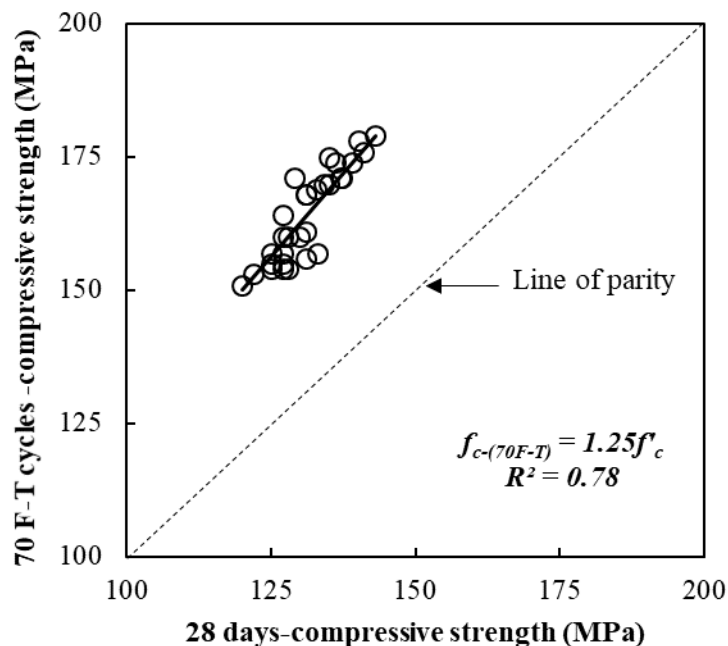
Figure 4.5 Effects of freezing and thawing cycles on the compressive strengths of UHPCs
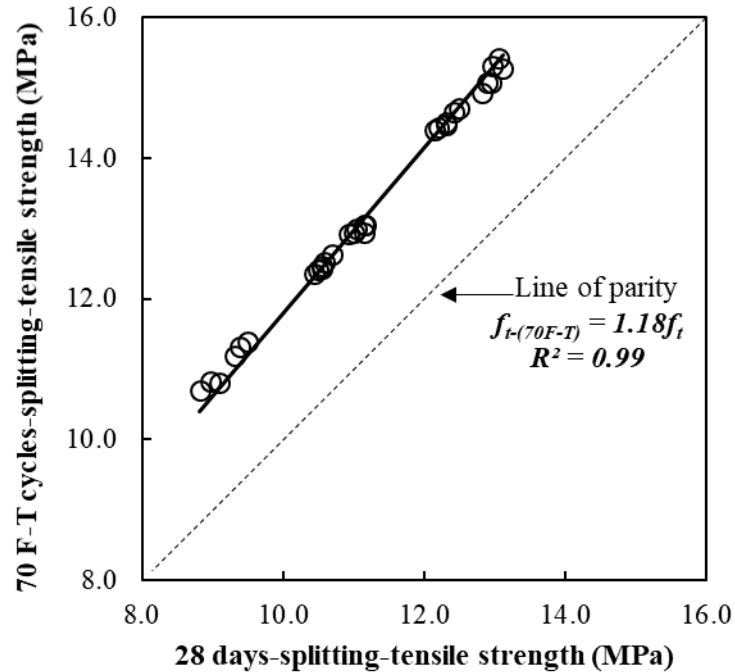
Figure 4.6 Effects of freezing and thawing cycles on the splitting-tensile strength of UHPCs

4.3.2 Freezing and Thawing of UHPCs

The results of F-T testing for the studied UHPCs, as they varied by pozzolanic-material compositions and steel fiber contents and shapes, at different F-T cycles are presented in Table 4.5. After the completion of 70 F-T cycles, the mass loss varied from 0.05 to 0.55%. As mentioned in Table 4.1, similar mass losses were also reported in previous studies (Karim et al., 2019; Wang et al., 2012). The acceptable minimum mass loss percentage of concrete after F-T cycles was reported to be less than 5%, depicting very high quality of the studied UHPCs (RILEM TC 176-IDC, 2002). The influence of pozzolanic material combinations, steel fiber contents, and steel fiber shapes on resistance to freezing and thawing of the studied UHPCs are discussed in the sections to follow. In addition, relationships have been developed between strength and mass loss of the studied UHPCs.

Table 4.5 Mass losses/gains at different freezing and thawing cycles

Mixture Designation	Mass loss/gain at different freezing and thawing cycles (%)							
	0	10	20	30	40	50	60	70
C100	0.000	0.020	0.015	-0.030	-0.100	-0.130	-0.200	-0.400
SF5	0.000	0.025	0.030	0.020	-0.020	-0.020	-0.060	-0.175
F15SF5	0.000	0.023	0.026	0.010	-0.020	-0.030	-0.080	-0.150
N15SF5	0.000	0.021	0.025	-0.020	-0.070	-0.100	-0.140	-0.190
F20	0.000	0.010	0.000	-0.060	-0.120	-0.200	-0.340	-0.470
F30	0.000	0.001	-0.030	-0.080	-0.150	-0.300	-0.440	-0.550
C100-H2%	0.000	0.053	0.040	0.000	-0.050	-0.097	-0.167	-0.380
SF5-H2%	0.000	0.068	0.065	0.063	0.040	0.023	-0.017	-0.140
F15SF5-H2%	0.000	0.057	0.050	0.044	0.020	0.004	-0.046	-0.125
N15SF5-H2%	0.000	0.054	0.030	0.013	-0.020	-0.067	-0.107	-0.175
F20-H2%	0.000	0.043	0.030	-0.027	-0.080	-0.167	-0.308	-0.470
F30-H2%	0.000	0.032	-0.010	-0.048	-0.150	-0.268	-0.408	-0.530

| Mixture | Mass loss/gain at different freezing and thawing cycles (%) | | | | | | | |
Designation	0	10	20	30	40	50	60	70
C100-S2%	0.000	0.056	0.042	0.000	-0.045	-0.078	-0.150	-0.350
SF5-S2%	0.000	0.069	0.064	0.069	0.040	0.024	-0.020	-0.110
F15SF5-S2%	0.000	0.043	0.045	0.060	0.030	0.001	-0.045	-0.080
N15SF5-S2%	0.000	0.055	0.030	0.020	-0.010	-0.045	-0.092	-0.100
F20-S2%	0.000	0.042	0.030	-0.023	-0.080	-0.135	-0.280	-0.446
F30-S2%	0.000	0.025	-0.010	-0.043	-0.140	-0.228	-0.383	-0.479
C100-H3%	0.000	0.053	0.040	0.046	0.046	-0.057	-0.126	-0.320
SF5-H3%	0.000	0.055	0.044	0.043	0.052	0.096	-0.012	-0.100
F15SF5-H3%	0.000	0.059	0.050	0.044	0.022	-0.012	-0.025	-0.070
N15SF5-H3%	0.000	0.053	0.030	0.013	-0.010	-0.041	-0.072	-0.090
F20-H3%	0.000	0.040	0.030	-0.027	-0.060	-0.122	-0.260	-0.380
F30-H3%	0.000	0.039	-0.010	-0.048	-0.100	-0.145	-0.340	-0.430
C100-S3%	0.000	0.056	0.042	0.048	0.049	-0.037	-0.105	-0.300
SF5-S3%	0.000	0.060	0.047	0.056	0.055	0.100	-0.009	-0.083
F15SF5-S3%	0.000	0.061	0.047	0.029	0.022	-0.009	-0.017	-0.054
N15SF5-S3%	0.000	0.043	0.042	0.041	-0.005	-0.022	-0.054	-0.075
F20-S3%	0.000	0.041	-0.004	-0.006	-0.058	-0.108	-0.211	-0.353
F30-S3%	0.000	0.042	-0.010	-0.046	-0.090	-0.116	-0.290	-0.407

Note: mass gain (+), mass loss (-)

4.3.2.1 Influence of Pozzolanic-Material Combinations

The F-T resistance of the studied plain UHPCs, as a function of mass loss, is shown in Figure 4.7 and Table 4.5. Nearly all studied UHPCs gained mass up to 20 F-T cycles due to the continued hydration of the pozzolanic materials. Peng et al. (2019) studied the mass loss of high performance concrete (HPC) and found mass gain of HPC during initial stages of F-T cycles. Comparable findings were also reported by others (Graybeal, 2006; Wang et al., 2017).

Plain UHPCs containing fly ash replacing 20 or 30%, by weight, of Portland cement showed the highest mass loss after 70 F-T cycles. The freezing environment, coupled with the slower rate of hydration reaction, delayed the strength development of the fly ash-containing UHPCs, and made them comparatively weaker in resisting the internal hydrostatic stress generated from the F-T regimes (Naik et al. 2005). In contrast, plain UHPCs made with silica fume and fly ash (F15SF5) as a partial replacement of Portland cement displayed the lowest mass losses amongst all studied UHPCs. Silica fume played a major role in the early-age strength development of UHPCs to resist against the early-age F-T effect, whereas fly ash improved the long-term strength and late F-T resistance (Khan and Abbas, 2017). The wider particle size distribution of the combined silica fume and fly ash provided an opportunity for small capillary pore sizes, resulting in a less permeable concrete matrix (Figure 4.1). A synergistic effect, albeit in a lesser extent, was also observed for the UHPCs made with 5% silica fume and 15% natural pozzolan (N15SF5) as a partial replacement of Portland cement.
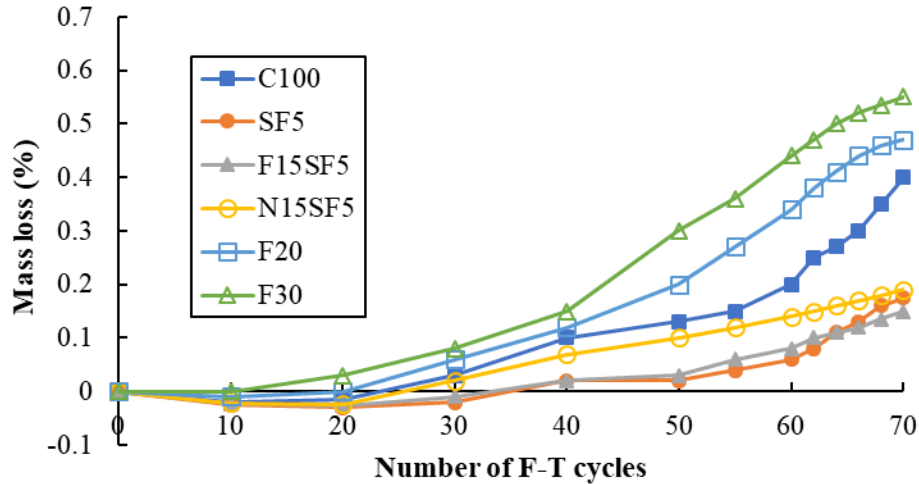
Figure 4.7 Mass losses of plain UHPCs as a function of freezing and thawing (F-T) cycles

4.3.2.2 Influence of Steel Fiber Content and Shape

The percentage of mass loss of the studied UHPCs containing 2 and 3% hooked and straight steel fibers is documented in Table 4.5. In general, the introduction of fibers improved the F-T resistance of the studied UHPCs, and the UHPCs made with 3% steel fibers produced lower mass losses, as compared to the companion UHPCs containing 2% steel fibers. Overall, hooked fibers increased the mass loss resistance of the studied UHPCs by 9 and 30% for 2 and 3% volumetric contents, respectively, when compared with the companion plain UHPCs. Once straight fibers were used, the resistance to mass loss increased by 19 and 38%, respectively. The reduction of the mass loss percentage, with increases in fiber content, can be attributed to the anticipated increase in the matrix stiffness of the fiber-containing UHPCs. Mu et al. (2002) also found that the increase of fiber in the concrete resulted in lower F-T damage as compared to the companion plain concrete. The presence of steel fibers acted as a bridge to arrest the development of tensile cracks inside the concrete (Zollo 1997). A similar finding was also reported by Zhang et al. (2019). The percentage mass loss relationships between plain and fiber-reinforced UHPCs, having coefficients of determination (R^2) values greater than 0.85, are documented in Figures 4.8 and 4.9. The effect of steel fiber shape is presented in Figure 4.10. As can be seen, the addition of 2 and 3% straight steel fibers to the UHPCs resulted in average increases in mass loss resistance by 10%, as compared to those of the UHPCs made with the hooked fibers, possibly due to better interfacial bonding between the matrix and straight fibers. Yoo et al. (2017) concluded that straight steel fibers displayed better fiber distribution compared to the companion deformed fibers and resulted in better bond strength.
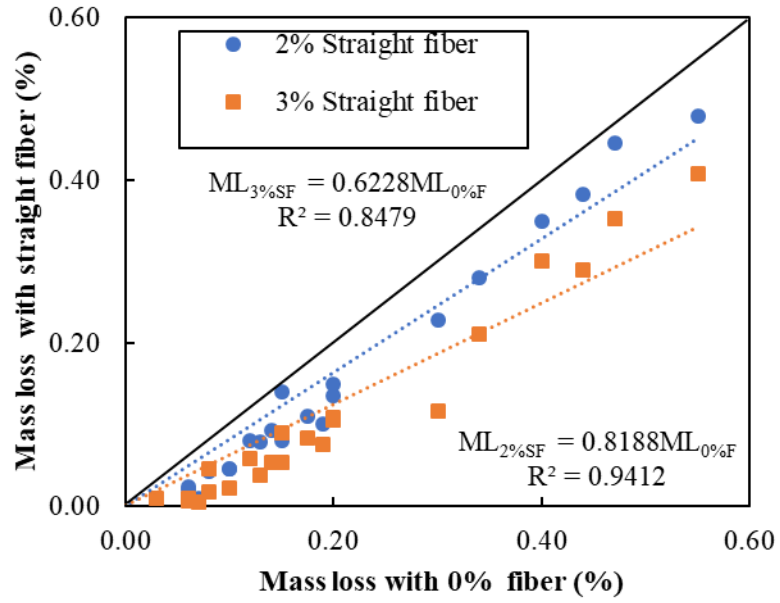
Figure 4.8 Effects of straight steel fiber content on F-T performance
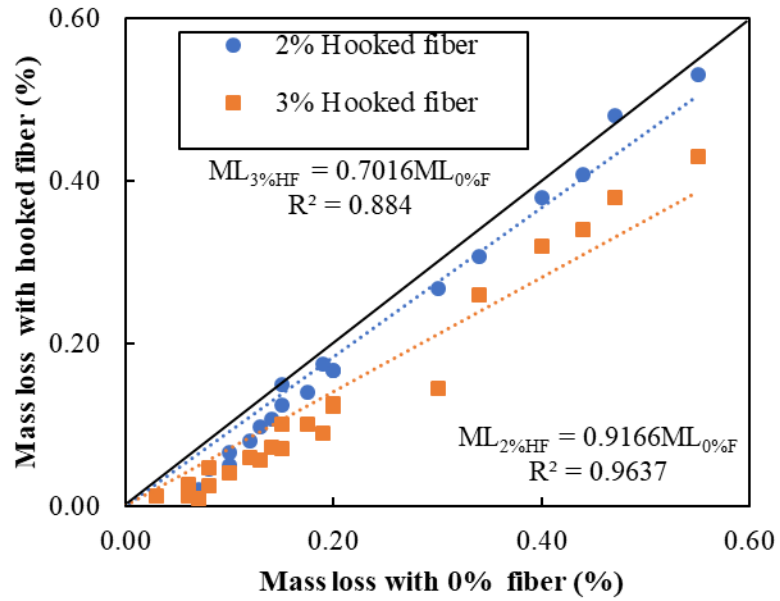
Figure 4.9 Effects of hooked steel fiber content the F-T performance
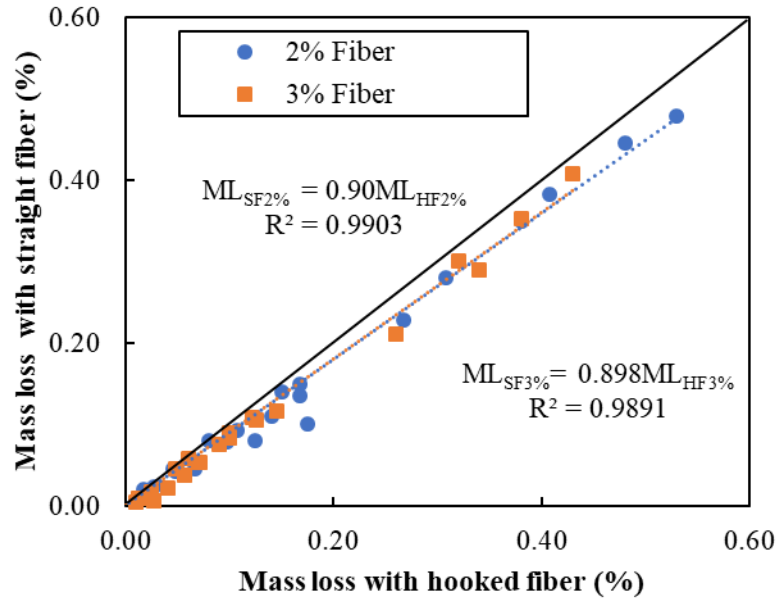
Figure 4.10 Effects of steel fiber shape on F-T performance

4.3.3 Correlation Between UHPCs Bulk Properties and Mass Loss

A suitable correlation, at a 95% confidence level, between compressive strength (pre- and post-exposed F-T cycles) and mass loss was found, and the results are shown in Figure 4.11. As can be seen, increases in the compressive strength of the UHPCs led to increased resistance against F-T regimes. This behavior can be attributed to the following reasons: (i) as most of the pores inside the UHPCs are gel pores, and water in gel pores does not freeze above -78°C (Mehta and Monteiro, 2014), only a small amount of free water (water-to-cementitious materials ratio = 0.21) was available inside the concrete to freeze and generate hydraulic pressure inside the concrete; (ii) high cementitious-material contents, with low water-to-cementitious-material ratios resulted in very strong microstructures, high density, and low permeability for the studied UHPCs (Peng et al., 2011; Dobias et al., 2016); (iii) the absence of coarse aggregate produced very low porosity and a less interconnected porous matrix; (iv) the high flowability of the fresh UHPCs developed well compacted mixtures; (v) the presence of steel fiber minimized the effects of tensile stress developed during F-T cycles; (vi) the ternary mixture of pozzolanic materials resulted in excellent particle size distribution to reduce the porosity of the UHPCs; and (vii) continuous curing during the F-T regimes increased the resistance against F-T deterioration.

89
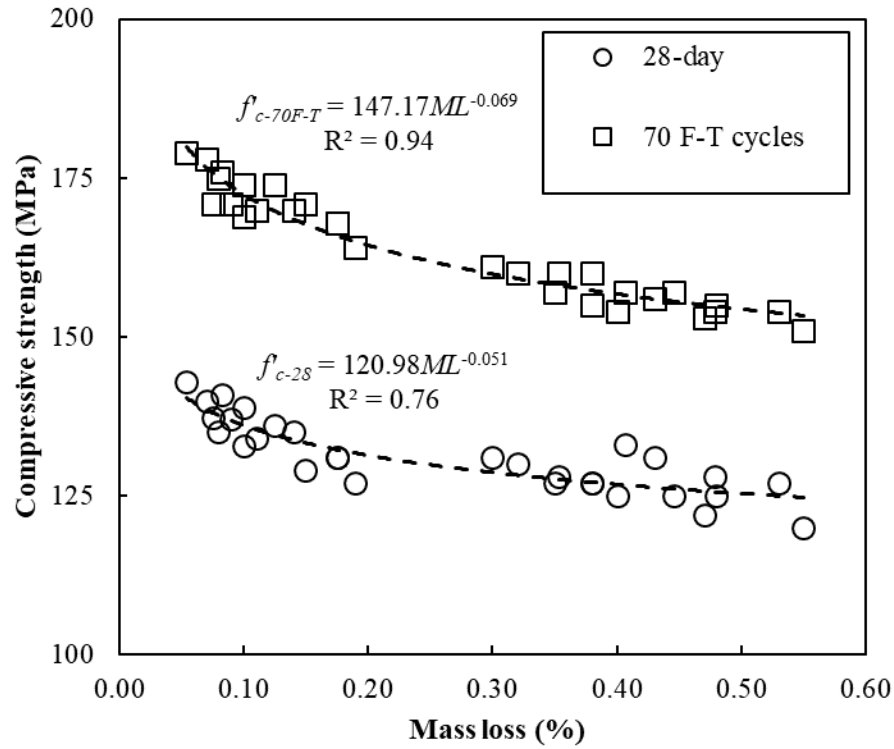
Figure 4.11 Correlation between compressive strength and mass loss percentage

Figure 4.12 represents the relationship between splitting-tensile strength and mass loss after 70 F-T cycles for the studied UHPCs made with 0, 2, and 3% steel fiber contents. In general, with UHPCs splitting-tensile strength increases, F-T mass losses decreased. The relationship between splitting-tensile strength and percentage mass loss, having a coefficient of determination (R^2) of more than 0.88, are documented in Figure 4.12.
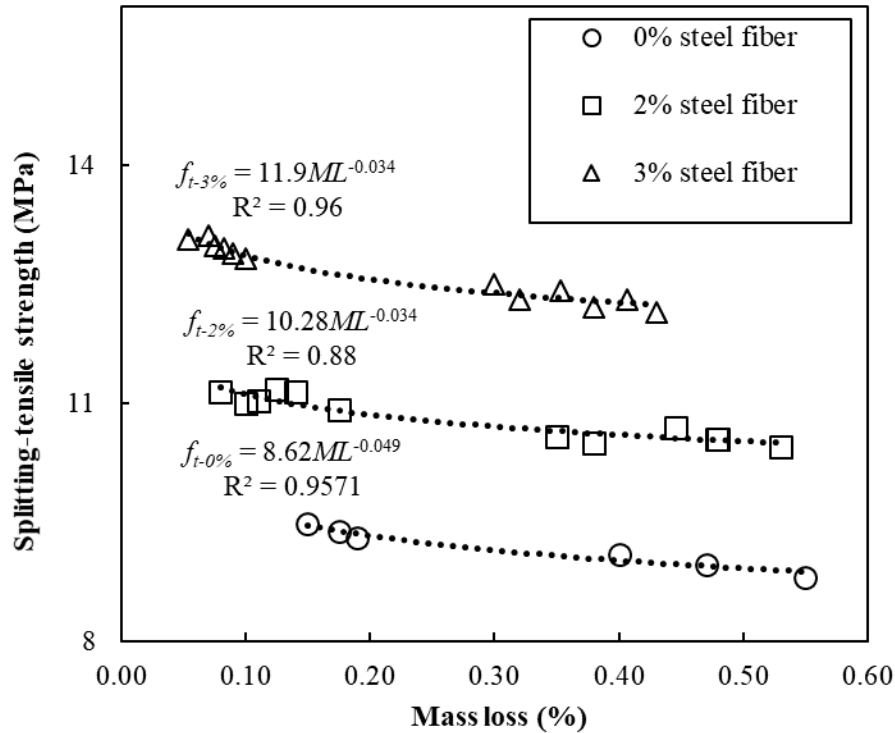
Figure 4.12 Correlation between splitting-tensile strength and mass loss percentage

4.4 Conclusions

Based on the results of this research, the following conclusions can be drawn:

(1) The studied UHPCs displayed mass losses only after 20 F-T cycles. The low water-to-cementitious-materials ratios, very high cementitious-materials content, steel fibers, and favorable curing environment produced a very dense matrix, which resulted in the high resistance against freezing and thawing for the studied UHPCs.

(2) The UHPC made with the ternary-blend pozzolanic materials showed the highest F-T resistance. A wider particle size distribution, and the availability of both primary and secondary pozzolanic materials, for a continued hydration reaction, contributed to the improved F-T resistance of the UHPC containing ternary-pozzolanic materials.

(3) Amongst the studied pozzolanic materials combinations, the 28-day cured UHPCs containing 15% fly ash and 5% silica fume showed the highest resistance to F-T regime, whereas the UHPCs containing only fly ash produced the contrary.

(4) The inclusion of steel fibers had a positive influence in improving the F-T resistance of the studied UHPCs. At least a 30% improvement in F-T resistance was obtained for the UHPCs containing 3% steel fiber, as compared to the companion plain UHPCs.

(5) The UHPCs containing straight fibers exhibited nearly a 10% higher resistance against repeated F-T cycles, as compared to the hooked steel fibers.

References

1. Ahlborn, T. T. M., Harris, D. K., Misson, D. L., & Peuse, E. J. (2011). Characterization of strength and durability of ultra-high-performance concrete under variable curing conditions. Transportation research record, 2251(1), 68-75.

2. Alkaysi, M., El-Tawil, S., Liu, Z., & Hansen, W. (2016). Effects of silica powder and cement type on durability of ultra high performance concrete (UHPC). *Cement and Concrete Composites*, 66, 47-56.

3. Alsalman, A., Dang, C. N., & Hale, W. M. (2017). Development of ultra-high performance concrete with locally available materials. Construction and Building Materials, 133, 135-145.

4. An, M., Wang, Y., & Yu, Z. (2019). Damage mechanisms of ultra-high-performance concrete under freeze–thaw cycling in salt solution considering the effect of rehydration. Construction and Building Materials, 198, 546-552.

5. Carbonell Muñoz, M. A., Harris, D. K., Ahlborn, T. M., & Froster, D. C. (2014). Bond performance between ultrahigh-performance concrete and normal-strength concrete. Journal of Materials in Civil Engineering, 26(8), 04014031.

6. Detwiler, R. J., Dalgleish, B. J., & Brady, R. (1989). Assessing the durability of concrete in freezing and thawing. ACI Materials Journal, 86(1), 29-35.

7. Dobias, D., Pernicova, R., Mandlik, T. (2016). Water transport properties and depth of chloride penetration in ultra high performance concrete. Key Engineering Materials, 711, 137–142.

8. Granger, S., Loukili, A., Pijaudier-Cabot, G., & Chanvillard, G. (2007). Experimental characterization of the self-healing of cracks in an ultra high performance cementitious material: Mechanical tests and acoustic emission analysis. Cement and Concrete Research, 37(4), 519-527.

9. Graybeal, B. (2006). "Material property characterization of ultra-high performance concrete." Rep. No. FHWA-HRT-06-103, Federal Highway Administration, Washington, DC.

10. Gu, C., Sun, W., Guo, L., Wang, Q., Liu, J., Yang, Y., & Shi, T. (2018). Investigation of microstructural damage in ultrahigh-performance concrete under freezing-thawing action. *Advances in Materials Science and Engineering*, 2018, 1-10.

11. S. Jacobsen, E.J. Sellevold, Self healing of high strength concrete after deterioration by freeze/thaw, Cem. Concr. Res. 26 (1) (1996) 55–62.

12. Jalal, M., Pouladkhan, A., Harandi, O. F., & Jafari, D. (2015). Comparative study on effects of Class F fly ash, nano silica and silica fume on properties of high performance self compacting concrete. Construction and Building Materials, 94, 90-104.

13. Karakurt, C., & Bayazıt, Y. (2015). Freeze-thaw resistance of normal and high strength concretes produced with fly ash and silica fume. *Advances in Materials Science and Engineering*, 2015.

14. Karim, R., Najimi, M., & Shafei, B. (2019). Assessment of transport properties, volume stability, and frost resistance of non-proprietary ultra-high performance concrete. *Construction and Building Materials*, 227, 117031.

15. Khan, M. I., & Abbas, Y. M. (2017). Curing optimization for strength and durability of silica fume and fuel ash concretes under hot weather conditions. *Construction and Building Materials*, 157, 1092-1105.

16. Langan, B. W., Weng, K., & Ward, M. A. (2002). Effect of silica fume and fly ash on heat of hydration of Portland cement. Cement and Concrete research, 32(7), 1045-1051.

17. Le Hoang, A., & Fehling, E. (2017). Influence of steel fiber content and aspect ratio on the uniaxial tensile and compressive behavior of ultra high performance concrete. Construction and Building Materials, 153, 790-806.

18. Lee, M. G., Chiu, C. T., & Wang, Y. C. (2005). "The study of bond strength and bond durability of reactive powder concrete." Journal of ASTM International, 2(7), 485–494.

19. Lee, M. J., Lee, M. G., Huang, Y., & Lee, K. L. (2013). UHPC precast concrete under severe freeze-thaw conditions. *International Journal of Engineering and Technology*, 5(4), 452.

20. Magureanu, C., Sosa, I., Negrutiu, C., & Heghes, B. (2012). Mechanical properties and durability of ultra-high-performance concrete. *ACI Materials Journal*, 109(2), 177-183.

21. Matte, V., & Moranville, M. (1999). Durability of reactive powder composites: influence of silica fume on the leaching properties of very low water/binder pastes. *Cement and Concrete Composites*, 21(1), 1-9.

22. Mehta, P. K., & Monteiro, P. J. (2014). Concrete: microstructure, properties, and materials. McGraw-Hill Education.

23. Meng, W., & Khayat, K. H. (2018). Effect of hybrid fibers on fresh properties, mechanical properties, and autogenous shrinkage of cost-effective UHPC. Journal of Materials in Civil Engineering, 30(4), 04018030.

24. Mu, R., Miao, C., Luo, X., & Sun, W. (2002). Interaction between loading, freeze–thaw cycles, and chloride salt attack of concrete with and without steel fiber reinforcement. Cement and Concrete Research, 32(7), 1061-1066.

25. Naik, T. R., Kraus, R. N., Ramme, B. W., & Chun, Y. M. (2005). Decing Salt-Scaling Resistance: Laboratory and Field Evaluation of Concrete Containing up to 70% Class C and Class F Fly Ash. Journal of ASTM International, 2(7), 1-12.

26. Park, J. J., Yoo, D. Y., Park, G. J., & Kim, S. W. (2017). Feasibility of reducing the fiber content in ultra-high-performance fiber-reinforced concrete under flexure. Materials, 10(2), 118. doi:10.3390/ma10020118

27. Peng, H., Liu, Y., Cai, C. S., Yu, J., & Zhang, J. (2019). Experimental investigation of bond between near-surface-mounted CFRP strips and concrete under freeze-thawing cycling. Journal of Aerospace Engineering, 32(1), 04018125.

28. Peng, Y. Z., Chen, K., & Hu, S. G. (2011). Durability and microstructure of ultra-high performance concrete having high volume of steel slag powder and ultra-fine fly ash. Advanced Materials Research, 255, 452-456.

29. Piérard, J., Dooms, B., & Cauberg, N. (2013, October). Durability evaluation of different types of UHPC. In Proceedings of the RILEM-fib-AFGC International Symposium on Ultra-High Performance Fiber-Reinforced Concrete (pp. 275-284).

30. Ragalwar, K., Heard, W. F., Williams, B. A., & Ranade, R. (2020). Significance of the particle size distribution modulus for strain-hardening-ultra-high performance concrete (SH-UHPC) matrix design. *Construction and Building Materials*, 234, 117423.

31. Smarzewski, P., & Barnat-Hunek, D. (2017). Effect of fiber hybridization on durability related properties of ultra-high performance concrete. International Journal of Concrete Structures and Materials, 11(2), 315-325.

32. Sorelli, L., Constantinides, G., Ulm, F. J., & Toutlemonde, F. (2008). The nano-mechanical signature of ultra high performance concrete by statistical nanoindentation techniques. Cement and Concrete Research, 38(12), 1447-1456.

33. Wang, C., Yang, C., Liu, F., Wan, C., & Pu, X. (2012). Preparation of ultra-high performance concrete with common technology and materials. *Cement and Concrete Composites*, 34(4), 538-544.

34. Wang, Y., An, M. Z., Yu, Z. R., Han, S., & Ji, W. Y. (2017). Durability of reactive powder concrete under chloride-salt freeze–thaw cycling. Materials and Structures, 50(1), 18.

35. Wille, K., Naaman, A. E., & Parra-Montesinos, G. J. (2011). Ultra-High Performance Concrete with Compressive Strength Exceeding 150 MPa (22 ksi): A Simpler Way. *ACI Materials Journal*, 108(1), 46-54.

36. Yalçınkaya, Ç., & Yazıcı, H. (2017). Effects of ambient temperature and relative humidity on early-age shrinkage of UHPC with high-volume mineral admixtures. *Construction and Building Materials*, 144, 252-259.

37. Yang, S. L., Millard, S. G., Soutsos, M. N., Barnett, S. J., & Le, T. T. (2009). Influence of aggregate and curing regime on the mechanical properties of ultra-high performance fibre reinforced concrete (UHPFRC). *Construction and Building Materials*, 23(6), 2291-2298.

38. Yoo, D. Y., Kim, M. J., Kim, S. W., & Park, J. J. (2017). Development of cost effective ultra-high-performance fiber-reinforced concrete using single and hybrid steel fibers. Construction and Building Materials, 150, 383-394.

39. Zhang, P., Li, Q., Chen, Y., Shi, Y., & Ling, Y. F. (2019). Durability of steel fiber-reinforced concrete containing SiO2 Nano-Particles. Materials, 12(13), 2184. doi:10.3390/ma12132184

40. Zollo, R. F. (1997). Fiber-reinforced concrete: an overview after 30 years of development. Cement and concrete composites, 19(2), 107-122.

CHAPTER 5-ABRASION RESISTANCE OF ULTRA-HIGH PERFORMANCE CONCRETE FOR RAILWAY SLEEPERS

Abstract

This study aimed to determine the abrasion resistance of ultra-high performance concretes (UHPCs) for railway sleepers. Test samples were made with different cementitious material combinations and varying steel fiber contents and shapes, using conventional fine aggregate. A total of 25 UHPCs and two high strength concretes (HSCs) were selected to evaluate their depth of wear and bulk properties. The results of the coefficient of variation (CV), relative gain in abrasion, and abrasion index of the studied UHPCs were also obtained and discussed. Furthermore, a comparison was made on the resistance to wear of the selected UHPCs with those of the HSCs typically used for prestressed concrete sleepers. The outcomes of this study revealed that UHPCs displayed excellent resistance against abrasion, well above that of HSCs. Amongst the utilized cementitious material combinations, UHPCs made with silica fume as a partial replacement of cement performed best against abrasion, whereas mixtures containing fly ash showed the highest depth of wear. The addition of steel fibers had a more positive influence on the abrasion resistance than it did on compressive strength of the studied UHPCs.

Keywords: Abrasion resistance; Railway sleeper; Wear; Ultra-high-performance concrete; High strength concrete; Cementitious materials; Steel fiber.

5.1 Introduction

Presently, timber is the most widely used material in producing railway sleepers. Every year, the U.S. replaces approximately 14 million timber sleepers (Railway Technology, 2020). However, timber is susceptible to physical and mechanical degradations that lead to early-age replacements. The scarcity and maintainability of wood as a sleeper material became a problem over time, and many countries needed an alternative material for sleeper production. The new requirements of different codes and standards called for a sleeper element that allowed reliable connectivity for the rail, as well as longer service life and higher lateral track stiffness. Moreover, the loading patterns of a new generation of high-speed railway tracks are different from conventional ones. These new types of railway demand additional features from the rail track system in terms of physical, mechanical, and durability aspects, which timber sleepers lack. In this context, prestressed concrete sleepers have become popular for use in high-speed tracks (Bezgin 2017).

During the early 1960s, when prestressed concrete was adopted by the railway industry, the service life expectancy of prestressed concrete sleepers was about 50 years, which is 20 years more than that of timber sleepers. However, due to the increase in load, speed, and traffic volumes in railway transport systems, prestressed concrete has failed to perform well in many cases (Kaewunruen & Remennikov, 2009; Manalo et al., 2010; Parvez & Foster, 2017; Janeliukstis et al., 2019). As a point of reference, in 1997, about 120,000 concrete sleepers installed by Amtrak lasted only four years before replacements were made (Zeman, 2009). In addition, early deterioration of concrete because of cracking, tensile fracture, low flexural stiffness, and substantial self-weight, as well as its low capacity for rail seat abrasion, has made it challenging for the railway industry to use prestressed concrete as a railway sleeper, especially on high-speed tracks (Ferdous & Manalo, 2014).

Over the last three decades, researchers in different parts of the world have been investigating the failures of concrete sleepers and looking for sustainable solutions. Among many factors that affect the mechanical properties and durability of concrete, one of the common reasons for deterioration is abrasion (Figure 5.1). Most commonly, concrete pavement, railway concrete sleepers, bridge piers, and industrial floors have been severely affected due to abrasion stresses generated from friction, skidding, sliding, or rubbing (Liu, 1981;

Dhir et al., 1991; Remennikov & Kaewunruen, 2014). According to American Society for Testing and Materials (ASTM), abrasion is defined as "physical wear due to hard particles or protuberances forced against and moving a solid interface." American Concrete Institute (ACI) defines abrasion damage as "wearing away of a surface by rubbing and friction" (ACI Manual of Concrete Practice Index, 2015). Per ASTM, abrasion resistance is expressed either in terms of wear index, weight loss, depth of wear, or wear cycles. In prestressed concrete sleepers, failure is caused either by rail-seat abrasion, hydro abrasive erosion, or hydraulic pressure cracking. Rail-seat abrasion occurs due to the relative movements between the rail pad and concrete rail seat, which subsequently result in the gradual wearing away of the cement paste from the concrete by frictional forces. Several factors are responsible for rail-seat abrasion, including (i) water presence, (ii) heavy axle loads, (iii) fastener failure, (iv) shoulders or sleeper pads, (v) steep track gradients, and (vi) track curves greater than two degrees (Reiff et al., 2012; Riding et al., 2019).

Figure 5.1 Prestressed concrete rail seat abrasion (a) Reiff et al. (2012), (b) Zeman et al. (2009)

Resistance to concrete abrasion depends on many factors, including water-to-cementitious materials ratio, compressive strength, aggregate quality, aggregate-paste interface, aggregate fineness, curing, and surface finishing (Smith, 1958; Li & Zhou, 2011). Over the years, a number of researches have addressed concrete pavement, sleeper, and bridge deterioration due to surface wear (Li & Ou, 2006; Yoshitake et al., 2016; Scott & Safiuddin, 2015; Ngamkhanong et al., 2017; Ngamkhanong et al., 2019; Li et al., 2017; You et al., 2019; Kernes et al., 2014; Kaewunruen et al., 2017). Ghafoori and Sukandar (1995) stated that the testing condition had more impact on abrasion resistance than the strength of concrete. Naik et al. (2002) observed that for high-strength concrete, up to 30% of class C fly ash replacement gave similar abrasion resistance compared to concrete without fly ash. Additionally, Atis (2002) concluded that the presence of fly ash improved the micromorphology of calcium-silicate-hydrate (C-S-H) gel, which resulted in enhanced cohesion between aggregate and paste, and improvement in abrasion resistance. Further, Siddique (2003) replaced fine aggregate with up to 40% class F fly ash and found that 40% improvement in abrasion resistance. In another study, Ghafoori and Diawara (2007) showed increases in abrasion resistance by incorporating up to 10% silica fume in the concrete as a partial replacement of fine aggregate. Later, Ghafoori et al. (2015) reported that self-compacting concrete performed better than the conventional vibratory placed concrete in resisting abrasion. They also investigated the effect of the cement content and water-to cementitious materials ratio, and concluded that an increase of cement content and a decrease of water-to-cement ratio improved abrasion resistance (Ghafoori et al., 2014; Ghafoori et al., 2015). Another investigation done by Ghafoori and Dutta (1995) showed that a higher aggregate-cement ratio reduced resistance to abrasion, and that compaction energy played important role in resisting concrete wear. In other research, Sadegzadeh et al. (1987) studied the influence of various surface finishing techniques on wear resistance, and identified that the near surface porosity of concrete controlled its wear performance. Additionally, Nanni (1989) concluded that the moisture condition of concrete's surface had a significant effect on abrasion performance.

Ngamkhanong et al. (2017) studied the effect of surface abrasion on the impact capacity of prestressed concrete sleepers. They concluded that surface abrasion reduced the moment capacity of the studied

sleepers. Ngamkhanong et al. (2019) further concluded that surface abrasion reduced the strength and impact capacity of concrete sleepers. Another study by Li et al. (2017) showed that abrasion at the rail seat had less influence on creep and shrinkage than it did on the bottom of a sleeper. Later, You et al. (2019) concluded that increases in concrete's tensile strength also increased the cracking load capacity of railway sleepers, whilst ultimate load capacity remained unchanged. Then Kernes et al. (2014) improved the abrasion performance of concrete sleepers by grinding off the top mortar paste layer. Although many studies tried to minimize or solve the problem of concrete deterioration caused by abrasion, it still remains a major concern for prestressed concrete sleeper abrasion performance.

According to the Portland Cement Association (PCA, 2020), "Ultra-high performance concrete (UHPC) is a concrete material that has a minimum specified compressive strength of 120 MPa with specified durability, tensile ductility, and toughness requirements; fiber are generally included in the mixture to achieve specified requirements." Because of the very high production costs, which are about 10 to 20 times higher than the conventional concrete (Yang et al., 2009; Ragalwar et al., 2020), only a few proprietary mixtures have been used by different researchers in the assessment of UHPC properties. To compensate for the very high production cost of UHPCs, Karim et al. (2019) used masonry sand in place of expensive quartz sand and compared the results with those of the proprietary UHPCs. Further, Arora et al. (2019) combined coarse and fine aggregates using a compressible packing model to achieve a compressive strength of 150 MPa. To reduce the total cost, Yang et al. (2019) utilized supplementary cementitious material such as fly ash and slag as a partial replacement of cement. Meng et al. (2017) employed hybrid fibers and evaluated the fresh and mechanical properties of non-proprietary UHPCs. In another study, Zmetra et al. (2017) used UHPC to repair an existing bridge girder and reported that successful restoration of the damaged section. The superior strength and improved longevity potential of UHPC can increase the targeted lifespan of the concrete structure significantly with minimum maintenance costs, thus compensating for its initial production cost.

While there has been growing attention to UHPCs' fresh and mechanical properties, there have been limited published studies on their abrasion resistance (Table 5.1). In one study, Graybeal and Tanesi (2007) used ASTM C 944 to determine the abrasion resistance of UHPCs by measuring the amount of concrete abraded off from the concrete's surface. They found that steam-treated UHPC significantly enhanced the wear resistance, as compared to that of customarily cured samples. However, their testing was limited to only 400 revolutions. Further, Zhao et al. (2017) utilized the nano-scratch test, as per BS 812-113, to evaluate wear performance of UHPC, and compared it with high performance concrete (HPC). They concluded that UHPC showed a 50% higher abrasion resistance than that of HPC. Additionally, Pyo et al. (2018) compared the effect of aggregate type and size on abrasion resistance, and found that the UHPCs made with coarser aggregates produced lower abrasion resistance than the UHPCs batched with finer aggregate sizes.

Table 5.1 Studies on UHPC abrasion

Ref.	Variations	Binder composition	Test details	No. of revolution	$f'c$ (MPa)	Depth of abrasion (mm)	Mass loss (g)
Pyo et al. (2018)	SN1.5[a] SD1.5[a] SB1.5[a] HSC	1C, 0.05-0.25SF[c]; 0-1.5% steel fiber; w/c=0.22-0.30	ASTM C 944: Load- 44 lb, 200 rpm[e]	16000	161 151 130 67.8	0.23 0.39 0.43 2	2.5 4.05 4.87 2[f]
Zhao et al. (2017)	UHPC HPC[b]	415-520C, 0-160F,0-120SF[d]; 0-1% steel fiber; w/c=0.20	BS 812-113: Load- 4.4 lb, 60 rpm[e]	6000		1.9 3.1	

96

Graybeal and Tanesi (2007)	UHPC	712C, 231SF[d]; 2% steel fiber; w/c=0.20	ASTM C 944: Load-44 lb, 200 rpm[f]	400	1

Note: [a]SN-River sand (no coarse aggregate), SD-Dolomite and river sand, SB-Basalt and river sand; [b]HPC-High-performance concrete; [c]volume fraction; [d]weight (kg/m³ of concrete); [e]rpm-revolution per minute; [f]at 4000 revolution

Amongst the past studies, no investigation has focused on the abrasion resistance of UHPCs for railway sleepers. To this end, the purpose of this study was: (1) to determine the abrasion resistance of selected UHPCs made with different cementitious material combinations, and varying steel fiber contents and shapes; (2) to ascertain the parameters influencing the wear resistance of UHPCs; and (3) to compare the resistance to wear of the studied UHPCs with those of the high strength concrete (HSC) typically used in the production of railway sleepers.

5.2 Experimental Program

5.2.1 Materials

In the production of the UHPC mixtures, ASTM Type V Portland cement, class F fly ash, and silica fume were used as cementitious materials. The chemical characteristics of the cementitious materials are presented in Table 5.2. Two types of locally produced fine aggregates were used. Their size gradation varied from 0.075 mm to 4.75 mm. To achieve the maximum packing density with the minimum porosity, a uniquely size-graded manufactured fine aggregate was determined. To this end, the relative density was measured for the graded aggregates at different distribution moduli (0.20-0.25), using the modified Andreasen and Andersen model. Maximum packing density was obtained from the distribution modulus of 0.21. The gradation of the fine aggregate is given in Table 5.3. The combined fine aggregates had specific gravity of 2.80 and water absorption of 0.45%.

To observe the effects of fiber shape, two types of low carbon steel fiber (straight and hooked), with the aspect ratio of 43, were incorporated into the total volume of concrete. A commercially available polycarboxylate-based high-range water-reducing admixture (HRWRA) was used to achieve the desired flowability of the studied UHPCs. To produce HSCs, ASTM Type V Portland cement and locally available fine and coarse aggregates were used. The fine aggregate had specific gravity of 2.78 and water absorption of 0.81%, whereas the coarse aggregate had specific gravity of 2.76 and water absorption of 0.82%. Both fine and coarse aggregate complied with the ASTM C33 gradation requirements.

Table 5.2 Chemical compositions of UHPC and HSC cementitious materials (percentage mass)

Composition	Type V cement (%)	Class F fly ash (%)	Silica fume (%)
SiO_2	21	59.93	94.72
CaO	62.4	4.67	-
Al_2O_3	4	22.22	-
Fe_2O_3	3.7	5.16	-
MgO	2.6	-	-
SO_3	2.2	0.38	0.23
$Na_2O + K_2O$	0.54	1.29	0.47
Loss on Ignition (LOI)	2.0	0.32	2.82

Table 5.3 Aggregate gradation of UHPCs as per modified Andreasen and Andersen model

Sieve no.	Sieve opening (mm)	Percentage retained
#8	2.38	23.5

#16	1.19	20.1
#30	0.595	17.0
#50	0.297	15.1
#100	0.149	13.0
#200	0.074	11.3

5.2.2 Mixture Proportions of UHPCs and HSCs

A total of 25 UHPCs and two HSCs were used to determine their abrasion resistance through depth of wear. The unit content of the mixture constituents of the selected UHPCs and HSCs is given in Table 5.4. To observe the effect of secondary cementitious materials, cement was replaced with 20 and 30% class F fly ash; 5% silica fume; and combined 15% fly ash and 5% silica fume, in addition to the control UHPC (100% cement). The water-to-cementitious materials ratio of 0.21 remained constant for all UHPCs. The actual water content of the UHPCs varied because of the variation in the HRWRA dosage percentage. The dosage of HRWRA varied from 10.1 to 14.3 kg/m^3 depending on the cementitious material combination and the percentage of steel fiber used. The UHPCs with steel fiber and silica fume required higher amounts of HRWRA in order to maintain the desired flowability. Two types of steel fibers, hooked and straight, were used at the levels of 2 and 3% of the total volume of concrete.

For the studied high-strength concretes (HSCs), representing the typical concretes used in prestressing railway sleepers, two cement contents of 445 and 564 kg/m^3, HSC1 and HSC2, respectively, were used. The water-to-cement ratio was kept constant at 0.275. To accelerate the hydration process of HSCs, a 2% non-chloride accelerating admixture was used, in addition to the HRWRA. A constant workability of 125±25 mm was maintained for the studied HSCs.

Table 5.4 Mixture proportion of UHPCs and HSCs

Mixture designation[a]	C[b]	F[b]	SF[b]	FA[b]	CA[b]	HRWRA[b]	w/cm	W[b]	Steel Fibers	Flow (mm)	Unit weight (kg/m^3)
						kg/m^3					
C100	1101	-	-	1174	-	12.1	0.21	226	-	248	2470
C100-H2%	1101	-	-	1174	-	13.2	0.21	226	156	241	2536
C100-S2%	1101	-	-	1174	-	13.2	0.21	226	156	256	2531
C100-H3%	1101	-	-	1174	-	14.3	0.21	225	234	251	2585
C100-S3%	1101	-		1174	-	14.3	0.21	225	234	271	2592
SF5	1046	-	39	1174	-	12	0.21	215	-	273	2451
SF5-H2%	1046	-	39	1174	-	13.1	0.21	214	156	247	2512
SF5-S2%	1046	-	39	1174	-	13.1	0.21	214	156	240	2506
SF5-H3%	1046	-	39	1174	-	14.1	0.21	214	234	255	2551
SF5-S3%	1046	-	39	1174	-	14.1	0.21	214	234	250	2583
F20	881	163	-	1174	-	11	0.21	215	-	270	2405
F20-H2%	881	163	-	1174	-	12	0.21	215	156	271	2475
F20-S2%	881	163	-	1174	-	12	0.21	215	156	247	2491
F20-H3%	881	163	-	1174	-	13	0.21	214	234	240	2540
F20-S3%	881	163	-	1174	-	13	0.21	214	234	255	2543
F30	771	244	-	1174	-	10.1	0.21	210	-	250	2374
F30-H2%	771	244	-	1174	-	11.2	0.21	209	156	269	2440
F30-S2%	771	244	-	1174	-	11.2	0.21	209	156	270	2446
F30-H3%	771	244	-	1174	-	12.2	0.21	208	234	246	2498
F30-S3%	771	244	-	1174	-	12.2	0.21	208	234	238	2506
F15SF5	881	122	39	1174	-	11.5	0.21	214	-	253	2388
F15SF5-H2%	881	122	39	1174	-	12.5	0.21	214	156	248	2483
F15SF5-S2%	881	122	39	1174	-	12.5	0.21	214	156	264	2490

Mixture designation[a]	C[b]	F[b]	SF[b]	FA[b]	CA[b]	HRWRA[b]	w/cm	W[b]	Steel Fibers	Flow (mm)	Unit weight *(kg/m³)*
					kg/m³						
F15SF5-H3%	881	122	39	1174	-	13.5	0.21	213	234	265	2535
F15SF5-S3%	881	122	39	1174	-	13.5	0.21	213	234	243	2535
HSC1	386	-	-	933	1040	3.2	0.275	103	-	-	-
HSC2	504	-	-	846	1034	2.5	0.275	136	-	-	-

Note: 1 kg/m³ = 1.685 lb/yd³
[a] C100: 100% Cement; SF5: 95% cement and 5% silica fume; F20: 80% cement and 20% class F fly ash; F30: 70% cement and 30% class F fly ash; F15SF5: 80% cement and 15% class F fly ash and 5% silica fume; S2% and S3% represents 2% and 3% straight steel fibers; H2% and H3% represents 2% and 3% hooked steel fibers.
[b] C: Cement; F: Class F fly ash; SF: Silica fume; HRWRA: High-range water reducing admixture; CA: Coarse aggregate; FA: Fine aggregate; W: Actual water.

5.2.3 Mixing, Sampling, Curing, and Testing

Due to the high quantity of small-sized particles, coupled with the low water-to-cementitious materials ratio and addition of steel fibers, a longer mixing time and higher energy were required for the production of UHPCs, as compared to traditional concrete. The mixing time, mixing speed, mixing sequence, temperature, and relative humidity were closely monitored and uniformly maintained. In this study, the UHPCs' dry cementitious materials were first mixed for five minutes in a Hobert-type mixing machine. To reduce agglomeration of particles, fine aggregates were slowly added, and the combined materials were dry-mixed for another five minutes. Afterwards, nearly 90% of the mixing water was added and mixed for a period of five minutes before the remainder of water and HRWRA were added. Finally, steel fibers were slowly introduced to the matrix, and mixing continued for additional three to five minutes until a well-dispersed mixture was attained. The flow properties of the studied UHPCs were evaluated according to the ASTM C230 (as all the UHPCs were self-compacting, 25 drops of blow were skipped) before they were poured into cylinders (50 mm diameter and 100 mm height) and cubes (300 x 300 x 300 mm). The specimens were kept for 24 hours in a controlled, moist curing room at $22 \pm 3°C$ and 95% relative humidity. After 24 hours, specimens were demolded and returned to the moisture room for an additional 27 days.

A pan-style counter-current mixer was used to batch the studied HSCs. After pouring freshly-mixed concrete into the molds, specimens were densified using a vibrating table. The curing method and duration used for the HSCs were similar to those of the UHPCs.

The 28-day cured UHPCs and HSCs were tested for compressive strength, splitting-tensile resistance, and abrasion resistance as per ASTM C39, ASTM C496, and ASTM C779 (Procedure C, ball bearings), respectively. The UHPCs elastic modulus was measured as per ASTM C469. The adopted abrasion test was used to simulate high contact stresses, impact, and sliding friction. This method simulates traffic wear and extreme weather conditions, thus making it suitable for UHPC applications. Moreover, AREMA recommends that the ASTM C779 procedure C should be used to ascertain the abrasion performance of railway sleeper (2009). The abrasion test setup is shown in Figure 5.2. The apparatus consisted of 12 equally spaced 18-mm diameter steel balls inside a bearing plate. A continuous water flow was maintained during testing to remove abraded particles. The depth of abrasion was measured using a dial gauge that could read to the nearest 0.025 mm. The abrasion resistance was evaluated every 30 seconds for 20 minutes of testing or until a 3.0 mm depth of wear was reached.
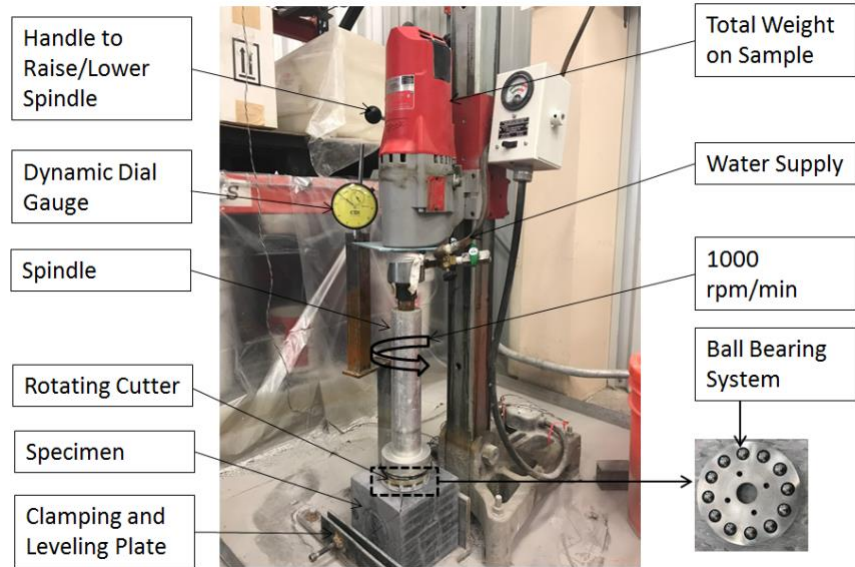
Figure 5.2 Abrasion test setup in accordance with ASTM C 779, Procedure C, ball bearings

5.3 Results and Discussion

5.3.1 Fresh and Bulk Properties of UHPCs and HSCs

The characteristics of the UHPCs' fresh properties are summarized in Table 5.4. The mini-slump flow was measured immediately upon completion of mixing. A satisfactory flow spread diameter of 250±25 mm was attained for all studied UHPCs. As can be seen in Table 5.4, the demolded unit weight of the UHPCs varied from 2374 to 2592 kg/m^3. The presence of steel fiber increased the unit weight of the studied UHPCs.

The compressive strengths of the studied UHPCs and HSCs are presented in Figure 5.3. The 28-day cured silica fume containing UHPCs provided a slightly better compressive strength than the 28-day cured fly ash containing mixtures due to their higher reactivity during that curing period. Overall, the compressive strength of UHPCs improved marginally with the introduction of steel fiber, with a similar result for both straight and hooked fibers. The mixtures with 2% hooked or straight fibers experienced a small increase of 2 to 8% in compressive strength, in comparison with the companion plain UHPCs. A slightly higher increment (4 to 13%) was found for the mixtures with 3% steel fibers. The minor improvement in compressive strength maybe attributed to the enhanced micro-crack arrest when fibers were used. As can be seen in Figure 5.3, an increase in cement content from 386 to 504 kg/m^3 resulted in a nearly 10% improvement in the compressive strength of the studied HSCs. When compared to the plain UHPC (C100), HSC1 and HSC2 produced 33 and 26% lower compressive strengths, respectively.
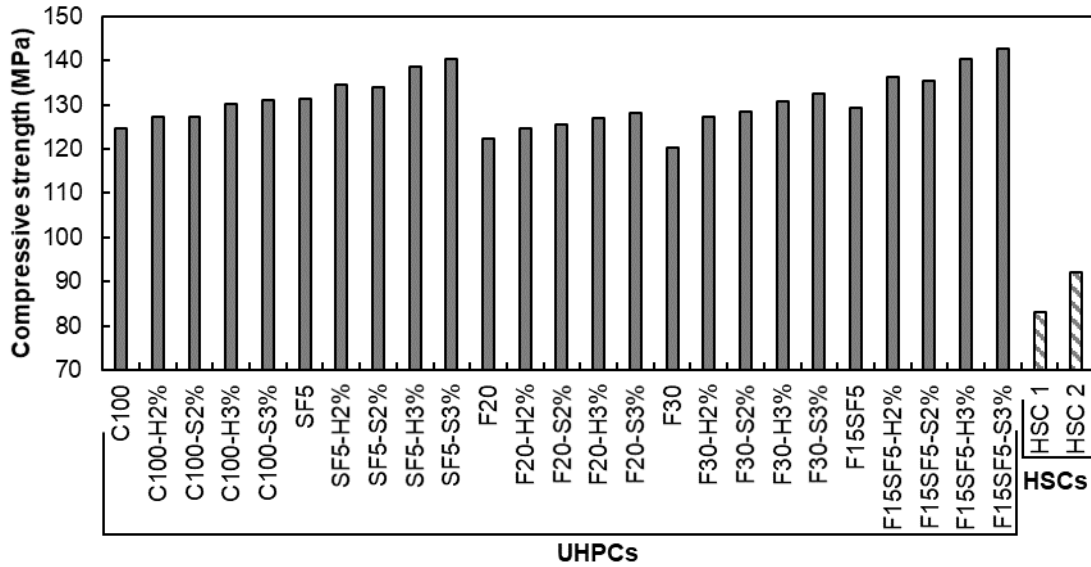
Figure 5.3 Compressive strength of the studied UHPCs and HSCs

Figure 5.4 shows the 28-day splitting-tensile strength of the studied plain and fiber-reinforced UHPCs using different cementitious materials combinations. The average splitting-tensile strength of the studied UHPCs varied from 8.8 to 13.1 MPa. The UHPCs containing silica fume as a partial replacement of cement performed best amongst the studied mixtures. The incorporation of steel fibers significantly improved the splitting-tensile strength of the studied UHPCs. The addition of 2% hooked steel fiber resulted in a 17% improvement in splitting-tensile strength, as compared to that of the companion plain UHPC. With the introduction of 3% hooked fiber, the corresponding gain in the average splitting-tensile strength was nearly 37%. In comparison, test specimens having 2 and 3% straight fibers increased their average splitting-tensile strengths by 18 and 38%, respectively. This can be attributed to the anticipated increase in the matrix stiffness of the fiber-reinforced UHPCs. Additionally, steel fibers managed to distribute localized stress to the surrounding concrete and acted as a crack arrester.

As presented in Figure 5.4, HSCs show, on average, 42% lower splitting-tensile strength as compared to that of the plain UHPC (C100). This can be attributed to a lower cementitious materials content and higher water-to-cementitious materials ratio, as well as the presence of coarse aggregates, along with variation of the physical properties of the coarse and fine aggregates of the studied HSCs. Once steel fibers were added, the fiber-reinforced UHPC (C100) produced an average 54% higher splitting-tensile resistance than that of the studied HSCs.

Figure 5.4 Splitting-tensile strength of the studied UHPCs and HSCs

Figure 5.5 represents the 28-day elastic moduli of the UHPCs. As can be seen, fibers had minimal effects on the elastic moduli of the studied UHPCs. When comparing fiber-reinforced UHPCs to plain UHPCs, the inclusion of 2 and 3% hooked steel fibers resulted in average elastic moduli increases of 3 and 6%, respectively. In comparison, the improvements in the elastic moduli of the UHPCs made with 2 and 3% straight steel fibers were 4 and 8%, respectively. As can be seen in Figure 5.5, the elastic moduli of the studied HSCs were found to be nearly 3% lower than the plain UHPC (C100).
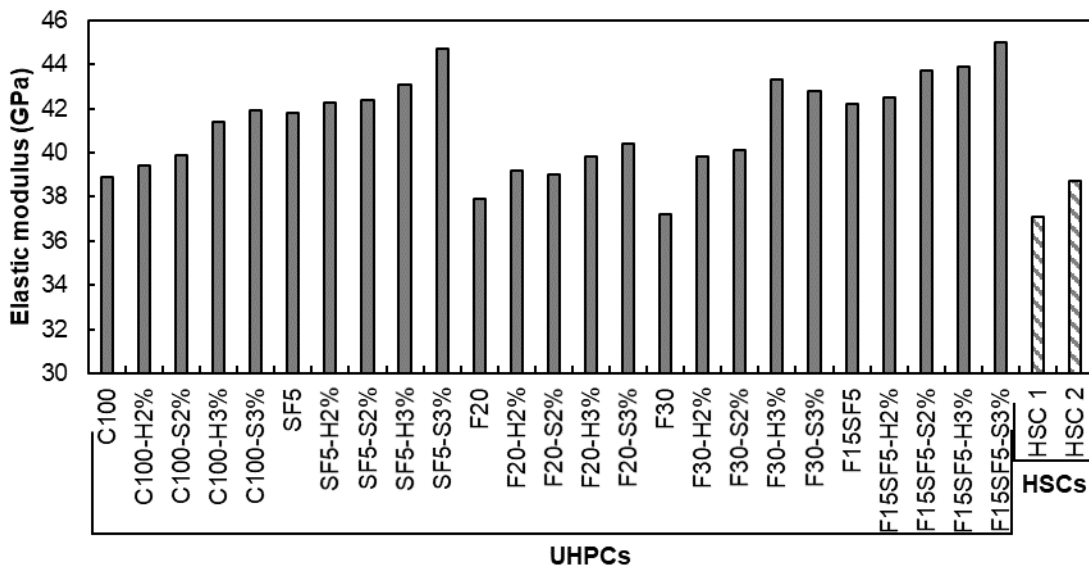
Figure 5.5 Elastic modulus of the studied UHPCs and HSCs

102

5.3.2 Resistance to Wear of UHPCs

The results of abrasion depth for the studied UHPCs, as varied by cementitious material combinations and steel fiber content and type, at different time intervals are presented in Table 5.5. The ultimate depth of abrasion varied from 0.43 to 0.65 mm, reflecting the high surface quality of the studied UHPCs. The influence of cementitious material combinations, steel fiber content, and steel fiber shape on the resistance to wear of the studied UHPCs are discussed in the sections to follow. Additionally, the results of coefficient of variation (CV) and relative gain in abrasion, along with the abrasion index (AI) and concrete surface conditions after the abrasion tests of the studied UHPCs are presented and discussed.

Table 5.5 Depth of wear at different time intervals

Mixture Designation	Depth of wear at various time interval (min)					
	1	2	5	10	15	20
C100	0.12	0.20	0.40	0.53	0.57	0.59
C100-H2%	0.10	0.19	0.32	0.46	0.49	0.51
C100-S2%	0.10	0.18	0.30	0.42	0.46	0.49
C100-H3%	0.09	0.16	0.29	0.40	0.44	0.45
C100-S3%	0.09	0.15	0.28	0.40	0.43	0.45
SF5	0.07	0.12	0.27	0.43	0.50	0.55
SF5-H2%	0.07	0.11	0.26	0.38	0.43	0.48
SF5-S2%	0.06	0.09	0.24	0.37	0.43	0.48
SF5-H3%	0.05	0.09	0.23	0.35	0.41	0.43
SF5-S3%	0.04	0.08	0.22	0.35	0.40	0.43
F20	0.10	0.20	0.46	0.58	0.62	0.65
F20-H2%	0.07	0.15	0.35	0.49	0.52	0.54
F20-S2%	0.07	0.15	0.34	0.46	0.50	0.52
F20-H3%	0.06	0.11	0.27	0.39	0.44	0.46
F20-S3%	0.06	0.12	0.28	0.38	0.43	0.46
F30	0.08	0.15	0.31	0.51	0.60	0.63
F30-H2%	0.08	0.13	0.29	0.43	0.48	0.53
F30-S2%	0.06	0.11	0.26	0.39	0.46	0.51
F30-H3%	0.05	0.10	0.24	0.36	0.41	0.45
F30-S3%	0.05	0.09	0.23	0.34	0.40	0.45
F15SF5	0.07	0.15	0.35	0.49	0.52	0.54
F15SF5-H2%	0.07	0.15	0.30	0.42	0.46	0.48
F15SF5-S2%	0.07	0.14	0.31	0.46	0.48	0.50
F15SF5-H3%	0.07	0.12	0.27	0.36	0.42	0.44
F15SF5-S3%	0.05	0.10	0.24	0.36	0.41	0.43

1 mm = 0.0394 in.

5.3.2.1 Influence of Cementitious Materials Combinations

A typical depth of wear of the plain UHPCs as a function of time is shown in Figure 5.6. From Table 5.5 and Figure 5.6, the following observations can be made:

- UHPCs containing fly ash replacing 20 or 30% Portland cement showed the lowest abrasion resistance after 20 minutes of testing. The presence of fly ash delayed the strength development of the 28-day cured UHPCs, and made them comparatively weaker in resisting wear. A comparison between UHPCs F20 and F30 showed a slightly higher depth of wear for up to 12 minutes of the testing. Afterwards, UHPC F20 displayed a slightly lower depth of wear, compared to that of the UHPC F30. This finding may be attributed to the higher coefficient of variation displayed by the

103

UHPC F20, as compared to that of the UHPC F30, during the initial period of testing. As testing progressed, this trend reversed itself, resulting in a marginally lower depth of wear for UHPC F20.

- In contrast, the UHPCs made with silica fume displayed the lowest abrasion depth, as silica fume produced more cementitious activities during the 28-day curing period, resulting in the UHPCs with denser and stronger microstructures.
- With increases in time, the rate of abrasion decreased. A major change in the rate of abrasion occurred at about five minutes of testing.
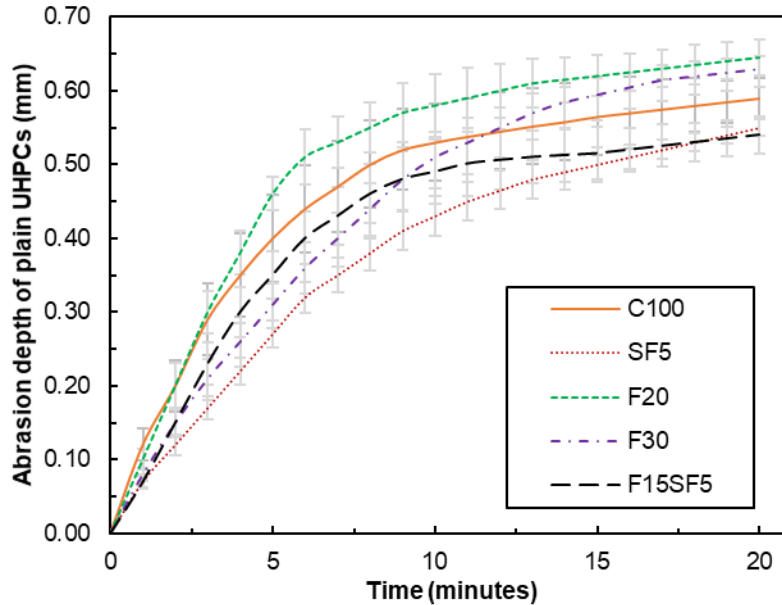
Figure 5.6 Depth of wear of plain UHPCs as a function of time

5.3.2.2 Influence of Steel Fiber Content and Shape

The abrasion resistances of the UHPCs containing 2 and 3% hooked and straight fibers are documented in Table 5.5. In general, the introduction of fibers improved the abrasion resistance of the studied UHPCs, and the UHPCs made with 3% steel fibers produced lower abrasion depths, as compared to the companion UHPCs containing 2% steel fibers. When 2% hooked steel fiber was added, after 20 minutes of testing, the resistance to abrasion improved by 10, 13, 16, 16, and 9% for the mixtures C100, SF5, F20, F30, and F15SF5, respectively. With the introduction of 3% hooked fiber, the corresponding gains in abrasion resistance were 23, 22, 29, 29, and 20%, respectively, for the same cementitious materials combinations. In comparison, test samples containing 2% straight fibers increased abrasion resistance by 18, 14, 19, 19, and 7%, respectively. The improvements in abrasion of the UHPCs containing 3% straight steel fibers were nearly identical to those of the companion mixtures made with 3% straight fiber.

Overall, hooked fibers increased the abrasion resistance of the studied UHPCs by 15 and 26% for 2 and 3% volumetric contents, respectively, when compared with those of the companion plain UHPCs (Figure 5.7a). Once straight fibers were used, the resistance to wear increased by 17% and 27%, respectively (Figure 5.7b). The reduction in the depth of wear, with increases in fiber content, can be attributed to the anticipated increase in the matrix stiffness of the fiber-containing UHPCs. Depth of wear relationships between plain and fiber-reinforced UHPCs, having coefficient of determination (R^2) values greater than 0.97 at 95% confidence level, are documented in Figure 5.7.
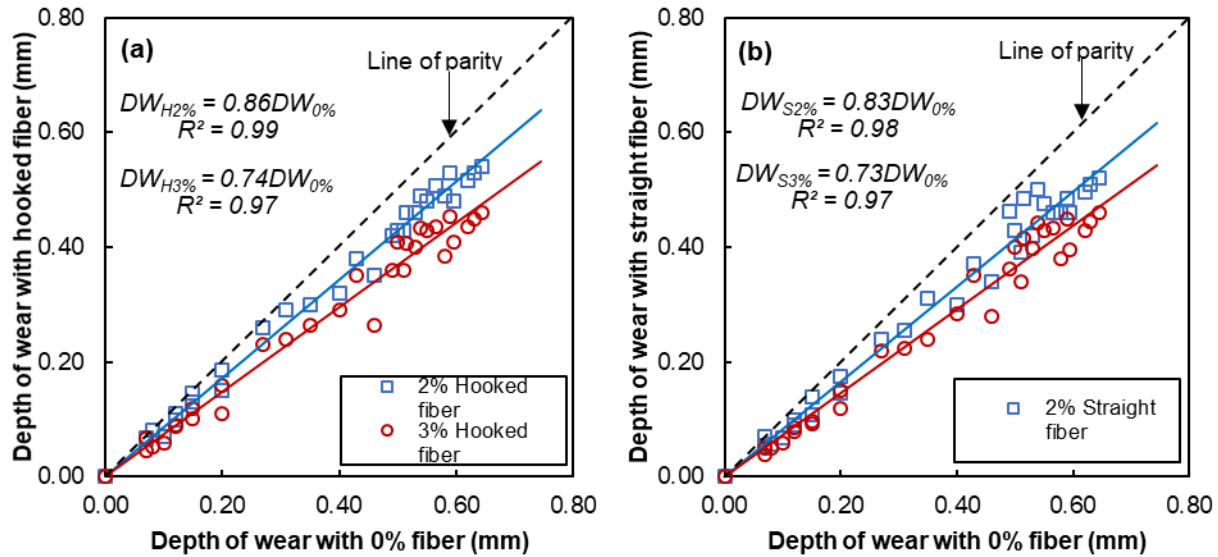
Figure 5.7 Effect of steel fiber content on the depth of wear (a) effect of hooked fiber, (b) effect of straight fiber

The effect of fiber shape on the depth of wear of the studied UHPCs is presented in Figure 5.8. From the parity plot, it can be seen that the shape of fiber had negligible influence on abrasion resistance. Mixtures containing 2% and 3% straight fibers showed 4% and 1% increases in abrasion resistance, respectively, when compared with the companion UHPCs made with hooked fibers. Correlations between straight and hooked fibers, as shown in Figure 5.8, stood at the R^2 values of 0.98 and 0.99, respectively.

The addition of 2 and 3% steel fibers to the studied UHPCs resulted in average increases in compressive strengths of 3 and 7%, respectively, when compared to those of the plain UHPCs. In comparison, the improvements in the abrasion resistances of the UHPCs made with 2 and 3% steel fibers were 15 and 24%, respectively. These observations portray that the addition of steel fibers had more influence on the wear resistance than it did on the compressive strengths of the studied UHPCs.
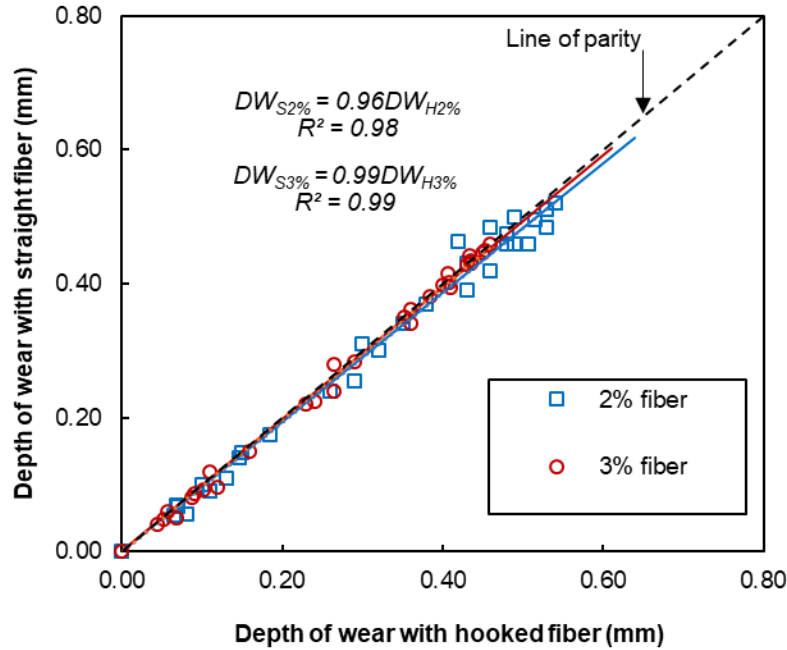
Figure 5.8 Effect of steel fiber shape on depth of wear

To determine the relative gain of abrasion depth of the studied UHPCs with respect to the testing duration, abrasion depth ratios at 1.0, 2.0, 5.0, 10.0, and 15.0 minutes to the 20 minutes depth of wear were determined by dividing the abrasion at the time t to the final abrasion depth. The relative gains in abrasion are shown in Table 5.6 and Figure 5.9. The rate of abrasion gain reduced with the testing duration. Moreover, all studied UHPCs attained nearly 85% of their ultimate depth of wear in the first 10 minutes of testing. The relative gains in abrasion remained independent of cementitious materials compositions, steel fiber content (2% and 3% fiber), and steel fiber shape (hooked and straight). The UHPCs without fibers produced average relative gains of 15, 28, 60, 86, and 95% after 1.0, 2.0, 5.0, 10.0, and 15.0 mins., respectively. In comparison, fiber-reinforced UHPCs showed average relative gains of 14, 26, 58, 84, and 93% at the same time intervals. The higher initial gains in wear of the studied UHPCs can be attributed to the higher concentrations of abrasive force, due to the smaller ball bearing contact surface, as well as lower surface stiffness of the top mortar paste layer.

Table 5.6 Relative gain of abrasion depth of UHPC mixture at 28 days

Mixture designation	Rate of wear of UHPCs at various testing time (min)					
	1	2	5	10	15	20
C100	0.20	0.34	0.68	0.90	0.96	1.00
C100-H2%	0.19	0.35	0.60	0.87	0.96	1.00
C100-S2%	0.21	0.36	0.62	0.87	0.95	1.00
C100-H3%	0.20	0.35	0.64	0.88	0.96	1.00
C100-S3%	0.19	0.33	0.63	0.88	0.96	1.00
SF5	0.13	0.22	0.49	0.78	0.91	1.00
SF5-H2%	0.14	0.23	0.54	0.79	0.90	1.00
SF5-S2%	0.12	0.19	0.51	0.78	0.91	1.00
SF5-H3%	0.10	0.20	0.53	0.82	0.95	1.00
SF5-S3%	0.09	0.19	0.51	0.82	0.93	1.00
F20	0.16	0.31	0.71	0.90	0.96	1.00
F20-H2%	0.13	0.28	0.65	0.91	0.95	1.00

F20-S2%	0.13	0.28	0.65	0.88	0.95	1.00
F20-H3%	0.13	0.24	0.58	0.84	0.95	1.00
F20-S3%	0.13	0.26	0.61	0.83	0.93	1.00
F30	0.13	0.24	0.49	0.81	0.94	1.00
F30-H2%	0.15	0.25	0.55	0.81	0.91	1.00
F30-S2%	0.11	0.21	0.50	0.76	0.90	1.00
F30-H3%	0.12	0.23	0.53	0.80	0.91	1.00
F30-S3%	0.11	0.21	0.51	0.76	0.89	1.00
F15SF5	0.13	0.28	0.65	0.91	0.95	1.00
F15SF5-H2%	0.14	0.30	0.61	0.86	0.94	1.00
F15SF5-S2%	0.14	0.28	0.62	0.93	0.97	1.00
F15SF5-H3%	0.16	0.28	0.61	0.83	0.94	1.00
F15SF5-S3%	0.20	0.34	0.68	0.90	0.96	1.00
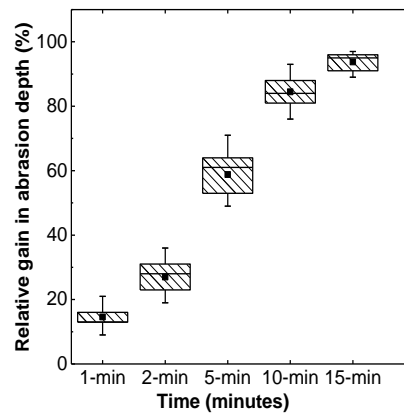
Figure 5.9 Relative gain of abrasion depth as a function of time

5.3.2.3 Coefficient of Variation (CV)

The concrete surfaces in contact with the molds (4 surfaces) were tested to ascertain the acceptability of the test results. Following each abrasion test, the abrasion path of the test specimen was carefully examined, and when the abrasion path was not uniform, the result was discarded. Table 5.7 and Figure 5.10 present the coefficients of variations (CV) of the abrasion depth after 1.0, 2.0, 5.0, 10.0, 15 and 20.0 minutes. During the initial testing period, a fully leveled-seating of the abrasion apparatus on the concrete surface could not be achieved, resulting in higher CVs. With progress in testing, a more uniform concrete path was developed, and lower than 10% CVs were observed for most of the studied UHPCs after testing durations of 20 minutes. On average, the CVs for the plain UHPCs were 27, 18, 15, 12, and 7% after 1.0, 5.0, 10.0, 15 and 20.0 minutes of testing, respectively. In comparison to the plain UHPCs, the fiber-reinforced mixtures displayed higher CVs at the levels of 36, 23, 17, 12, and 9%, respectively, for the same time intervals.

Table 5.7 Coefficient of variation (CV) for abrasion test of UHPC mixtures

Mixture designation	CV for wear test of UHPCs at various testing time (min)					
	1	2	5	10	15	20
C100	36.42	34.86	29.35	19.45	18.63	8.97
C100-H2%	42.68	36.32	31.54	20.46	22.39	10.73
C100-S2%	38.03	19.31	15.25	16.24	12.70	9.01
C100-H3%	47.59	37.54	27.23	21.59	16.54	11.61
C100-S3%	46.37	35.20	18.07	6.40	6.94	5.93
SF5	23.18	22.93	13.49	12.39	9.54	3.97
SF5-H2%	25.63	24.82	17.32	16.30	12.61	8.56
SF5-S2%	38.20	43.21	16.74	15.95	9.83	5.55
SF5-H3%	29.32	33.52	20.05	19.32	11.75	10.61
SF5-S3%	26.84	17.81	18.00	16.87	10.04	7.59
F20	28.39	31.20	9.97	14.58	8.94	7.52
F20-H2%	34.00	31.87	35.43	16.32	7.89	8.35
F20-S2%	19.32	21.57	18.41	10.35	6.84	8.16
F20-H3%	48.21	36.04	33.21	14.86	12.73	8.83
F20-S3%	42.62	32.19	27.58	16.41	13.52	8.27
F30	21.20	23.24	18.17	13.52	7.51	5.50
F30-H2%	31.78	25.64	26.94	19.47	16.31	12.14
F30-S2%	33.42	19.63	21.42	13.54	9.62	8.17
F30-H3%	41.47	38.21	32.14	18.92	17.52	12.41
F30-S3%	45.21	36.07	21.57	20.79	12.64	11.42
F15SF5	27.58	26.71	18.64	17.54	13.57	9.21
F15SF5-H2%	40.11	45.37	17.58	16.75	10.32	5.83
F15SF5-S2%	31.96	36.54	21.85	21.06	12.81	11.56
F15SF5-H3%	28.85	32.98	19.73	19.01	11.56	10.44
F15SF5-S3%	26.17	17.36	17.55	16.45	9.79	7.40
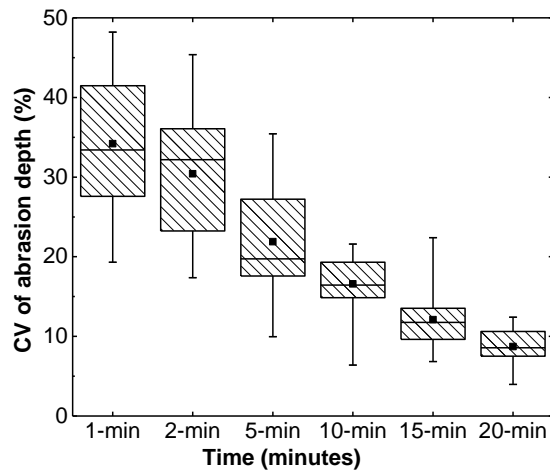
Figure 5.10 Coefficient of variation of abrasion depth of the studied UHPCs as a function of time

5.3.2.4 Abrasion Index

108

An abrasion index (*AI*) was also used to examine the resistance to wear of the studied UHPCs. The index of *AI* was calculated using the following formula (Smith, 1958):

$$AI = \frac{\sqrt{R}}{P} \qquad (5.1)$$

where *AI* is abrasion index, *R* is the ball race revolution (in thousands), and *P* is the depth of abrasion (in mm or in.).

Based on the results presented in Table 5.8 and Figure 5.11, several observations can be made:
- Due to their strong microstructures, the studied UHPCs produced very high abrasion indices. As a reference, the accepted AI for roadways and industrial settings is 1.20.
- The UHPCs made with 5% silica fume, as a replacement of total cementitious materials, showed the highest abrasion indices, whereas UHPCs containing fly ash produced the contrary.
- On average, UHPCs at 20-min testing duration displayed 7 and 15% higher AIs, as compared to those of the 10- and 15-min testing durations, respectively.
- The addition of steel fibers had a positive impact on the abrasion indices of the studied UHPCs. The inclusion of steel fibers increased AI by 22% on average, as compared to that of the plain UHPCs. The abrasion indices also improved with increases in fiber content from 2 to 3% (6% improvement).

Table 5.8 Abrasion index of UHPCs

Mixture Designation	Abrasion index of UHPCs at various testing time (min)					
	1	2	5	10	15	20
C100	8.3	7.1	5.6	6.0	6.9	7.6
C100-H2%	10.0	7.6	7.0	6.9	7.6	8.4
C100-S2%	10.0	8.1	7.5	7.5	8.4	9.2
C100-H3%	11.1	8.8	7.7	7.9	8.9	9.9
C100-S3%	11.6	9.4	7.9	7.9	8.9	9.9
SF5	14.3	11.8	8.3	7.4	7.7	8.1
SF5-H2%	15.4	12.9	8.6	8.3	9.0	9.3
SF5-S2%	18.2	15.7	9.3	8.5	9.0	9.4
SF5-H3%	22.2	16.1	9.7	9.0	9.5	10.4
SF5-S3%	25.0	17.7	10.2	9.0	9.7	10.4
F20	10.0	7.1	4.9	5.5	6.2	6.9
F20-H2%	14.3	9.4	6.4	6.5	7.5	8.3
F20-S2%	14.7	9.6	6.6	6.9	7.8	8.6
F20-H3%	17.2	12.9	8.4	8.2	8.9	9.7
F20-S3%	16.7	11.8	8.0	8.3	9.0	9.7
F30	12.5	9.4	7.2	6.2	6.5	7.1
F30-H2%	12.3	10.9	7.7	7.4	8.1	8.4
F30-S2%	17.9	13.0	8.8	8.1	8.4	8.8
F30-H3%	18.9	13.9	9.3	8.8	9.4	9.9
F30-S3%	20.4	15.2	9.9	9.3	9.8	10.0
F15SF5	14.3	9.4	6.4	6.5	7.5	8.3
F15SF5-H2%	14.7	9.7	7.5	7.5	8.4	9.1
F15SF5-S2%	14.3	10.1	7.2	6.8	8.0	8.9
F15SF5-H3%	14.7	11.8	8.4	8.8	9.5	10.3
F15SF5-S3%	20.0	14.6	9.3	8.7	9.3	10.1
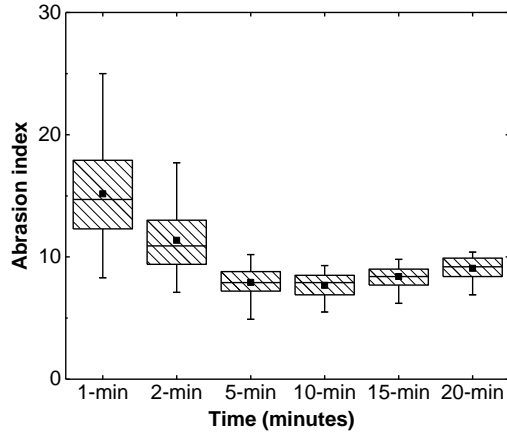
Figure 5.11 Abrasion index of the studied UHPCs as a function of time

5.3.3 Relationship Between Compressive Strength, Splitting-Tensile Strength, and Elastic Modulus with Depth of Wear

The relationship between the depth of wear (DW) and compressive strength (f_c') of the 28-day cured UHPCs (at a 95% confidence level) is shown in Figure 5.12 and Equation 5.2. As can be seen, with increases in compressive strength, the depth of wear of the studied UHPCs decreased. A similar trend was also reported by Pyo et al., (2018). The correlation between the depth of wear and the splitting-tensile strength (f_t) of the studied UHPCs is shown in Figure 5.13 and Equation 5.3. Pyo et al. (2018) developed a correlation between the tensile strength of UHPC with mass loss, and found that the tensile strength of concrete played a positive role in reducing the mass loss after an abrasion test. Figure 5.14 and Equation 5.4 document the relationship between depth of wear and elastic modulus (E_c) of the studied UHPCs.

$$DW= 9333.6f'_c{}^{-2.02} \qquad R^2 = 0.60 \qquad (5.2)$$
$$DW= 4.3f_t{}^{-0.90} \qquad R^2 = 0.93 \qquad (5.3)$$
$$DW= 314.1E_c{}^{-1.735} \qquad R^2 = 0.60 \qquad (5.4)$$

110
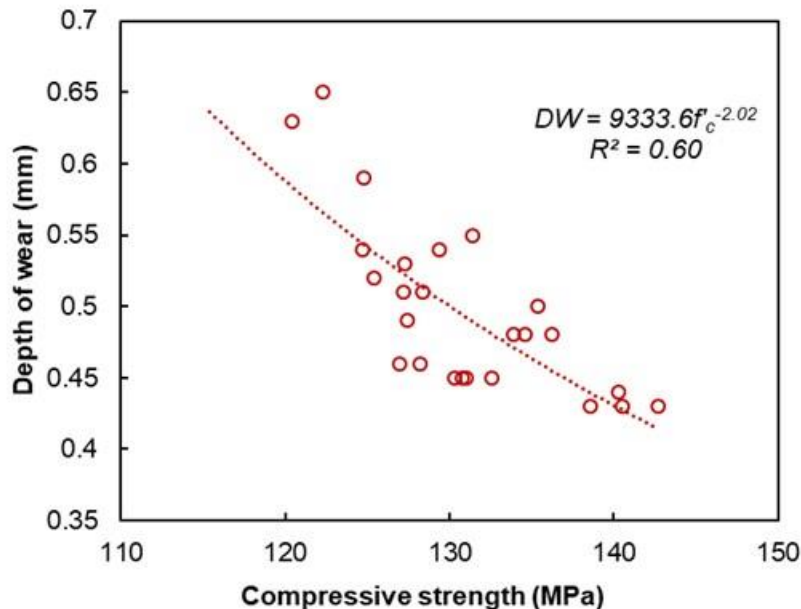
Figure 5.12 Correlations between UHPCs' compressive strength and depth of wear

$$DW = 4.3f_t^{-0.90}$$
$$R^2 = 0.93$$
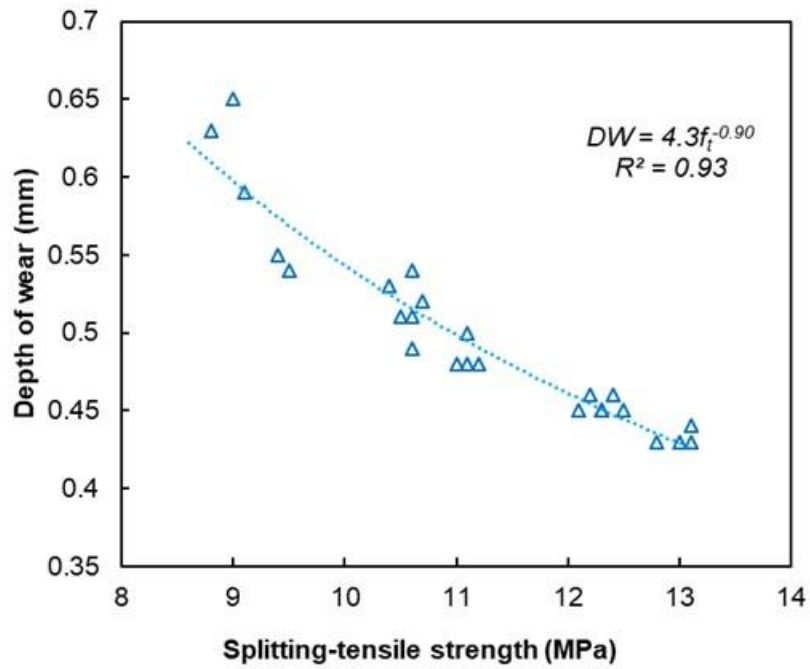
Figure 5.13 Correlations between UHPCs' splitting-tensile strength and depth of wear

$$DW = 314.1E_c^{-1.735}$$
$$R^2 = 0.6$$
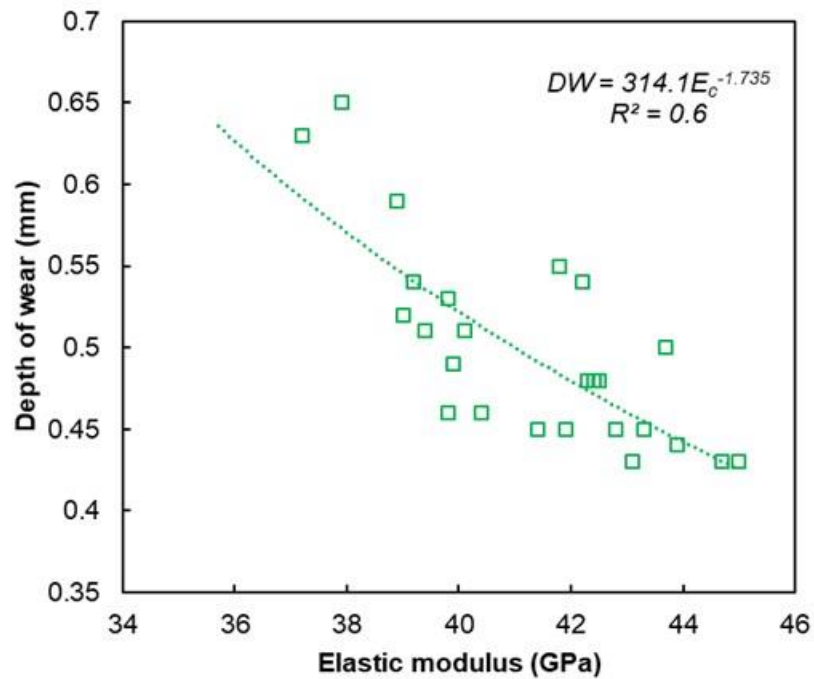
Figure 5.14 Correlations between UHPCs' elastic modulus and depth of wear

5.3.4 Observation of UHPC Surface After Abrasion Test

The abraded surfaces of the typical UHPCs (with and without fibers) after completion of the tests are shown in Figure 5.15. As shown in Figure 5.15a, both fine aggregate and pastes were integrally worn away. This was due to the strong bond action between the aggregate and paste. As shown in Figure 5.15b, the orientation of steel fibers played a role in resistance to wear. Steel fibers parallel to the contact surface acted jointly with the matrix to increase concrete stiffness and abrasion resistance. Those fibers not parallel to the concrete surface generated shadow zones just below the fibers to protect the underlying matrix against wear.
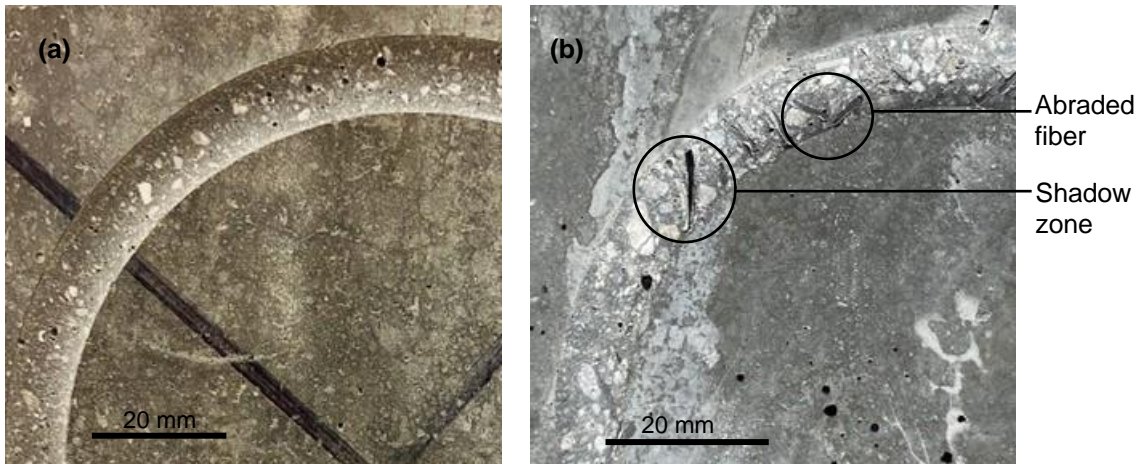
Figure 5.15 The abraded surface of typical UHPC after 20 minutes of testing, (a) plain UHPC (b) steel fiber reinforced UHPC

5.3.5 Comparison Between UHPCs and HSCs

The compressive strength and depth of wear of the studied UHPCs (plain and fiber-reinforced) were compared with those of the two high strength concretes (HSC1 and HSC2), and the results are presented in Figure 5.16. As can be seen, HSC2 exhibited 11% improvement in abrasion resistance, over that of HSC1, while its compressive strength increased by nearly 10%. In comparison to the HSCs, the plain UHPC-C100 displayed an approximately 16% increase in wear resistance, whereas its compressive strength improved by nearly 30%. The introduction of steel fibers in the UHPC-C100 widened the gap between the two concrete types by a nearly 32% improvement in wear resistance, whereas their compressive strengths remained nearly unchanged. The significantly higher cementitious material content used in the studied UHPCs, as compared to those of the HSCs, had more influence in improving compressive strength than it did in improving its resistance to wear.

A comparison between the depths of wear and splitting-tensile strengths of the studied HSCs and UHPCs are illustrated in Figure 5.17. Plain HSC2 displayed a 6% increase in splitting-tensile strength as compared to that of the HSC1, whereas the abrasion resistance increased by 11%. UHPC C100 produced a 42% higher splitting-tensile strength compared to those of the HSCs. With the introduction of steel fibers, the improvement in splitting-tensile strength increased to 54%. The aforementioned results indicate that the steel fibers improved splitting-tensile strength and resistance to wear more than they did compressive strength.

While elastic the moduli of the plain HSCs and UHPCs were nearly identical, the depth of wear decreased by 11% for plain UHPCs as compared to HSCs (Figure 5.5). The addition of steel fibers slightly improved

the elastic moduli of UHPCs (3% improvement) as compared to the HSCs, whereas the improvement to wear was 32%.

After 20-min of testing, HSC1 and HSC2 showed an AI of 6.0 and 6.8, respectively. In comparison, the plain UHPC (C100) produced an AI of 7.6, an increase of 16% compared to those of the HSCs. Once steel fibers were incorporated, the fiber-reinforced UHPCs displayed 32% higher AIs, as compared to those of the studied HSCs.
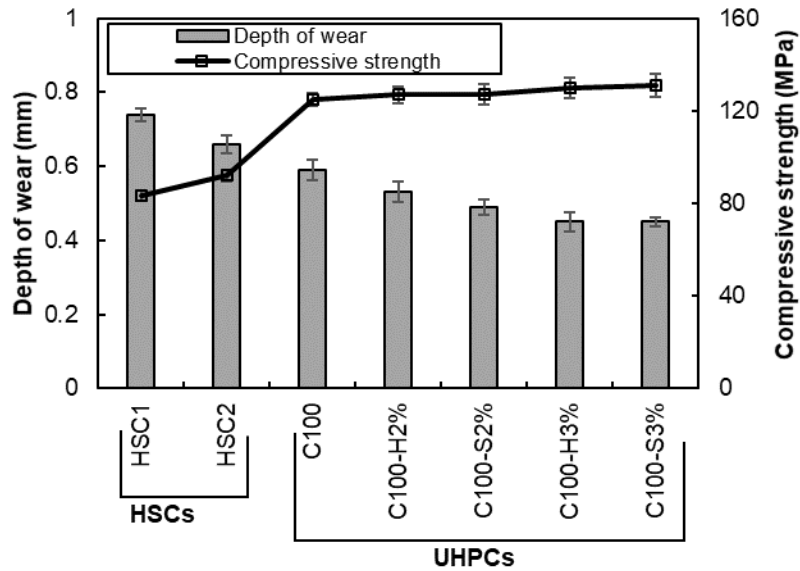
Figure 5.16 Comparison between UHPC with HSC in terms of wear and compressive strength
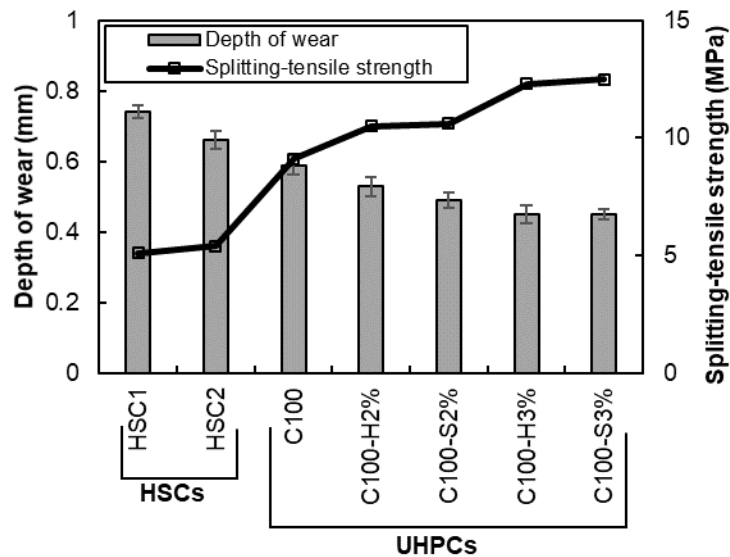
Figure 5.17 Comparison between UHPC with HSC in terms of wear and splitting-tensile strength

5.4 Conclusions

Based on the results of this study, the following conclusions can be drawn:

113

(1) The studied UHPCs displayed excellent compressive, splitting-tensile, and stiffness properties. The variations in cementitious materials combinations had a less positive effect on splitting-tensile resistance and elastic moduli than they had on compressive strength. The low water-to-cementitious materials ratio, very high cementitious materials content, and customized natural aggregate gradation produced a very dense matrix, which resulted in the excellent resistance to wear displayed by the studied UHPCs.

(2) Amongst the studied cementitious materials combinations, the 28-day cured UHPCs containing silica fume showed the highest resistance to wear, whereas the UHPCs containing fly ash produced the contrary.

(3) The addition of steel fibers improved the abrasion resistance of the studied UHPCs. The inclusion of steel fibers had more influence in improving the abrasion resistance (20%) than it did on the compressive strength (5%) of the studied UHPCs. Minimal differences in wear resistance and compressive strength were observed between the straight and hooked steel fibers.

(4) Nearly 85% of the UHPCs' ultimate wear was attained in the first 10 minutes of testing.

(5) The relative gain in abrasion of the studied UHPCs was independent of cementitious materials compositions or steel fiber content or type.

(6) The higher cementitious materials content of the UHPCs, as compared to those of the HSCs, enhanced the compressive strength more than the resistance to wear. In contrast, the increased in cementitious materials contents of the studied HSCs improved the resistance to wear more than the bulk properties.

(7) Railway sleepers made with UHPC can produce superior bulk properties and resistance to wear, as compared to the currently used prestressed concrete sleepers.

References

1. ACI Manual of Concrete Practice Index ACI Concrete Terminology, American Concrete Institute (2015), 38800 Country Club, Dr. Farmington Hills, MI 48331.
2. AREMA Manual for Railway Engineering (2009) American Railway Engineering and Maintenance-of-Way Association (AREMA), Landover, Maryland, V 1, Ch. 30.
3. Arora, A., Almujaddidi, A., Kianmofrad, F., Mobasher, B., & Neithalath, N. (2019). Material design of economical ultra-high performance concrete (UHPC) and evaluation of their properties. Cement and Concrete Composites, 104, 103346.
4. Atiş, C. D. (2002). High volume fly ash abrasion resistant concrete. Journal of Materials in Civil Engineering, 14(3), 274-277.
5. Bezgin, N. Ö. (2017). High performance concrete requirements for prefabricated high speed railway sleepers. Construction and Building Materials, 138, 340-351.
6. Dhir, R. K., Hewlett, P. C., & Chan, Y. N. (1991). Near-surface characteristics of concrete: abrasion resistance. Materials and Structures, 24(2), 122. https://doi.org/10.1007/BF02472473
7. Ferdous, W., & Manalo, A. (2014). Failures of mainline railway sleepers and suggested remedies–review of current practice. Engineering Failure Analysis, 44, 17-35.
8. Ghafoori, N., & Diawara, H. (2007). Strength and wear resistance of sand-replaced silica fume concrete. ACI Materials Journal, 104(2), 206.
9. Ghafoori, N., & Dutta, S. (1995). Laboratory investigation of compacted no-fines concrete for paving materials. Journal of Materials in Civil Engineering, 7(3), 183-191.
10. Ghafoori, N., & Sukandar, B. M. (1995). Abrasion resistance of concrete block pavers. ACI Materials Journal, 92(1), 25-36.
11. Ghafoori, N., Najimi, M., & Aqel, M. A. (2014). Abrasion resistance of self-consolidating concrete. Journal of Materials in Civil Engineering, 26(2), 296-303.
12. Ghafoori, N., Najimi, M., & Sobhani, J. (2015). Modelling the abrasion resistance of self-consolidating concrete. Magazine of Concrete Research, 67(17), 938-953.
13. Graybeal, B., & Tanesi, J. (2007). Durability of an ultrahigh-performance concrete. Journal of Materials in Civil Engineering, 19(10), 848-854.

14. Janeliukstis, R., Clark, A., Papaelias, M., & Kaewunruen, S. (2019). Flexural cracking-induced acoustic emission peak frequency shift in railway prestressed concrete sleepers. Engineering Structures, 178, 493-505.
15. Kaewunruen, S., & Remennikov, A. M. (2009). Progressive failure of prestressed concrete sleepers under multiple high-intensity impact loads. Engineering Structures, 31(10), 2460-2473.
16. Kaewunruen, S., Ngamkhanong, C., Janeliukstis, R., & You, R. (2017, July). Influence of surface abrasions on dynamic behaviours of railway concrete sleepers. In Proceedings of the 24th International Congress on Sound and Vibration, London, UK (pp. 20-24).
17. Karim, R., Najimi, M., & Shafei, B. (2019). Assessment of transport properties, volume stability, and frost resistance of non-proprietary ultra-high performance concrete. Construction and Building Materials, 227, 117031.
18. Kernes, R. G., Shurpali, A. A., Edwards, J. R., Dersch, M. S., Lange, D. A., & Barkan, C. P. (2014). Investigation of the mechanics of rail seat deterioration and methods to improve the abrasion resistance of concrete sleeper rail seats. Proceedings of the Institution of Mechanical Engineers, Part F: Journal of Rail and Rapid Transit, 228(6), 581-589.
19. Li, B., Ke, G., & Zhou, M. (2011). Influence of manufactured sand characteristics on strength and abrasion resistance of pavement cement concrete. Construction and Building Materials, 25(10), 3849-3853.
20. Li, D., Ngamkhanong, C., & Kaewunruen, S. (2017, October). Influence of surface abrasion on creep and shrinkage of railway prestressed concrete sleepers. In IOP Conference Series: Materials Science and Engineering (Vol. 245, No. 3, p. 032040). IOP Publishing.
21. Li, H., Zhang, M. H., & Ou, J. P. (2006). Abrasion resistance of concrete containing nano-particles for pavement. Wear, 260(11-12), 1262-1266.
22. Liu, T. C. (1981). Abrasion resistance of concrete. ACI Journal Proceedings, 78(5), 341-350.
23. Manalo, A., Aravinthan, T., Karunasena, W., & Ticoalu, A. (2010). A review of alternative materials for replacing existing timber sleepers. Composite Structures, 92(3), 603-611.
24. Meng, W., Valipour, M., & Khayat, K. H. (2017). Optimization and performance of cost-effective ultra-high performance concrete. Materials and Structures, 50(29), DOI: 10.1617/s11527-016-0896-3.
25. Naik, T. R., Singh, S. S., & Ramme, B. W. (2002). Effect of source of fly ash on abrasion resistance of concrete. Journal of Materials in Civil Engineering, 14(5), 417-426.
26. Nanni, A. (1989). Abrasion Resistance of Roller Compacted Concrete. ACI Materials Journal, 86(6), 559-565.
27. Ngamkhanong, C., Li, D., & Kaewunruen, S. (2017, October). Impact capacity reduction in railway prestressed concrete sleepers with surface abrasions. In IOP Conference Series: Materials Science and Engineering (Vol. 245, No. 3, p. 032048). IOP Publishing. DOI:10.1088/1757-899X/245/3/032048
28. Ngamkhanong, C., Li, D., Remennikov, A. M., & Kaewunruen, S. (2019). Dynamic capacity reduction of railway prestressed concrete sleepers due to surface abrasions considering the effects of strain rate and prestressing losses. International Journal of Structural Stability and Dynamics, 19(01), 1940001. DOI: 10.1142/S0219455419400017
29. Parvez, A., & Foster, S. J. (2017). Fatigue of steel-fibre-reinforced concrete prestressed railway sleepers. Engineering Structures, 141, 241-250.
30. PCA (2020). Ultra-High Performance Concrete. Portland Cement Association (PCA) https://www.cement.org/learn/concrete-technology/concrete-design-production/ultra-high-performance-concrete. Accessed 5th February 2020
31. Pyo, S., Abate, S. Y., & Kim, H. K. (2018). Abrasion resistance of ultra-high performance concrete incorporating coarser aggregate. Construction and Building Materials, 165, 11-16.
32. Ragalwar, K., Heard, W. F., Williams, B. A., & Ranade, R. (2020). Significance of the particle size distribution modulus for strain-hardening-ultra-high performance concrete (SH-UHPC) matrix design. Construction and Building Materials, 234, 117423.
33. Railway Technology (2020) At a Glance: Railway Sleeper Materials. https://www.railway-technology.com/features/feature92105/. Accessed 25th April 2020

34. Reiff, R., Walker, R., Schreiber, P., Wilson, N., & Thompson, H. (2012). Assessment of Rail Seat Abrasion Patterns and Environment (No. DOT/FRA/ORD-12/07). United States. Federal Railroad Administration.
35. Remennikov, A. M., & Kaewunruen, S. (2014). Experimental load rating of aged railway concrete sleepers. Engineering Structures, 76, 147-162.
36. Riding, K. A., Peterman, R. J., Guthrie, W. S., Brueseke, M., Mosavi, H., & Daily, K. (2019). A Study of Environmental and Track Factors that Contribute to Abrasion Damage of Concrete Ties (No. DOT/FRA/ORD-19/38). United States. Department of Transportation. Federal Railroad Administration. Office of Research, Development, and Technology.
37. Sadegzadeh, M., Page, C. L., & Kettle, R. J. (1987). Surface microstructure and abrasion resistance of concrete. Cement and Concrete Research, 17(4), 581-590.
38. Scott, B. D., & Safiuddin, M. (2015). Abrasion resistance of concrete–Design, construction and case study. Concrete Research Letters, 6(3), 136-148.
39. Siddique, R. (2003). Effect of fine aggregate replacement with Class F fly ash on the abrasion resistance of concrete. Cement and Concrete Research, 33(11), 1877-1881.
40. Smith, F.L. (1958) Effect of aggregate quality on resistance of concrete to abrasion. Cement and Concrete, American Society for Testing and Materials, Philadelphia, ASTM STP 205, 91-105.
41. Yang, R., Yu, R., Shui, Z., Gao, X., Xiao, X., Zhang, X., Wang, Y. & He, Y. (2019). Low carbon design of an Ultra-High Performance Concrete (UHPC) incorporating phosphorous slag. Journal of Cleaner Production, 240, 118157.
42. Yang, S. L., Millard, S. G., Soutsos, M. N., Barnett, S. J., & Le, T. T. (2009). Influence of aggregate and curing regime on the mechanical properties of ultra-high performance fibre reinforced concrete (UHPFRC). Construction and Building Materials, 23(6), 2291-2298.
43. Yoshitake, I., Ueno, S., Ushio, Y., Arano, H., & Fukumoto, S. (2016). Abrasion and skid resistance of recyclable fly ash concrete pavement made with limestone aggregate. Construction and Building Materials, 112, 440-446.
44. You, R., Goto, K., Ngamkhanong, C., & Kaewunruen, S. (2019). Nonlinear finite element analysis for structural capacity of railway prestressed concrete sleepers with rail seat abrasion. Engineering Failure Analysis, 95, 47-65.
45. Zeman, J. C., Edwards, J. R., Barkan, C. P., & Lange, D. A. (2009, June). Failure mode and effect analysis of concrete ties in North America. In Proc. of the 9th International Heavy Haul Conference (pp. 270-278).
46. Zhao, S., Van Dam, E., Lange, D., & Sun, W. (2017). Abrasion resistance and nanoscratch behavior of an ultra-high performance concrete. Journal of Materials in Civil Engineering, 29(2), 04016212.
47. Zmetra, K. M., McMullen, K. F., Zaghi, A. E., & Wille, K. (2017). Experimental study of UHPC repair for corrosion-damaged steel girder ends. Journal of Bridge Engineering, 22(8), 04017037.

CHAPTER 6-BEHAVIOR OF RAILWAY TIES MADE USING ULTRA-HIGH-PERFORMANCE CONCRETE

6.1 Introduction

With the recent technological developments in the railway industry, there have been only a few applications for utilization of advanced cement-based materials. Modern railway tracks require safe, durable, environmentally sustainable, and cost-effective ties. In current railway systems, outside of North America, Portland cement prestressed concrete (PC) has taken over has been dominant material for railway ties, which transfer vehicle load from rails to substructures. Presently available PC ties have a number of concerns not meeting the requirements of railway tracks. Enhancing the construction and durability of railway tie is a significant concern in the contemporary railway sector, as the expense of tie replacement is substantial, and there is a growing need for greater axial load, operational speed, and tonnage capacity.

Many researchers offered different solutions to improve the performance of PC ties. To lessen abrasion, Peters and Mattson (2004) covered the rail-seat region with cast-in-place steel plates. Later, Peters (2007) employed epoxy to minimize abrasion in the rail-seat area. This alternative, however, labor-intensive, necessitates track closures while the epoxy is being applied and allowed to cure, and there is a chance that the epoxy would eventually wear out. The application of multi-layer abrasion-resistant pad assembly (Peters and Mattson, 2004), the placement of metallic aggregates in the rail-seat region, and the addition of fly ash and silica fume to the concrete in the rail-seat area (Shurpali et al., 2013) were suggested as preventive measures (Wu et al., 2001).

With a combination of long and short steel fibers, Sadeghi et al. (2016) developed steel fiber reinforced concrete (SFRC) prestressed ties with 0.50% by volume of steel fibers. According to the AREMA test handbook, repeated loading tests were carried out (American Railway Engineering and Maintenance-of-Way Association, AREMA, 2014). The steel fiber reinforced concrete (SFRC) ties displayed better toughness and endurance and withstood repeated loading for three million cycles without failure. Parvez and Foster (2017) employed steel fibers combined with prestressing to reduce the impact of fatigue and concluded that a 0.50% of fibers is necessary for effective performance in SFRC structural members under fatigue. Yang et al. (2017) observed that the bending and fatigue capabilities of ties can be enhanced by incorporating steel fiber reinforcement, resulting in a reduction of crack propagation and brittle shear failure when compared to ties without such reinforcement. However, as noted by Bae and Pyo (2020), there is an upward trend in electrical conductivity with an increase in the quantity of steel fiber. The circulation of stray current through conventional steel reinforcement is recognized for causing accelerated corrosive damage to steel fibers. Owing to a limited understanding of stray current-induced corrosion in Steel Fiber-Reinforced Concrete (SFRC), the 'Guangzhou Metro Line 3' project in China opted to cancel the use of SFRC as the primary lining material (Tang, 2017).

PC ties typically use high strength concrete, which allows for prestressing forces to be introduced during the early stages of curing, speeding up the manufacturing process. European standards mandate a minimum compressive strength of 45 MPa (6525 psi), while Australia specifies 50 MPa (7250 psi). The International Union of Railways suggests minimum tensile and compressive strengths for concrete ties of 3 MPa (435 psi) and 50 MPa (7250 psi), respectively. In addition, it is worth noting that the American Railway Engineering and Maintenance-of-Way Association (AREMA) requires a minimum compressive strength of 48 MPa for concrete ties. Recently, concrete with 60-80 MPa compressive strengths than traditional high strength concrete has been used to fabricate new types of ties with improved structural capacities (Bae et al., 2020). The use of advanced chemical admixtures and fibers, specialized aggregate with excellent packing density, very high binder content, low water-to-cementitious materials ratio, and customized mixing and curing has resulted in the development of ultra-high-performance concrete (UHPC). Zi et al. (2012) reported that, with the increase of compressive strength of concrete, the resistance of the PC tie also

increased against freezing and thawing. In comparison to the concrete currently used for railroad ties, a mixture containing slag partially substituting for Type III Portland cement demonstrated improved resistance to freeze-thaw cycles (Shin et al., 2016). According to Ahmed et al. (2022), cracking load for UHPC ties under the static bending tests more than doubled that for the PC ties made of conventional concrete.

UHPC has the potential to mitigate the existing problems of the railway ties and be a viable alternative to the PC ties currently used in practice. The following statements provide summary of the reasons of using UHPC for railway ties:

(i) Strength and Durability: UHPC has an extremely high compressive strength, typically exceeding 150 MPa, which makes it capable of withstanding heavy loads and high impact forces from moving trains. It also has excellent resistance to wear and freeze and thaw, ensuring a long service life even in harsh environments (Hasnat and Ghafoori, 2021a, 2021b, 2021c).

(ii) Early Strength Development: UHPC typically rapidly develops strength, which can expedite construction schedules and minimize disruption to rail operations (Hasnat and Ghafoori, 2021c).

(iii) Reduced Maintenance: The durability of UHPC reduces the need for frequent maintenance or replacement of railway ties. This can result in cost savings and minimum disruptions to rail operations (Hasnat and Ghafoori, 2021a, 2021b, 2021c).

(iv) Lightweight Design: UHPC can be engineered to have a high strength-to-weight ratio, which allows for lighter and more efficient designs of railway ties/sleepers. This can lead to easier handling during installation and the reduced transportation costs.

(v) Customizability: UHPC can be tailored to meet specific design requirements, such as different track geometries, load capacities, and environmental conditions. This flexibility allows for optimized designs that can enhance the performance and safety of railway tracks.

(vi) Sustainability: UHPC often contains high-quality, locally available materials and supplementary cementitious binders, and its long service life can reduce the need for frequent replacements, resulting in lower resource consumption and reduced environmental impact compared to the currently used PC railway ties (Hasnat and Ghafoori, 2021a, 2021b, 2021c).

Ties play a crucial role in converting the locally applied axle load into a distributed load on the ballast and ensuring the alignment of the rails in the transverse direction (Carrasco et al., 2012). It is well-established that the distribution of moments on the ties is highly influenced by the deformation of the ballast caused by the axle load over time and other environmental factors. While many researchers have examined the use of conventional concrete or high-strength concrete for PC ties, only a few studies have investigated the application of UHPCs in the production of railway ties. Bae and Pyo (2020) used post-tensioned prestressed fiber-reinforced UHPC ties to assess the static and dynamic behavior of ties. They observed that during dynamic tests on the rail-seat section, the load was 6% higher when the crack width reached 0.5 mm (0.02 in), compared to the reference load. However, this increase was lower compared to the static cases. These results suggest that the cracks were not completely closed once they were initiated under dynamic load conditions, and the delay in cracking was not greater than that observed in static cases. As mentioned earlier, while use of steel fibers may have detrimental effect on the fiber-reinforced UHPC ties, plain UHPC offers exceptional mechanical properties, durability, lightweight design, customizability, fast setting time, and sustainability. UHPC's high strength; and resistance to freeze-thaw, wear and corrosion making it suitable for heavy loads and harsh environmental conditions while reducing maintenance needs and minimizing disruptions to rail operations.

6.2 Experimental Program

The described section outlines an experimental study that aims to validate the predicted behavior and gather firsthand data on the performance of ultra-high-performance concrete (UHPC) railway ties. The study is

motivated by previous discussions on the topic and seeks to conduct experiments to validate the anticipated outcomes and collect experimental data on to the flexural and cyclic performance of UHPC railway ties.

6.2.1 Test Specimen and Test Matrix

The American Railway Engineering and Maintenance-of-Way Association (AREMA) has its own design recommendations and standards. It considers factors such as tie length and spacing, axle load, train speed, and a safety factor in its design method. According to AREMA standard the tie is linear-elastic as they do not consider the non-linearity of the tie. The minimum splitting tensile strength of plain UHPC is 6 MPa, whereas high-strength concrete typically exhibits tensile strengths ranging from 3 to 4 MPa. Due to UHPCs higher tensile strength compared to the concrete used for PC ties, UHPC tie is anticipated to exhibit a greater cracking load even without any prestressing. To represent actual condition, the studied UHPC ties have been chosen to have an overall average length of 2362 mm (93 in), in accordance with the AREMA requirements for standard railway ties. To increase the load distribution area to the ballast, a trapezoidal section was selected for constructing the ties. The average width near the ballast bearing area was selected as 229 mm (9 in), while the average width near the rail seat area was reduced to 191 mm (7.5 in). The average depth near the ballast bearing area was set at 203 mm (8 in), and the average depth near the rail seat area was selected as 191 mm (7.5 in). The average clear cover of 25 mm (1 inch) was maintained at the center of the span (section B-B), while an average cover of 37 mm (1.5 inches) was maintained near the support location (section A-A). The longitudinal flexural reinforcements included four No. 7 steel bars (nominal diameter of 22.2 mm) with an average center to center spacing of 83 mm (3.25 in) between two bars. The reinforcement ratio (ρ) near the support was 0.0236 (A-A), and at the center span, it is 0.0277 (B-B). To prevent premature shear failure, No. 4 rebar (nominal diameter of 12.5 mm) with 135° hook was placed at a center-to-center spacing of 83 mm (3.25 in) along the entire span of the tie, in accordance with the ACI 318 (2019) code requirement.

The structural design of concrete ties mostly relies on estimating the flexural demand and in some cases shear capacity that a tie is expected to experience both at the rail-seat and in the center region. A total of five UHPC railway ties were manufactured and tested. Two specimens were used to evaluate the center moment capacity with variations in the strength grade of the main/longitudinal reinforcing bars. Two other ties were subjected to cyclic loading conditions. The fifth tie was tested to evaluate the rail-seat moment capacity. The specimens were designated as follows: M468C, C468C, M468S, M738C, and C738C. In the designation, the first letter indicates whether the specimen was subjected to monotonic (M) or cyclic (C) loading. The number following it indicates the yield strength of the longitudinal steel reinforcing bar, and the last letter indicates the loading location, either near the tie center (C) or the rail-seat (R). For instance, M468C indicates a tie with a monotonic loading condition, having 468 MPa yield strength of steel reinforcing bar as the main reinforcement, and the loading is applied near the center of the tie. The testing matrices is summarized in Table 6.1.
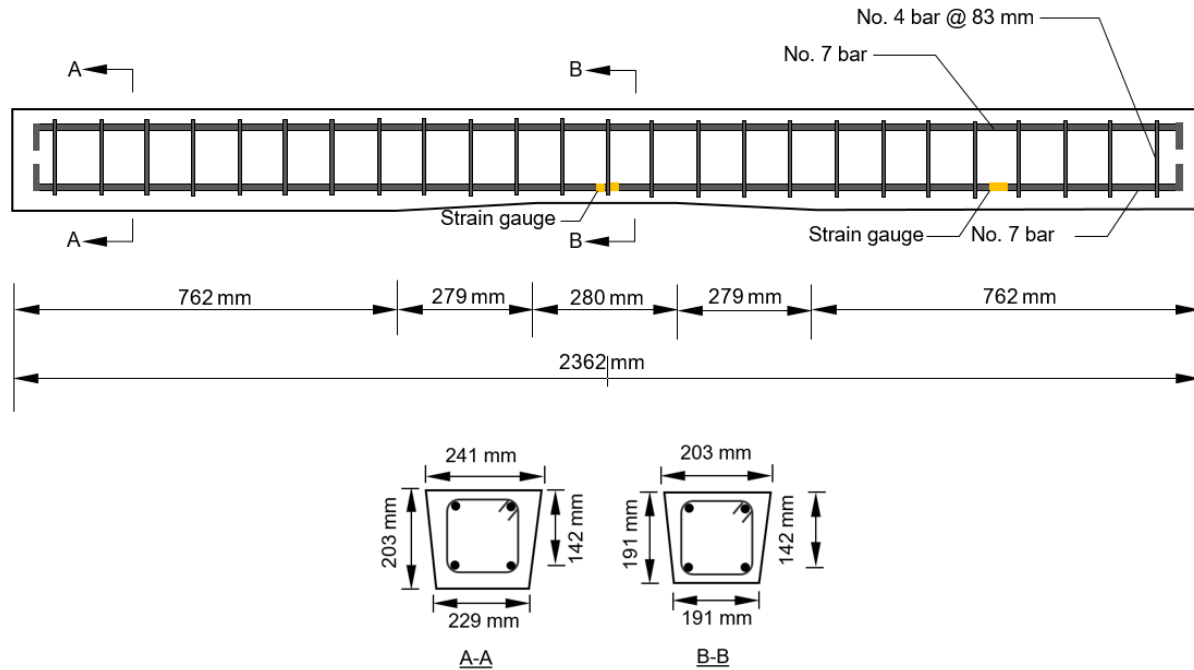
Figure 6.1 Specimen geometry and reinforcing details

Table 6.1 Test matrix

Specimen	Loading type	Loading location
M468C	Monotonic	Center
C468C	Cyclic	Center
M468R	Monotonic	Rail-seat
M738C	Monotonic	Center
C738C	Cyclic	Center

6.2.2 Material Properties

An optimized Ultra-High-Performance Concrete (UHPC) was chosen based on the mechanical, transport, and durability properties discussed in the previous chapters (Chapter 2 to 5). A consistent water-to-cementitious materials ratio of 0.21 was maintained during the preparation of all UHPC ties. A ternary cementitious blend was selected, in which Type V cement was partially replaced with 15% fly ash and 5% silica fume, serving as partial replacements for Type V cement. A commercially available polycarboxylate-based high-range water-reducing admixture (HRWRA) was used to achieve the UHPC's desired flowability of 250±25 mm (10±1 in). The mixing process of the selected UHPC was described in section 2.2.5 of Chapter 2. Cylindrical specimens (50 mm diameter and 100 mm height) were also prepared to evaluate the concrete strength of the UHPC ties. The cylinders prepared alongside the ties followed the same curing process as the ties. The cylinders were tested on the same day as the corresponding tie test. A summary of the compressive strength of the studied UHPC ties is presented shown in Figure 6.2. The compressive strength of the UHPC ties ranged from 167 to 173 MPa (24215 to 25085 psi), with an average standard deviation of 2.51 MPa (364 psi).
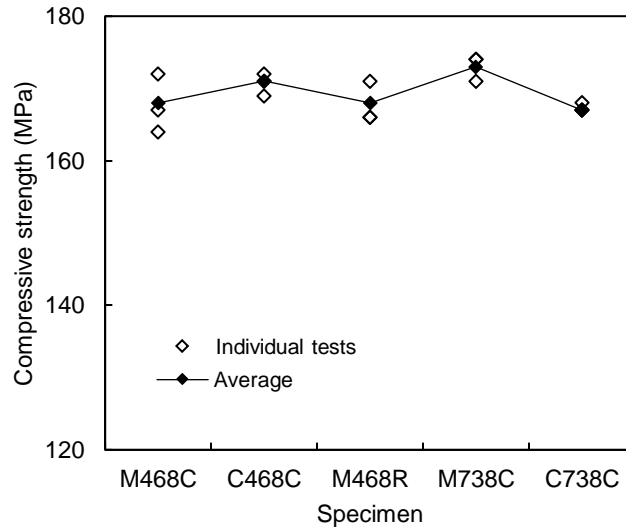
Figure 6.2 Compressive strength of UHPC

Three types of steel reinforcement were used, including two grades of No. 7 bars as longitudinal reinforcements and No. 4 bars as transverse reinforcements. To match the high strength resulting from the use of very high-strength concrete in this study, high-strength steel was also employed in addition to the standard 468 MPa steel bar. The first bar type was ASTM A615 rebar with a yield strength of 468 MPa (67.9 ksi), whereas the second type was ASTM A615 high strength steel rebar with a yield strength of 738 MPa (107 ksi). The yield strength of Grade 738 was determined by drawing a line parallel to the linear portion of the stress-strain response at 0.002 strain. No. 4 rebars with a yield strength of 432 MPa (62.7 ksi) was used for shear reinforcements. The properties of the steel reinforcements used in this study are documented in Table 6.2. The stress-strain response of the no. 7 steel reinforcement is presented in Figure 6.2 provided by the manufacturer. While the stress-strain response the grade 468 was not available, a typical stress-strain response is presented in Figure 6.3.

Table 6.2 Steel rebar properties

Rebar ID	Diameter (mm)	f_y (MPa)	f_u (MPa)	Elongation (%)
738-No.7	22.2	738	932	5.9%
468-No.7	22.2	468	746	15%
468-No.4	12.5	432	656	15%

Note: 1 MPa =145 psi
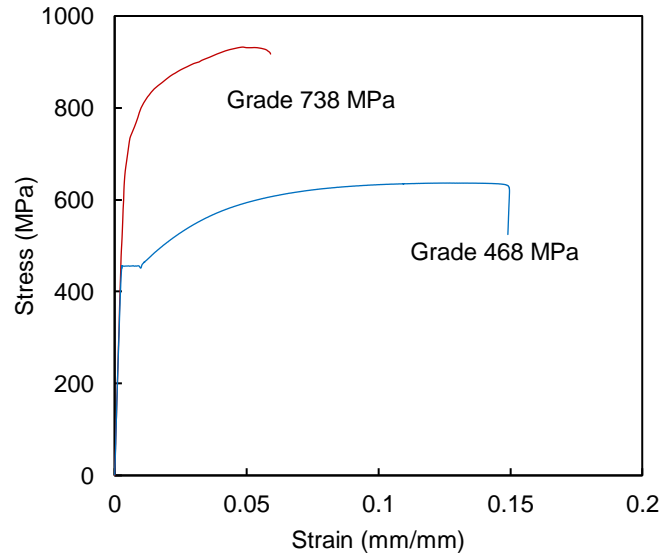
Figure 6.3 Typical stress-strain response of No. 7 bars (Mill Report, CMC Steel, 2021)

6.2.3 Fabrication of Reinforced Concrete Railway Tie

In the production of the UHPC ties, several steps were followed meticulously to ensure the design and quality control were not compromised. These steps included building formwork, constructing steel cages, mounting strain gauges on rebars, batching freshly-mixed UHPCs, and curing. Each step was carried out methodically to maintain the highest standards of production and quality assurance. Rebar strain gauges were attached at the critical sections of the UHPC ties to assess the strain and yielding behavior of the longitudinal steel bars. To protect the strain gauges from any possible damage, a layer of epoxy and aluminum foil was wrapped around them (see Figure 6.4). The formwork, steel reinforcing cage, and pouring of freshly-mixed UHPC in the reinforcing cage are shown in Figure 6.5.

To prevent moisture loss and surface cracks, the UHPC ties were covered with plastic immediately after completion of casting. Three hours after placement, two layers of moist burlap were placed on the exposed surface and wet curing continued inside the laboratory for 28 days (Figure 6.6 and 6.7).

Figure 6.4 Strain gauge application

122

Figure 6.5 Fabrication of UHPC tie specimen

Figure 6.6 Curing of UHPC tie specimens using moist burlap

Figure 6.7 UHPC tie specimens after removed from formwork

6.2.4 Test Setup

Figures 6.8 and 6.9 illustrate the schematic and actual setup for the UHPC tie center moment under monotonic and cyclic loading conditions. Cyclic loading tests help in evaluating the sleeper's resistance to fatigue and its ability to withstand repeated loading cycles without failure. The tie had an effective span of 1524 mm (60 inches), with both static vertical loading and cyclic bending applied at the center of the span.. For rail-seat moment capacity test, the effective span was reduced to 559 mm (22 inches) as presented in Figures 6.10 and 6.11. All the tests conducted as per AREMA guidelines. A temporary support was provided to maintain the stability of the tie during setup. However, once the load was applied, no reaction force was transferred to that temporary support. Ties were seated on two W section (W12x40) supports welded with 25 mm (1 inch) thick plates at the bottom and top. A steel plate with a width of 152 mm, length of 250 mm, and thickness of 25 mm (6x10x1 inch) was positioned between the contact point of the pin with a diameter of 25 mm (1 inch) and the center of the tie where the load was applied. To minimize the lateral reaction force, lubricant was applied at the contact point between the steel plate and the pin. Two linear variable differential transformers (LVDTs) (one in the 25 mm away from front and one in the 25 mm away

from the back) were attached at the bottom of the tie specimen to evaluate the load-deflection responses. A hydraulic jack was used to apply the vertical load, which was correlated with the data from the LVDTs.
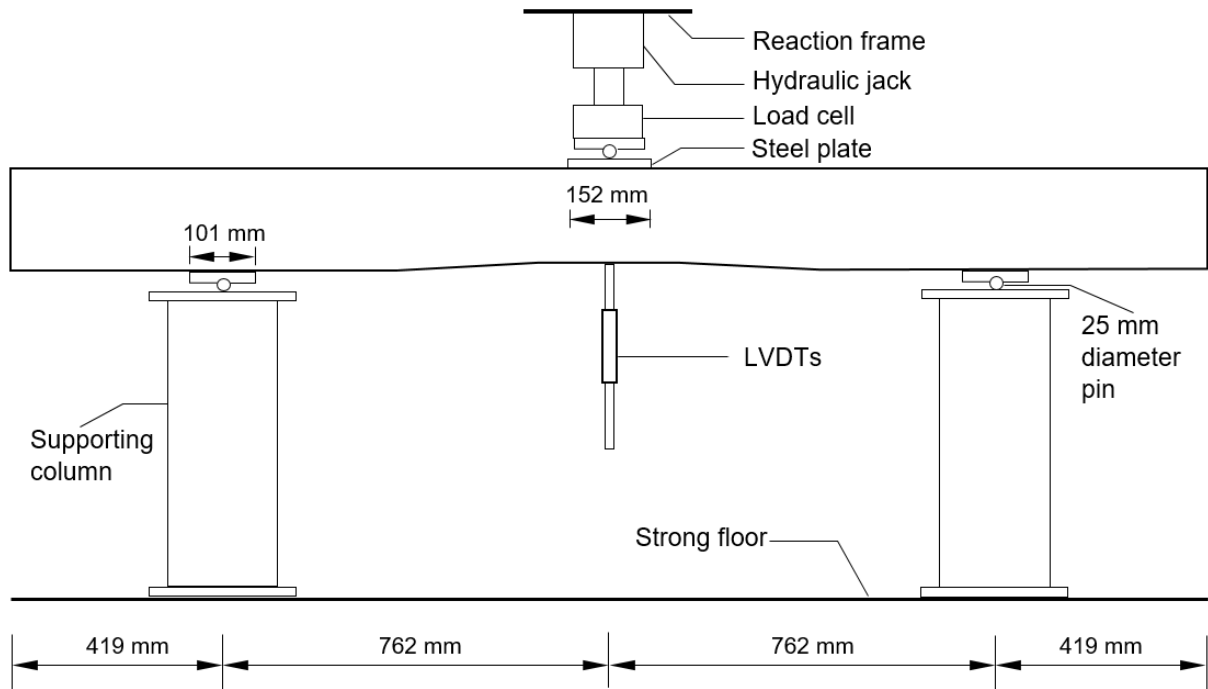
Figure 6.8 Schematic of test setup for railway tie specimen under negative center point bending (1 mm = 0.039 in)

Figure 6.9 Actual test setup for railway tie specimen under negative center point bending
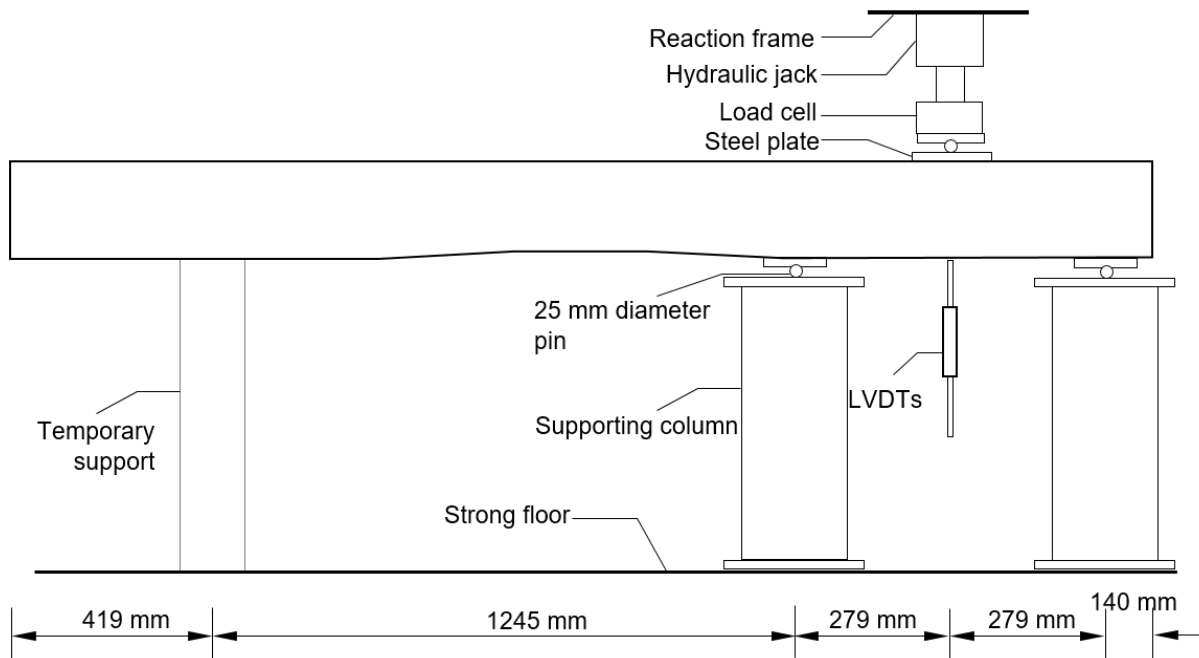
Figure 6.10 Schematic of test setup for railway tie specimen under rail-seat bending (1 mm = 0.039 in)

Figure 6.11 Actual test setup for railway tie specimen under rail-seat bending

6.2.5 Loading and Data Acquisition
In this study, UHPC tie specimens were tested under two loading schemes: monotonic and cyclic tests. The monotonic test gradually increased load (less than 20 kN/minute) with pauses at 5 kips to measure crack development. Cyclic tests, showcased in Figure 6.12, involved repeated cycles of loading and unloading. At each 22.5 kN (5 kips) level, the load was released then reapplied twice before moving to the next level. After every cycle, the load was fully removed. This pattern repeated for two cycles per level, each with a

127

22.5 kN (5 kips) increment, until yielding at 156 kN (35 kips). Beyond yielding, the load increment halved to 11.1 kN (2.5 kips).

The displacement and strain of the UHPC ties were measured at the critical sections, as shown in Figure 6.8 and 6.10. To ensure most accurate displacement data along the width of the ties, two linear variable differential transformers (LVDTs) were positioned at the bottom of the span centerline for displacement measurements. Similarly, strain gauges were attached to the tensile longitudinal reinforcing bars, as depicted in Figures 6.8 and 6.10. Additionally, a crack measurement scale was used to determine the width and development of cracks at different loading levels.
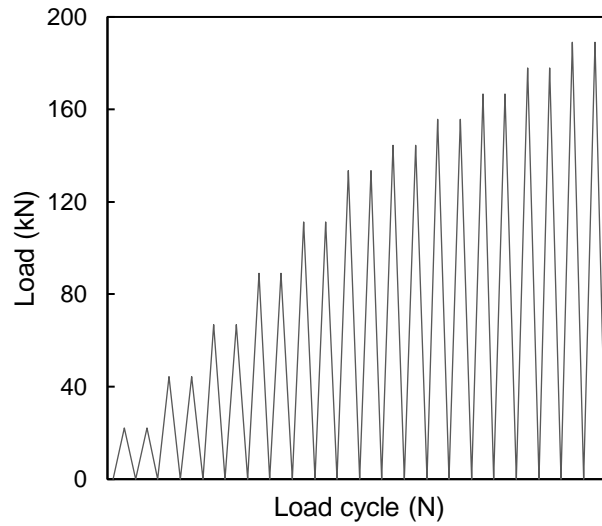
Figure 6.12 Load scheme for cyclic loading test of C468C

6.3 Results and Discussion

The experimental findings are presented in the following sections, providing information on observed failure modes, the relationship between load and deflection, damage map, crack developments, and load-steel strain relationships of the UHPC ties. Additionally, theoretical load capacity of the UHPC ties are also discussed.

6.3.1 Summary of Test Results

Tables 6.3 and 6.4 summarizes the cracking load (P_{cr}), yield load (P_y), peak load (P_u), deflection at yield and peak load (Δ_y and Δ_u), energy absorption (area under load-deflection curve), maximum crack width at the critical sections (76 mm from center bottom of the midspan of two supports or the edge of the steel plate seating between the jack and the tie), and failure mode of the tested UHPC ties. The yield load, P_y in a load-deflection curve is determined based on the change in slope of the load-deflection response, transitioning from linear elastic to non-linear behavior. Under monotonic loading condition tested for center negative moment, the peak load varied from 182.9 to 214.7 kN (41.1 to 48.26 kips). Under cyclic loading condition, the peak load varied from 190.0 to 196.7 kN (42.72 to 44.22 kips) for the same type and configuration. The predicted maximum peak load was determined using ACI 318 for doubly reinforced concrete sections, utilizing the material properties provided in Tables 6.2 and Figure 6.2, respectively. The ratio of the predicted peak load capacity to the experimental peak load capacity matched very well, with a minimum variation of 2% and a maximum variation of 8%. The UHPC ties made using 468 MPa (67.9 ksi) rebars sustained more deflection in both monotonic and cyclic loading conditions compared to the ties made with

738 MPa (107 ksi) steel under center negative moment test. However, the tie tested at support negative moment test showed the lowest deformation with the highest peak load and crack width compared to the rest of the tested UHPC ties. The energy absorption of the ties was determined by calculating the area under the load-deflection response (Zhou and Wang, 2018). The energy absorption of ties made using 468 MPa (67.9 ksi) rebars showed higher energy absorption compared to that of the 738 MPa (107 ksi) rebars. Figures 6.12 to 6.16 present the studied ties at the beginning and at the completion of the test. A detailed discussion is presented in the sections to follow.

Table 6.3 Summary of experimental and predicted load capacity of UHPC ties

ID	$P_{cr\text{-}exp}$ (kN)	$P_{y\text{-}exp}$ (kN)	$P_{u\text{-}exp}$ (kN)	$P_{u\text{-}pr\text{-}flex}$ (kN)	$P_{u\text{-}pr\text{-}shear}$ (kN)	$\dfrac{P_{u-pr-flex}}{P_{u-exp}}$	$\dfrac{P_{u-pr-sh}}{P_{u-exp}}$
M468C	22.2	127	183	175	270	0.96	1.48
C468C	12.9	129	190	175	270	0.92	1.42
M468R	28.3	216	288	-	282	-	0.98
M738C	27.0	-	215	205	271	0.95	1.26
C738C	21.4	-	199	205	270	1.03	1.36

Note: $P_{cr\text{-}exp}$: Cracking load; $P_{y\text{-}exp}$: Yield load; $P_{u\text{-}exp}$: Ultimate load; $P_{u\text{-}pr\text{-}flex}$: Predicted ultimate load; 1 kN=0.224 kip

Table 6.4 Crack width, energy absorption, and failure mode of UHPC ties

ID	Crack width (mm)	Energy absorption (kN-m)	Failure mode
M468C	1.00	2.87	Flexural (steel yielding, concrete crushing)
C468C	1.40	3.20	Flexural (steel yielding, concrete crushing)
M468R	2.50	1.41	Shear (steel yielding, concrete crushing)
M738C	1.00	1.96	Flexural (steel yielding, concrete crushing)
C738C	1.00	1.86	Flexural (steel yielding, concrete crushing)

1 mm=0.0394 in; 1 kN=0.224 kip
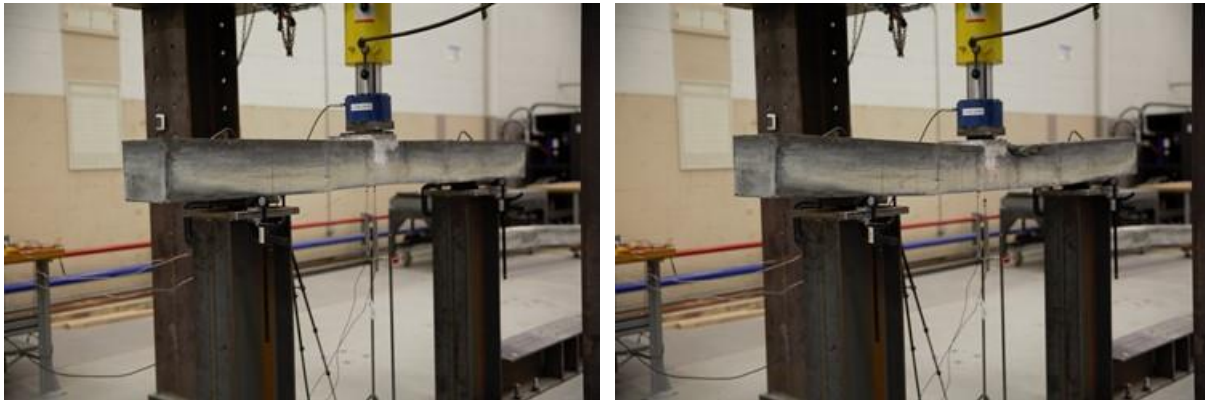
Figure 6.13 M468C tie at start and end of loading
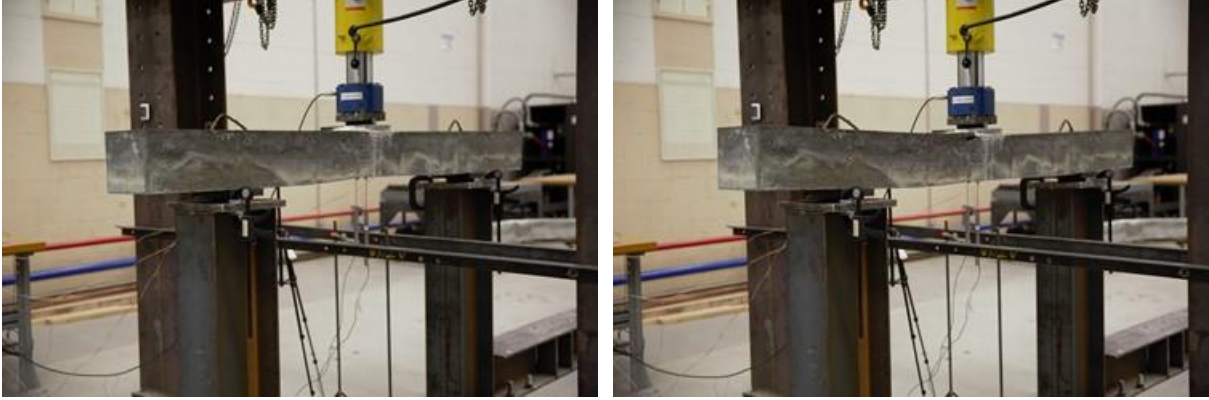
Figure 6.14 M738C tie at start and end of loading

Figure 6.15 M468R tie at start and end of loading

Figure 6.16 C468Ctie at start and end of loading
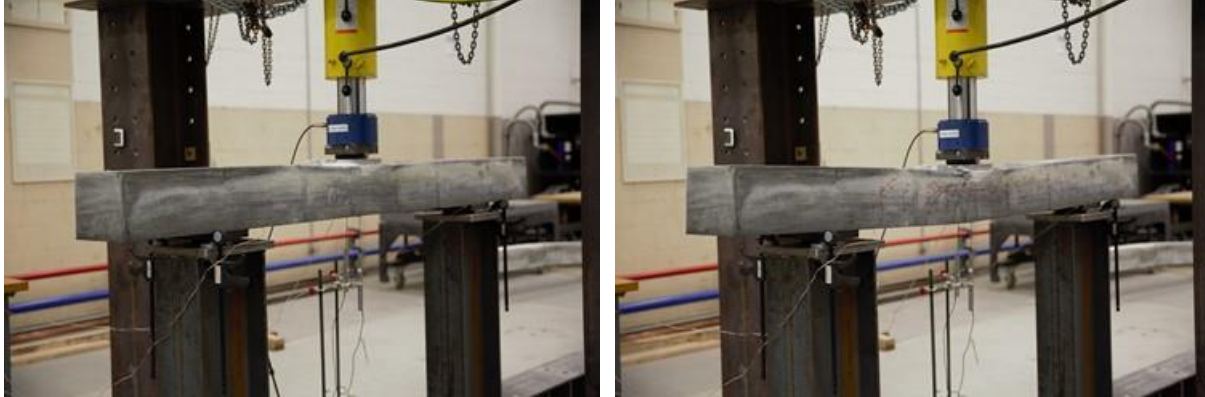
Figure 6.17 C738C at start and end of loading

6.3.2 Load-Deflection Responses

The load-deflection (P-Δ) responses of the studied UHPC ties are depicted in Figure 6.18. Table 6.4 lists the measured loads and deflection at ultimate load, and ultimate deflection at failure. Prior to the application of load by the hydraulic jack, a load of 0.67 kN (0.15 kip) had already been applied to the specimen, resulting from the self-weight of the load cell and steel plates sitting on it. Under center negative bending test, the minimum first cracking load of 12.9 kN was observed for specimen C468C and maximum cracking load of 27 kN for specimen M738C The slight difference in the cross-section might have played a role in the difference in the cracking load. After the formation of the initial crack, the specimens exhibited a consistent linear response in the P-Δ response until the yielding of steel. For rail seat bending test, the first crack of specimen M468R specimen was identified at the bottom of the center of the testing span, occurring at approximately P=28.3 kN (6.3 kips).

In general, under monotonic loading, M738C exhibited a 17% higher ultimate load compared to M468C, mostly controlled by the crushing of concrete at the compression zone of the beam where the load was applied to. M738C demonstrated a 40% lower displacement at the peak load in comparison to M468C. This implies that UHPC ties with grade 468 bars exhibited greater ductility, allowing for increased energy absorption before failure and resulting in higher deflection compared to those with Grade 738 bars.

When compared the effect of steel grade under cyclic loading, C738C demonstrated a 5% higher ultimate load compared to its counterpart, C468C. Both C468C and C738C ties exhibited load capacities comparable to their respective ties tested under monotonic loading. C468C showcased a 4% higher ultimate load capacity than M468C, while C738C displayed an 8% lower ultimate load capacity than M738C. As depicted in Figure 6.18, the stiffness observed during unloading and reloading stages before yielding occurred was remarkably consistent. This uniformity suggests that the bond slip between the reinforcing elements and the surrounding concrete was minimal. This outcome is attributed to the use of Ultra-High-Performance Concrete (UHPC), known for its superior bonding properties and durability. Furthermore, the similarity in stiffness implies that if yielding of the ties were to happen due to unexpected overloading, it would not significantly affect the stiffness of the ties in practical applications. This finding provides reassurance regarding the performance of the ties in real-world scenarios. In essence, it suggests that despite the occurrence of yielding under extreme loads, the overall structural integrity and performance of the ties remain largely unaffected.

Due to the short span length and larger sectional size, M468S sustained more than 50% higher ultimate load when compared to the companion tie tested under monotonic center moment capacity test. The effective

span for support moment capacity test was 559 mm (22 in), whereas the effective span of monotonic center moment capacity test was 1524 mm (60 in).
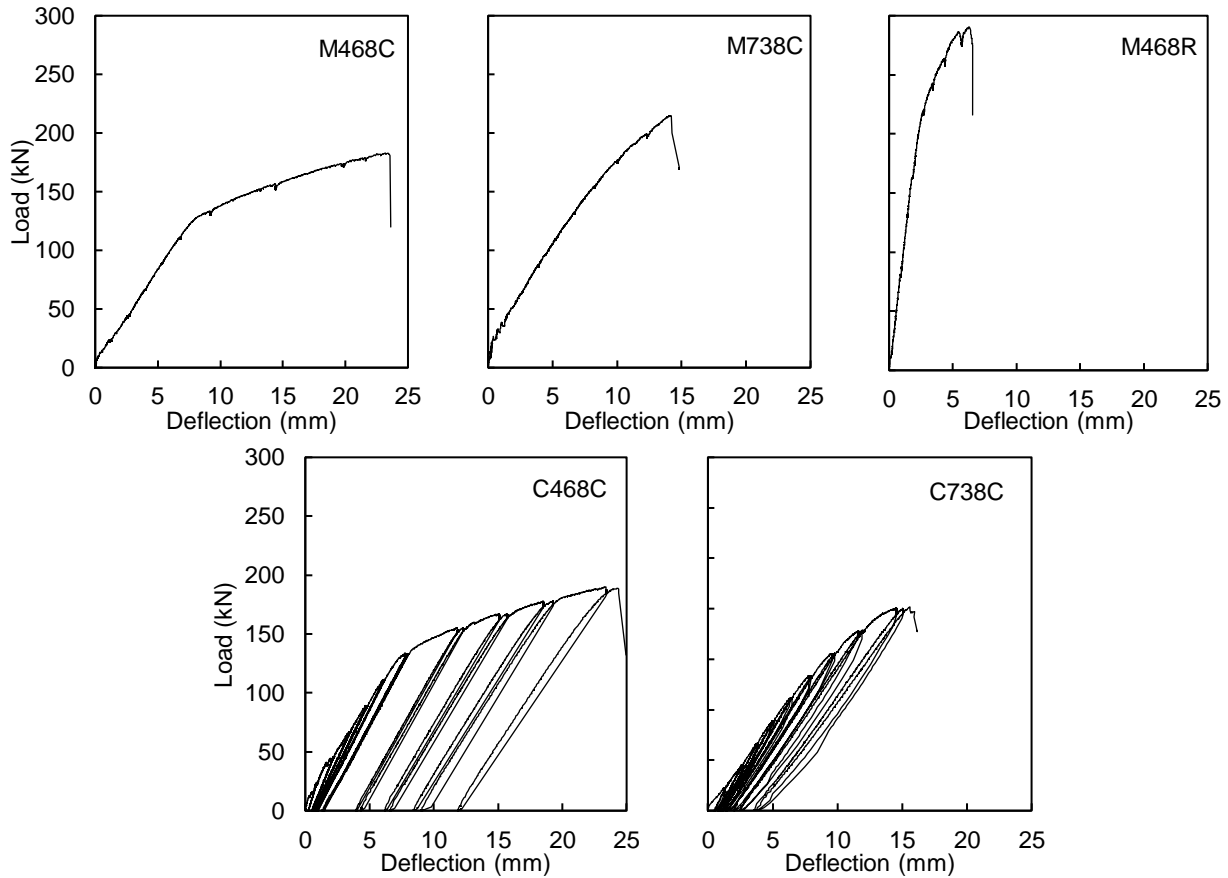
Figure 6.18 Load-deflection responses

6.3.3 Damage Map

Figure 6.19 illustrates the crack pattern observed in the tested UHPC ties. The ties subjected to monotonic loading for the center negative moment test exhibited a flexural-type failure. Vertical cracks initiated from the point of maximum moment (center span) and extended to the location of the top reinforcing bar. Additionally, flexural shear cracks were evident near the support location. Although, the deflection of M468C was much higher than the M738C, M738C showed higher number of cracks than the corresponding M468C. The UHPC ties tested under cyclic loading showed a slightly higher crack frequency than the corresponding ties tested under monotonic loading and the cracks were spread evenly along the length of the span. As illustrated in Figures 6.20d and 6.20e, there was no change in the unloading pattern, as no slope change can be seen in the load-deflection responses. Additionally, no evidence of longitudinal rebar slippage was found for the ties tested under cyclic loading. The cracks observed in the short span test were similar to those in the center negative moment test, originating from the bottom of the center span. However, there was a sudden failure due to the very high shear force generated by the loading of the short span (250 mm) which resulted in a complete separation of concrete from the rebars as shown in Figure 6.20. The theoretical shear capacity of the tie was 281 kN (63.2 kips), while the ultimate load capacity was 288 kN (64.7 kips), surpassing the shear capacity of the tie and triggering sudden shear failure.

132
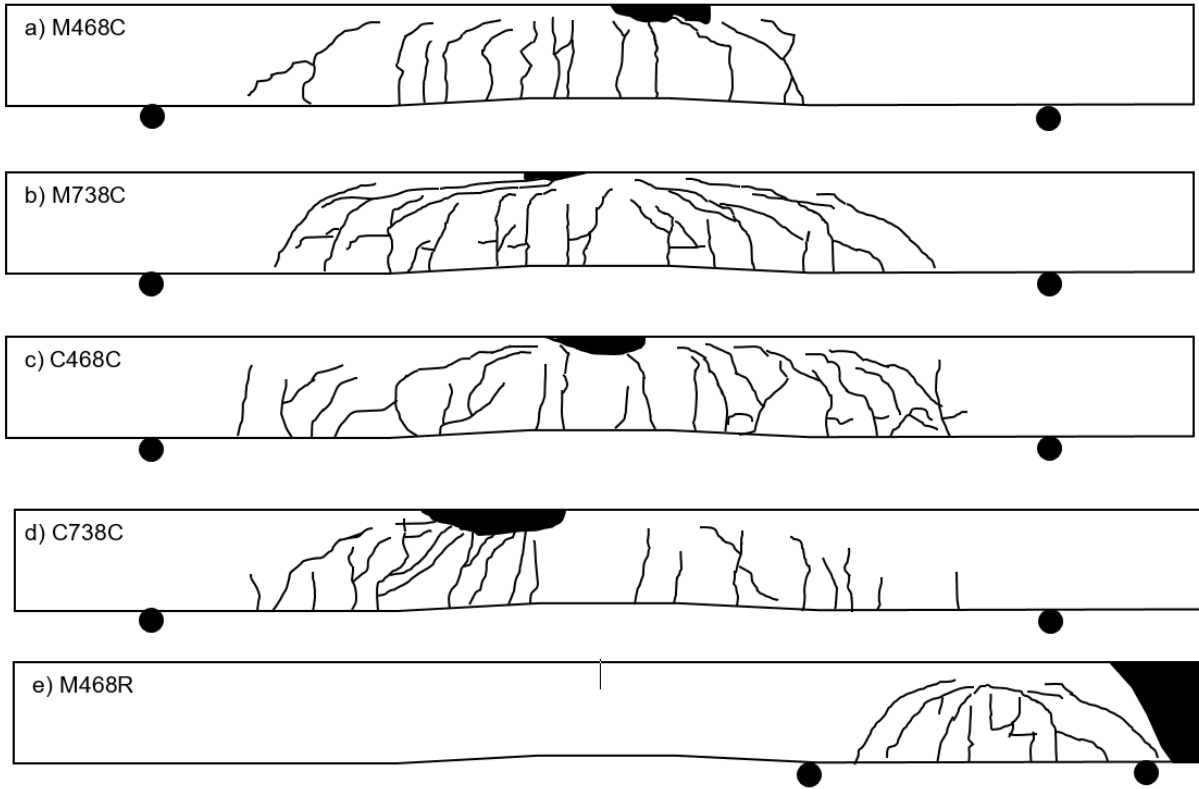
Figure 6.19 Crack patterns of UHPC ties
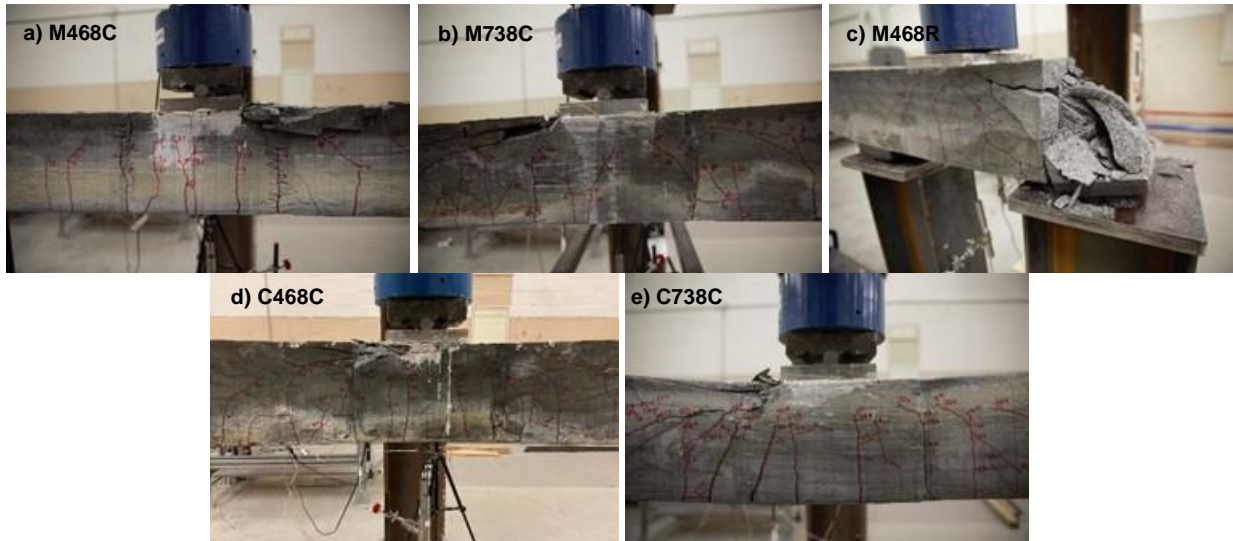
Figure 6.20 Closeup view of the UHPC ties after failure

6.3.4 Crack Development with Load Increment

The maximum crack widths measured at the critical sections are displayed in Figures 6.21. For the ties tested under center negative monotonic and cyclic loading, the critical sections are located at the mid-span. Crack width linearly widened with the increase in load and wider crack can be observed at the load when steel rebars started to yield. Conversely, ties made using 738 MPa (107 ksi) steel showed no significant change in slope in the load-crack width response until they reach its peak load. These findings further support the influence of steel rebar type and grade on the specimens crack widening behavior. When comparing the UHPC ties under monotonic and cyclic loading conditions, crack width at the critical section was found to be 40% higher in the ties made using 468 MPa (67.9 ksi) rebar. This can be attributed to the repeated loading applied to the tie during cyclic loading, which may have caused some permanent deformation. As a result, there was an increase in crack opening due to the unrecoverable plastic deformation of the longitudinal steel bar after yielding. This accumulation of deformation occurred over multiple loading cycles. However, once 738 MPa (107 ksi) steel rebar was used, no differences were observed for the UHPC ties under monotonic and cyclic loading, respectively.

The crack opening observed for the UHPC tie subjected to the rail seat test is considerably wider than that of the other ties tested under center negative bending. This finding can be due to the shorter span length with a higher peak load, which resulted in a wider crack at the critical section. The maximum crack width ranged from 0.05 to 0.10 mm for all the UHPC ties, except for the tie tested at the support location (M468S). In the case of this tie, the maximum inclined crack was reported to be 0.40 mm before it ultimately failed in shear.

134
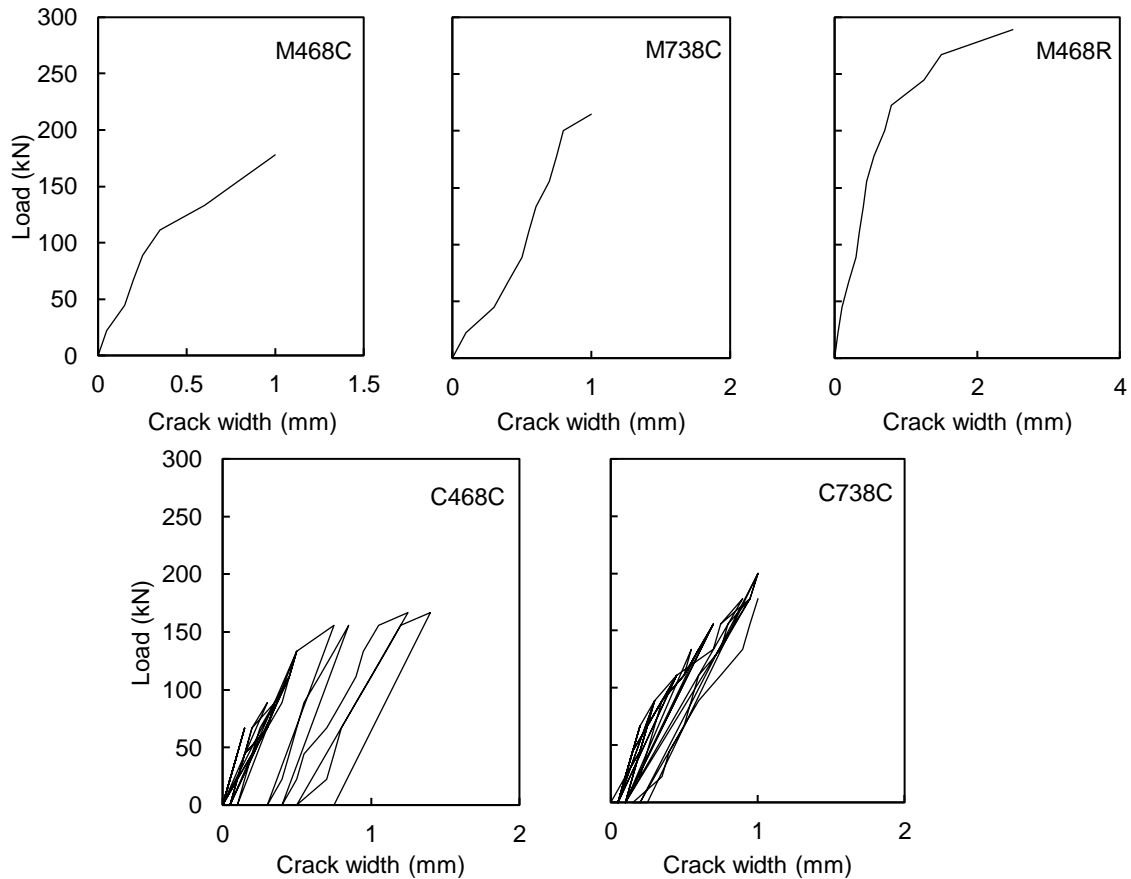
Figure 6.21 Crack width of UHPC ties

6.3.5 Load-Strain Responses

Figures 6.22 depict the load versus strain response of the longitudinal steel rebars at the critical sections of the UHPC ties. A clear yielding of the 468 MPa (67.9 ksi) steel rebars can be observed with a yielding strain of 0.0024 at a load level of 125.9 kN (28.3 kips). However, no clear change of slope in the load-strain response is seen for the UHPC tie made using 738 MPa (107 ksi) steel rebar. This suggests that, unlike the 738 MPa steel bars, the 468 MPa grade steel bars were not negatively affected by the cyclic loading. This finding can be attributed to the post-yield strain of the grade 468 bar, which was significantly higher than the overall strain behavior of the grade 738 bar (Figure 6.3). The ultimate strains of 0.00736 and 0.00735 were recorded before the strain measurement stopped for the UHPC ties made with 468 and 738 MPa (67.9 and 107 ksi) steel rebars, respectively. The load versus strain response for the tie tested at rail seat using 468 MPa (67.9 ksi) steel bars showed a similar trend, with a clear decrease in slope observed after yielding of the rebars at a strain level of 0.00276. For the ties subjected to cyclic loading, there was a notable variation in the strain observed for C468C and C738C. One possible reason for this disparity could be the detachment of the strain gauge from the steel surface after a certain number of cycles, particularly for the C468C tie. This detachment limited comparing the ultimate strain.
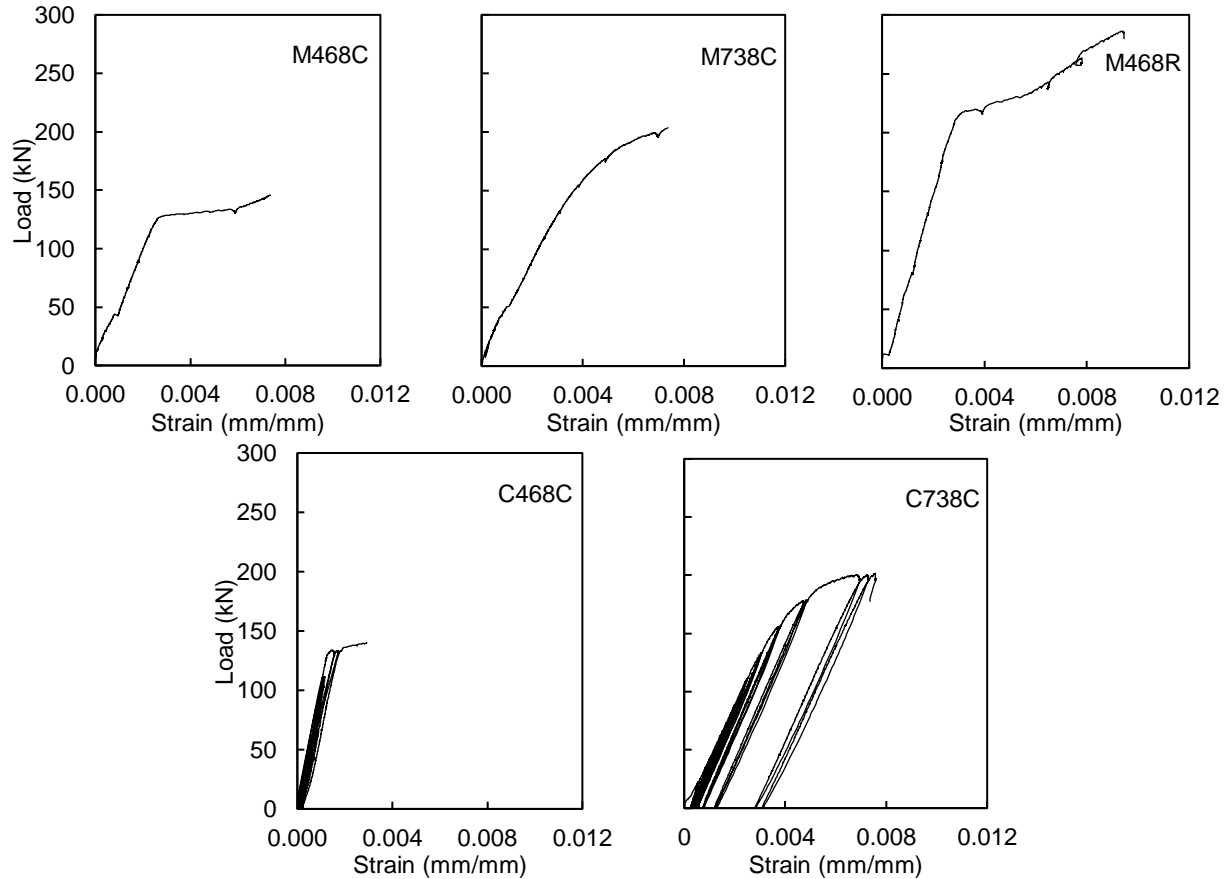
Figure 6.22 Load vs steel strain at the critical sections of UHPC ties

6.4 Conclusions

Based on the results of this study, the following conclusions can be drawn:

- Under monotonic and cyclic loading conditions, the peak load varied with good agreement between predicted and experimental values. The actual monotonic center negative moment testing of both M468C and M738C ties exceeded the required AREMA load capacity.
- Overall, the ties made with grade 468 steel reinforcing bars demonstrated higher ductility and superior performance in energy absorption.
- For both monotonic and cyclic loading, the UHPC ties made with grade 468 steel reinforcing bars exhibited clear yielding and higher deflection. While the UHPC tie with grade 738 reinforcing bars sustained a higher ultimate load, it showed a lower displacement at the peak load.
- Due to its shorter span length and larger sectional size, the UHPC tie tested under monotonic support negative moment capacity test showed a higher ultimate load compared to the tie tested under monotonic center moment capacity test.
- Both C468C and C738C ties performed similarly to their monotonic counterparts, indicating good performance under cyclic loading. C468C showed slightly higher ultimate load capacity and better energy absorption compared to M468C. C738C had the same displacement at peak load as M738C. The UHPC ties made with grade 468 steel bars demonstrated higher ductility, allowing for more plastic deformation and greater deflection before failure under cyclic loading.

136

- The UHPC ties tested under monotonic loading for center negative moment exhibited flexural type failure with vertical cracks initiating from the location of maximum moment (center span). M468C displayed a higher deflection value than the M738C, while the M738C had a higher number of cracks compared to the M468C. The crack pattern in the short span test was similar to the center negative moment test, with sudden shear failure due to the high shear forces.
- The UHPC ties tested under cyclic loading showed slightly higher crack frequencies compared to the ties tested under monotonic loading and the cracks were more evenly distributed along the span length. No obvious slope slippage of the longitudinal rebars was observed in the ties tested under cyclic loading, indicating good bond behavior between the rebars and the concrete.
- For both monotonic and cyclic loading, the load-strain response of the UHPC ties indicated clear yielding for the ties made with 468 MPa steel rebars, while no distinct change in the slope of load-strain response was observed for the tie made with 738 MPa steel rebars.
- Under cyclic loading conditions, the unloading and reloading stiffness before yielding were remarkably similar. This similarity indicates minimal bond slip, which can be attributed to the use of UHPC. Furthermore, it suggests that unexpected overloading causing yielding will not significantly affect the stiffness of the ties in practical applications, thus providing reassurance regarding their performance.

References

1. ACI Committee, & International Organization for Standardization. (2008). Building code requirements for structural concrete (ACI 318-08) and commentary. American Concrete Institute.
2. AREMA Manual for Railway Engineering (2014) American Railway Engineering and Maintenance-of-Way Association (AREMA), Landover, Maryland, V 1, Ch. 30.
3. Hasnat, A., & Ghafoori, N. (2021a). Properties of ultra-high performance concrete using optimization of traditional aggregates and pozzolans. Construction and Building Materials, 299, 123907.
4. Hasnat, A., & Ghafoori, N. (2021b). Abrasion resistance of ultra-high-performance concrete for railway sleepers. Urban Rail Transit, 7(2), 101-116.
5. Hasnat, A., & Ghafoori, N. (2021c). Freeze–Thaw Resistance of Nonproprietary Ultrahigh-Performance Concrete. Journal of Cold Regions Engineering, 35(3), 04021008.
6. Parvez, A., & Foster, S. J. (2017). Fatigue of steel-fibre-reinforced concrete prestressed railway sleepers. Engineering Structures, 141, 241-250.
7. Peters N, Mattson SR. CN 60E concrete tie development. In: AREMA conference proc. Landover, Maryland; 2004.
8. Peters, S. R. (2007). Abrasion Testing of Epoxy-Coated Concrete Ties (Using Symons Product No. 301 Epoxy), JA Cesare & Associates.
9. Sadeghi, J., Tolou Kian, A. R., & Shater Khabbazi, A. (2016). Improvement of mechanical properties of railway track concrete sleepers using steel fibers. Journal of Materials in Civil Engineering, 28(11), 04016131.
10. Shin, H. O., Yang, J. M., Yoon, Y. S., & Mitchell, D. (2016). Mix design of concrete for prestressed concrete sleepers using blast furnace slag and steel fibers. Cement and Concrete Composites, 74, 39-53.
11. Shurpali, A. A., Kernes, R. G., Edwards, J. R., Dersch, M. S., Lange, D. A., & Barkan, C. P. (2013, February). Investigation of the mechanics of rail seat deterioration (RSD) and methods to improve the abrasion resistance of concrete sleeper rail seats. In 10th International heavy haul association conference, New Delhi, India (pp. 4-6).
12. Wu, Z., Shi, C., He, W., & Wu, L. (2016). Effects of steel fiber content and shape on mechanical properties of ultra high performance concrete. Construction and building materials, 103, 8-14.
13. Zi, G., Lee, S. J., Jang, S. Y., Yang, S. C., & Kim, S. S. (2012). Investigation of a concrete railway sleeper failed by ice expansion. Engineering Failure Analysis, 26, 151-163.

14. Certified Mill Test Report (2021) (Heat No. 4107479), CMC Steel Arizona, 11444 E. E Germann Rd., Mesa, AZ 85212.

APPENDIX A

Given,
Tie Length = 7'-9" (2362 mm)
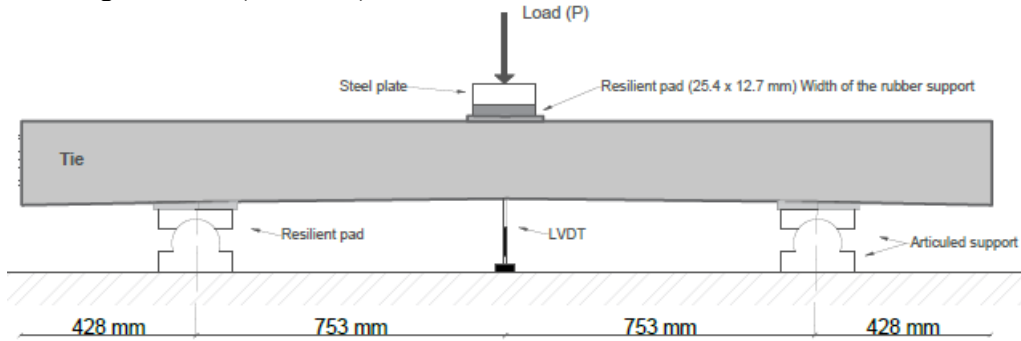
Step 1: Unfactored bending moment at centerline of rail seat
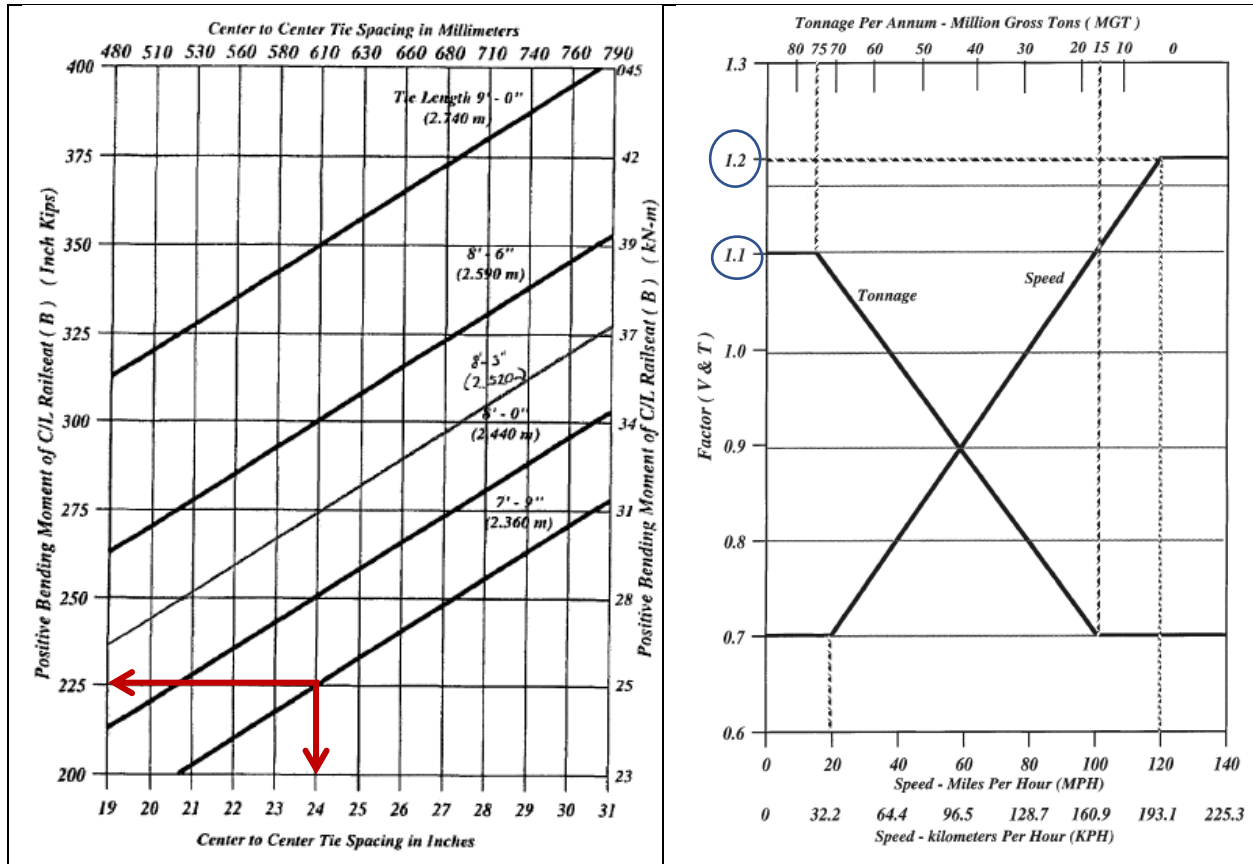
M= BxVxT

M = the factored design positive bending moment at the center of the rail seat

B = the bending moment in inch kips (kN-m) taken from Figure 30-4-3. For a particular tie length and spacing

V = is the speed factor obtained from Figure 30-4-4

T = the tonnage factor obtained from Figure 30-4-4

B =225 k-in for 7'-9" tie with 24" spacing

V =1.2 (for speed>120 MPH)

T= 1.1 (Tonnage> 75 MGT)

$M_{R+} = 225 \times 1.2 \times 1.1 = 297 \ k-in = 24.75 \ k-ft$

Again

Table 30-4-1. Bending Moment Calculations

Tie Length	Rail Seat Negative	Center Negative	Center Positive
7'-9" (2.360 m)	0.72M	1.13M	0.61M
8'-0" (2.440 m)	0.64M	0.92M	0.56M
8'-3" (2.520 m)	0.58M	0.77M	0.51M
8'-6" (2.590 m)	0.53M	0.67M	0.47M
9'-0" (2.740 m)	0.46M	0.57M	0.40M

$M_{R-} = 0.72M_{R+} = 213.84 \ k-in = 17.82 \ k-ft$

$M_{C-} = 1.13M_{R+} = 335.61 \ k-in = \mathbf{27.97 \ k-ft}$

$M_{C+} = 0.61M_{R+} = 181.17 \ k-in = 15.1 \ k-ft$

B =270 k-in for 7'-9" tie with 30" spacing

$M_{R+} = 270 \times 1.2 \times 1.1 = 356.4 \ k-in = 29.7 \ k-ft$

$M_{R-} = 0.72M_{R+} = 256.68 \ k-in = 21.39 \ k-ft$

$M_{C-} = 1.13M_{R+} = 402.72 \ k-in = \mathbf{33.56 \ k-ft}$

$M_{C+} = 0.61M_{R+} = 217.44 \ k-in = 18.12 \ k-ft$

APPENDIX B

Table B1. Plain UHPC compressive strength data for $V_A/V_{cm}=0.80$ (MPa)

ID	1-day			7-day			28-day			90-day		
	A	B	C	A	B	C	A	B	C	A	B	C
C100	62.1	63.9	65.6	106.6	104.3	106.3	136.3	130.2	133.3	150.2	152.0	156.6
F10	56.5	57.5	55.4	101.6	102.2	102.1	137.2	130.6	133.7	-	-	-
F20	52.1	53.9	51.0	94.5	92.5	95.2	132.1	125.5	128.6	156.9	157.0	161.0
F30	52.7	53.3	52.2	102.0	104.3	103.3	137.1	130.5	133.5	158.6	159.1	162.4
F40	48.0	49.0	47.0	95.7	98.3	99.3	128.3	122.1	124.9	155.3	156.4	159.5
N10	55.1	56.9	54.2	98.1	97.8	98.5	133.2	127.1	129.8	164.5	164.0	168.5
N20	53.1	54.9	52.2	98.1	99.7	97.7	131.5	125.0	128.0	149.3	150.1	153.7
N30	47.1	48.9	46.2	97.7	98.4	102.5	135.0	127.7	130.4	141.5	142.4	145.5
S10	58.1	59.9	57.2	93.0	94.2	94.2	128.5	122.0	125.0	165.3	166.7	169.7
S20	62.4	63.6	65.9	115.0	108.5	111.5	136.3	130.1	133.2	147.9	148.6	151.8
S30	63.4	64.6	65.9	111.0	110.7	110.4	136.4	130.4	133.4	150.7	151.4	154.3
SF5	72.4	73.6	75.9	116.0	120.1	117.1	143.7	137.2	140.2	163.5	163.8	167.5
SF10	73.4	74.6	75.9	118.9	120.3	121.5	152.2	145.8	148.8	166.8	166.9	170.7
SF15	74.4	75.6	76.9	123.0	116.4	119.6	152.3	145.9	148.9	-	-	-
F15SF5	70.4	71.6	73.9	115.2	116.1	115.3	143.8	137.3	140.3	145.7	146.5	149.7
N15SF5	69.4	70.6	72.9	116.2	115.9	103.2	142.3	135.9	138.9	148.8	149.7	152.2
S15SF5	68.4	69.6	71.9	100.3	102.6	121.5	132.1	125.5	128.5	137.7	138.4	141.3
F20SF10	63.4	64.6	65.9	119.5	121.6	109.9	151.2	144.8	147.8	129.7	130.4	133.4
N20SF10	58.4	59.6	60.9	109.0	112.5	110.3	147.2	140.6	143.7	134.6	135.7	138.6
S20SF10	64.4	65.6	66.9	109.9	109.0	112.5	141.3	134.7	138.2	146.7	147.5	150.6
F30SF20	52.1	53.9	51.0	97.5	98.9	97.5	130.1	122.6	126.5	137.0	137.7	140.9
N30SF20	55.1	56.9	54.2	91.9	90.7	91.3	122.2	115.6	119.2	131.8	132.5	135.3
S30SF20	56.5	57.5	55.4	99.2	99.1	98.4	131.2	124.8	127.8	147.7	148.8	151.6
F15S15SF10	58.4	59.6	60.9	107.4	108.2	109.2	135.0	128.5	131.3	142.7	147.6	140.1
F10S20SF10	59.4	60.6	61.9	106.1	102.3	102.8	134.2	127.6	130.7	149.4	154.4	146.7
F20N20SF10	53.1	54.9	52.2	73.0	71.8	73.2	127.0	120.5	123.3	153.1	157.0	150.3

Table B2. Plain UHPC compressive strength data for $V_A/V_{cm}=1.0$ (MPa)

ID	1-day			7-day			28-day			90-day		
	A	B	C	A	B	C	A	B	C	A	B	C
C100	61.2	63.8	60.0	98.3	101.1	101.1	130.0	125.9	127.2	149.1	152.6	152.4
F10	53.0	56.0	51.1	87.1	89.7	90.3	127.9	131.0	126.1	-	-	-
F20	50.1	52.9	48.2	85.1	88.2	88.8	130.0	124.9	127.1	152.8	155.8	155.4
F30	49.0	51.9	47.1	81.1	84.2	84.5	124.8	127.9	123.0	148.8	151.7	150.9
F40	45.1	47.9	43.2	70.1	73.2	73.6	117.8	120.9	115.0	144.2	148.8	148.2
N10	52.1	55.0	50.2	93.1	96.1	96.4	128.0	124.9	125.1	142.7	145.7	144.9
N20	53.1	55.9	51.2	85.1	88.2	88.8	124.5	121.5	125.6	142.3	146.7	146.4
N30	49.0	51.9	47.1	83.1	86.2	86.6	119.5	116.5	120.6	130.9	134.6	134.3
S10	64.1	66.9	62.2	99.3	102.1	102.1	128.4	125.6	129.6	146.3	150.7	149.9
S20	63.0	66.0	61.1	96.1	99.2	99.5	130.4	127.5	131.6	146.8	149.7	149.4
S30	66.9	69.8	65.0	100.3	103.1	103.1	128.4	125.6	129.6	145.3	149.7	148.9
SF5	70.0	72.9	68.1	110.3	113.1	113.1	141.4	138.5	142.5	169.8	172.9	172.4
SF10	73.1	75.9	71.2	120.3	123.1	123.1	148.4	145.5	149.5	172.0	177.0	176.4
SF15	74.1	77.0	72.2	122.3	125.1	125.1	152.4	149.5	153.5	175.8	179.0	178.4
F15SF5	63.0	66.0	61.1	109.3	112.1	112.1	135.5	137.8	138.4	163.8	166.9	166.4
N15SF5	58.9	61.8	57.0	103.3	106.1	106.1	132.5	134.8	135.4	156.8	159.8	159.4
S15SF5	65.9	68.8	65.0	111.3	114.1	114.1	130.4	132.8	133.3	157.0	160.8	160.4
F20SF10	58.9	61.8	57.0	99.3	102.1	102.1	138.5	140.8	141.4	142.0	145.7	144.9
N20SF10	55.9	58.8	54.0	101.3	104.1	104.1	134.5	136.8	137.4	148.3	152.7	152.4
S20SF10	61.2	63.8	60.0	107.1	105.1	105.1	133.5	135.8	136.4	143.7	146.7	146.4
F30SF20	50.9	53.8	48.1	85.3	83.3	83.7	124.9	127.0	128.0	142.3	146.7	146.4
N30SF20	52.1	55.0	50.2	88.1	85.3	85.6	118.5	120.9	121.5	127.6	130.6	129.8
S30SF20	53.1	55.9	51.2	89.7	92.3	88.8	120.6	122.9	123.4	132.7	135.6	135.4
F15S15SF10	51.4	53.6	49.3	91.7	93.3	90.8	122.4	126.1	126.3	138.8	141.6	141.4
F10S20SF10	46.1	48.9	44.1	86.9	89.5	85.0	129.2	128.9	122.8	143.0	148.2	146.4
F20N20SF10	44.1	46.9	42.2	69.1	71.8	67.0	121.0	120.4	114.0	146.8	151.2	148.9

Table B3. Plain UHPC compressive strength data for $V_A/V_{cm}=1.2$ (MPa)

ID	1-day			7-day			28-day			90-day		
	A	B	C	A	B	C	A	B	C	A	B	C
C100	60.4	61.8	61.1	97.9	102.1	98.4	123.9	126.3	123.4	152.7	150.2	147.2
F10	53.2	54.9	52.7	89.0	93.2	89.6	120.6	124.5	121.4	149.1	152.6	149.4
F20	51.5	52.9	50.8	82.0	86.1	82.5	120.6	123.4	120.3	148.8	151.7	148.4
F30	49.3	50.7	49.1	78.9	82.9	79.3	117.5	121.5	118.3	148.0	151.7	148.4
F40	45.2	47.0	44.8	71.9	75.8	72.2	110.5	114.5	111.2	140.2	144.7	141.3
N10	53.3	54.7	52.8	85.9	90.1	86.4	119.7	122.5	119.3	144.7	147.8	144.3
N20	50.7	53.0	51.3	82.0	86.1	82.5	116.5	120.4	117.3	135.3	139.7	136.2
N30	49.6	50.4	49.3	78.9	82.9	79.3	113.5	117.4	114.3	146.2	149.9	146.6
S10	61.0	61.2	61.3	93.9	98.2	94.5	120.6	124.5	121.4	140.2	144.7	141.3
S20	55.4	56.6	54.9	86.8	91.1	87.3	117.7	120.4	117.3	137.6	140.6	137.3
S30	56.5	57.7	56.0	89.0	93.2	89.6	116.5	120.4	117.3	165.3	170.0	166.7
SF5	64.1	66.0	63.6	106.7	111.3	107.4	129.9	132.4	129.4	162.9	166.0	162.5
SF10	70.4	71.6	70.2	114.7	119.4	115.4	135.5	139.5	136.4	-	-	-
SF15	71.2	72.7	70.8	116.7	121.5	117.5	137.7	140.6	137.4	151.9	154.6	151.4
F15SF5	60.2	61.6	59.8	98.1	102.5	98.8	126.4	130.5	127.3	148.3	152.7	148.4
N15SF5	58.0	59.5	57.6	93.9	98.2	94.5	125.6	128.5	125.3	147.6	150.7	147.3
S15SF5	63.0	64.4	62.6	101.7	106.3	102.4	121.4	125.6	122.2	130.0	133.6	130.3
F20SF10	58.1	59.6	57.7	94.9	99.3	95.5	128.6	132.4	129.4	143.0	146.7	143.3
N20SF10	58.3	59.7	57.9	96.8	101.3	97.4	127.4	131.5	128.3	143.3	147.8	144.3
S20SF10	61.8	63.3	61.5	98.1	102.5	98.8	128.7	131.5	128.3	126.6	129.6	126.2
F30SF20	44.1	45.5	43.7	72.9	76.8	73.2	113.5	117.4	114.3	118.5	122.5	119.3
N30SF20	43.7	45.3	43.4	73.9	77.9	74.3	111.6	114.5	111.2	123.6	126.6	123.2
S30SF20	49.1	50.4	48.8	81.0	85.0	81.4	115.6	118.4	115.3	125.7	128.6	125.3
F15S15SF10	46.9	48.3	46.5	79.9	84.0	80.3	113.5	117.4	114.3	128.3	132.6	129.2
F10S20SF10	44.8	46.3	45.3	78.0	81.9	78.4	110.0	113.1	112.1	135.0	139.9	135.3
F20N20SF10	38.8	40.3	40.1	69.9	73.7	70.2	113.0	104.0	108.4	-	-	-

Table B4. Plain UHPC splitting-tensile strength data for $V_A/V_{cm}=0.80$, $V_A/V_{cm}=1.00$, and $V_A/V_{cm}=1.20$ (MPa)

ID	0.80			1.00			1.20		
	A	B	C	A	B	C	A	B	C
C100	9.5	9.9	8.7	9.6	9.0	9.4	9.3	9.0	9.2
F10	9.5	9.9	8.7	9.5	8.9	9.2	9.3	9.0	9.1
F20	9.7	10.1	8.9	9.5	9.0	9.2	9.2	8.9	9.0
F30	9.4	9.8	8.6	9.2	8.7	9.0	8.9	8.7	8.8
F40	9.2	9.7	8.5	8.8	8.4	8.6	8.2	8.0	8.1
N10	9.5	9.9	8.7	9.5	9.0	9.2	9.2	8.9	9.0
N20	9.4	9.8	8.6	9.2	8.7	8.9	9.1	8.8	8.9
N30	8.8	9.3	8.1	8.9	8.5	8.7	8.7	8.5	8.6
S10	8.8	9.3	8.1	9.2	8.6	9.0	9.1	8.8	9.0
S20	9.5	9.9	8.7	9.5	8.9	9.3	9.4	9.1	9.3
S30	8.9	9.4	8.2	9.2	8.6	9.0	9.0	8.7	8.9
SF5	10.0	10.3	9.0	9.9	9.2	9.6	9.6	9.3	9.5
SF10	10.8	11.0	9.7	10.4	9.7	10.1	10.0	9.7	9.9
SF15	11.2	11.3	10.0	10.9	10.2	10.6	10.5	10.2	10.4
F15SF5	10.0	10.3	9.0	9.9	9.3	9.6	9.7	9.4	9.6
N15SF5	9.7	10.1	8.9	9.8	9.2	9.5	9.5	9.2	9.3
S15SF5	9.6	10.0	8.8	9.8	9.2	9.6	9.7	9.4	9.6
F20SF10	10.0	10.3	9.0	10.2	9.6	9.9	9.4	9.1	9.2
N20SF10	9.8	10.2	8.9	10.1	9.5	9.8	9.3	9.0	9.1
S20SF10	10.6	10.8	9.6	10.1	9.5	9.8	9.5	9.2	9.3
F30SF20	9.5	9.9	8.7	9.5	8.9	9.2	8.9	8.6	8.7
N30SF20	10.3	10.6	9.4	9.6	9.1	9.3	8.7	8.4	8.5
S30SF20	9.4	9.8	8.6	9.0	8.5	8.7	8.5	8.2	8.3
F15S15SF10	-	-	-	8.9	8.3	8.6	8.8	8.5	8.6
F10S20SF10	9.0	9.1	9.4	9.4	8.9	9.2	9.3	9.1	9.2
F20N20SF10	9.1	9.1	9.3	9.4	9.0	9.2	9.2	9.0	9.1

APPENDIX C

Table C1. Compressive strength of the studied UHPCs

ID	28-day (MPa)				365-day (MPa)		
	A	B	C	D	A	B	C
C100	125.3	126.4	125.2	121.3	158.5	161.3	157.2
F10	125.4	122.5	123.7	117.2	160.5	165.8	160.7
F20	123.5	122.3	124.3	118.4	165.1	164.2	162.6
MS5	135.4	135.6	130.5	128.5	177.2	176.3	173.1
F15MS5	137.4	141.5	135.6	128.8	178.4	183.8	177.8
F10MS10	138.5	146.9	140.2	133.6	187.2	183.2	178.4
F15MS15	149.8	145.6	145.2	140.2	193.2	196.9	191.1
C100-3%	135.7	131.4	125.7	124.4	159.5	165.4	159.0
F10-3%	139.5	137.2	140.0	134.9	161.6	166.8	160.7
F20-3%	125.6	131.4	130.3	123.1	164.0	166.5	162.1
MS5-3%	129.1	127.4	126.2	124.9	175.8	179.5	177.7
F15MS5-3%	145.5	147.4	140.4	139.0	177.8	183.5	182.0
F10MS10-3%	143.4	149.9	144.7	140.0	188.5	185.4	184.1
F15MS15-3%	154.1	155.6	149.9	147.1	193.8	193.3	195.5

Table C2. Absorption of the studies UHPCs

Mixture	ID	Absorption-immersion (%)	Absorption-immersion and boiling (%)	Bulk density (after immersion) (kg/m^3)	Bulk density (immersion and boiling) (kg/m^3)	Apparent density (kg/m^3)	Vol. of permeable void (%)
C100	A	1.196	1.473	2312	2319	2365	3.366
	B	1.553	1.899	2344	2352	2414	4.384
	C	1.777	2.045	2350	2357	2424	4.722
SF5	A	1.082	1.244	2443	2447	2491	3.006
	B	0.996	1.173	2422	2426	2467	2.812
	C	1.159	1.310	2434	2438	2484	3.151
F20	A	1.285	1.545	2425	2431	2486	3.699
	B	1.302	1.550	2415	2420	2475	3.695
	C	1.224	1.490	2413	2420	2472	3.552
F15SF5	A	1.020	1.133	2346	2349	2385	2.632
	B	1.057	1.168	2340	2342	2380	2.704
	C	0.827	0.955	2345	2348	2378	2.221
F10SF10	A	0.925	1.076	2323	2326	2360	2.477
	B	0.967	1.120	2316	2319	2354	2.568
	C	0.905	1.065	2304	2308	2340	2.431
C100-3%	A	1.476	1.660	2447	2451	2512	4.004
	B	1.200	1.415	2448	2453	2505	3.423
	C	1.486	1.703	2438	2443	2505	4.090
SF5-3%	A	0.765	0.937	2466	2470	2505	2.294
	B	0.925	1.017	2464	2466	2503	2.483
	C	0.528	0.690	2454	2458	2483	1.685
F20-3%	A	1.340	1.614	2462	2469	2528	3.922
	B	1.234	1.501	2504	2511	2569	3.712
	C	1.434	1.728	2485	2493	2559	4.235
F15SF5-3%	A	0.991	1.092	2562	2564	2609	2.771
	B	1.024	1.133	2553	2556	2602	2.864
	C	1.017	1.108	2561	2563	2608	2.808
F10SF10-3%	A	0.547	0.646	2532	2535	2560	1.626
	B	0.571	0.667	2531	2534	2560	1.679
	C	0.466	0.589	2532	2535	2558	1.486

Note: 1 kg/m^3 = 0.0624 lb/yd^3

Table C3. RCPT results of plain UHPCs

ID	Charge passed (Coulomb)			
	A	B	C	D
C100	724	626	695	714
F10	756	835	778	763
F20	885	827	870	844
SF5	476	435	462	450
F15SF5	436	354	406	422
F10SF10	296	235	282	279
F15SF15	216	165	196	208

Table C4. Surface resistivity data of the studied plain UHPCs

ID	SAMPLE	TIME (MIN)						
		0	10	20	30	40	50	60
C100	SAMPLE 1	53.6	54.6	55.7	52.6	51.1	50.5	49.5
		47	51.5	46.2	47.7	46.6	51.1	50.4
		49.8	46.2	46.7	47.0	46.9	51.2	50.9
		47.7	49.9	54.0	46.8	47.8	49.2	51.1
	SAMPLE 2	53.3	51.2	50.8	51.3	49.7	48.9	44.9
		46.5	47.9	44.8	46.4	48.6	47.8	48.2
		55.1	51.1	50.1	49.3	48.8	48.6	48.7
		52.7	53.3	53.1	50.8	49.9	51.7	50.2
	SAMPLE 3	52.3	51.1	50.6	50.6	53.3	49.5	48.9
		52.3	52.8	50.9	52.0	46.9	46.8	48.6
		53.2	51.0	50.7	48.0	46.7	49.5	48.3
		49.5	49.4	50.4	50.3	47.7	49.5	45.9
SF5	SAMPLE 1	94.3	90.1	79.1	75.7	72.3	72.7	68.5
		88.2	81.1	78.9	78.3	75.7	77.7	76.5
		87.2	80.8	73.2	77.7	77.9	81.5	82.5
		82.8	84.3	83.5	78.0	80.6	84.2	84.6
	SAMPLE 2	88.7	86.8	84.9	76.5	79.4	79.5	72.5
		82.7	83.9	75.6	80.2	81.8	74.6	76.8
		83.3	86.5	78.8	84.2	82.5	84.5	77.5
		89.6	86.9	84.2	81.9	78.0	76.4	77.5
	SAMPLE 3	85	87.7	73.5	77.7	75.0	81.6	74.3
		86.8	92.0	84.2	83.0	78.6	79.1	76.2
		76.8	92.0	83.5	82.0	79.8	78.7	79.8
		84.1	79.9	79.9	83.5	77.3	79.0	76.4
F10	SAMPLE 2	45.8	46.8	48.6	47.5	45.0	42.8	42.5
		47.1	46.1	47.1	45.3	45.1	44.7	44.2
		44.7	48.8	50.2	48.1	45.9	45.5	44.9
		45.1	48.4	48.6	45.5	43.4	44.7	40.8
	SAMPLE 1	47.4	47.1	48.0	45.3	45.5	44.3	44.9
		47.1	47.9	48.6	47.1	45.9	44.4	46.5
		47.9	45.6	48.9	45.7	45.6	43.3	43.7
		47.2	48.1	46.2	45.8	44.7	44.3	44.4
F20	SAMPLE 0	48.6	47.3	47.3	46.6	47.3	45.5	45.4
		49.1	47.3	48.3	45.2	44.2	43.5	43.4
		46.1	46.6	44.9	44.4	44.2	42.5	42.5
		48.2	47.6	48.1	47.2	46.5	45.0	44.9
	SAMPLE 1	50.3	47.7	48.6	48.5	45.9	43.7	43.3
		49	47.0	47.1	46.5	46.0	45.6	45.1
		49.5	49.8	50.2	49.1	46.8	46.4	45.8

ID	SAMPLE	TIME (MIN)						
		0	10	20	30	40	50	60
		49.2	49.4	48.6	46.4	44.3	45.6	41.6
		48.3	48.0	48.0	46.2	46.4	45.2	45.8
	SAMPLE 2	48	48.9	48.6	48.0	46.8	45.8	47.4
		48.9	46.5	48.9	46.6	46.5	44.2	44.5
		48.1	49.1	46.2	46.7	45.6	45.2	45.3
		49.6	48.2	47.3	47.5	48.2	46.4	46.3
	SAMPLE 3	50.1	48.2	48.3	46.1	45.1	44.4	44.3
		47	47.5	44.9	45.2	45.1	43.4	43.3
		49.5	48.6	48.1	48.1	47.4	45.9	45.8
		112	111.7	109	105.9	105.2	104.9	94.9
	SAMPLE 1	111	111.4	108.4	104.1	104.5	103.5	106.7
		114.7	108.4	97	100.7	101.4	102.1	96.4
		107.8	100.3	103.8	97.8	99.9	97.5	102.1
		107.1	104	99.2	96.4	98.1	97	95.9
F15SF5	SAMPLE 2	101	98	99.3	101.3	94.7	98.3	94.3
		110.4	104.2	105.1	103.2	102.6	96.5	99.8
		111.6	99.1	107	99.1	98	93.4	99.2
		105	104.3	102.9	98.4	103.4	95.3	100.1
	SAMPLE 3	110	110	103.9	100.5	99.1	105	97
		107.6	102.9	107.2	101.3	99.6	101	105.6
		103	108	96.5	106.2	100.1	100	99
		223	231	233	233	217	215	212
	SAMPLE 1	225	215	211	215	196	204	201
		224	223	219	228	207	205	209
		224	217	217	189	188	184	181
		224	220	217	218	213	213	202
F10SF10	SAMPLE 2	232	232	212	217	218	214	214
		227	219	220	216	209	217	217
		231	228	220	213	208	208	208
		227	224	213	211	212	208	204
	SAMPLE 3	215	214	220	210	204	213	201
		212	222	213	213	211	207	204
		213	202	201	207	204	202	206
		279.9	274.9	279.1	242.9	242.9	240.2	239.1
	SAMPLE 1	270.4	258.9	258.9	265	259.3	259	259.5
		275.3	274.8	279	269.9	258.4	267.6	257.1
		273.2	281.2	271.6	268.8	265.4	264.2	259.9
F15SF15		287.7	283.4	271.5	269.4	273.3	265.2	260.5
		285.6	279.3	275.8	277.4	270.6	269.8	254.3
	SAMPLE 2	290.6	278.2	278.2	273.3	265.5	273.6	273.7
		292.2	289.7	281.3	271.7	265.6	267.5	265.9

ID	SAMPLE	TIME (MIN)						
		0	10	20	30	40	50	60
	SAMPLE 3	284.9	294.2	297.4	294.2	276.1	273.5	269.3
		286.9	288.3	264.5	271.3	274.6	269.7	270.1
		282	277.3	273.7	283.3	261.5	263.9	267.7
		280.2	274.5	264.9	270.6	249.9	262.8	258.9

APPENDIX D

Table D1. Effect of F-T on compressive strength of UHPCs

ID	28-day compressive strength (MPa)				28-day compressive strength-after 70 FT (MPa)		
	A	B	C	D	A	B	C
C100	125.1	127.0	123.4	125.7	156.4	152.7	151.7
SF5	134.2	131.0	135.1	130.4	170.9	165.1	167.6
F15SF5	129.1	132.8	124.4	134.2	176.3	165.7	168.3
N15SF5	125.4	128.6	128.5	125.7	167.5	160.5	163.0
F20	126.2	120.5	123.9	119.7	156.0	151.0	151.6
F30	121.6	120.5	118.6	121.4	152.6	149.4	150.2
C100-H2%	129.8	125.7	125.2	128.4	157.2	152.9	154.6
SF5-H2%	135.3	137.3	132.9	136.4	172.4	167.6	169.2
F15SF5-H2%	137.0	138.3	134.4	133.9	176.8	171.2	173.6
N15SF5-H2%	131.1	130.5	131.7	130.9	168.8	167.2	167.5
F20-H2%	125.6	123.9	126.5	124.2	156.8	153.2	154.6
F30-H2%	125.8	124.2	129.5	128.8	156.9	151.1	152.5
C100-S2%	131.7	123.5	130.2	124.9	161.0	153.0	155.5
SF5-S2%	139.5	131.5	136.2	132.5	173.0	167.0	168.6
F15SF5-S2%	132.5	137.5	133.5	136.2	177.3	172.7	174.0
N15SF5-S2%	133.2	132.1	133.5	132.5	170.3	167.7	168.4
F20-S2%	126.4	124.8	125.5	123.2	158.3	155.7	156.3
F30-S2%	126.3	125.4	130.6	127.4	157.4	150.7	152.0
C100-H3%	130.7	130.3	129.7	129.0	161.3	158.7	159.7
SF5-H3%	140.6	138.1	137.0	140.0	176.4	171.6	173.2
F15SF5-H3%	138.1	139.4	138.6	140.4	182.7	173.3	175.0
N15SF5-H3%	135.9	136.5	135.7	137.5	172.7	169.3	170.3
F20-H3%	128.3	126.5	125.5	128.5	163.4	156.6	158.2
F30-H3%	129.1	130.2	132.6	128.4	160.0	153.0	154.5
C100-S3%	125.8	134.0	132.8	127.2	165.8	156.2	158.5
SF5-S3%	138.7	139.7	140.3	137.7	180.0	173.0	174.6
F15SF5-S3%	140.0	141.6	144.4	138.4	180.6	177.4	178.4
N15SF5-S3%	131.6	134.1	135.6	132.8	177.0	165.0	167.5
F20-S3%	126.2	127.6	129.2	126.8	162.7	157.3	158.5
F30-S3%	131.0	132.5	132.5	133.5	159.3	154.7	155.5

Table D2. Effect of F-T on Splitting tensile strength of UHPCs

ID	28-day splitting-tensile strength (MPa)				Splitting-tensile strength-after 70 FT (MPa)		
	A	B	C	D	A	B	C
C100	6.1	6.1	6.0	-	7.4	7.2	7.0
SF5	6.3	6.2	6.2	-	7.8	7.5	7.4
F15SF5	6.2	6.4	6.3	-	7.7	7.5	7.5
N15SF5	6.3	6.1	6.1	-	7.7	7.4	7.2
F20	6.1	5.9	5.9	-	7.4	7.0	6.9
F30	6.0	5.8	5.8	-	7.2	7.0	7.0
C100-H2%	7.1	6.9	6.9	-	8.4	8.2	8.1
SF5-H2%	7.5	7.4	7.3	-	8.7	8.6	8.5
F15SF5-H2%	7.5	7.4	7.4	-	8.8	8.6	8.6
N15SF5-H2%	7.4	7.2	7.2	-	8.8	8.5	8.4
F20-H2%	7.2	6.9	6.9	-	8.6	8.2	8.1
F30-H2%	6.9	7.0	6.9	-	8.3	8.1	8.0
C100-S2%	7.1	7.0	7.0	-	8.4	8.3	8.2
SF5-S2%	7.4	7.3	7.3	-	8.9	8.5	8.5
F15SF5-S2%	7.5	7.4	7.3	-	8.8	8.7	8.6
N15SF5-S2%	7.4	7.3	7.2	-	8.7	8.6	8.6
F20-S2%	7.2	7.1	7.0	-	8.6	8.2	8.0
F30-S2%	7.1	7.1	7.0	-	8.5	8.1	8.1
C100-H3%	8.3	8.1	8.1	-	9.8	9.6	9.6
SF5-H3%	8.7	8.4	8.4	-	10.1	9.9	9.9
F15SF5-H3%	8.9	8.6	8.6	-	10.4	10.0	10.0
N15SF5-H3%	8.7	8.5	8.5	-	10.2	9.9	10.0
F20-H3%	8.2	8.2	8.1	-	9.7	9.5	9.6
F30-H3%	8.2	8.0	8.0	-	9.8	9.3	9.3
C100-S3%	8.4	8.3	8.2	-	9.9	9.7	9.7
SF5-S3%	8.7	8.5	8.5	-	10.3	9.9	9.8
F15SF5-S3%	8.8	8.7	8.7	-	10.4	10.2	10.2
N15SF5-S3%	8.8	8.5	8.6	-	10.5	9.9	9.9
F20-S3%	8.4	8.2	8.2	-	10.1	9.5	9.4
F30-S3%	8.4	8.1	8.0	-	9.9	9.4	9.3

Table E1. Depth of abrasion of UHPCs at different time

Mixture ID	Time interval (min)																				
	0	1	2	3	4	5	6	7	8	9	10	11	12	13	14	15	16	17	18	19	20
	Depth of Abrasion (mm)-28 days																				
C100	0.00	0.05	0.08	0.14	0.18	0.23	0.28	0.32	0.35	0.38	0.40	0.42	0.43	0.44	0.45	0.46	0.47	0.47	0.48	0.48	0.49
SF5	0.00	0.07	0.12	0.17	0.22	0.27	0.32	0.35	0.38	0.41	0.43	0.45	0.47	0.48	0.49	0.50	0.51	0.52	0.53	0.54	0.55
F20	0.00	0.10	0.20	0.30	0.38	0.46	0.51	0.53	0.55	0.57	0.58	0.59	0.60	0.61	0.62	0.62	0.63	0.63	0.64	0.64	0.65
F30	0.00	0.08	0.15	0.21	0.26	0.31	0.36	0.40	0.44	0.48	0.51	0.53	0.55	0.57	0.59	0.60	0.61	0.62	0.62	0.63	0.63
F15SF5	0.00	0.04	0.08	0.11	0.15	0.20	0.25	0.30	0.35	0.39	0.40	0.41	0.42	0.43	0.44	0.44	0.44	0.44	0.45	0.45	0.45
N15SF5	0.00	0.04	0.08	0.12	0.16	0.21	0.27	0.31	0.33	0.34	0.36	0.37	0.38	0.39	0.40	0.42	0.42	0.43	0.44	0.45	0.46
C100-H2%	0.00	0.10	0.20	0.29	0.35	0.40	0.44	0.47	0.50	0.52	0.53	0.54	0.55	0.55	0.56	0.57	0.57	0.58	0.58	0.59	0.59
SF5-H2%	0.00	0.07	0.13	0.18	0.24	0.28	0.33	0.37	0.39	0.41	0.41	0.42	0.43	0.43	0.44	0.44	0.44	0.45	0.45	0.46	0.46
F20-H2%	0.00	0.07	0.15	0.23	0.30	0.35	0.40	0.43	0.46	0.48	0.49	0.50	0.51	0.51	0.51	0.52	0.52	0.53	0.53	0.54	0.54
F30-H2%	0.00	0.06	0.13	0.20	0.26	0.30	0.34	0.38	0.41	0.43	0.44	0.45	0.45	0.46	0.46	0.46	0.47	0.47	0.47	0.48	0.48
F15SF5-H2%	0.00	0.07	0.14	0.20	0.25	0.31	0.36	0.41	0.43	0.45	0.46	0.47	0.47	0.48	0.48	0.48	0.49	0.49	0.50	0.50	0.50
N15SF5-H2%	0.00	0.07	0.14	0.20	0.26	0.32	0.35	0.38	0.39	0.40	0.41	0.42	0.43	0.44	0.45	0.46	0.47	0.48	0.49	0.50	0.51
C100-S2%	0.00	0.06	0.11	0.17	0.22	0.27	0.31	0.34	0.36	0.38	0.40	0.41	0.42	0.43	0.44	0.45	0.46	0.47	0.49	0.50	0.51
SF5-S2%	0.00	0.04	0.08	0.13	0.17	0.21	0.24	0.27	0.28	0.30	0.32	0.33	0.35	0.36	0.37	0.39	0.40	0.41	0.42	0.43	0.44
F20-S2%	0.00	0.05	0.09	0.14	0.18	0.22	0.26	0.29	0.32	0.34	0.36	0.37	0.38	0.39	0.40	0.41	0.42	0.43	0.44	0.45	0.46
F30-S2%	0.00	0.05	0.09	0.14	0.18	0.23	0.25	0.28	0.31	0.33	0.34	0.35	0.36	0.37	0.39	0.40	0.41	0.42	0.43	0.44	0.45
F15SF5-S2%	0.00	0.05	0.10	0.15	0.20	0.25	0.30	0.33	0.35	0.37	0.38	0.39	0.40	0.41	0.42	0.44	0.45	0.46	0.47	0.48	0.48
N15SF5-S2%	0.00	0.05	0.11	0.16	0.21	0.26	0.31	0.35	0.37	0.39	0.41	0.42	0.43	0.44	0.45	0.46	0.47	0.47	0.48	0.48	0.49
C100-H3%	0.00	0.10	0.17	0.22	0.26	0.29	0.31	0.33	0.34	0.36	0.37	0.39	0.40	0.41	0.42	0.43	0.44	0.45	0.46	0.47	0.48
SF5-H3%	0.00	0.04	0.09	0.14	0.19	0.24	0.27	0.30	0.32	0.34	0.35	0.37	0.38	0.39	0.40	0.41	0.42	0.42	0.42	0.43	0.43
F20-H3%	0.00	0.06	0.11	0.17	0.22	0.27	0.30	0.34	0.36	0.37	0.39	0.40	0.41	0.42	0.43	0.44	0.44	0.45	0.45	0.46	0.46
F30-H3%	0.00	0.06	0.11	0.16	0.22	0.26	0.29	0.33	0.35	0.37	0.38	0.39	0.41	0.42	0.43	0.43	0.44	0.45	0.45	0.45	0.46
F15SF5-H3%	0.00	0.05	0.10	0.15	0.20	0.24	0.28	0.31	0.33	0.35	0.36	0.38	0.39	0.40	0.41	0.42	0.42	0.43	0.43	0.44	0.44
N15SF5-H3%	0.00	0.06	0.11	0.15	0.21	0.26	0.29	0.32	0.34	0.36	0.38	0.39	0.40	0.41	0.42	0.43	0.43	0.44	0.45	0.45	0.46
C100-S3%	0.00	0.11	0.21	0.26	0.30	0.33	0.36	0.37	0.38	0.40	0.41	0.42	0.43	0.44	0.45	0.45	0.46	0.46	0.47	0.47	0.48

Mixture ID	Time interval (min)																				
	0	1	2	3	4	5	6	7	8	9	10	11	12	13	14	15	16	17	18	19	20
	Depth of Abrasion (mm)-28 days																				
SF5-S3%	0.00	0.07	0.14	0.20	0.24	0.28	0.30	0.32	0.34	0.35	0.36	0.37	0.38	0.39	0.39	0.40	0.41	0.41	0.42	0.43	0.43
F20-S3%	0.00	0.11	0.18	0.23	0.27	0.31	0.33	0.34	0.36	0.37	0.38	0.39	0.40	0.41	0.42	0.43	0.44	0.44	0.45	0.45	0.46
F30-S3%	0.00	0.10	0.17	0.23	0.27	0.30	0.32	0.34	0.36	0.37	0.39	0.40	0.41	0.42	0.42	0.43	0.44	0.44	0.44	0.45	0.45
F15SF5-S3%	0.00	0.08	0.17	0.22	0.25	0.28	0.30	0.32	0.33	0.35	0.36	0.37	0.38	0.39	0.40	0.41	0.41	0.42	0.43	0.43	0.43
N15SF5-S3%	0.00	0.10	0.18	0.23	0.27	0.30	0.32	0.34	0.35	0.36	0.37	0.38	0.38	0.39	0.40	0.41	0.42	0.42	0.43	0.43	0.44

ACKNOWLEDGEMENTS

ABOUT THE AUTHORS

Ariful Hasnat

Mr. Ariful Hasnat was a graduate research assistant when he worked on this research project. He obtained his Bachelor degree from the University of Asia Pacific, Bangladesh, and his Master's degree from the Bangladesh University of Engineering and Technology, Bangladesh

Nader Ghafoori, Ph.D

Dr. Nader Ghafoori is a professor in structure engineering in the Department of Civil and Environmental Engineering and Construction at the University of Nevada, Las Vegas. His research interests include durability, strength, and behavior of concrete systems; design and performance of advanced construction materials; rheology and workability of cement-based materials; optimization of chemical admixtures and supplementary cementitious materials in concrete; and use of industrial by-products and recycled aggregates in concrete. He has a Ph.D. in structure engineering from the University of Miami.